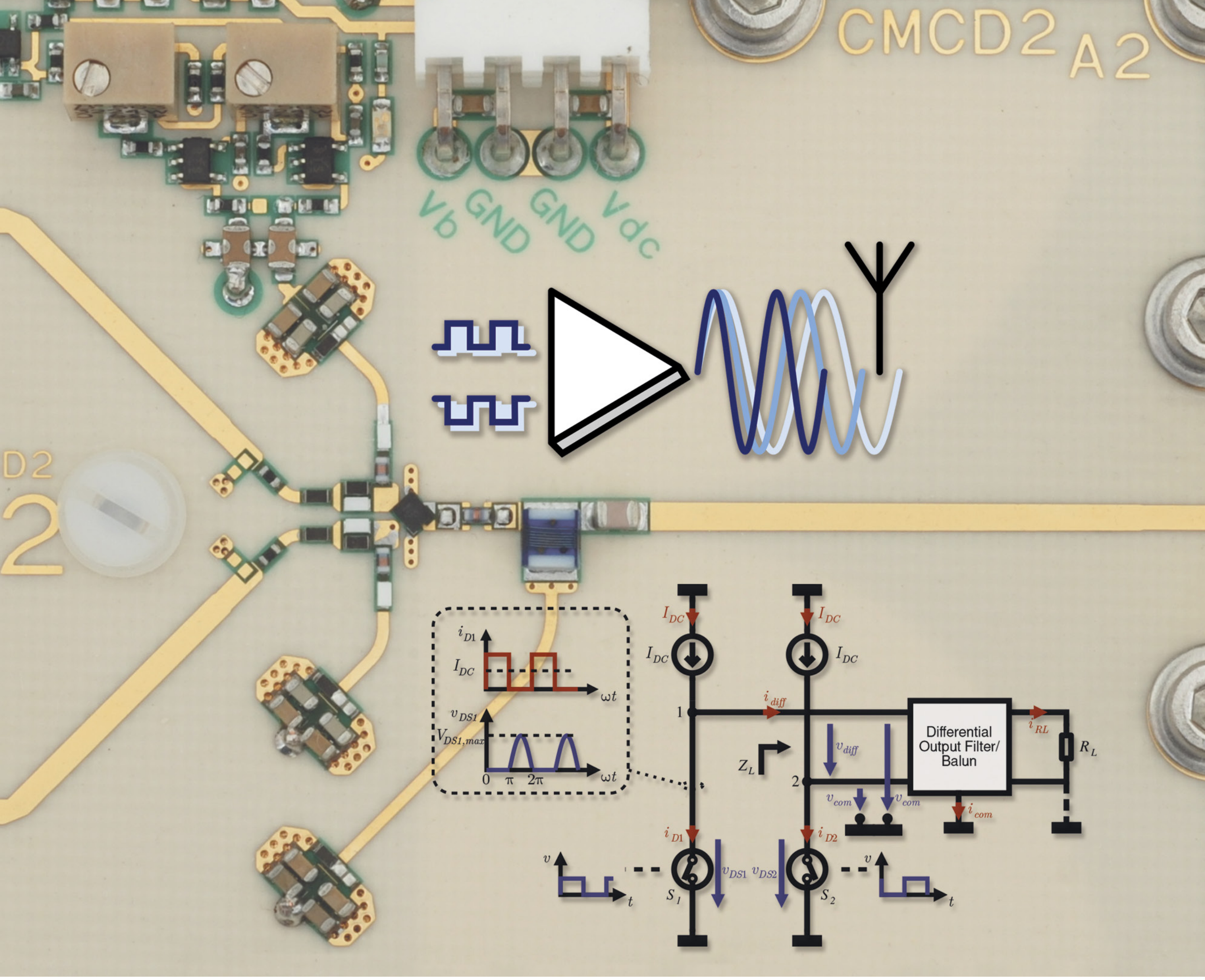

FAU Forschungen, Reihe B, Medizin, Naturwissenschaft, Technik 24

Michael Kamper

Differential Switched Mode RF Power Amplifiers

FAU
UNIVERSITY
PRESS

Michael Kamper

Differential Switched Mode RF Power Amplifiers

FAU Forschungen, Reihe B

Medizin, Naturwissenschaft, Technik

Band 24

Herausgeber der Reihe:
Wissenschaftlicher Beirat der FAU University Press

Michael Kamper

Differential Switched Mode RF Power Amplifiers

Erlangen
FAU University Press
2018

Bibliografische Information der Deutschen Nationalbibliothek:
Die Deutsche Nationalbibliothek verzeichnet diese Publikation in der Deutschen Nationalbibliografie; detaillierte bibliografische Daten sind im Internet über http://dnb.d-nb.de abrufbar.

Bitte zitieren als
Kamper, Michael. 2018. *Differential Switched Mode RF Power Amplifiers.* FAU Forschungen, Reihe B, Medizin, Naturwissenschaft, Technik Band 24. Erlangen: FAU University Press,
DOI: 10.25593/978-3-96147-152-2.

ORCID iD 0000-0001-5696-8801
Email michael.kamper@fau.de

Verlag und Auslieferung:

FAU University Press, Universitätsstraße 4, 91054 Erlangen

Druck: docupoint GmbH

ISBN: 978-3-96147-151-5 (Druckausgabe)
eISBN: 978-3-96147-152-2 (Online-Ausgabe)
ISSN: 2198-8102
DOI: 10.25593/978-3-96147-152-2

Differential Switched Mode RF Power Amplifiers

Differentielle geschaltete HF Leistungsverstärker

Der Technischen Fakultät der
Universität Erlangen-Nürnberg

zur Erlangung des Grades

DOKTOR-INGENIEUR

vorgelegt von

Michael Kamper

aus Neumarkt

Als Dissertation genehmigt von
der Technischen Fakultät der
Universität Erlangen-Nürnberg

Tag der mündlichen Prüfung:	7. März 2018
Vorsitzender des Promotionsorgans:	Prof. Dr.-Ing. Reinhard Lerch
Gutachter:	Prof. Dr.-Ing. Georg Fischer
	PD Dr. Rüdiger Quay

Acknowledgements

This thesis would not have been possible without the support of many people. First of all, I would like to express my gratitude to my supervisor Prof. Dr.-Ing. Georg Fischer for his guidance, support and motivation during my entire research. I also thank PD Dr. Rüdiger Quay from Fraunhofer IAF for his time spent on reviewing the thesis.

I would like to extend my gratitude to Gerald Ulbricht (Fraunhofer IIS) for giving me the opportunity to pursue my PhD study at the Radio Communication Systems Department of Fraunhofer IIS in collaboration with the Friedrich-Alexander-University Erlangen-Nürnberg (FAU). I am grateful to Prof. Dr.-Ing. Robert Weigel for giving me the opportunity to work at the Institute for Electronics Engineering (LTE) at FAU.

During my work at FAU and Fraunhofer IIS I had the chance to meet and work with numerous highly qualified and congenial people. From FAU I would like to express my gratitude to Christian Musolff, whose great idea to take part in the IEEE MTT-S power amplifier competition resulted in numerous fruitful discussions and a rapid learning curve in practical RF PA design. Long nights of lab work to optimize our PAs were rewarded with several 1st prizes. Many thanks go to Zeid Abou-Chahine for being part of the team as well. I would also like to mention Roman Agethen, Bernhard Höher and Andre Schwarzmeier, friends and fellow students on the way through the academic career path.

From Fraunhofer IIS I am grateful to Hans Adel, who assisted me with the antenna measurements. I also express my gratitude to Jan Bauer, Lars Weisgerber and Martin Wohler for their help with the antenna design and lots of useful hints. Thank you very much Alexander Popugaev for reviewing this thesis. I would like to thank my friends, colleagues and roommates at Fraunhofer IIS, namely Rafael Psiuk, Markus Polster, Johannes Arendt, Alexander Jaschke, Christian Kelm and Felix Auer for their encouragement, cooperation and for the good times we had. Many thanks go to Dmitrii Kondakov (St. Petersburg Polytechnic University) for his collaboration with the balun design and his friendship.

I am grateful to my family for supporting and encouraging me throughout my life. Especially, I would like to thank my parents for giving me the opportunity to follow my ambitions.

Finally, my heartfelt thanks go to my wife Oxana. I cannot imagine having completed this thesis without her love, endless patience and unlimited support.

Erlangen, July 2018
Michael Kamper

Summary

The continued, rapid evolution of wireless communication systems has been steadily shifting the focus of research onto the power amplifier (PA) in the transmission chain. On the one hand, new standards and the fragmentation of the frequency spectrum premise agile wideband, linear and efficient transmitters. On the other hand, the digitization of the analog radio frequency (RF) domain, carried out to realize flexible, low-cost software-defined radio transmitters, has reached the power amplifier.

Switched mode operation is used to implement a digital input interface and optimize the efficiency of RF amplifiers by minimizing the current-voltage overlap at the transistor. Differential (push-pull) operation is used to enhance the bandwidth of an amplifier by taking advantage of the symmetry to match even harmonics.

This work discusses differential switched mode operation to design simultaneously efficient and wideband PAs. Using the example of the current mode class-D (CMCD) amplifier, the required harmonic output impedances in differential and common mode are derived from the ideal waveforms. In order to implement the required output impedances with a large bandwidth, this thesis presents a novel manufacturing technique for a low-parasitic lumped-element output filter.

To attach a single-ended load to the differential PA, a balun is needed. The influence of output network imbalance on the efficiency is analyzed, to assess the required balun bandwidth. Furthermore, wideband and efficient planar baluns are examined and an optimized tapered planar balun for a PA bandwidth of up to 100% is offered.

A 100 mW demonstrator PA is built with this balun and with a balun-integrated lumped-element output filter. The drain efficiency is over 60% for a range of 415 MHz to 1100 MHz, which corresponds to a bandwidth of 90%. The PA maintains a drain efficiency of $>$70% and a power-added efficiency (PAE) of $>$67% for an octave bandwidth (500 MHz to 1 GHz). A high-power 25 W demonstrator PA is presented to verify the scalability of the proposed design methods for CMCD PAs. The measured peak drain efficiency is about 80% and the peak PAE is 72% at 635 MHz. The PA maintains high efficiency for an output power range of 7 W to 25 W. Therefore, this amplifier could be used, e.g., as the core PA of an EER (Envelope Elimination and Restoration) amplifier system.

Finally, the integration of antennas as differential loads for differential PAs is examined. An implementation of a dipole integrated 100 mW CMCD PA, a so-called “amplitenna”, is offered. The measured over-the-air (OTA) peak

efficiency is within a range of 67% to 81% at 870 MHz and includes the resistive and matching losses of the antenna.

This thesis achieves important progress towards the goal of a fully digital RF power amplifier. The potentials of differential switched mode PAs are demonstrated both by theoretical analyses and practical implementations. The presented methods and solutions can contribute to the design of PAs with improved performance, such as enhanced efficiency and bandwidth.

Kurzfassung

Die kontinuierlich, rasant fortschreitende Weiterentwicklung von drahtlosen Kommunikationssystemen, lenkt den Forschungsfokus auf den Leistungsverstärker in der Sendekette. Einerseits erfordern neue Standards und die Fragmentierung des Frequenzspektrums agile Sendesysteme mit hoher Bandbreite, Linearität und Effizienz. Andererseits ist die Digitalisierung der analogen HF Signalverarbeitungskette, die nötig ist um flexible und kostengünstige Sendesysteme (Stichwort „Software Defined Radio, SDR”) zu realisieren, beim Leistungsverstärker angelangt.

Der Schaltbetrieb von HF Leistungsverstärkern wird zur Effizienzoptimierung angewandt, indem die verlustbehaftete Überlappung von Strom und Spannung am Transistor vermieden wird. Des Weiteren ermöglicht der Schaltbetrieb eine digitale Ansteuerung des Verstärkers. Der differentielle (auch: Gegentakt-) Betrieb wird zur Erhöhung der Bandbreite von Verstärkern verwendet und nutzt die inhärente Terminierung geradzahliger Harmonischer durch einen symmetrischen Aufbau.

Diese Arbeit behandelt den differentiellen Schaltbetrieb um Leistungsverstärker zu ermöglichen, die gleichzeitig effizient sind und eine hohe Bandbreite aufweisen. Am Beispiel eines stromgesteuerten Klasse-D-Verstärkers (Current Mode Class-D, CMCD) werden die nötigen harmonischen Impedanzen des Ausgangsnetzwerkes im Gleich- und im Gegentakt aus den idealen Strom- und Spannungsverläufen abgeleitet. Um die nötigen Ausgangsimpedanzen über eine große Bandbreite implementieren zu können, wird in dieser Arbeit eine neuartige Aufbautechnik zur HF-optimierten Anbindung von konzentrierten Bauelementen im Ausgangsfilter vorgestellt.

Um eine erdbezogene Last an einen differentiellen Verstärker anzuschließen, wird ein Balun benötigt. Zur Abschätzung der erforderlichen Bandbreite für den Balun wird der Einfluss einer Asymmetrie im Ausgangsnetzwerk auf die Effizienz analytisch untersucht. Im Weiteren werden breitbandige und effiziente planare Balunstrukturen behandelt. Ein optimierter konisch-zulaufender (tapered) Balun in Streifenleitungstechnik für Verstärker mit Bandbreiten von bis zu 100% wird vorgestellt.

Anschließend wird ein 100 mW Verstärker mit diesem Balun und dem optimierten Ausgangsfilter aufgebaut. Der Prototyp erreicht eine Draineffizienz von über 60% im Bereich von 415 MHz bis 1100 MHz, was einer Bandbreite von 90% entspricht. Im Bereich einer Oktave (500 MHz bis 1 GHz) wird sogar eine Draineffizienz von über 70% und eine leistungsaddierte Effizienz (PAE)

von über 67% erreicht. Um die Skalierbarkeit der Designmethoden für CMCD Verstärker zu demonstrieren, wird ein Verstärker mit höherer Leistung (25 W) vorgestellt. Dieser Prototyp erreicht eine Spitzeneffizienz von 80% und eine PAE von 72% bei 635 MHz. Über einen Bereich von 7 W bis 25 W wird eine hohe Effizienz beibehalten. Daher eignet sich dieser Verstärker als Teil eines Systems mit Versorgungsspannungsmodulation (Envelope Elimination and Restoration, EER).

Im letzten Schritt wird die Integration von Antennen als differentielle Last eines ebenfalls differentiellen Verstärkers untersucht und ein Prototyp eines 100 mW Klasse-D-Verstärkers mit Dipolantenne (Stichwort: „Amplitenna") entwickelt. Die gemessene Spitzeneffizienz der abgestrahlten Leistung liegt im Bereich von 67% bis 81% bei 870 MHz und beinhaltet die Verluste an der Antenne.

Diese Arbeit ist ein wichtiger Schritt hin zur Realisierung eines volldigitalen HF Leistungsverstärkers. Die Vorteile des differentiellen Schaltbetriebs werden sowohl auf theoretischer Basis, als auch in Form von praktischen Aufbauten demonstriert. Die vorgestellten Methoden können als Grundlage zur Entwicklung von verbesserten Verstärkern hinsichtlich Effizienz und Bandbreite dienen.

Contents

1 Introduction and Motivation

1.1 Motivation

The digitalization of the world has started with the information age. Nowadays, analog information is represented, saved and processed by binary symbols. With ADCs and DACs[1] operating in the GSa/s domain, analog signals can be recorded and reproduced with a high dynamic range at microwave frequencies. Anti-aliasing and reconstruction filters are used to remove quantization noise.

Similar to analog information, analog power can be represented and processed by a binary coded stream of quantized "packets" of energy. Class-D audio amplifiers use switched transistors in conjunction with a reconstruction filter in order to efficiently convert a binary encoded audio signal from the digital into the analog domain at a high power for the purpose of driving a speaker. In the same way, switched mode radio frequency (RF) power amplifiers (PA) convert a binary encoded RF signal into a high-power analog signal to drive an antenna.

Digital audio amplifiers operate at relatively low switching speeds in the MHz range and can be implemented with state-of-the-art MOS[2] transistor technologies. The reconstruction filter can be designed from simple lumped capacitive and inductive components. Switched mode RF PAs require the transistors to run at GHz switching speeds. Advanced power transistors and reconstruction filters are needed and parasitic properties of the components have to be identified and either minimized or embedded in the design.

The following sections will motivate RF switched mode operation from different perspectives: PA efficiency, system design and RF bandwidth.

1.1.1 Principle Function of Switched Mode Power Amplifiers

A power amplifier is a three-port device. It consists of an input port which supplies the input power P_{in}, an output port with the output power P_{out} and a DC supply port with P_{DC}. It is mainly defined by gain, linearity, bandwidth and efficiency.

---

[1] ADC: analog-to-digital converter; DAC: digital-to-analog converter

[2] MOS: metal oxide semiconductor

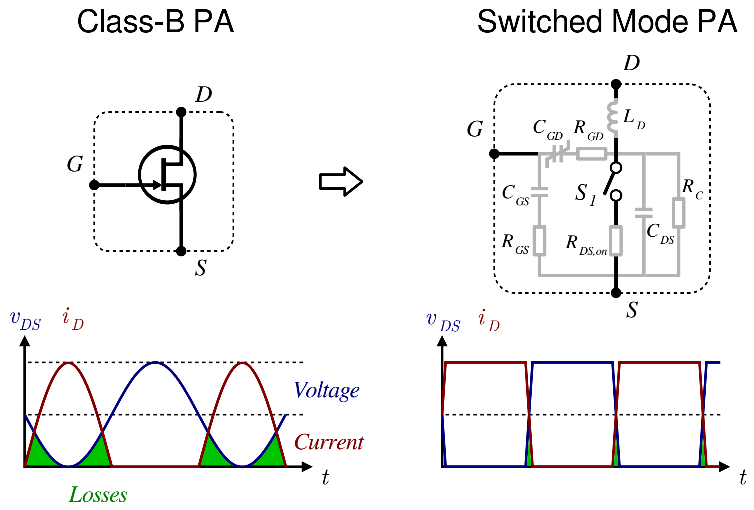

Figure 1.1.: High-efficiency operation of a transistor in switched mode

Gain is the relationship of P_{in} and P_{out} and linearity indicates how good P_{out} represents P_{in} scaled by the gain. Efficiency is the relationship of P_{DC} and P_{out} and bandwidth shows the behavior on the frequency axis.

Two basic amplifier operating points can be differentiated:

- In a linear amplifier the transistor is used as a transconductance device.
- In a switched mode amplifier the transistor is used as a switch.

A transconductance device in linear operation has a voltage-current overlap. The drain-to-source voltage v_{DS} and the drain current i_D of a class-B amplifier is indicated in Fig. 1.1. By overdriving the transistor at the input, compression occurs at the output, hence, losses from voltage-current overlap are reduced.

A high frequency switched mode operation places special demands on the transistor. To drive the transistor far into compression, a high RF gain is required. And, as Fig. 1.1 indicates, switched mode waveforms are broadband due to their harmonic frequency content. Therefore, parasitic elements at the input and output of the active device have to be considered and either have to be compensated or minimized, depending on the amplifier circuit concept.

Switched mode operation implies that the input signal is a “digital” binary waveform and, therefore, no amplitude information can be amplified.

1.1.2 Motivation - Efficiency

A discussion about the efficiency of a power amplifier is a discussion about losses. Losses in power amplifiers mainly occur due to losses at the active element, the transistor. The passive circuitry of the output network induces additional losses. However, dissipation at the transistor is defined by the voltage and current waveforms at the transistor and therefore by the amplifier class. Thus, the power loss at the transistor $P_{T,loss}$ is

$$P_{T,loss} = \frac{1}{T} \int_{0}^{T} v_{DS}\left(t\right) \cdot i_{D}\left(t\right) dt. \tag{1.1}$$

With the definition of drain efficiency $\eta = \frac{P_{out}}{P_{DC}}$ the drain efficiency η_{ideal} of the ideal (lossless) power amplifier is

$$\eta_{ideal} = \frac{P_{DC} - P_{T,loss}}{P_{DC}} = 1 - \frac{P_{T,loss}}{P_{dc}}. \tag{1.2}$$

The peak efficiency of the ideal power amplifier is:

- $\eta_{ideal} = 78.5\%$ in class-B due to the voltage-current overlap of a half-wave rectified sine waveform and a full sine waveform [1].
- $\eta_{ideal} = 100\%$ in switched mode due to no voltage-current overlap.

In both cases (linear and switched mode) the output waveforms have a harmonic frequency content. Therefore, η_{ideal} premises an infinite harmonic bandwidth with an ideal harmonic matching network for class-B as well as for switched mode operation. However, compared to the theoretical 78.5% in class-B, only in switched mode operation 100% efficiency can be reached. In reality the parasitic properties of the transistor (e.g. on-resistance) limit the efficiency.

The binary nature of the RF input signal does not allow amplitude information to be amplified. Therefore, backoff operation is not possible in switched mode. To a certain degree, amplitude variations can be transmitted if a class-B operating point is chosen in backoff.

Advanced PA concepts involving switch mode amplifiers enable high-efficiency backoff operation through supply modulation (Envelope Elimination and Restoration, EER), load modulation (outphasing PA) and input oversampling (class-S PA).

1.1.3 Motivation - System Design

Certain advantages of switch mode operation can be identified from a system design perspective, in particular the implementation of low-cost transmitters and the immunity to reverse intermodulation.

In switched mode operation only a change of frequency is possible and the amplitude information is suppressed. Therefore, the modulation signal has to have a constant envelope. Suitable modulation schemes are, e.g., frequency modulation (FM) or, more generally speaking, modulation signals with a continuous phase change. The term continuous phase modulation (CPM) denominates this family of modulation schemes.

A popular CPM implementation is minimum-shift keying (MSK, Fig. 1.2).

The power efficiency of CPM waveforms is very high [2]. However, the spectral efficiency of complex modulation schemes (e.g., quadrature amplitude modulation, QAM or orthogonal frequency division multiplexing, OFDM) is higher compared to CPM. Additionally, the implementation complexity of an optimal CPM receiver is higher. On the other hand, the implementation complexity of the transmitter rises with linearity requirements and therefore with the signal complexity.

The use of a switched mode transmitter is subject to the communication scenario (Fig. 1.3):

- In a broadcast scenario (e.g., terrestrial digital video broadcast, 2nd generation, DVB-T2) a single complex transmitter feeds multiple simple, low-cost

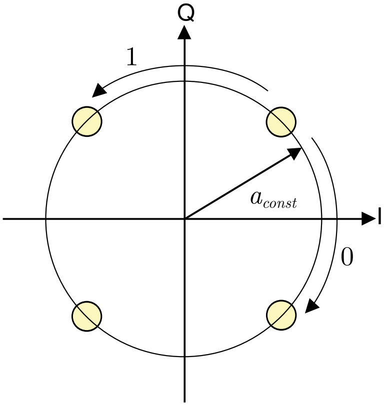

Figure 1.2.: Minimum shift keying - a continuous phase change of $\frac{\pi}{2}$ encodes the digital information

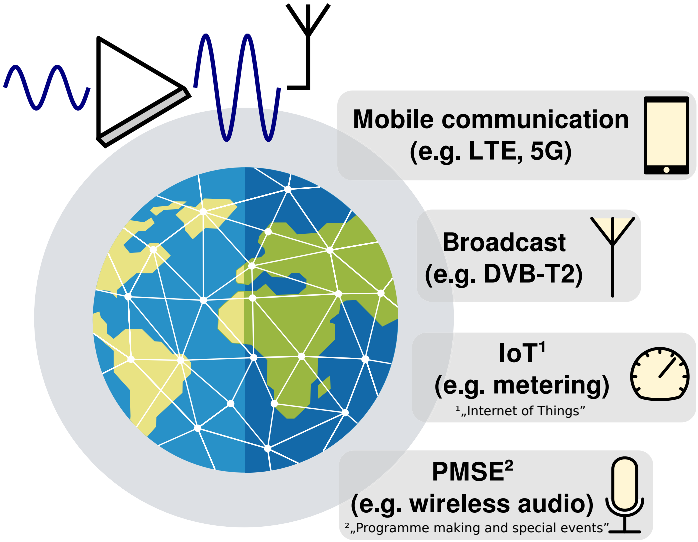

Figure 1.3.: Popular communication scenarios

receivers. The data rate is high and, therefore, OFDM is a suitable modulation scheme with a high spectral efficiency.

- In an Internet of Things (IoT) scenario (e.g., for wireless meter reading) multiple low-cost, efficient transmitters (often battery powered) are accompanied by a single complex and sensitive receiver. The data rate is low and CPM (e.g., MSK) is a suitable modulation scheme with a high power efficiency.

- In a program making and special events (PMSE) scenario (e.g., wireless audio links) low-cost, efficient transmitters (often battery powered) feed complex sensitive receivers. Medium data rates with CPM (e.g., FM, MSK) yield a high power efficiency.

- In a mobile communication scenario (e.g., cellular phone networks) the communication downlink consists of a complex transmitter (base station) and a simple receiver (handset). The data rates are high and, therefore, OFDM is a suitable modulation scheme just like in the broadcast scenario. In the communication uplink a simple efficient transmitter (battery powered handset) is accompanied by a complex receiver (base station). The data rate is medium. Modulation schemes with a relatively high power and spectral efficiency are single-carrier waveforms with a low crest factor.

> For instance, in long term evolution (LTE) the handset uses single-carrier frequency-division multiple access (FDMA) [3].

To sum up, a transmitter with a switched mode power amplifier is most suitable for IoT and PMSE scenarios using CPM modulation schemes. In mobile communication the data uplink might as well be implemented with a switched mode PA.

The reverse intermodulation distortion is also known as transmitter intermodulation and indicates the distortion products which are excited by feeding RF power reversely into the transmitter output. It is an important measure that has to be considered in environments, where high extrinsic power levels have to be expected like mobile communication networks as well as telemetry and multimedia networks.

In [4] the author has shown that switched mode operation produces less transmitter intermodulation compared to a linear amplifier class, that is, a switched mode amplifier is more robust to extrinsic signals.

Summing up, from a system designers view switched mode PAs are suitable for simple, robust and efficient transmitters. This includes battery powered applications, transmitters without digital pre-distortion (DPD), applications with high extrinsic power levels and applications with low to medium data rates.

Switched mode operation is more than just efficiency optimization.

1.1.4 Motivation - RF bandwidth

Fig. 1.4 shows a diagram with four quadrants depicting amplifier linearity versus RF bandwidth. In opposition to linear PAs, switched mode operation is limited to applications requiring low linearity and a low RF bandwidth.

In recent years, however, PMSE or IoT applications are moving towards higher RF bandwidths. The main reason is an increased design flexibility, which is necessary due to

- the fragmentation of the frequency spectrum as a result of the worldwide reallocation of, e.g., television (TV) whitespace [5, 6],
- wideband frequency hopping, e.g., for telegram splitting [7] and the use of carrier aggregation (CA) in fourth and fifth generation (4G, 5G) mobile services.

Therefore, wideband switched mode PAs are needed. The harmonic matching network of a switched mode PA fundamentally limits the bandwidth. However, differential circuits can help to shift these limits (see Section 2.2 of this work).

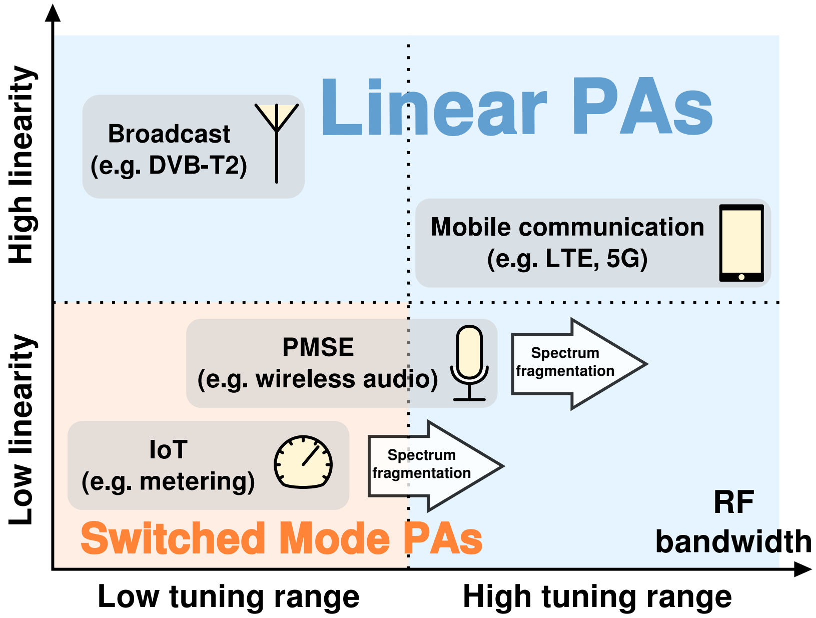

Figure 1.4.: Linearity and RF bandwidth requirements of different communication scenarios - wideband switched mode PAs are needed due to spectrum fragmentation

1.2 Thesis Contribution

The aim of this work is to

- motivate the use of differential (i.e., push-pull) architectures for switched mode power amplifiers,
- present solutions for flexible, efficient and wideband switched mode amplifiers.

The author's main contributions are

- the analysis of the output network and the required harmonic termination of the current mode class-D amplifier,
- the study of wideband and efficient planar baluns for current mode class-D amplifiers,
- the development of a novel manufacturing technique of a balun-integrated lumped-element output network,

- the integration of antennas as differential loads for current mode class-D amplifiers.

Several authors have published papers on differential current mode class-D (CMCD) PAs [8–11]. However, the presented amplifiers are mostly narrowband or optimized for a single frequency.

A few papers have studied the optimum waveforms and impedances for differential (push-pull) switched mode operation [12–14]. Differential large-signal measurements are demonstrated in [15]. The harmonic impedance of differential structures has not been calculated analytically.

Several papers on wideband class-F PAs have been published as well [16, 17]. The harmonic matching network fundamentally limits the bandwidth to less than an octave.

Wideband baluns for differential PAs have been studied in literature [18, 19]. However, planar implementations suffer from high losses [20]. Coaxial baluns are bulky and, as [19] states, "[...] each balun is assembled by hand, the quality of the assembly is variable and it is difficult to find faults in the balun once the whole PA has been assembled".

Equivalent circuit models for baluns have been developed in [20]. They have not been verified or extended for broadside coupled and tapered baluns.

A few authors have examined the integration of antennas with power amplifiers [21], including the harmonic tuning for class-F PAs [22]. However, the integration of differential loads with switched mode PAs has not been studied yet. Over-the-air (OTA) measurements of such designs have been demonstrated [23]. A comparative measurement of two independent methods has not been shown yet.

1.3 Thesis Outline

This thesis can be divided into two parts. Chapters 1 to 3 (mainly) show the state-of-the-art, whereas chapters 4 to 6 describe the author's contributions.

Chapter 1 motivates the use of switched mode power amplifiers.

Chapter 2 defines the ideal switched mode amplifier and shows the fundamental bandwidth limitations in single-ended and differential configuration. Afterwards, the differential current mode class-D (CMCD) amplifier is introduced.

Chapter 3 gives a short introduction of RF power transistors. Afterwards, the theory and limits of switched mode operation are discussed on the basis of a simplified switched mode transistor model. The chapter is completed by a look at the input signal, the input network and amplifier stability in switched mode operation.

After a short introduction to mixed mode S-parameters, Chapter 4 discusses the output network of differential switched mode PAs. The calculation of ideal harmonic impedances is followed by a discussion of output network imbalance, which is mostly caused by the balun. After the analysis of the DC supply network, optimized output filters, which are needed to implement the harmonic impedances, are calculated and compared. Finally, the author offers a novel manufacturing technique for low-parasitic lumped-element output networks.

Chapter 5 discusses wideband and low-loss baluns for differential PAs. An introduction to coupled line baluns is followed by an analysis of an enhanced balun model. Tapered structures offer a wider bandwidth and two tapered balun implementations are therefore compared. Finally, the theory of wideband CMCD operation is supported by a wideband class-D demonstrator PA. A second high-power PA shows the scalability of the concept.

Chapter 6 motivates the integration of differential switched mode PAs into differential antennas. After an introduction to the input impedance of thin linear dipoles and an overview of wideband antennas, a so-called “amplitenna” is implemented. An over-the-air (OTA) measurement in an anechoic chamber completes the chapter.

2 Differential Switched Mode Power Amplifiers

This chapter discusses differential switched mode amplifiers. After an introduction to the requirements and the building blocks of an ideal switched mode amplifier, differential architectures are motivated by a closer look at the bandwidth limiting features of efficient amplifier classes. Afterwards, the differential current mode class-D amplifier is presented and its loss mechanisms are identified and calculated.

The main contribution of this chapter is the calculation of the maximum theoretical bandwidth in single-ended and differential switched mode configuration.

2.1 The Ideal Switched Mode Amplifier

Generally, there are two competing requirements for the RF signal at the transistor and at the output of an efficiency optimized power amplifier. At the transistor, an efficient waveform with no voltage-current overlap and therefore a high η_{ideal} is desired. However, at the PA output an amplified representation of the input signal with low harmonic and spurious signal content is requested.

The demand for a transistor waveform with no voltage-current overlap leads to the first requirement for every switched mode amplifier: the transistor is driven into switching operation. However, every periodic switching process is associated with a fast change of voltage $\frac{dv}{dt}$ or current $\frac{di}{dt}$ in the time domain and, therefore, a harmonic voltage or current spectrum in the frequency domain in addition to the fundamental component. This harmonic spectrum is unwanted at the output not only due to regulatory issues. The harmonic voltages or currents are absorbed by the load and add up to the total power loss, thus they degrade the efficiency of the amplifier.

The generation of harmonic voltages or currents is inherent in a switched mode system, hence they have to be isolated from the load in a non-resistive, reflective way. In other words, the proper harmonic output impedances have to be set, the second requirement for ideal switched mode amplifier design. Harmonic impedance termination can be done either by one or more frequency dependent and reflective filters or by choosing a design topology with intrinsically matched harmonics, e.g., differential amplifiers.

Fig. 2.1 explains the harmonic tuning using the example of the inverse class-F amplifier. The DC biased transistor is modeled as a switched current source and,

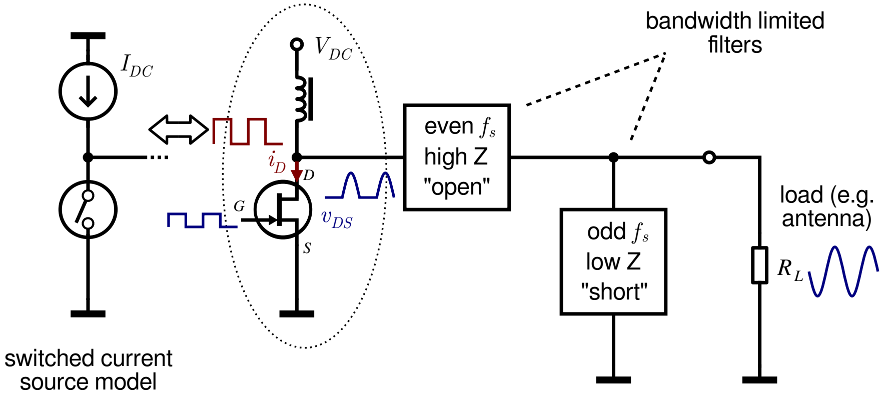

Figure 2.1.: Inverse class-F amplifier with harmonically tuned output filters

therefore, a rectangular drain current with odd harmonics appears at the output. The odd harmonics are shorted by a filter. The voltage at the transistor is shaped to a half-wave rectified sine signal with even harmonics by a high impedance output filter. Thereby efficient voltage and current waveforms at the transistor are synthesized.

As shown in Fig. 1.1, a transistor in switched mode is modeled as a switch with parasitic resistive, inductive and capacitive elements. The reactive components are quickly charged and discharged during switching and this energy is usually entirely absorbed in parasitic resistive elements. Therefore, a switching at zero voltage (ZVS) or at zero current (ZCS) is highly desired, which is the third requirement for an ideal switched mode PA.

Last but not least, the power gain is crucial in every switched mode amplifier system. For example, a gain of only 10 dB reduces the power-added efficiency (PAE, [24]) by up to 10%. In linear operation, the gain of the amplifier is optimized by matching the impedance of the RF source to the capacitive input reactance of the transistor. In switched mode operation, the transistor is by far in compressive region, which highly reduces the amplifier gain. Additionally, the input is slightly detuned by the nonlinear capacitive feedback of the output to the input (C_{GD} in Fig. 1.1). Therefore, a high gain in linear operation and subsequently in switched mode is the fourth requirement for every ideal switched mode PA.

Table 2.1 sums up the four prerequisites for ideal switched mode amplifier design.

Table 2.1.: Requirements for the ideal switched mode power amplifier with high efficiency and low distortion

1. Transistor in switching operation
2. Proper harmonic output impedances
3. Zero voltage / zero current switching
4. High gain

2.2 Bandwidth Limitations

An inverse class-F amplifier has to be tuned for all harmonic frequencies individually using band-limited reflective filters with high and low impedance Z (Fig. 2.2 (left)). Fig. 2.2 (right) shows a symmetrically extended version of the inverse class-F PA, the so-called current mode class-D (CMCD) amplifier. The CMCD amplifier involves a differential signal output, therefore the load has no reference to ground. At first sight this attribute will emerge negative qualities, like the necessity of a bandwidth limiting and lossy balun to attach single-ended loads. However positive features can be derived from the symmetry of the CMCD design.

At the two transistor drains of the CMCD PA a half-rectified voltage waveform appears, just like in inverse class-F (Fig. 2.1). The fundamental content of these two voltage waveforms is in opposite phase. However, the even harmonic content (2nd, 4th, ...) is in-phase (this will be later calculated in Section 2.3.1). Therefore, the harmonic spectrum is high-impedance (assuming an ideal symmetric load). This means that in differential CMCD configuration the even harmonics are inherently matched and no filters are needed.

Let us have a look at an inverse class-F power amplifier with second and third harmonic frequency controlled impedances at the frequency axis (Fig. 2.3). The tuned harmonic bandwidth regions are defined by their lower (f_{Ln}) and upper (f_{Un}) edges. In single-ended configuration, the maximum bandwidth $B_{max} = f_{max} - f_{min}$ is defined by the upper edge of the second harmonic filter f_{U2} and the lower edge of the third harmonic filter f_{L3} by

$$f_{U2} = f_{L3}. \tag{2.1}$$

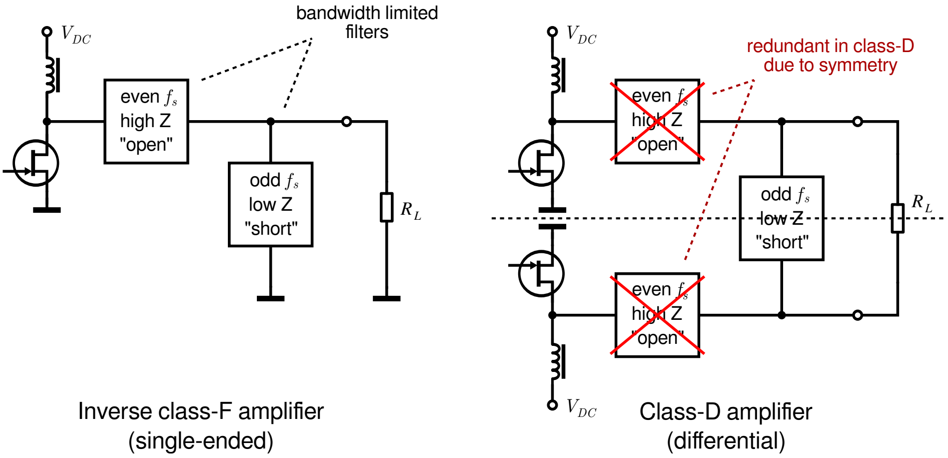

Figure 2.2.: Filter configuration of harmonically tuned amplifiers in single-ended and differential configuration

Taking into account the harmonic relationships $f_{U2} = 2 \cdot f_{U1}$ and $f_{L3} = 3 \cdot f_{L1}$ and the definition for the percent bandwidth $B_{\%}$,

$$B_{\%} = 2 \cdot \frac{f_{U1} - f_{L1}}{f_{U1} + f_{L1}}, \tag{2.2}$$

the maximum inverse class-F bandwidth $B_{\%,classF}$ can be calculated to

$$\boxed{B_{\%,classF} = 2 \cdot \frac{\frac{1}{2}f_{U2} - \frac{1}{3}f_{U2}}{\frac{1}{2}f_{U2} + \frac{1}{3}f_{U2}} = 40\%}. \tag{2.3}$$

In this example it is tolerated that the 3rd and 4th harmonic overlap and the 4th harmonic is not tunable for the whole bandwidth. Limiting the controlled impedance space to only the first three harmonic frequencies is usually sufficient to achieve a high efficiency [25].

The differential class-D amplifier involves inherently tuned even harmonics (Fig. 2.3), therefore B_{max} can be extended till the lower edge of the third harmonic filter f_{L3} by

$$f_{U1} = f_{L3}. \tag{2.4}$$

With $f_{L3} = 3 \cdot f_{L1}$, the maximum class-D bandwidth $B_{\%,classD}$ is defined to

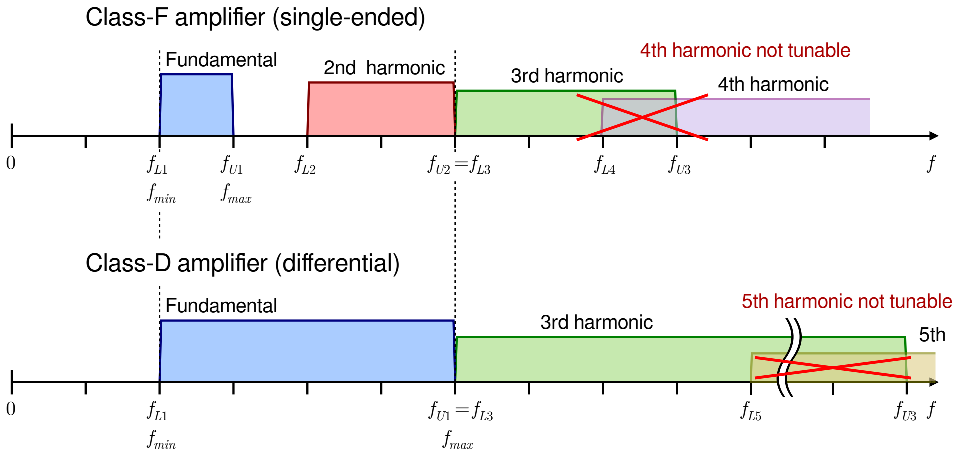

Figure 2.3.: Bandwidth of harmonically tuned amplifiers in single-ended and differential configuration

$$\boxed{B_{\%,classD} = 2 \cdot \frac{f_{L3} - \frac{1}{3} f_{L3}}{f_{L3} + \frac{1}{3} f_{L3}} = 100\%}. \tag{2.5}$$

Similar to the inverse class-F case, the 5th harmonic frequency is not tunable for this bandwidth configuration.

To sum up, one can say, that the differential configuration (current mode class-D) offers a considerably higher tunable bandwidth of 100% compared to the single-ended inverse class-F amplifier (40%) with the assumption that the 2nd and 3rd harmonic frequencies can be tuned over the whole bandwidth.

2.3 The Current Mode Class-D Amplifier

2.3.1 Ideal CMCD Amplifier

Fig. 2.4 shows the ideal class-D amplifier in the current mode configuration. It uses two active devices, shown as switches, that are both tied to ground [4]. The active devices switch a constant current I_{DC} in push-pull operation at a differential output load. The inverse configuration is the voltage mode class-D (VMCD) amplifier with two stacked switches and a switched voltage source at a single-ended load. The VMCD is uncommon in discrete RF design due to difficulties involved with the floating source connection of the upper transistor.

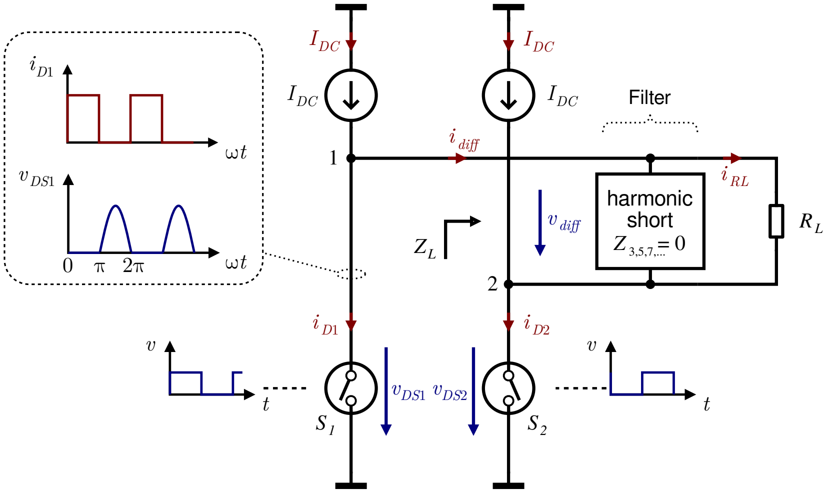

Figure 2.4.: Ideal current mode class-D (CMCD) amplifier configuration

On the other hand, an additional balun is required to attach a single-ended load at the CMCD.

The two switches S_1 and S_2 represent the transistors and are driven by 180° phase-delayed input signals at the switching frequency f_s. The constant current I_{DC} by the two current sources is switched and, therefore, the drain currents i_{D1} and i_{D2} have a rectangular shape. The drain current can be mathematically described by its Fourier series:

$$i_{D1/2}\left(\omega t\right) = I_{DC}\left[1 \pm \frac{4}{\pi}\sum_{n=1,3,5,...}^{\infty}\frac{1}{n}\sin\left(n\omega t\right)\right]. \tag{2.6}$$

The peak current $I_{D,max}$ at the switches is twice the DC current I_{DC}.

$$\boxed{I_{D,max} = 2 \cdot I_{DC}} \tag{2.7}$$

The differential output current $i_{diff}\left(\omega t\right)$ is given by the difference of the drain currents i_{D1} and i_{D2}:

$$i_{\mathit{diff}}\left(\omega t\right)=\frac{1}{2}\left(i_{D2}\left(\omega t\right)-i_{D1}\left(\omega t\right)\right)=-I_{DC}\left[\frac{4}{\pi}\sum_{n=1,3,5,\dots}^{\infty}\frac{1}{n}\sin\left(n\omega t\right)\right]. \tag{2.8}$$

The output filter is tuned to f_s and short-circuits harmonic content of the rectangular current $i_{\mathit{diff}}\left(\omega t\right)$, thus the load current $i_{RL}\left(\omega t\right)$ through the load R_L is reduced to the fundamental component. $\hat{v}_{\mathit{diff}}$ is the amplitude of the voltage at R_L. It is related to I_{DC} by

$$\hat{v}_{\mathit{diff}}=R_L\cdot\hat{i}_{RL}=R_L\cdot\frac{4}{\pi}I_{DC}. \tag{2.9}$$

With $\hat{v}_{\mathit{diff}}$ and R_L, the output power P_{out} of the CMCD can be calculated to

$$\boxed{P_{out}=\frac{1}{2}\frac{\hat{v}_{\mathit{diff}}^2}{R_L}=\frac{8}{\pi^2}R_LI_{DC}^2}. \tag{2.10}$$

The drain-source voltage waveforms $v_{DS1}\left(\omega t\right)$ and $v_{DS2}\left(\omega t\right)$ are defined by

$$0\leq\omega t\leq\pi,\ S_1\text{ on (closed)}, S_2\text{ off (open)}:\begin{cases}v_{DS1}\left(\omega t\right) & =0\\ v_{DS2}\left(\omega t\right) & =-v_{\mathit{diff}}\left(\omega t\right)\end{cases} \tag{2.11}$$

$$\pi\leq\omega t\leq 2\pi,\ S_1\text{ off (open)}, S_2\text{ on (closed)}:\begin{cases}v_{DS1}\left(\omega t\right) & =v_{\mathit{diff}}\left(\omega t\right)\\ v_{DS2}\left(\omega t\right) & =0\end{cases} \tag{2.12}$$

with

$$v_{\mathit{diff}}\left(\omega t\right)=\hat{v}_{\mathit{diff}}\sin\left(\omega t\right)=R_L\cdot\frac{4}{\pi}I_{DC}\sin\left(\omega t\right). \tag{2.13}$$

From equations 2.11, 2.12 and 2.13, one can conclude that the voltages at the switches have a half-wave rectified sine shape with the maximum drain voltage $V_{DS,max}=\hat{v}_{\mathit{diff}}$.

The drain-source voltage $v_{DS1/2}\left(\omega t\right)$ can be mathematically described by its Fourier series with

$$v_{DS1/2}\left(\omega t\right) = \frac{1}{\pi}\hat{v}_{diff}\left[1 \pm \frac{\pi}{2}\sin\left(\omega t\right) - \sum_{n=2,4,6,\ldots}^{\infty}\frac{2}{n^2-1}\cos\left(n\omega t\right)\right]. \quad (2.14)$$

One can see that the drain fundamental voltages of $v_{DS1}\left(\omega t\right)$ and $v_{DS2}\left(\omega t\right)$ appear in opposite phase (ωt-term), whereas the harmonic voltages appear in-phase ($n\omega t$-term). This is important for the calculation of the maximum bandwidth of the class-D amplifier in Section 2.2 and the harmonic termination in Chapter 4.

Fig. 2.5 sums up the current and voltage waveforms at the switches of the current mode class-D amplifier. There is no current-voltage overlap, i.e., no inherent losses at the active devices. Additionally the currents are switched at the voltage minimum - there is a zero voltage switching (ZVS) condition.

Fig. 2.6 shows a practical lumped element implementation of the current mode class-D amplifier. The ideal switches are implemented using field effect transistors (FETs T_1 and T_2). The ideal current sources are replaced by DC voltage sources V_{DC} with inductors (L_{RFC}, radio frequency chokes). The output filter is designed as a simple LC parallel tank circuit with L_P and C_P tuned to the switching frequency f_s. Additionally, a balun is added to attach the single-ended load R'_L.

I_{DC} can be expressed by V_{DC} as follows. The radio frequency chokes L_{RFC} force the average voltage during half a cycle of $v_{diff}\left(\omega t\right)$ to be equivalent to V_{DC} [9]:

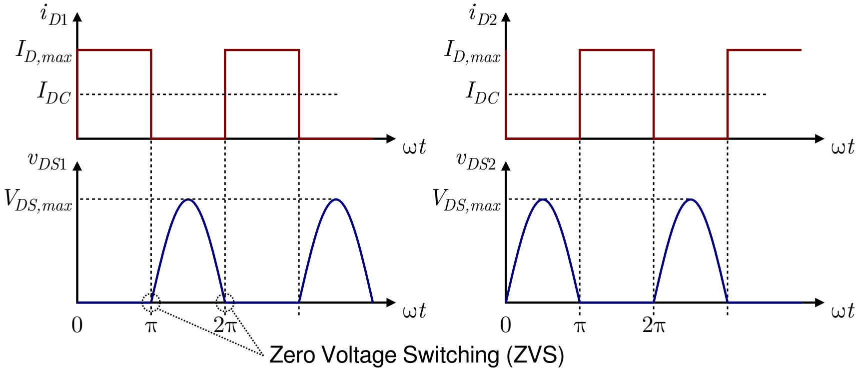

Figure 2.5.: Ideal CMCD current and voltage waveforms

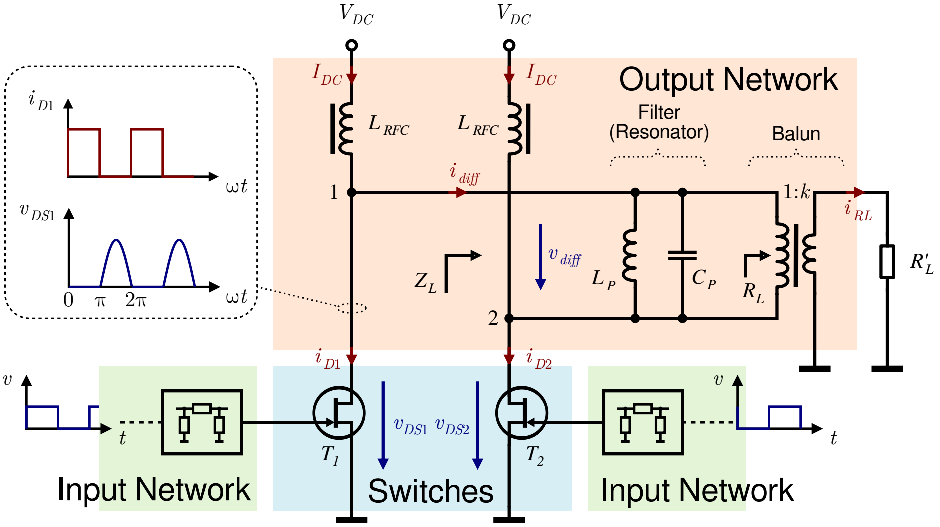

Figure 2.6.: Lumped element current mode class-D amplifier implementation and building blocks

$$\frac{1}{2\pi}\int_{0}^{\pi} v_{diff}(\omega t)d\omega t = V_{DC}. \tag{2.15}$$

With 2.13 the differential voltage amplitude $\hat{v}_{diff}$ is included to

$$\boxed{\hat{v}_{diff} = V_{DS,max} = \pi \cdot V_{DC}}. \tag{2.16}$$

The DC current I_{DC} is then given by

$$I_{DC} = \frac{\pi^2}{4} \cdot \frac{V_{DC}}{R_L}. \tag{2.17}$$

The optimum output load R_L expressed by V_{DC} and I_{DC} is

$$\boxed{R_L = \frac{\pi^2}{4} \cdot \frac{V_{DC}}{I_{DC}}}. \tag{2.18}$$

The balun transforms the differential output signal to attach the single-ended load R'_L. The transformation ratio of $1 : k$ yields the output resistance ratio

$$\boxed{R_L = k \cdot R'_L}. \tag{2.19}$$

The total output power P_{out} expressed by V_{DC} is

$$\boxed{P_{out} = \frac{1}{2}\frac{\hat{v}_{diff}^2}{R_L} = \frac{\pi^2}{2}\frac{V_{DC}^2}{R_L} = \frac{\pi^2}{2}\frac{V_{DC}^2}{k \cdot R_L'}}. \tag{2.20}$$

Fig. 2.6 depicts three different building blocks of the CMCD PA, which will be examined independently:

- *Input network*: Input matching network and DC-bias feed of the switched transistors,
- *Switches*: Switched RF transistors,
- *Output network*: DC-supply feed of the switched transistors, harmonic output matching network and balun function.

Chapter 3 of this work gives an overview of RF transistors in switched mode operation and optimized input matching networks. Chapters 4, 5 and 6 focus on the design of the output network.

2.3.2 Real CMCD Amplifier and Loss Mechanisms

Fig. 2.7 shows the current mode class-D amplifier as implemented in Fig. 2.6 with its major parasitic elements. For the following analysis the design is assumed to be fully symmetric (with the exception of the output balun). The input voltages v_{in1} and v_{in2} are 180° phased-delayed. Based on this assumption, the CMCD amplifier can be divided into four parts, which will be independently examined and their loss mechanisms will be identified:

- Transistor
- DC Supply Network
- Output Filter
- Balun

On this basis an estimation of the drain efficiency η of the real CMCD amplifier can be carried out. A similar study has been conducted in [8], therefore this section and Sections 3.2.2 and 4.5.1 will repeat and extend the findings of earlier works.

A closer look at the transistor will be taken in Chapter 3 of this work. The loss mechanisms of the transistor are identified in Section 3.2.2, resulting in the following efficiency factors:

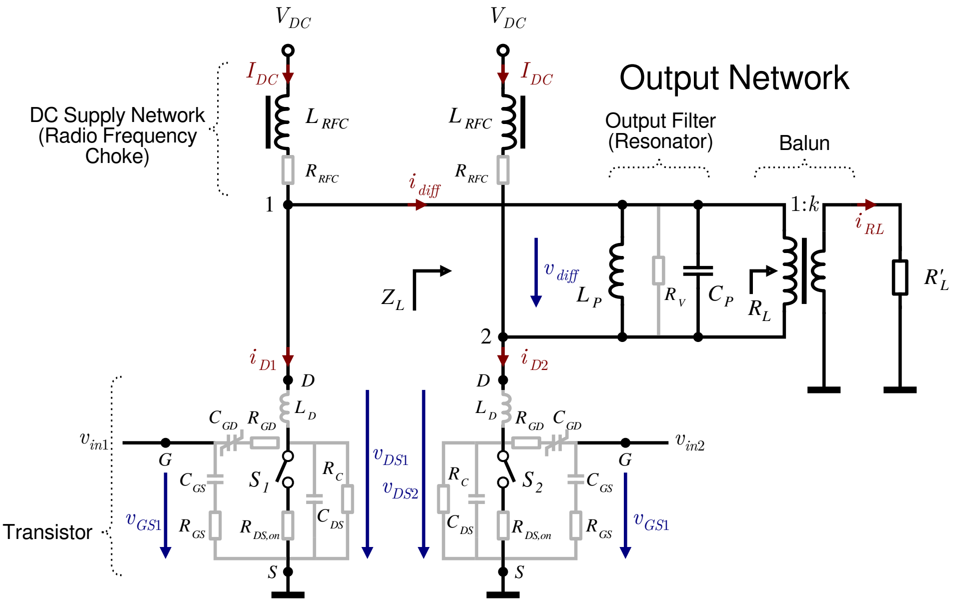

Figure 2.7.: Major parasitic elements of the current mode class-D amplifier

- η_{TR}: losses due to the parasitic on-resistance and drain-to-source capacitance of the transistor,
- η_{TT}: losses due to the limited transition time of the transistor,
- η_{LD}: losses due to the parasitic drain (and source) inductance.

The DC supply network, that is, the radio frequency chokes (RFCs), will be dimensioned and their loss mechanism will be calculated in Section 4.4. The resistive losses of the real RFCs are described by the efficiency factor η_{RFC}.

The output filter will be discussed in Section 4.5 of this work. The loss mechanisms are described by η_{PO}, the losses due to higher harmonic power in the output signal, and η_{PP}, the (resistive) losses in the filter.

So far it has been assumed that the current mode class-D circuit is fully symmetrical. However, every real circuit will be slightly unbalanced and therefore degrade the ideal CMCD operation. This asymmetry greatly depends on the design and implementation (e.g., printed circuit board, PCB layout) of the output network including the output balun and implementation of the whole amplifier. The losses due to the imbalance of the output network (including the balun) are given by the efficiency factor η_{BI}. The losses in the balun are given by the efficiency factor η_{BL}. A closer look at the unbalanced CMCD PA will be taken in Section 4.3 and at the balun in Chapter 5.

Summary of Loss Mechanisms of the CMCD PA

A mathematical transition from the calculated efficiency factors to the drain efficiency η is shown as follows. The drain efficiency is calculated from the sum of the individual loss powers $P_{loss,i}$ and the DC power by

$$\eta = 1 - \frac{P_{loss}}{P_{DC}} = 1 - \frac{\sum_{i=1}^{N} P_{loss,i}}{P_{DC}}. \tag{2.21}$$

For small partial loss powers ($P_{loss,i} \ll P_{DC}$), the total efficiency η can be approximated by the product of individual efficiencies η_i with

$$\eta \gtrsim \prod_{i=1}^{N} \eta_i. \tag{2.22}$$

This product gives a lower bound for the total efficiency. It is assumed that the individual loss mechanisms do not interdepend.

The drain efficiency η is given by

$$\eta = \eta_{TR} \cdot \eta_{TT} \cdot \eta_{LD} \cdot \eta_{RFC} \cdot \eta_{PO} \cdot \eta_{PP} \cdot \eta_{BI} \cdot \eta_{BL}. \tag{2.23}$$

The power-added efficiency is given by

$$\mathrm{PAE} = \eta_{TR} \cdot \eta_{TT} \cdot \eta_{LD} \cdot \eta_{RFC} \cdot \eta_{PO} \cdot \eta_{PP} \cdot \eta_{BI} \cdot \eta_{BL} \cdot \left(1 - \frac{1}{G}\right). \tag{2.24}$$

3 RF Transistors in Switched Mode Operation

This chapter studies RF transistors in switched mode operation. A short introduction to RF power transistor technologies is followed by the presentation of a model for switched mode operation. Subsequently, the theory and limits of switched mode operation are discussed by means of harmonic signal content in the non-ideal switched mode waveform and the calculation of loss mechanisms in class-D operation. Finally, the chapter examines the input network and the optimum transistor stabilization in switched mode operation.

The main contribution of this chapter is the extension of a transistor switched mode model with an off-state resistor R_C*, the calculation of the drain inductive losses at the transistor and the proposal of a method to trade off in-band stability for gain.*

3.1 Introduction to RF Power Transistors

3.1.1 RF Power Transistor Types and Applications

From the first appearance in the patents by Lilienfeld [26] to date solid state transistor devices have replaced competitive technologies in almost all RF applications. Covering a broad range of frequencies up to the THz regime and powers up to several kilowatts, transistors offer an unrivaled flexibility for the RF designer. If classified according to the physical principle, solid state transistors can be subdivided into either bipolar junction transistors (BJT) or field effect transistors (FET). [27] compares and evaluates the two in terms of RF performance based on current technological limits.

Figure 3.1.: Symbols of a bipolar junction transistor (left) and a field effect transistor (right)

Bipolar Junction Transistor

The BJT is a current controlled device. By applying a small current at the "control" base pin, an amplified current can be "collected" at the collector pin. The bipolar junction transistor is generally difficult to scale for high frequencies and high powers. The width of the base layer leads to a trade-off between resistance, i.e., emitter efficiency and charge velocity, i.e., transition frequency. The current density is defined by the size of the emitter, however, a larger emitter will also lead to a larger parasitic base-emitter capacity. The doping of the base leads to a compromise between resistance, that is, emitter efficiency, and gain. The base-emitter leakage current increases with temperature, therefore the BJT is prone to thermal runaway. To address this issue, one needs to add balance resistors, which reduce gain and efficiency. The invention of the heterojunction bipolar transistor (HBT) has optimized the RF performance of the bipolar junction transistor, however HBTs still suffer from low efficiency and limited power capability.

Field Effect Transistor

The FET is a charge controlled device. By applying a voltage and therefore controlling the charge at the "control" gate pin, the current flow between drain and source pin can be adjusted. The input voltage controls the output current, the FET is a transconductance device. The field effect transistor scales very well for high frequencies and high powers. The positive temperature coefficient of on-resistance $R_{DS,on}$ eliminates a thermal runaway of the transistor in hot areas. Therefore, the current capability can be increased by extending the width of the gate without affecting the length, that is, the transition frequency. Consequently, the power capability of the device can be easily increased at the only cost of a lower output impedance. RF optimized FET designs like the laterally-diffused metal-oxide-semiconductor (LDMOS) FET and the (pseudomorphic) high electron mobility transistor ((p)HEMT) offer superior RF performance at high power and efficiency.

Both bipolar junction transistors and field effect transistors are used in RF power amplifiers. Selection of a certain device is subject to technological and economical demands. Nevertheless, when it comes to medium and high RF powers and high efficiencies, FETs dominate both in research and development. Consequently, this work will focus on the use of FET active devices, though most of the conclusions can be easily transferred to designs with bipolar junction transistors.

3.1.2 Semiconductor Materials

Table 3.1 sums up the properties of the three most common semiconductor material systems for RF power devices: silicon (Si), gallium arsenide (GaAs) and gallium nitride (GaN). The maximum supply voltage V_{DC} of the power amplifier

Table 3.1.: Semiconductor material properties [28]

Material	**Si**	**GaAs**	**GaN**
Band gap energy [eV]	1.1	1.4	3.4
Breakdown E field [$\mathrm{MV} \cdot \mathrm{cm}^{-1}$]	0.3	0.4	3.0
Electron mobility [$\mathrm{cm}^2\mathrm{V}^{-1}\mathrm{s}^{-1}$]	1300	6000	1500
Saturated velocity [$\mathrm{cm} \cdot \mathrm{s}^{-1}$]	$1.0 \cdot 10^7$	$1.3 \cdot 10^7$	$2.7 \cdot 10^7$
Thermal conductance [$\mathrm{W} \cdot \mathrm{cm}^{-1} {}^{\circ}\mathrm{K}^{-1}$]	1.5	0.5	1.5

depends largely on the band gap energy and the breakdown electrical (E) field of the semiconductor material. In this respect gallium nitride offers superior characteristics. A raise of the supply voltage translates to a raise of the output impedance. GaN power devices offer output impedances close to 50 Ω, compared to their Si LDMOS and GaAs counterparts in the sub-10 Ω region. Consequently, a low transformation ratio of the impedance matching network enables the design of efficient wideband PAs [28].

The RF performance in terms of transit frequency depends on the electron mobility and the saturated velocity. The large electron mobility of GaAs enables transistor designs in the triple-digit GHz regime. The big saturated velocity of GaN at least partially counterbalances the low electron mobility. Additionally, a larger saturated velocity and a higher supply voltage in combination with the good thermal conductance allow a higher power density in the device.

The high power density facilitates high-power RF applications with GaN transistors. At lower powers GaAs still offers a slightly superior RF performance in terms of transit frequency compared to GaN. GaN and GaAs transistors are generally more efficient than their Si LDMOS counterparts. On the other hand LDMOS transistors are produced on a standard silicon substrate and in many cases offer the most cost-efficient solution.

3.1.3 RF Power Transistor Design

Upon the examination of solid state FET devices, one has to differentiate two control mechanisms. The gate control pin can be either insulated - by applying a voltage at the gate, a conductive inversion zone is created in the doped semiconductor, the device is “normally off” - or it can be formed by a material junction -

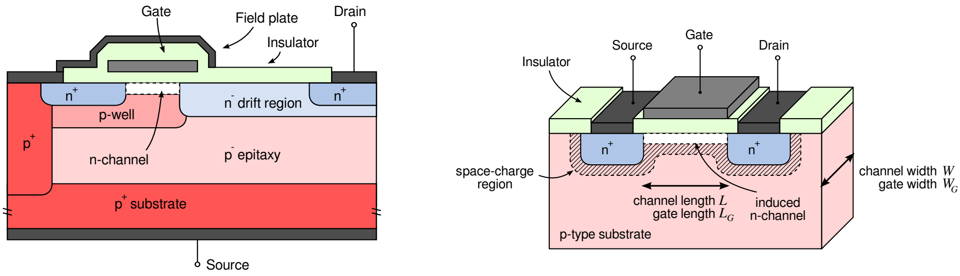

Figure 3.2.: Physical structure of the LDMOS transistor (left) compared to the MOSFET (right) [27]

by applying a voltage at the gate, a non-conductive depletion region is created in the doped semiconductor, the device is “normally on”.

The gate insulated metal oxide semiconductor field effect transistor (MOSFET) is usually silicon-based and has been advanced to the RF power optimized LDMOS transistor. In Fig. 3.2 the physical structure of the LDMOS transistor compared to the MOSFET highlights a few design optimizations. The lateral and vertical extension of the n-channel is reduced. A thin channel provides more gain and a short channel optimizes transition frequency and efficiency. A field plate above the gate is connected to the source and provides shielding from the drain potential, reducing feedback capacitance C_{GD}. Increased spacing between gate and drain provides additional isolation and optimizes gate-drain breakdown voltage. The bottom side of the transistor is connected to source through a low-resistive / low-inductive p+ region.

The RF optimized junction gate metal semiconductor field effect transistor (MESFET) is shown in Fig. 3.3 (left). Substrates with high electron mobility or high saturated velocity like GaAs and GaN are used to optimize charge transfer and therefore transition frequency. A T-shaped gate decreases gate length L_G and hence reduces gate capacitances C_{GS} and C_{GD} and increases the cutoff frequency. By the variation of source-gate and source-drain contact spacing, the breakdown voltages or the channel resistance (i.e., the efficiency) can be optimized. A recessed gate can shift threshold voltage and increase gain.

The pseudomorphic high electron mobility transistor (pHEMT) in Fig. 3.3 (right) optimizes the electron channel. By sandwiching a very thin layer of a narrow-gap semiconductor between two layers of high band-gap semiconductors, a thin (10 nm ≅ 33 atom layers [27]) electron channel narrow enough for quantized states is created. The electrons move only in a two-dimensional layer. The so-called two-dimensional electron gas (2-DEG) has a very high mobility in the range of 1000000 $\frac{\mathrm{cm}^2}{\mathrm{Vs}}$ and a low sheet resistance.

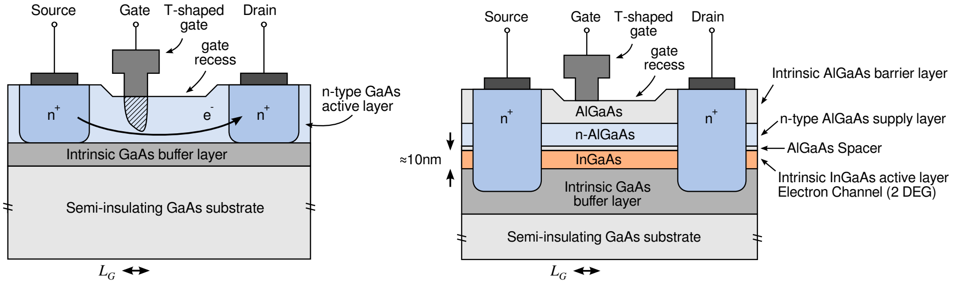

Figure 3.3.: Physical structure of the RF optimized MESFET transistor (left) and the pHEMT (right) [27]

3.2 Theory and Limits of Switched Mode Operation

3.2.1 Modeling of the Transistor in Switched Mode Operation

Fig. 3.4 shows a common small-signal equivalent circuit representation of the intrinsic solid-state transistor (as illustrated in [27]). In a simplified large-signal switched mode implementation, the current source in Fig. 3.4 is replaced by a simple two-state switch.

Fig. 3.5 shows the parasitic switch-mode models of a field effect transistor used in this work. Similar models have been used in [29], [30] and [8] and have shown sufficient accuracy for calculating losses in switched mode amplifier applications.

R_{GS}, C_{GS} and L_G form an RCL-circuit at the gate G of the transistor and therefore limit the rise time of the input signal. The parasitic resistance $R_{DS,on}$ is the on-resistance of the switch S_1 and includes the bulk resistors R_D and R_S in Fig. 3.4. The parasitic capacitor C_{DS} describes the drain-to-source capacitance of the transistor. To account for R_{DS} in the off-state of the switch, the resistor R_C

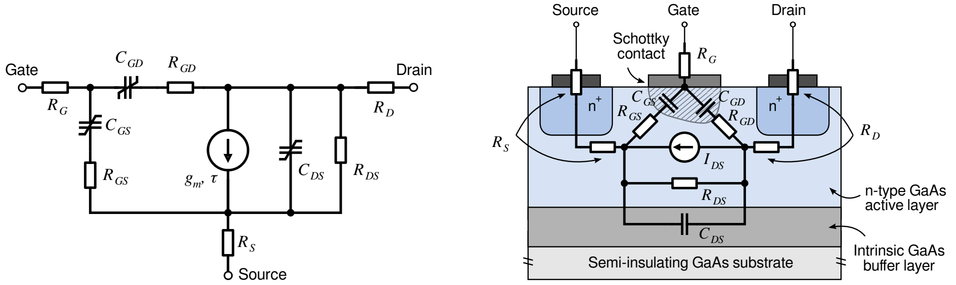

Figure 3.4.: Small-signal equivalent circuit model of the intrinsic MESFET transistor and its physical origin [27]

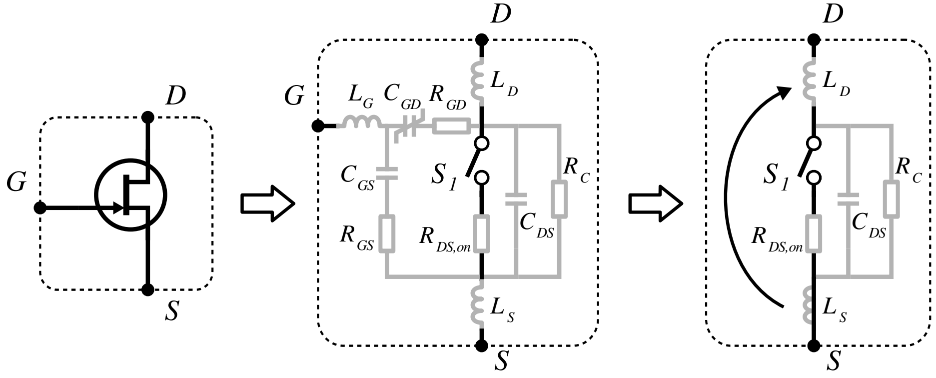

Figure 3.5.: Switch-mode parasitic model of a field effect transistor (in the center) and simplified model for loss calculation (right)

is added in parallel to C_{DS}. C_{GD} represents the parasitic gate-to-drain capacitance and therefore the internal feedback of the drain to the gate. C_{GD} is strongly nonlinear and counteracts the switching operation, thereby reducing the gain of the switched transistor. The losses in C_{GD} are characterized by R_{GD}. [30] has shown that the modeling of the gate-to-drain capacitor C_{GD} as the only bias-dependent capacitance is sufficient in switched mode operation. C_{GS} and C_{DS} will remain static. The inductances L_D and L_S represent the package parasitic inductive components of the drain D and source S connection of the transistor, respectively. To calculate the losses in switched mode operation, the model is further simplified (Fig. 3.5, right) and the package parasitic inductive effects are combined in one inductor at the drain terminal L_D. As will be shown later, L_D is critical for the CMCD operation and a minimized drain inductance is preferred.

3.2.2 *Transistor Loss Mechanisms and Loss Calculation*

Influence of on-resistance and output capacitance

As shown in Fig. 2.5 in Section 2.3.1, the current in the ideal CMCD is switched at zero voltage at the transistor drains. There is a zero voltage switching (ZVS) condition. Therefore, the parasitic output capacitance can be absorbed in the output filter. However, this assumption is not true for a non-zero on-resistance.

In modern RF optimized transistors, the feedback capacitance C_{GD} is highly optimized and considerably smaller than the drain-to-source capacitance, that is, $C_{GD} \ll C_{DS}$ (e.g., *Wolfspeed* CGH27030S GaN HEMT with $C_{GD} = 0.4\,\text{pF}$ and $G_{DS} = 2.0\,\text{pF}$ [31]). Therefore, for loss calculations the output capacitance is reduced to C_{DS}.

The drain current at the first transistor i_{D1} is depicted in Fig. 2.5 and is given by

$$\begin{aligned} i_{D1}(\omega t) &= \begin{cases} 2I_{DC} - \frac{dv_{DS2}(\omega t)}{dt} \cdot C_{DS} - v_{DS2}(\omega t) \cdot \frac{1}{R_C} & 0 \leq \omega t \leq \pi, \\ & \text{switch } S_1 \text{ on} \\ \frac{dv_{DS1}(\omega t)}{dt} \cdot C_{DS} + v_{DS1}(\omega t) \cdot \frac{1}{R_C} & \pi \leq \omega t \leq 2\pi, \\ & \text{switch } S_1 \text{ off} \end{cases} \\ &= \begin{cases} 2I_{DC} - V_{DS,max} \cdot \omega \cos(\omega t) \cdot C_{DS} - V_{DS,max} \cdot \sin(\omega t) \cdot \frac{1}{R_C} \\ -V_{DS,max} \cdot \omega \cos(\omega t) \cdot C_{DS} - V_{DS,max} \cdot \sin(\omega t) \cdot \frac{1}{R_C} \end{cases} \end{aligned} \tag{3.1}$$

with

$$v_{DS1}(\omega t) = -V_{DS,max} \cdot \sin(\omega t)$$

for $\pi \leq \omega t \leq 2\pi$ and

$$v_{DS2}(\omega t) = V_{DS,max} \cdot \sin(\omega t)$$

for $0 \leq \omega t \leq \pi$.

The voltage at the first transistor v_{DS1} can expressed by

$$v_{DS1}(\omega t) = \begin{cases} i_{D1}(\omega t) \cdot R_{DS,on} & 0 \leq \omega t \leq \pi, \text{ switch } S_1 \text{ on} \\ -V_{DS,max} \sin(\omega t) & \pi \leq \omega t \leq 2\pi, \text{ switch } S_1 \text{ off} \end{cases}, \tag{3.2}$$

assuming the losses at $R_{DS,on}$ dominate in the on-state of the switch ($R_{DS,on} \ll \frac{1}{\omega C_{DS}} \parallel R_C$). The power loss at the first transistor $P_{T,loss,1}$ due to the non-zero on-resistance $R_{DS,on}$ is given with $V_{DS,max} = \pi V_{DC}$ by

$$P_{T,loss,1} = \frac{1}{2\pi} \int_0^{2\pi} i_{D1}(\omega t) \cdot v_{DS1}(\omega t)\, d\omega t \tag{3.3}$$

and

$$\begin{aligned} P_{T,loss,1} &= 2I_{DC}^2 R_{DS,on} + \frac{1}{4}\left(\pi V_{DC}\omega_s C_{DS}\right)^2 R_{DS,on} \\ &+ \frac{1}{4}\pi^2 V_{DC}^2 \frac{R_{DS,on}}{R_C^2} - 4I_{DC}V_{DC}\frac{R_{DS,on}}{R_C} + \frac{1}{4}\pi^2 V_{DC}^2 \frac{1}{R_C}. \end{aligned} \tag{3.4}$$

With $R_C \to \infty$ $P_{T,loss,1}$ is reduced to

$$P_{T,loss,1} = 2I_{DC}^2 R_{DS,on} + \frac{1}{4}\left(\pi V_{DC}\omega_s C_{DS}\right)^2 R_{DS,on}. \tag{3.5}$$

Assuming a symmetrical design, the losses at the transistors are equally large. The efficiency factor η_{TR} for the resistive losses at the transistor is

$$\begin{aligned} \eta_{TR} &= 1 - \frac{2P_{T,loss,1}}{P_{DC}} \\ &= 1 - \frac{4I_{DC}^2 R_{DS,on} + \frac{1}{2}\left(\pi V_{DC}\omega_s C_{DS}\right)^2 R_{DS,on}}{2V_{DC}I_{DC}} \\ &- \frac{\frac{1}{2}\pi^2 V_{DC}^2 R_{DS,on}\frac{1}{R_C^2} - 8I_{DC}V_{DC}R_{DS,on}\frac{1}{R_C} + \frac{1}{2}\pi^2 V_{DC}^2 \frac{1}{R_C}}{2V_{DC}I_{DC}}. \end{aligned} \tag{3.6}$$

With 2.18, η_{TR} can be written as a function of the optimum load R_L by

$$\boxed{\begin{aligned} \eta_{TR} = 1 &- \frac{\pi^2 R_{DS,on}}{2R_L} - \left(\omega_s C_{DS}\right)^2 R_L R_{DS,on} \\ &- \frac{R_L R_{DS,on}}{R_C^2} + \frac{4R_{DS,on}}{R_C} - \frac{R_L}{R_C} \end{aligned}}. \tag{3.7}$$

With $R_C \to \infty$ η_{TR} is reduced to

$$\boxed{\eta_{TR} = 1 - \frac{\pi^2 R_{DS,on}}{2R_L} - \left(\omega_s C_{DS}\right)^2 R_L R_{DS,on}}. \tag{3.8}$$

Fig. 3.6 (left) shows the efficiency factor η_{TR} as a function of optimum load R_L for different values of $R_{DS,on}$ and C_{DS} at $f_s = 900\,\mathrm{MHz}$ and $R_C \to \infty$. At the right side C_{DS} is fixed at 1 pF and η_{TR} given for different values of $R_{DS,on}$ and R_C.

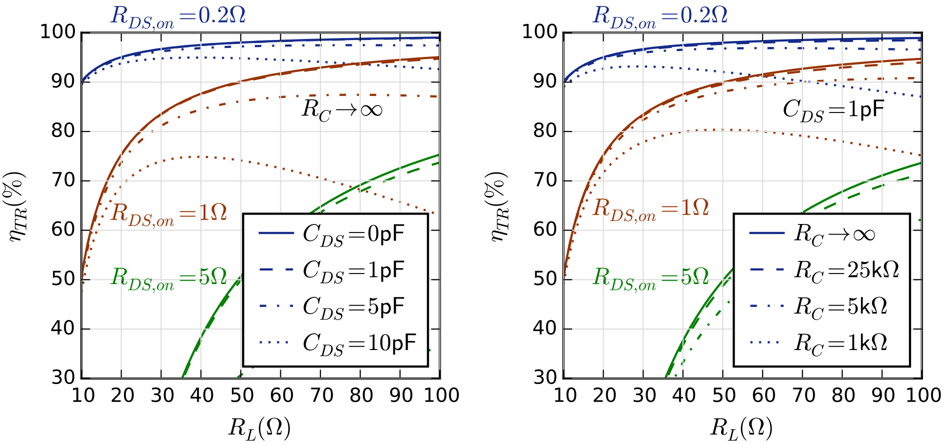

Figure 3.6.: Efficiency factor η_{TR} as a function of optimum load R_L for different values of $R_{DS,on}$ and C_{DS} at $f_s = 900\,\text{MHz}$ and $R_C \rightarrow \infty$ (left) and different values of $R_{DS,on}$ and R_C at $f_s = 900\,\text{MHz}$ and $C_{DS} = 1\,\text{pF}$ (right)

Influence of rise and fall time of the transistor

A real transistor has a non-zero transition time. Switching won't occur instantaneously but with a non-zero rise and fall time due to the RC circuit at the transistor input formed by the gate resistance R_{GS} and the gate-to-source capacitance C_{GS} as well as the feedback elements C_{GD} and R_{GD} and the bond wire inductance L_G. [8] models the real switching behavior of the transistor with a trapezoid drain current waveform with the rise / fall time τ in radians (Fig. 3.7).

Fourier decomposition of the trapezoidal drain current i_{D1} gives

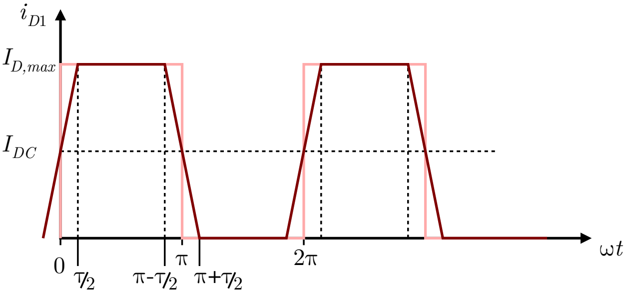

Figure 3.7.: Trapezoidal drain current i_{D1} modeled with rise and fall time τ

$$i_{D1}\left(n\omega t\right) = I_{DC}\left[1 + \frac{8}{\pi}\frac{1}{\tau}\sum_{n=1,3,5,\ldots}^{\infty}\frac{1}{n^2}\sin\left(n\frac{\tau}{2}\right)\sin\left(n\omega t\right)\right] \tag{3.9}$$

with the fundamental amplitude $\hat{i}_{D1}(1)$, which will appear at the load,

$$\hat{i}_{D1}(1) = \frac{8}{\pi}I_{DC}\frac{1}{\tau}\sin\left(\frac{\tau}{2}\right). \tag{3.10}$$

The efficiency factor η_{TT} is then calculated with the fundamental drain current amplitude $\hat{i}_{D1}(1)$ and the differential voltage amplitude $\hat{v}_{diff}$ by

$$\eta_{TT} = \frac{P_{out}}{P_{DC}} = \frac{\frac{1}{2}\hat{v}_{diff}\hat{i}_{D1}(1)}{2V_{DC}I_{DC}}. \tag{3.11}$$

With $\hat{v}_{diff} = V_{DS,max} = \pi V_{DC}$ (Equation 2.16), η_{TT} is

$$\boxed{\eta_{TT} = \frac{2\sin\left(\frac{\tau}{2}\right)}{\tau}}. \tag{3.12}$$

Looking at Fig. 3.7 one might wonder about the phase shift of $-\frac{\tau}{2}$ compared to the ideal drain current waveform. This assumption simplifies the Fourier decomposition. However, the differential voltage $\hat{v}_{diff}$ will have the same phase shift and the absolute phase is not needed for calculating the efficiency.

Influence of the drain inductance of the transistor

The inductance L_D represents parasitic, inductive components at the drain terminal of the transistor. Moreover, L_D can include inductive source parasitics (e.g., vias). Any inductance at the transistor's drain or source terminals lies in series with the output network of the CMCD amplifier. In opposition to the drain-source voltage, the current is hard switched (Fig. 2.5), there is no zero current switching (ZCS). As a first approximation one can assume that all saved energy (from switching) in L_D will be lost.

The saved magnetic energy E_{LD} of inductor L_D at every switching cycle is given by

$$E_{LD} = \frac{1}{2}L_D I_{D,max}^2. \tag{3.13}$$

The power loss P_{LD} at the switching frequency f_s is obtained with equation 2.7 by

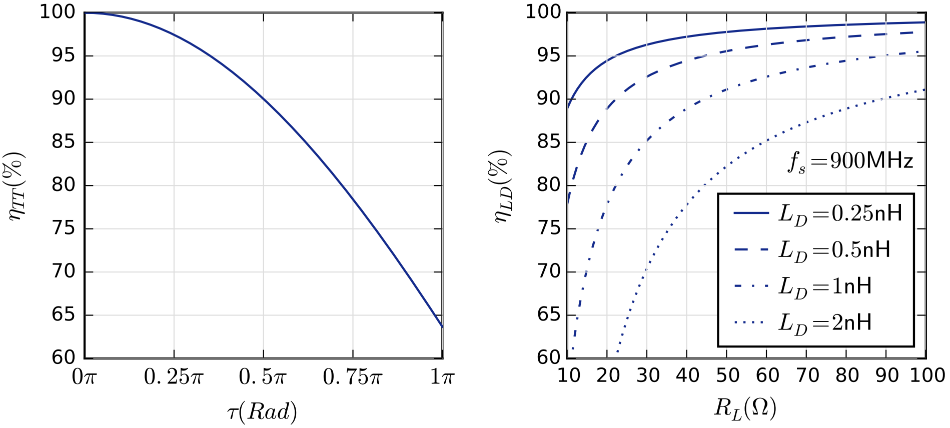

Figure 3.8.: Efficiency factor η_{TT} as a function of rise time τ (left) and efficiency factor η_{LD} as a function of optimum load R_L for different values of L_D at $f_s = 900\,\text{MHz}$ (right)

$$P_{LD} = \frac{1}{2} L_D I_{D,max}^2 \cdot f_s = 2 L_D I_{DC}^2 \cdot f_s. \tag{3.14}$$

The efficiency factor η_{LD} for the influence of the (two) drain inductors is calculated as a function of optimum impedance R_L (Equation 2.18) by

$$\eta_{LD} = 1 - \frac{2P_{LD}}{P_{DC}} = 1 - \frac{4 L_D I_{DC}^2 \cdot f_s}{2 V_{DC} I_{DC}} \tag{3.15}$$

and

$$\boxed{\eta_{LD} = 1 - \frac{\pi^2}{2} \cdot \frac{L_D f_s}{R_L}}. \tag{3.16}$$

Fig. 3.8 (left) shows the efficiency factor η_{TT} as a function of rise time τ. At the right side the efficiency factor η_{LD} is shown as a function of the optimum load R_L for different values of drain inductance L_D at $f_s = 900\,\text{MHz}$.

3.2.3 The Class-D Amplifier in Backoff Operation

Similar to any switched mode amplifier architecture, in class-D the amplitude information of the amplifier's input signal is lost due to the highly compressive operation of the transistors.

Equation 2.20 shows that the output power of the ideal current mode class-D amplifier solely depends on the supply voltage V_{DC} and the load resistance R_L:

$$P_{out} = \frac{\pi^2}{2}\frac{V_{DC}^2}{R_L}. \tag{3.17}$$

In other words, there are two degrees of freedom to vary the output power, either by modulating the supply voltage or by modulating the load resistance. A third degree of freedom would be the operating point of the transistors. However, moving from class-D switched mode to a (slightly) linear operation, that is, class-AB, comes at the cost of efficiency and, as will be seen later in Section 3.3, stability. Load modulation is used in the outphasing amplifier concept or the Doherty amplifier. The EER amplifier concept uses a varying supply voltage to restore the amplitude modulation at the output of a switched mode PA.

To benchmark both load modulation and supply modulation equation 3.7 is used to calculate the efficiency of the switched transistor. It can be seen that the efficiency factor η_{TR} only depends on the load R_L and not on the supply voltage. The switching losses are load-dependent, however they are constant for a varying V_{DC}. Meanwhile it has to be noted that the gain of a transistor usually changes with the supply voltage. Towards lower V_{DC} the gain drastically decreases [32]. The typically low gain margin in compressive switched mode operation leaves only a limited range of V_{DC} to achieve a good PAE.

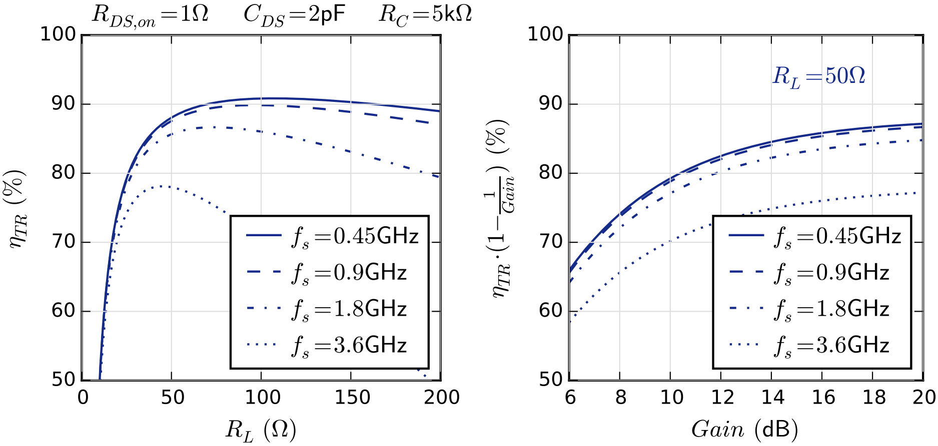

Figure 3.9.: Efficiency factor η_{TR} as a function of load resistance R_L, i.e., load modulation (left) and gain-weighted efficiency factor η_{TR} as a function of gain, i.e., supply modulation at $R_L = 50\,\Omega$ for different switching frequencies. The parasitics are extracted from the model of the *Wolfspeed* GaN HEMT CGH27030S [31].

Fig. 3.9 (left) shows the efficiency factor η_{TR} as a function of load resistance R_L for different switching frequencies f_s. The parasitic values $R_{DS,on}$, C_{DS} and R_C are extracted from the model of the *Wolfspeed* GaN HEMT CGH27030S [31]. At low switching frequencies a relatively large efficient load range is visible. At higher switching frequencies a load optimum can be noted which gradually decreases towards high switching frequencies. On the right side of Fig. 3.9 the load is kept constant at $R_L = 50\,\Omega$ and a gain-weighted efficiency $\eta_{TR} \cdot \left(1 - \frac{1}{Gain}\right)$ is given as a function of swept transistor gain to illustrate the influence of the transistor's supply-voltage-to-gain dependence.

3.3 Stability Considerations and Input Network

3.3.1 *Input Signal*

The two transistors in the current mode class-D amplifier are driven by 180° phased-delayed input signals v_{in1} and v_{in2} at the switching frequency f_s. Fig. 3.10 shows two input signal waveforms - a rectangular and a sinusoidal drive signal. The rectangular drive signal is modeled with a finite rise time τ and initially seems more likely to be a suitable drive signal for a switched mode PA. However, most sources in the GHz domain usually output a sinusoidal one-tone signal.

In order to compare the necessary input voltage amplitudes of rectangular and sinusoidal drive for a given fixed rise time τ, the input voltage waveform of the sinusoidal signal is given by

$$v_{in1}\left(\omega t\right) = \hat{v}_{in,sin} \cdot \sin\left(\frac{\omega t}{2\pi}\right) \tag{3.18}$$

with $\hat{v}_{in,sin}$ the amplitude of the sinusoidal input signal.

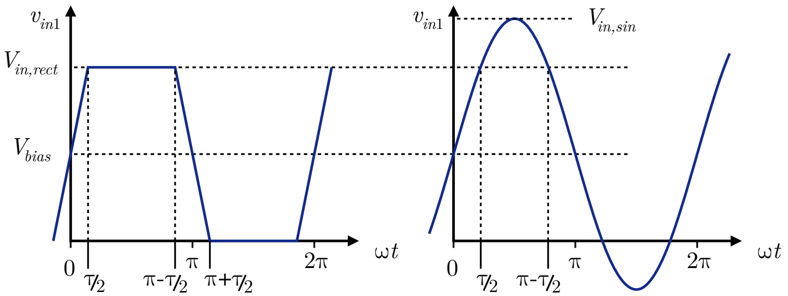

Figure 3.10.: Rectangular and sinusoidal input signal of the switched transistor modeled with rise and fall time τ

With $v_{in1}\left(\frac{\tau}{2}\right) = \hat{v}_{in,rect}$ the rectangular amplitude $\hat{v}_{in,rect}$ can be written as a function of $\hat{v}_{in,sin}$ by

$$\hat{v}_{in,rect} = \hat{v}_{in,sin} \cdot \sin\left(\frac{\tau}{2}\right). \tag{3.19}$$

For a given rise time of $\tau = \frac{2\pi}{10}$, $\hat{v}_{in,rect}$ equals to $0.31 \cdot V_{in,sin}$. In other words, the amplitude of the sinusoidal input has to be three times bigger compared to the rectangular amplitude to achieve the same rise time. For instance, $\tau = \frac{2\pi}{10}$ equals to a rise time of 100 ps at a switching frequency of 1 GHz.

The bias voltage V_{bias} in Fig. 3.10 is calculated by $V_{bias} = \frac{1}{2}\hat{v}_{in,rect}$. However, the optimum bias voltage is defined by the (nonlinear) transfer function of the transistor. Therefore, V_{bias} is optimized in simulation and measurement with respect to switching efficiency. Additionally, a logic circuit should turn off V_{bias} when no input signal is present, in order to avoid drawing excess current and keep the transistors in off-state.

3.3.2 Stability Considerations

The exponentially growing gain factor of RF transistors towards lower frequencies (see, e.g., [33]) in conjunction with device internal feedback mechanisms like the gate-to-drain capacitance C_{GD} can lead to self-oscillation. Therefore, measures have to be applied to the amplifier circuit to avoid unstable conditions within the scope of all operating states. However, these measures usually come at the expense of gain. Fig. 3.9 (right) depicts the influence of gain on the power-added efficiency. For instance, a gain of 10 dB reduces the PAE by up to 10%. In compressive switched mode operation, gain is especially critical and the efficiency yield of a switched mode PA can be easily consumed in comparison to a linear power amplifier.

The large-signal stability of an amplifier is influenced by four attributes [34]:

- bias point V_{bias} of the transistor,
- input power P_{in} at the input port,
- input matching Γ_S of the amplifier,
- output matching Γ_L of the amplifier.

To verify unconditional stability in an amplifying regime, that is, to prevent any instabilities leading to, for example, oscillating regimes, several tests are available as shown in [34]. These stability tests are carried out for all operating points of the amplifier including DC bias points, input powers and matching conditions.

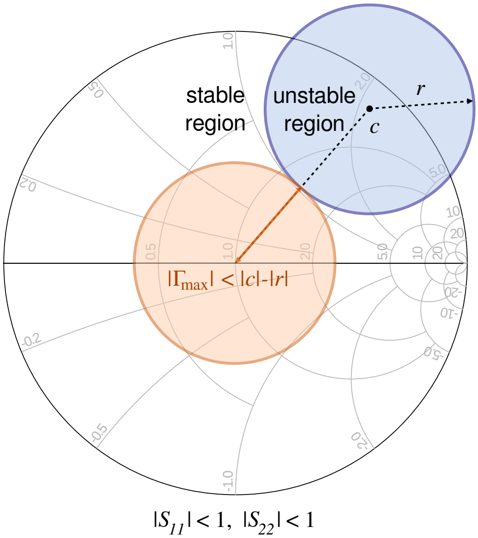

Figure 3.11.: Figure of merit for amplifier stability

In switched mode operation, however, there are only two levels of input powers corresponding to the switched transistor being in off-position ($P_{in} = 0\,\mathrm{W}$) and in on-position, i.e., compression ($P_{in} = P_{in,on}$). Additionally, there is only one V_{bias} level.

As for the input and the output matching, two cases have to be considered:

- out-of-band stability, $f < (f_s - \frac{B}{2})$ and $f > (f_s + \frac{B}{2})$: impedances are unknown or close to reflection (Γ very high) at harmonic frequencies $\rightarrow$ unconditional stability necessary,
- in-band stability, $(f_s - \frac{B}{2}) < f < (f_s + \frac{B}{2})$: impedances are controlled $\rightarrow$ conditional stability might apply.

The reflection coefficient Γ_{max} defines the maximum stable impedance space at either input or output. Fig. 3.11 visualizes this with the help of stability circles of unstable regions in the Smith chart. These stability circles are well defined with a midpoint c and a radius r in the Smith chart for each frequency f. The figure of merit $|\Gamma_{max}| < |c| - |r|$ has to apply.

The input impedance "seen" by the switched mode amplifier is usually well-defined in-band. The switched mode amplifier is integrated in a system with driver amplifiers and control logic. The driver's output impedance is fixed (Γ_{max} is known) and the PA is only active when the drivers are active too. The output of the amplifier is matched in-band with the load, e.g., an antenna. However, a varying voltage standing wave ratio (VSWR), e.g., due to reflections, deteriorates the matching conditions. The worst-case VSWR of an antenna VSWR_{max} is related to Γ_{max} by

$$\Gamma_{max} = \frac{\mathrm{VSWR}_{max} - 1}{\mathrm{VSWR}_{max} + 1}. \tag{3.20}$$

A VSWR of, e.g., $\mathrm{VSWR}_{max} = 9$ (bad antenna matching) leads to a requirement for the stable impedance space of $\Gamma_{max} = 0.8$.

In summary, unstable conditions can be narrowed down and avoided by amplifier design (system integration with driver and load), application (antenna VSWR) and auxiliary circuitry (DC bias control). Therefore, conditional stability is sufficient in certain cases and, as a new degree of freedom, can be used to optimize the gain of the switched mode amplifier.

3.3.3 Proposed Input Network

Common PA stabilization network implementations usually differentiate between low frequency and high frequency stabilization. Low frequency stability is typically maintained by lumped-element networks, whereas high frequency stability is accomplished by a combination of lumped components and distributed elements. Therefore, it is required that the wideband parasitic properties of all lumped components are known.

Fig. 3.12 shows the input circuit used in this work. It is derived from earlier works of the author and has proven to sufficiently maintain stability in GaN transistor-based power amplifier designs [35–37]. Capacitor C_S and shunt resistor R_1 in Fig. 3.12 form a first-order RC high-pass circuit for low frequency

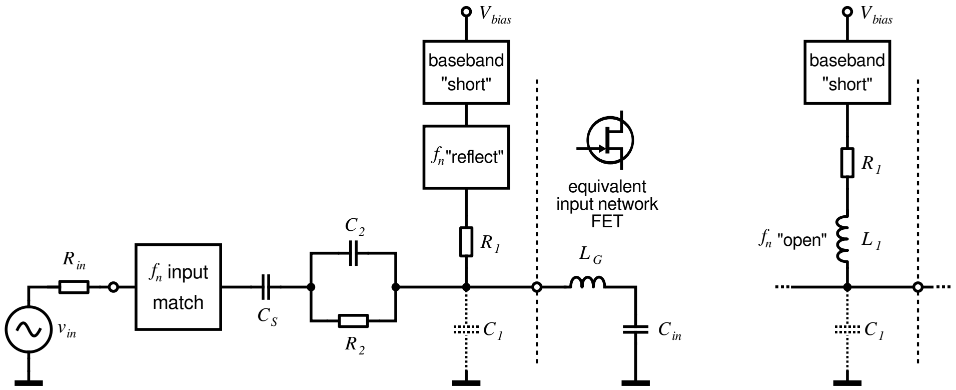

Figure 3.12.: Proposed input network for narrowband (left) and wideband (right) matching

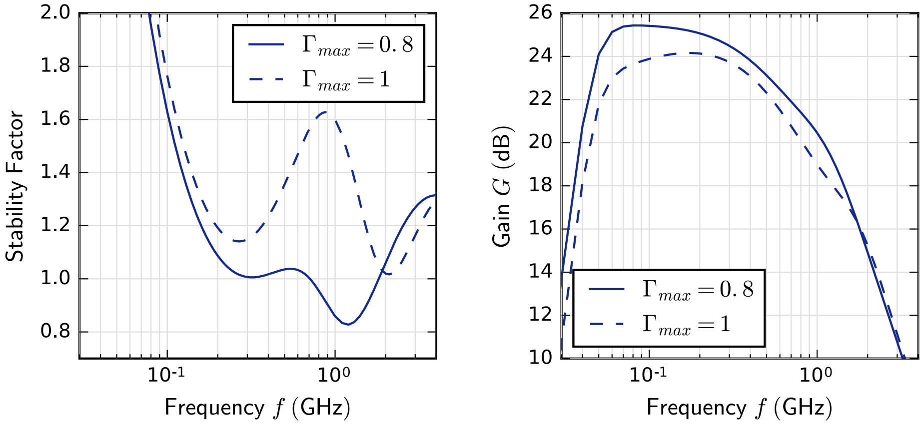

Figure 3.13.: Stability factor for the input network of the E-pHEMT ATF-541M4 optimized for stable output impedance spaces with $\Gamma_{max} = 1$ and $\Gamma_{max} = 0.8$ (left) and resulting power gain G as a function of frequency f (right). At $f = 900$ MHz the reduction of stable output-Γ results in 1.3 dB of additional gain.

stability. Additional low frequency damping is added by the parallel circuit R_2 and C_2. High frequency stability is maintained by the low-pass characteristic of the transistor-internal bond wire inductance L_G and the input capacitance C_{in} in conjunction with the external parasitic shunt capacitance C_1 and the input matching network.

High frequency stability is additionally influenced by the bias voltage connection. RF isolation has to be maintained either by individual harmonic traps (f_n "reflect" in Fig. 3.12 left) or by a wideband lumped-element solution (inductor L_1 in Fig. 3.12 right). L_1 has to be wide-band for RF including harmonics f_n but should be low impedance for the video (baseband) bandwidth. Suitable components with broadband performance are, for example, conical inductors provided by *Coilcraft* and *Piconics* [38]. The actual component position in Fig. 3.12 is not mandatory, provided that parasitics of all lumped elements are known.

In the following example, two input networks are optimized for the *Avago/Broadcom* GaAs E-pHEMT ATF-541M4 [33]. Fig. 3.13 (left) shows the stability factor for two stable output impedance spaces Γ for $\Gamma_{max} = 1$ and $\Gamma_{max} = 0.8$. The unstable impedance space (stability factor < 1) extends from 700 MHz to 1.9 GHz. This frequency range is assumed to be in-band and therefore controlled (and is close to the maximum 100% bandwidth of a CMCD PA, see Section 2.2). The resulting power gain G for the two input networks is shown in Fig. 3.13 (right) as a function of frequency f. At $f = 900$ MHz the reduction

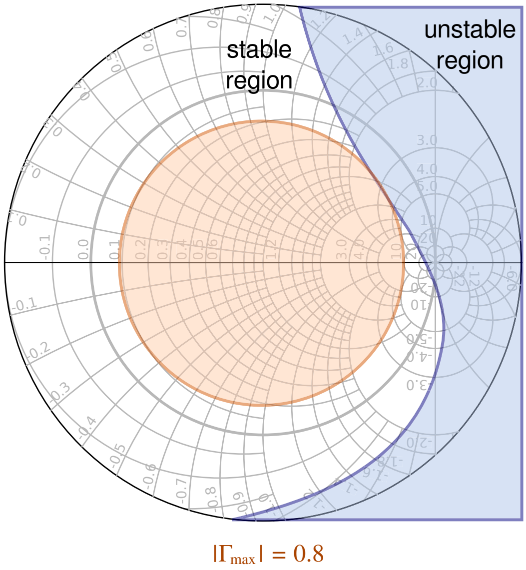

Figure 3.14.: Stable output impedance space Γ for the optimized input network of the E-pHEMT ATF-541M4 with $\Gamma_{max} = 0.8$

of stable output-Γ results in 1.3 dB of additional gain. Finally, Fig. 3.14 shows the optimized stable output impedance space for $\Gamma_{max} = 0.8$.

4 Output Network Analysis

This chapter discusses the output network of differential switched mode amplifiers. After a short motivation, the so-called mixed mode S-parameters are introduced and then used to define the optimum harmonic impedance space of the current mode class-D amplifier in common and differential mode. Afterwards, two output filter implementations are shown and an optimized manufacturing technique is proposed.

The main contribution of this chapter is the calculation of ideal harmonic output impedances of the CMCD PA, the analytical evaluation of the output network imbalance, the analysis of the DC supply network, the calculation and evaluation of a low-pass output filter and the low parasitic PCB implementation of discrete output filters.

4.1 Motivation

The output network of an RF power amplifier defines its mode of operation. The output network impedance sets the loadline and therefore the relationship of voltages and currents at the fundamental and harmonic frequencies. It suppresses harmonic signals from the amplifier output. Moreover, it transforms the output impedance of a differential amplifier design to the single-ended or (if preferred) differential load and therefore defines the output impedance of the amplifier. Last but not least, the output network implements the constant current sources for the switched transistors and isolates the DC supply voltage from the RF signals at the transistor drains. The output network has a significant influence on the total efficiency of the amplifier (see Fig. 4.1).

A loss of just 0.6 dB will result in a 10% reduction of total efficiency employing relatively efficient PAs (efficiency $> 70\%$). Poor output network design can ruin any efficiency enhancing qualities of switched mode PAs. Fig. 4.2 sums up the desired output network attributes.

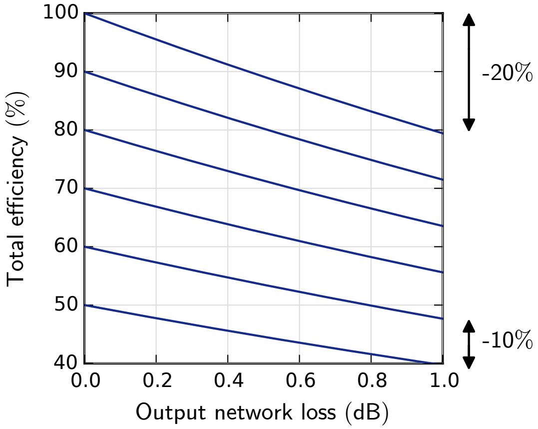

Figure 4.1.: Influence of the output network loss on the total efficiency of an amplifier

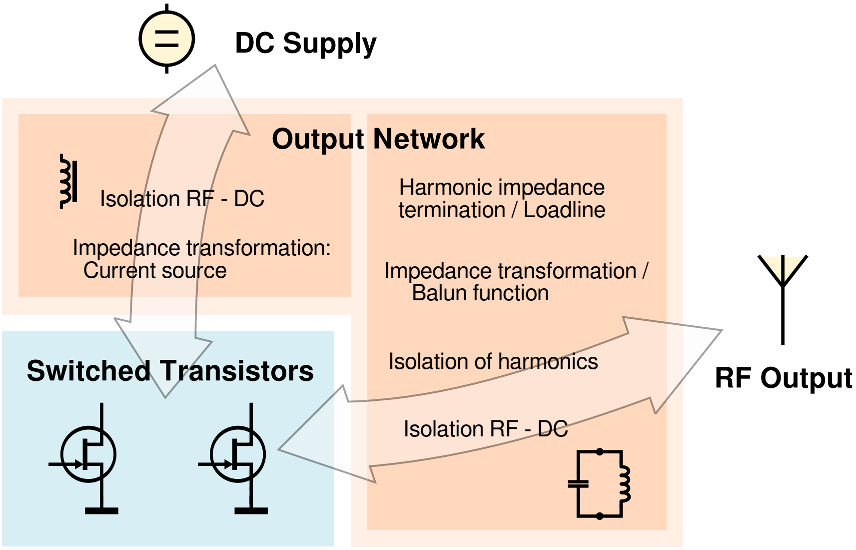

Figure 4.2.: Summary of output network attributes in efficient switched mode power amplifiers

4.2 Mixed Mode S-Parameters

The current mode class-D power amplifier has a differential output. Therefore, to attach a single-ended load, the differential output impedance of the PA has to be transformed to a single-ended one. The output network has to serve as a balun.

A balun, essentially being a mode and impedance transformer, is in reality a three-port device. The balanced input, which is composed of two ports, is a three line system, which can propagate two different modes [39, 40]. Consequently, every balun transformer can be fully described by a 3x3 S-matrix $\mathbf{S}$ with incident waves a and reflected waves b,

$$b = \mathbf{S} \cdot a \tag{4.1}$$

and the scattering parameters

$$\begin{bmatrix} b_1 \\ b_2 \\ b_3 \end{bmatrix} = \begin{bmatrix} S_{11} & S_{12} & S_{13} \\ S_{21} & S_{22} & S_{23} \\ S_{31} & S_{32} & S_{33} \end{bmatrix} \cdot \begin{bmatrix} a_1 \\ a_2 \\ a_3 \end{bmatrix} . \tag{4.2}$$

However, a single-ended S-parameter matrix of this three-port device will only give an indirect view of the mode conversion taking place in a balun, i.e., in the output network of a power amplifier. Therefore, a different description, the mixed mode S-parameter matrix, employing differential and common mode stimuli will be helpful. Fig. 4.3 shows a reduced two-port description of the balun with three stimuli: the differential mode stimulus a_{d1} , the common mode stimulus a_{c1} and the single-ended stimulus a_{s2}.

The so-called modal scattering matrix $\mathbf{S}_m$ is a 3x3 matrix defining the relationship between incident waves a_m and reflected waves b_m at the balun [41].

$$b_m = \mathbf{S}_m \cdot a_m \tag{4.3}$$

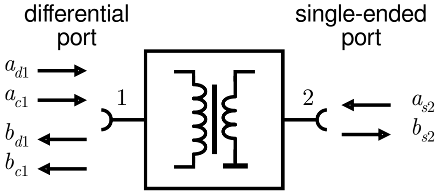

Figure 4.3.: A balun as a two-port device with mixed mode stimuli

With the three stimuli a_{d1}, a_{c1} and a_{s2}, $\mathbf{S}_m$ can be expressed by

$$\begin{bmatrix} b_{d1} \\ b_{c1} \\ b_{s2} \end{bmatrix} = \begin{bmatrix} S_{dd11} & S_{dc11} & S_{ds12} \\ S_{cd11} & S_{cc11} & S_{cs12} \\ S_{sd21} & S_{sc21} & S_{ss22} \end{bmatrix} \cdot \begin{bmatrix} a_{d1} \\ a_{c1} \\ a_{s2} \end{bmatrix}. \tag{4.4}$$

The resulting new set of modal scattering parameters has been renamed and can be distinguished from conventional nodal S-parameters. The scattering parameters indexed with "dd", "cc" and "ss" describe the reflection quantity of differential, common and single-ended signals, respectively. The indices "dc" and "cd" are conversion parameters and describe the conversion of modes at the differential port during reflection. The indices "sd", "ds", "sc" and "cs" describe the conversion of single-ended to mixed modes and vice versa during transmission between the two balun ports.

[41] shows that the modal S-matrix $\mathbf{S}_m$ can be derived from the nodal S-matrix $\mathbf{S}$ via the conversion matrices $\mathbf{M}_1$ and $\mathbf{M}_2$, which represent the relationship of differential mode (Z_d) and common mode (Z_c) impedances:

$$\boxed{\mathbf{S}_m = (\mathbf{M}_1\mathbf{S} + \mathbf{M}_2)\,(\mathbf{M}_1 + \mathbf{M}_2\mathbf{S})^{-1}}. \tag{4.5}$$

Z_d and Z_c are given as a function of odd- (Z_{0o}) and even-mode (Z_{0e}) impedances and the coupling constants k_{0o} and k_{0e}, which represent coupling in the differential network. Z_0 is the reference impedance (e.g., 50 Ω):

$$Z_d = 2Z_{0o} = 2k_{0o}Z_0, \tag{4.6}$$

$$Z_c = \frac{1}{2}Z_{0e} = \frac{1}{2}k_{0e}Z_0. \tag{4.7}$$

The odd- and even-mode impedances are generally not equal to Z_0 in differential systems with coupled lines [41].

The conversion matrices $\mathbf{M}_1$ and $\mathbf{M}_2$ of the mixed mode S-parameters are given by

$$\mathbf{M}_1 = \begin{bmatrix} \frac{1+k_{0o}}{2\sqrt{2k_{0o}}} & -\frac{1+k_{0o}}{2\sqrt{2k_{0o}}} & 0 \\ \frac{1+k_{0e}}{2\sqrt{2k_{0e}}} & \frac{1+k_{0e}}{2\sqrt{2k_{0e}}} & 0 \\ 0 & 0 & 1 \end{bmatrix} \tag{4.8}$$

and

$$\mathbf{M}_2 = \begin{bmatrix} \frac{1-k_{0o}}{2\sqrt{2k_{0o}}} & -\frac{1-k_{0o}}{2\sqrt{2k_{0o}}} & 0 \\ \frac{1-k_{0e}}{2\sqrt{2k_{0e}}} & \frac{1-k_{0e}}{2\sqrt{2k_{0e}}} & 0 \\ 0 & 0 & 0 \end{bmatrix}. \tag{4.9}$$

Older publications use a simplified description of the conversion matrices. If a system with weakly coupled or uncoupled transmission lines is given with $Z_0 = 50\,\Omega$, the impedances in differential mode and common mode can be estimated to be $Z_d = 100\,\Omega$ and $Z_c = 25\,\Omega$. Therefore, the coupling constants are calculated to $k_{0o} = k_{0e} = 1$. The conversion matrices are then reduced to

$$\mathbf{M}_1 = \sqrt{2} \begin{bmatrix} 1 & -1 & 0 \\ 1 & 1 & 0 \\ 0 & 0 & \sqrt{2} \end{bmatrix} \tag{4.10}$$

and

$$\mathbf{M}_2 = 0. \tag{4.11}$$

To calculate the mixed mode S-parameters, the nodal S-matrix $\mathbf{S}$ can be easily obtained from linear S-parameter simulation or measurement. However, the odd- and even-mode impedances and, therefore, the coupling constants k_{0o} and k_{0e} are more difficult to determine. Electro-magnetic (EM) simulations using, e.g., finite element methods (FEM) allow an accurate calculation of odd- and even-mode impedances in a system with coupled lines. As for measurement [41] suggests using time domain reflectometry (TDR) to characterize coupled lines.

The mixed-mode impedances $\mathbf{Z}_m$ are linked to the modal S-matrix $\mathbf{S}_m$ with the unit matrix $\mathbf{E}$ and the reference impedance Z_0 by

$$\boxed{\mathbf{Z}_m = Z_0 \left(\mathbf{E} - \mathbf{S}_m\right)^{-1} \left(\mathbf{E} + \mathbf{S}_m\right)}. \tag{4.12}$$

Input impedances of the output network / balun in differential mode Z_{dd11} and common mode Z_{cc11} are calculated accordingly.

4.3 Harmonic Termination

One of the main requirements for the ideal switched mode operation is the proper harmonic output impedance termination (compare Table 2.1). In Section 2.3.1, some impedances of the current mode class-D amplifier have already been determined in a visual way from the ideal voltage and current waveforms. In a mathematically correct approach this differential amplifier has to be described by differential mode (Z_{dd11}) and common mode (Z_{cc11}) impedances.

4.3.1 Ideal Harmonic Termination

Fig. 4.4 depicts the currents and voltages in differential mode (i_{diff} and v_{diff}) as well as common mode (i_{com} and v_{com}).

By recalling the current and voltage waveforms at the CMCD

$$i_{D1/2}\left(\omega t\right) = I_{DC}\left[1 \pm \frac{4}{\pi}\sum_{n=1,3,5,\ldots}^{\infty}\frac{1}{n}\sin\left(n\omega t\right)\right] \tag{4.13}$$

and

$$v_{DS1/2}\left(\omega t\right) = \frac{1}{\pi}V_{DS,max}\left[1 \pm \frac{\pi}{2}\sin\left(\omega t\right) - \sum_{n=2,4,6,\ldots}^{\infty}\frac{2}{n^2-1}\cos\left(n\omega t\right)\right] \tag{4.14}$$

from equations 2.6 and 2.14, the differential and common mode signals can be calculated according to Fig. 4.4. The current and the voltage in differential mode is then given by

$$\begin{aligned} i_{diff}\left(\omega t\right) &= I_{DC} - i_{D1}\left(\omega t\right) = i_{D2}\left(\omega t\right) - I_{DC} && (4.15)\\ &= -I_{DC}\left[\frac{4}{\pi}\sum_{n=1,3,5,\ldots}^{\infty}\frac{1}{n}\sin\left(n\omega t\right)\right] && (4.16)\end{aligned}$$

and

$$v_{diff}\left(\omega t\right) = v_{DS1}\left(\omega t\right) - v_{DS2}\left(\omega t\right) = V_{DS,max}\sin\left(\omega t\right). \tag{4.17}$$

The common mode current and voltage are

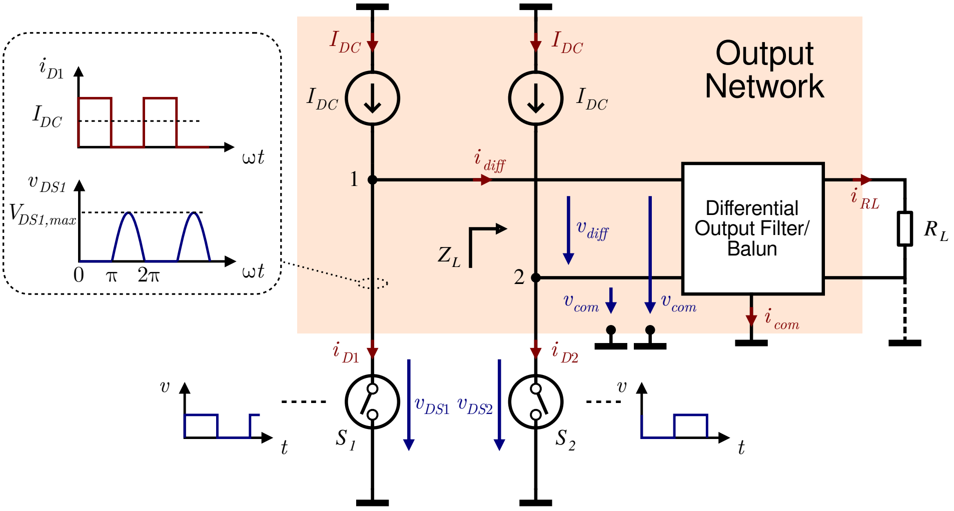

Figure 4.4.: Ideal current mode class-D amplifier with differential output filter

$$i_{com}(\omega t) = 2I_{DC} - (i_{D1}(\omega t) + i_{D2}(\omega t)) = 0 \tag{4.18}$$

and

$$\begin{aligned} v_{com}(\omega t) &= \frac{1}{2}(v_{DS1}(\omega t) + v_{DS2}(\omega t)) \\ &= \frac{1}{\pi} V_{DS,max}\left[1 - \sum_{n=2,4,6,\ldots}^{\infty} \frac{2}{n^2-1}\cos(n\omega t)\right]. \end{aligned} \tag{4.19}$$

The impedance in differential mode Z_{dd11} comes to

$$\boxed{Z_{dd11}(n) = \left|\frac{\hat{v}_{diff}(n)}{\hat{i}_{diff}(n)}\right|}, \tag{4.20}$$

with $\hat{v}_{diff}(n)$ and $\hat{i}_{diff}(n)$ the Fourier coefficients of the nth harmonic. This term is only defined for odd harmonics ($n = 1, 3, 5, \ldots$). For $n = 1$ the differential mode impedance is

$$Z_{dd11}(1) = \frac{\pi}{4}\frac{V_{DS,max}}{I_{DC}} = \frac{\pi^2}{4}\frac{V_{DC}}{I_{DC}} = R_L \tag{4.21}$$

with R_L the optimum output load of the CMCD PA as shown in 2.18. For higher odd harmonics Z_{dd11} is reduced to

$$Z_{dd11}\left(n = 3, 5, 7, ...\right) = 0. \tag{4.22}$$

The impedance in common mode Z_{cc11} is

$$\boxed{Z_{cc11}\left(n\right) = \left|\frac{\hat{v}_{com}\left(n\right)}{\hat{i}_{com}\left(n\right)}\right|}, \tag{4.23}$$

with $\hat{v}_{com}\left(n\right)$ and $\hat{i}_{com}\left(n\right)$ the Fourier coefficients of the nth harmonic and is only defined for even harmonics ($n = 2, 4, 6, ...$) with

$$Z_{cc11}\left(n = 2, 4, 6, ...\right) \rightarrow \infty. \tag{4.24}$$

Z_{cc11} additionally includes a DC term, therefore the output network has to be galvanically isolated from the ground terminal. This will be important in Chapter 5, when single-ended loads with baluns are implemented.

So far impedances have been calculated only from the ideal voltage and current waveforms at the CMCD PA. In this case the common mode impedance of the fundamental ($Z_{cc11}\left(1\right)$) is not defined and therefore can be set arbitrarily - the class-D PA will be terminated correctly. However, the given set of harmonic impedances does not define *where* the RF power is actually absorbed. Fig. 4.5 illustrates the mixed mode load impedance Z_L, which is composed of the load impedances Z_{diff} and Z_{com}. Ideally Z_{diff} should be equal to the output resistance R_L to implement $Z_{dd11}\left(1\right) = R_L$. The latter can also be shown by an arbitrary combination of Z_{diff} and Z_{com} as they are both connected in parallel in differential mode. In that case the RF power will be absorbed in both Z_{diff} and Z_{com}, reducing the power at the (differential) load R_L and ultimately derogating efficiency. For an ideal harmonically tuned *and* highly efficient current mode class-D amplifier, the common mode impedance Z_{cc11} for the fundamental has to be

$$Z_{cc11}\left(n = 1\right) \rightarrow \infty, \tag{4.25}$$

making sure that all the RF power is absorbed in the differential load R_L.

Table 4.1 sums up the ideal harmonic impedances at the CMCD amplifier.

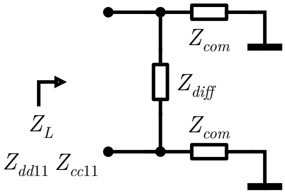

Figure 4.5.: Mixed mode load impedance Z_L composed of impedances Z_{diff} and Z_{com}

Table 4.1.: Ideal harmonic impedances at the CMCD PA

Harmonic frequency $n \cdot f_s$	**Impedance** Z_L	
	Differential mode (Z_{dd11})	Common mode (Z_{cc11})
Direct current (DC)	n.d.[1]	∞ (open)
Switching frequency f_s	R_L (load)	∞ (open)
Even harmonics n	n.d.[1]	∞ (open)
Odd harmonics n	0 (short)	n.d.[1]

---

[1] n.d.: impedance is undefined

4.3.2 Output Network Imbalance

The common mode termination for even harmonics ($Z_{cc11}\,(n = 2, 4, 6, ...) \rightarrow \infty$) is often neglected or overlooked in literature and a fully symmetrical design is assumed. However, in the (U)HF domain this is never the case.

The efficiency factor η_{BI} describes the influence of a finite common mode impedance Z_{cc11}, caused by an asymmetrical design on the CMCD efficiency. For the fundamental frequency ($n = 1$), $\eta_{BI}\,(n = 1)$ is calculated according to Fig. 4.5 by the ratio of powers absorbed into the impedances Z_{diff} and Z_{com}:

$$\eta_{BI}\,(n=1) = \frac{P_{diff}}{P_{diff} + P_{com}} = \frac{\frac{1}{Z_{diff}}}{\frac{1}{Z_{diff}} + \frac{1}{2Z_{com}}} = \frac{1}{1 + \frac{Z_{diff}}{2Z_{com}}}. \tag{4.26}$$

With $R_{cc11}\left(n=1\right)=\frac{1}{2}Z_{com}$ and $R_L = Z_{diff}$, $\eta_{BI}\left(n=1\right)$ is given by

$$\boxed{\eta_{BI}\left(n=1\right)=\frac{1}{1+\frac{R_L}{4R_{cc11}(1)}}}. \tag{4.27}$$

For the even harmonic frequencies $(n = 2, 4, ...)$, $\eta_{BI}\left(n=2,4,...\right)$ is as well calculated by the ratio of powers at the impedances Z_{diff} and Z_{com}:

$$\eta_{BI}\left(n=2,4,...\right)=\frac{P_{diff}\left(n=1\right)}{P_{diff}\left(n=1\right)+P_{com}\left(n=2,4,...\right)}. \tag{4.28}$$

With $P_{diff}\left(n=1\right)=P_{out}=\frac{1}{2}\frac{\hat{v}_{diff}^2}{R_L}$ from 2.10 and $\hat{v}_{diff}=V_{DS,max}$ from 2.16 and

$$P_{com}\left(n=2,4,...\right)=\frac{v_{com}^2\left(n=2,4,...\right)}{Z_{com}}=\frac{\frac{1}{\pi^2}V_{DS,max}^2\left(\frac{2}{n^2-1}\right)^2}{Z_{com}} \tag{4.29}$$

from 4.19 the efficiency factor $\eta_{BI}\left(n=2,4,...\right)$ is

$$\eta_{BI}\left(n=2,4,...\right)=\frac{\frac{1}{2}\frac{V_{DS,max}^2}{R_L}}{\frac{1}{2}\frac{V_{DS,max}^2}{R_L}+\frac{\frac{1}{\pi^2}V_{DS,max}^2\left(\frac{2}{n^2-1}\right)^2}{Z_{com}}}=\frac{1}{1+\frac{2}{\pi^2}\left(\frac{2}{n^2-1}\right)^2\frac{R_L}{Z_{com}}} \tag{4.30}$$

and with $R_{cc11}\left(n=1\right)=\frac{1}{2}Z_{com}$ it can by expressed by

$$\boxed{\eta_{BI}\left(n=2,4,...\right)=\frac{1}{1+\frac{2}{\pi^2}\left(\frac{2}{n^2-1}\right)^2\frac{R_L}{2R_{cc11}}}}. \tag{4.31}$$

Fig. 4.6 shows the efficiency η_{BI} as a function of a non-ideal common mode impedance $(Z_{cc11} = R_{cc11})$. The resistance R_{cc11} is swept for the fundamental and three even harmonic frequencies individually and then normalized to the load resistance R_L. Towards high resistances $R_{cc11}\left(n\right)$ the efficiency is 100%. Towards low $R_{cc11}\left(n\right)$ the efficiency degrades with the fundamental and the second harmonic having the greatest influence. The calculations have been verified with a *Keysight* ADS simulation of an ideal CMCD PA with an ideal differential termination $(Z_{dd11}\left(n=3,5,7,...\right)=0)$.

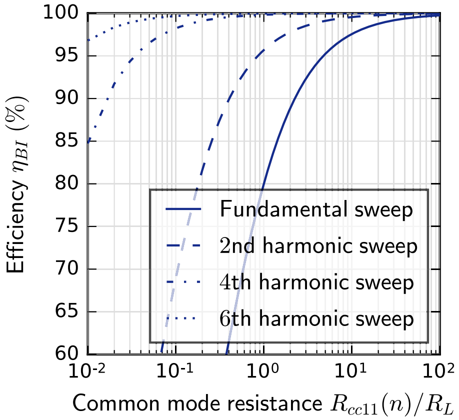

Figure 4.6.: Efficiency degradation of an ideal CMCD PA with non-ideal common mode termination by sweeping the R_{cc11} of the first and nth even harmonic

Using R_{cc11} as a purely resistive common mode impedance is assumed to be a worst case scenario compared to reactive loads. However, parasitic transmission lines in common mode can have a strong impact on the efficiency by transforming an “open” to a “short” condition. The balun design in Chapter 5 will (among other things) focus on the common mode impedance optimization.

4.4 Analysis of the DC Supply Network

The current mode class-D amplifier is a current switching architecture (opposed to the voltage switching VMCD PA). Therefore, constant current sources are needed, which can be implemented in the RF domain with DC biased inductors (Fig. 4.7). These so-called radio frequency chokes (RFC) supply the amplifier with the constant currents I_{DC} and therefore low DC losses are desirable. Furthermore, the RFCs isolate the RF from the DC domain, hence they are required to be high-impedance for the switching frequency and its harmonics.

DC losses are modeled by the parasitic series resistance R_{RFC}.

4.4.1 Dimensioning of the Radio Frequency Chokes

When dimensioning the radio frequency chokes, three items have to be considered:

- L_{RFC} should be sufficiently large to supply the energy of half an RF cycle (two inductors in the design),

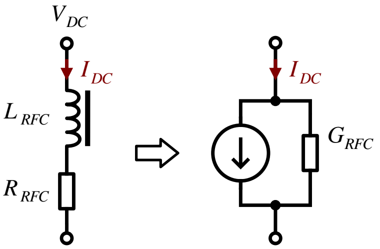

Figure 4.7.: Radio frequency chokes (RFC) with V_{DC} bias, modeled as current sources in the RF domain

- L_{RFC} should be as small as possible to minimize capacitive or resistive losses,
- L_{RFC} has to be high-impedance for the switching frequency and its harmonics.

The energy E_{RFC} saved in the inductor L_{RFC} is given by

$$E_{RFC} = \frac{1}{2} L_{RFC} I_{DC}^2. \tag{4.32}$$

With the fundamental component of the differential current $i_{diff}(\omega t)$ (Equation 2.8) and $T_s = \frac{1}{f_s}$, the fundamental energy of half an RF cycle $E_{RF,1}$ can be written as

$$E_{RF,1} = \int_0^{\frac{T_s}{2}} i_{diff}^2(\omega t) R_L dt = \int_0^{\frac{T_s}{2}} \left(\frac{4}{\pi} I_{DC} \sin(\omega t)\right)^2 R_L dt = \frac{4}{\pi^2} T_s I_{DC}^2 R_L. \tag{4.33}$$

With $E_{RFC} \geq E_{RF,1}$ the minimum value of L_{RFC} is

$$\boxed{L_{RFC} \geq \frac{8}{\pi^2} \frac{1}{f_s} R_L}. \tag{4.34}$$

In order to account for losses, L_{RFC} should be slightly overdimensioned.

Fig. 4.8 (left) shows the minimum inductance L_{RFC} as a function of load resistance R_L for different switching frequencies.

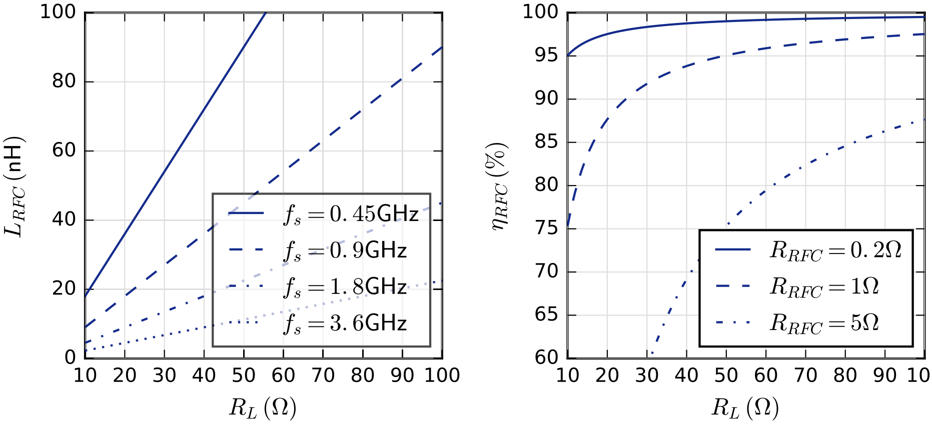

Figure 4.8.: Minimum inductance L_{RFC} as a function of load resistance R_L for different switching frequencies (left) and efficiency factor η_{RFC} as a function of load resistance R_L for different R_{RFC} (right)

4.4.2 *Influence of Parasitic Resistance*

At a constant DC current I_{DC}, the power loss P_{RFC} at the RFC inductor can be obtained by

$$P_{RFC} = I_{DC}^2 R_{RFC}. \tag{4.35}$$

The efficiency η_{RFC} is

$$\eta_{RFC} = 1 - \frac{2P_{RFC}}{P_{DC}} = 1 - \frac{2I_{DC}^2 R_{RFC}}{2V_{DC}I_{DC}} \tag{4.36}$$

and with the optimum impedance R_L (2.18) it can be expressed by

$$\boxed{\eta_{RFC} = 1 - \frac{\pi^2}{4}\frac{R_{RFC}}{R_L}}. \tag{4.37}$$

Fig. 4.8 (right) shows the efficiency factor η_{RFC} as a function of load resistance R_L for different R_{RFC}.

4.4.3 *Component Selection*

As shown earlier in Section 3.3.3, the so-called conical inductors provided by companies like *Coilcraft* and *Piconics* [38] offer a superior broadband performance compared to standard lumped inductors. Fig. 4.9 shows two components, a

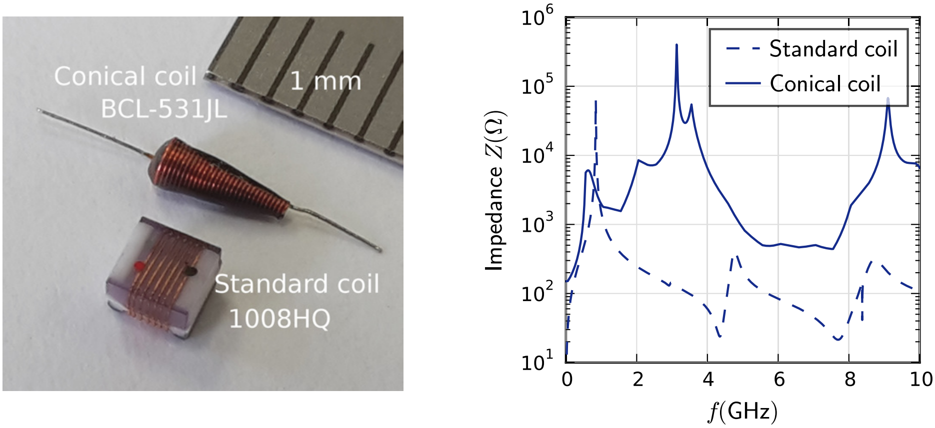

Figure 4.9.: *Coilcraft* standard lumped inductor 1008HQ with $L_{RFC} = 100\,\mathrm{nH}$ and *Coilcraft* conical inductor BCL-531JL with $L_{RFC} = 530\,\mathrm{nH}$ and comparable R_{RFC}

Coilcraft lumped inductor 1008HQ with $L_{RFC} = 100\,\mathrm{nH}$ and $R_{RFC} = 0.16\,\Omega$ and a *Coilcraft* conical inductor BCL-531JL with $L_{RFC} = 530\,\mathrm{nH}$ and $R_{RFC} = 0.15\,\Omega$, and compares them on the frequency axis.

4.5 Optimized Output Filter

4.5.1 LC Resonator Output Filter

As the Sections 2.3.1 and 4.3.1 have shown, the ideal CMCD is terminated at the output with a differential filter, which shorts differential harmonic content of the switched currents ($Z\,(n = 3, 5, 7, ...) = 0$) at the load. The simplest implementation of such a filter is a parallel LC resonator circuit with inductor L_P and capacitor C_P. Parasitic losses of the reactive components are characterized by the resistor R_V (Fig. 4.10 and Fig. 2.7).

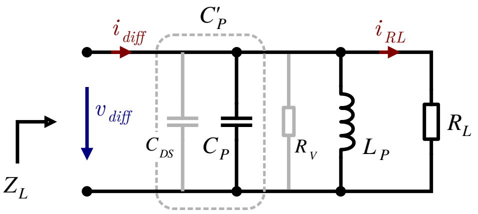

Figure 4.10.: Output filter in LC resonator circuit configuration

In order to ensure ideal harmonic termination, the resonance frequency of the output filter f_c has to be tuned to the switching frequency of the amplifier f_s,

$$f_c = f_s. \tag{4.38}$$

Assuming that L_D and R_C of the switched transistors (Fig. 2.7) are small, the parasitic drain-to-source capacitance C_{DS} and C_P can be merged in the combined capacitance $C'_P = C_P + C_{DS}$ and f_c is given by

$$f_c = \frac{1}{2\pi\sqrt{L_P C'_P}} = \frac{1}{2\pi\sqrt{L_P\left(C_P + C_{DS}\right)}}. \tag{4.39}$$

The loaded Q factor of the resonator Q_P can be obtained with the total parallel resistance $R_P = \frac{1}{\frac{1}{R_L}+\frac{1}{R_V}}$ by

$$Q_P = R_P \cdot \sqrt{\frac{C'_P}{L_P}} \tag{4.40}$$

and with 4.39 Q_p is

$$\boxed{Q_P = 2\pi f_c R_P C'_P = \frac{R_P}{2\pi f_c L_P}}. \tag{4.41}$$

In conjunction with f_c the 3 dB resonator bandwidth B_P can be given as a function of the loaded Q factor by

$$\boxed{B_P = \frac{f_c}{Q_P}}. \tag{4.42}$$

For a given R_P and f_c the loaded Q factor Q_P and, therefore, the bandwidth of the resonator depend on the selection of C'_P and L_P.

The 3 dB percent bandwidth $B_{P\%}$, as shown in equation 2.2 in Section 2.2, can be written as a function of Q_P with

$$\boxed{B_{P\%} = 2\cdot\frac{f_{U1} - f_{L1}}{f_{U1} + f_{L1}} = \frac{B_P}{f_c} = \frac{1}{Q_P}}. \tag{4.43}$$

Harmonic signal suppression of the resonator

The impedance of the loaded resonator Z_L is

$$Z_L(\omega) = \frac{1}{\frac{1}{R_P} + j\omega C'_P + \frac{1}{j\omega L_P}} = \frac{1}{\frac{1}{R_P} + j\left(\omega C'_P - \frac{1}{\omega L_P}\right)}. \tag{4.44}$$

With 4.41 and the harmonics of the switching frequency $\omega = n \cdot \omega_s = n \cdot 2\pi f_c$ and $\omega_c = \omega_s$ the impedance $Z_L(n)$ is

$$Z_L(n) = \frac{R_P}{1 + jR_P\left(n\omega_s C'_P - \frac{1}{n\omega_s L_P}\right)} = \frac{R_P}{1 + jQ_P\left(n - \frac{1}{n}\right)}. \tag{4.45}$$

The harmonic spectrum of the differential current i_{diff} has been calculated in equation 2.8 in Section 2.3.1 and is

$$i_{\mathit{diff}}(n\omega_s t) = \hat{\imath}_{\mathit{diff}}(n)\sin(n\omega_s t) \tag{4.46}$$

with the harmonic current amplitude

$$\hat{\imath}_{\mathit{diff}}(n) = \frac{4}{\pi n} I_{DC}. \tag{4.47}$$

To account for losses due to inadequate harmonic matching solely, the parasitic losses of the resonator now will be disregarded, i.e., $R_V \gg R_L$ and therefore $R_P = R_L$.

The real power at the load including the harmonic components is then given by $\hat{\imath}_{\mathit{diff}}$ and the real part of Z_L:

$$\begin{aligned} P_{out} &= \sum_{n=1,3,5,\ldots}^{\infty} \frac{1}{2}\left(\hat{\imath}_{\mathit{diff}}(n)\right)^2 \cdot \mathrm{Re}\{Z_L\} \\ &= \underbrace{\frac{8}{\pi^2} I_{DC}^2 \cdot R_L}_{fundamental\,power\,P_{out}(1)} + \underbrace{\sum_{n=3,5,7,\ldots}^{\infty} \frac{8}{\pi^2 n^2} I_{DC}^2 \cdot \frac{R_L}{1 + \left(n - \frac{1}{n}\right)^2 Q_P^2}}_{higher\,harmonics}. \end{aligned} \tag{4.48}$$

The nth harmonic power $P_{out}(n)$ is then

$$P_{out}(n) = \frac{8}{\pi^2 n^2} I_{DC}^2 \cdot \frac{R_L}{1 + \left(n - \frac{1}{n}\right)^2 Q_P^2}. \tag{4.49}$$

The efficiency factor η_{PO} describes the efficiency degradation by higher harmonic power at the output load due to the non-ideal harmonic impedance termination of the loaded resonator. η_{PO} is calculated by the ratio of the fundamental power $P_{out}(1)$ and the total power P_{out} with

$$\boxed{\eta_{PO} = \frac{P_{out}(1)}{P_{out}} = \frac{1}{1 + \sum_{n=3,5,7,\ldots}^{\infty} \frac{1}{n^2} \cdot \frac{1}{1+\left(n-\frac{1}{n}\right)^2 Q_P^2}}}. \tag{4.50}$$

The total harmonic distortion THD is given by the ratio of the sum of nth harmonic powers $P_{out}(n)$ and the fundamental power $P_{out}(1)$ and can be written as

$$\boxed{\mathrm{THD} = \frac{\sum_{n=3,5,7,\ldots}^{\infty} P_{out}(n)}{P_{out}(1)} = \sum_{n=3,5,7,\ldots}^{\infty} \frac{1}{n^2} \cdot \frac{1}{1+\left(n-\frac{1}{n}\right)^2 Q_P^2}}. \tag{4.51}$$

The selection of the Q_P results from a compromise:

- The minimum Q factor is determined by the minimum necessary bandwidth B_P (Equation 4.42).
- The maximum Q factor is given by the maximum permitted total harmonic distortion THD (Equation 4.51).

Apart from that, the Q_P design space is limited by the availability of lumped element device values and by parasitics.

Fig. 4.11 shows the efficiency η_{PO} and the total harmonic distortion THD (left) as well as the percent bandwidth $B_{P\%}$ (right) as a function of Q_P.

Influence of resistance R_V

The parasitic losses of the resonator are modeled by the resistor R_V. Due to the parallel circuit of R_L and R_V the efficiency factor η_{PP} of the resonator is calculated with the linear power ratio of load power and total power.

$$\boxed{\eta_{PP} = \frac{\frac{1}{2}\hat{v}_{diff}^2 \frac{1}{R_L}}{\frac{1}{2}\hat{v}_{diff}^2 \left(\frac{1}{R_L} + \frac{1}{R_V}\right)} = \frac{R_V}{R_V + R_L}} \tag{4.52}$$

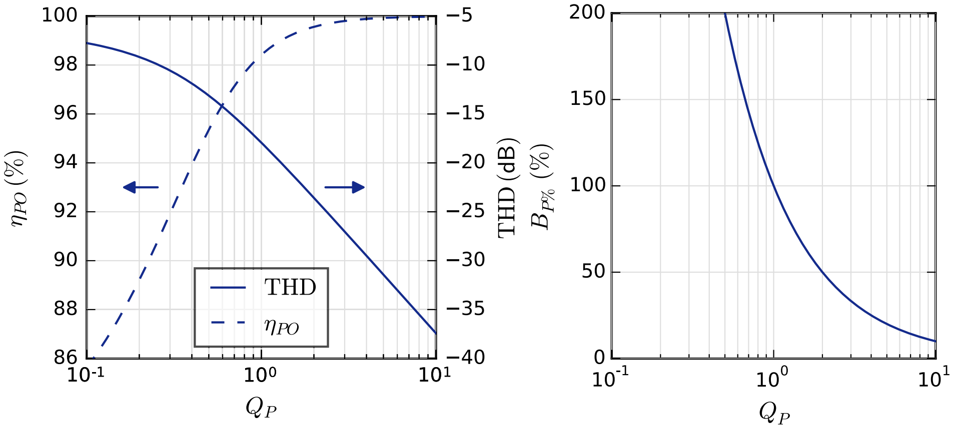

Figure 4.11.: Efficiency factor η_{PO} of the loaded LC resonator and total harmonic distortion THD as a function of quality factor Q_P (left) and 3 dB percent bandwidth $B_{P\%}$ as a function of Q_P (right)

4.5.2 Low-pass Output Filter

The bandwidth and distortion trade-off is an inherent issue of simple filter designs with only two elements like the LC resonator shown above. The maximum percent bandwidth $B_{\%}$ of a current mode class-D PA with three harmonics properly terminated is 100% (see Section 2.2). According to 4.43, a percent bandwidth of the LC resonator $B_{P\%} = 100\%$ results in a Q factor of 1 and, therefore, with 4.51 in a THD of only -17 dB (see Fig. 4.11 for a graphical depiction). This might be insufficient for a transmitter design. Additionally, the resonator bandwidth B_P is a 3 dB bandwidth and, therefore, the class-D matching conditions will be definitely violated at the edges of the tuning range, which results in efficiency and output power degradation. Hence, a filter characteristic with a higher slope is required.

Upon looking at the harmonic termination conditions derived in Section 4.3 in Table 4.1, one might notice that predetermined impedances are only defined for the fundamental frequency band and its even and odd harmonics. Thus, the previously implemented band-pass characteristic with the LC resonator is redundant for lower frequencies and a low-pass termination is considerably more suitable for the CMCD.

Bandwidth-wise a low-pass output filter simplifies the design of the output network. In fact every low-pass filter exhibits a percent bandwidth of 200% inherently. Consequently the output network can be designed and optimized solely for distortion and efficiency. There is no more bandwidth-distortion trade-off.

Low-pass Filter Theory

The general transfer function of a passive low-pass filter can be obtained from

$$H_{LP}\left(s\right) = \frac{1}{\prod_i \left(1 + a_i s + b_i s^2\right)} \tag{4.53}$$

with the terms $\left(1 + a_i s + b_i s^2\right)$ forming pairs of poles or single poles (with $b_i = 0$) in the denominator and the coefficients a_i and b_i defining the filter characteristic. The nth degree of the multiplied denominator gives the number of poles and defines the order of the filter. Each pole adds a –6 dB per octave or –20 dB per decade response. A pair of poles on the imaginary axis in the s-plane can be described by a quality factor, the pole quality Q_{LP}, by

$$Q_{LP} = \frac{\sqrt{b_i}}{a_i}. \tag{4.54}$$

The transfer function $H_{LP}\left(s\right)$ of a second order low-pass filter can be rewritten with Q_{LP} and with the resonance frequency ω_c, which is also the corner frequency separating pass- and stopband, by

$$H_{LP2}\left(s\right) = \frac{\omega_c^2}{s^2 + \frac{\omega_c}{Q_{LP}} s + \omega_c^2}, \tag{4.55}$$

as shown in [42].

The magnitude of this transfer function $G_{LP2}\left(\omega\right)$ can be obtained with $s = j\omega$ by

$$\left|H_{LP2}\left(j\omega\right)\right| = G_{LP2}\left(\omega\right) = \frac{\omega_c^2}{\sqrt{\omega^4 + \left(\frac{1}{Q_{LP}^2} - 2\right)\omega_c^2 \omega^2 + \omega_c^4}} \tag{4.56}$$

and with $\omega = n\omega_s$ it can be expressed as a function of the nth harmonic n by

$$G_{LP2}\left(n\right) = \frac{\omega_c^2}{\sqrt{n^4 \omega_s^4 + \left(\frac{1}{Q_{LP}^2} - 2\right)\omega_c^2 n^2 \omega_s^2 + \omega_c^4}}. \tag{4.57}$$

Now the switching frequency is normalized $\omega_s = 1$ and set to the resonance frequency $\omega_c = \omega_s = 1$.

The total harmonic distortion THD_{LP2} of the second order low-pass is then derived from $G_{LP2}(n)$ by

$$\boxed{\mathrm{THD}_{LP2} = \frac{\sum_{n=3,5,7,\ldots}^{\infty} G_{LP2}^2(n)}{G_{LP2}^2(n=1)} = \frac{1}{Q_{LP}^2} \sum_{n=3,5,7,\ldots}^{\infty} \frac{1}{n^4 + \left(\frac{1}{Q_{LP}^2} - 2\right) n^2 + 1}}. \tag{4.58}$$

The efficiency factor $\eta_{PO,LP2}$ is

$$\boxed{\eta_{PO,LP2} = \frac{G_{LP2}^2(n=1)}{\sum_{n=1,3,5,7,\ldots}^{\infty} G_{LP2}^2(n)} = \frac{1}{1 + \frac{1}{Q_{LP}^2} \sum_{n=3,5,7,\ldots}^{\infty} \frac{1}{n^4 + \left(\frac{1}{Q_{LP}^2} - 2\right) n^2 + 1}}}. \tag{4.59}$$

A comparison of the efficiency factor and the distortion of the second order low-pass with the recently derived equations for the LC resonator (Equation 4.50 and 4.51) yields equality of both calculations. This is hardly surprising, though, the LC resonator is a second order filter just like the low-pass calculated above.

To improve the stopband suppression and therefore THD, the second order low-pass filter is converted into a third order filter simply by adding an additional pole $(s + \omega_c)$ to the denominator of the transfer function $H_{LP3}(s)$,

$$H_{LP3}(s) = \frac{\omega_c^2}{(s + \omega_c)\left(s^2 + \frac{\omega_c}{Q_{LP}} s + \omega_c^2\right)}. \tag{4.60}$$

The magnitude of this transfer function $G_{LP3}(\omega)$ with $s = j\omega$ can be obtained by

$$\begin{aligned} |H_{LP3}(j\omega)| &= G_{LP3}(\omega) \\ &= \frac{\omega_c^2}{\sqrt{\omega^6 + \left(\frac{1}{Q_{LP}^2} - 1\right)\omega_c^2\omega^4 + \left(\frac{1}{Q_{LP}^2} - 1\right)\omega_c^4\omega^2 + \omega_c^6}} \end{aligned} \tag{4.61}$$

and with $\omega = n\omega_s$ it can be expressed as a function of the nth harmonic by

$$G_{LP3}\left(n\right) = \frac{\omega_c^2}{\sqrt{n^6\omega_s^6 + \left(\frac{1}{Q_{LP}^2} - 1\right)\omega_c^2 n^4 \omega_s^4 + \left(\frac{1}{Q_{LP}^2} - 1\right)\omega_c^4 n^2 \omega_s^2 + \omega_c^6}}. \tag{4.62}$$

The switching frequency is again normalized $\omega_s = 1$ and set to the resonance frequency $\omega_c = \omega_s = 1$.

The total harmonic distortion THD_{LP3} of the third order low-pass is then derived from $G_{LP3}\left(n\right)$ by

$$\boxed{\begin{aligned}\mathrm{THD}_{LP3} &= \frac{\sum_{n=3,5,7,\ldots}^{\infty} G_{LP3}^2\left(n\right)}{G_{LP3}^2\left(n=1\right)} \\ &= \frac{2}{Q_{LP}^2}\sum_{n=3,5,7,\ldots}^{\infty}\frac{1}{n^6 + \left(\frac{1}{Q_{LP}^2} - 1\right)n^4 + \left(\frac{1}{Q_{LP}^2} - 1\right)n^2 + 1}\end{aligned}}. \tag{4.63}$$

The efficiency factor $\eta_{PO,LP3}$ is

$$\boxed{\begin{aligned}\eta_{PO,LP3} &= \frac{G_{LP3}^2\left(n=1\right)}{\sum_{n=1,3,5,7,\ldots}^{\infty} G_{LP3}^2\left(n\right)} \\ &= \frac{1}{1 + \frac{2}{Q_{LP}^2}\sum_{n=3,5,7,\ldots}^{\infty}\frac{1}{n^6 + \left(\frac{1}{Q_{LP}^2} - 1\right)n^4 + \left(\frac{1}{Q_{LP}^2} - 1\right)n^2 + 1}}\end{aligned}}. \tag{4.64}$$

Fig. 4.12 (left) shows the distortion THD and the efficiency η_{PO} for the second order low-pass (LP 2nd, THD_{LP2} and $\eta_{PO,LP2}$) and the third order low-pass (LP 3rd, THD_{LP3} and $\eta_{PO,LP3}$) in comparison as a function of pole quality Q_{LP}. The third order low-pass improves the total harmonic distortion by approximately 7 dB.

In Fig. 4.12 (right) the magnitude of the low-pass transfer function G_{LP} is shown as a function of normalized frequency for different pole qualities Q_{LP}. The frequency is normalized to the resonance or corner frequency of the filter ω_c, therefore $\omega_c = 1$. The filter is maximally flat for $Q_{LP} = \frac{\sqrt{2}}{2}$, i.e., it shows a Butterworth response [42]. For higher quality factors some peaking occurs, i.e., the filter shows a Chebyshev response [42]. To get a good harmonic suppression

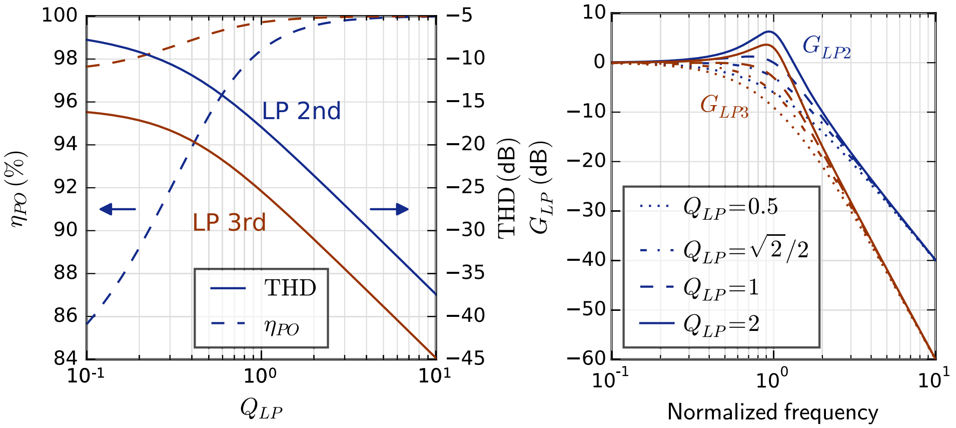

Figure 4.12.: Total harmonic distortion THD and efficiency η_{PO} as a function of pole quality factor Q_{LP} for a second (LP 2nd) and a third (LP 3rd) order low-pass filter (left) and magnitude of the low-pass transfer function G_{LP} as a function of normalized frequency for different pole qualities Q_{LP} (right)

in the stopband and a good THD, the amplifier band should be moved closely to the resonance of the filter ω_C. Thus, Q factors of $Q_{LP} \gg \frac{\sqrt{2}}{2}$ are highly desirable and the output filter will, therefore, have a Chebyshev characteristic. The inherent passband ripple of the Chebyshev filter will slightly detune the CMCD amplifier. However this is not an issue as will be shown later.

Third Order Low-pass Filter Design

The third order low-pass filter from Section 4.5.2 is derived from a second order filter by just adding another single pole at the real axis of the s-plane. The filter coefficients, however, are not optimized to represent a Chebyshev characteristic with a predefined passband ripple. The synthesis of an optimized balanced low-pass filter will be illustrated in this section.

Fig. 4.13 shows a balanced third order low-pass implementation of the output filter in ladder topology. It consists of two parallel capacitors C_P and two inductors L_S in series. The filter is singly terminated by the load R_L and driven by the current i_{diff} generated from the switched current sources of the CMCD. In [43] equations for calculating singly terminated Chebyshev low-pass filters are given. The normalized element values g_k are depicted in Fig. 4.13. Due to the infinite-impedance current generator at the input, the first element g_3 has to be in parallel. With the normalized corner frequency $\omega_c' = 1$, the normalized load resistance $g_0 = 1$ and R_{dB}, the Chebyshev passband ripple, the element values are

$$\beta = \ln\left(\coth\frac{R_{\mathrm{dB}}}{17.37}\right) \tag{4.65}$$

$$\gamma = \sinh\left(\frac{\beta}{2n}\right) \tag{4.66}$$

$$a_k = \sin\frac{\pi\,(2k-1)}{2n}, \quad k = 1, 2, ..., n \tag{4.67}$$

$$d_k = \left(\gamma^2 + \sin^2\frac{\pi k}{2n}\right)\cos^2\frac{\pi k}{2n}, \quad k = 1, 2, ..., n-1 \tag{4.68}$$

and

$$g_1 = \frac{a_1}{\gamma} \tag{4.69}$$

$$g_k = \frac{a_k a_{k-1}}{d_{k-1} g_{k-1}}, \quad k = 1, 2, ..., n. \tag{4.70}$$

The following equations are used to transform the normalized element values to given impedance levels and frequency scales.

For the normalized corner frequency $\omega'_c = 1$ and the normalized load resistance $g_0 = 1$, the reference resistance R_0 is given as a function of the differential load resistance R_L by

$$R_0 = \frac{1}{2g_0}R_L = \frac{1}{2}R_L. \tag{4.71}$$

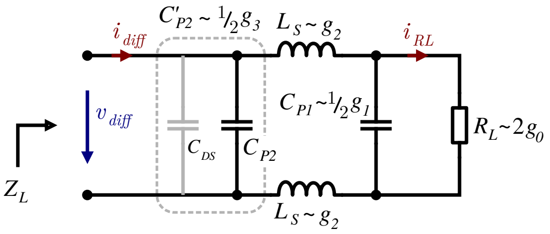

Figure 4.13.: Output filter in low-pass configuration

The parallel capacitors C_{P1} and C_{P2} with $C'_{P2} = C_{P2} + C_{DS}$ and the series inductors L_S are calculated as follows:

$$C_{P1} = \frac{1}{2}\frac{1}{\omega_c R_0} g_1, \tag{4.72}$$

$$C'_{P2} = \frac{1}{2}\frac{1}{\omega_c R_0} g_3, \tag{4.73}$$

$$L_S = \frac{R_0}{\omega_c} g_2. \tag{4.74}$$

For $n = 3$ and $R_{\text{dB}} = 0.1\,\text{dB}$ and at $f_c = \frac{\omega_c}{2\pi} = 1\,\text{GHz}$ and $R_L = 50\,\Omega$, the lumped element values are

$$g_1 = 0.5158 \qquad C_{P1} = 1.64\,\text{pF} \tag{4.75}$$

$$g_2 = 1.0864 \qquad L_S = 4.32\,\text{nH} \tag{4.76}$$

$$g_3 = 1.0895 \qquad C'_{P2} = 3.47\,\text{pF}. \tag{4.77}$$

The impedance of the loaded low-pass filter in Fig. 4.13 is given with $C'_{P2} = C_{P2} + C_{DS}$ by

$$\boxed{\begin{aligned} Z_L(\omega) = & \frac{1}{j\omega C'_{P2} + \frac{1}{2j\omega L_S + \frac{1}{j\omega C_{P1} + \frac{1}{R_L}}}} \\ = & \frac{\frac{1}{R_L} + j\left(\omega^5 \cdot d + \omega^3 \cdot e + \omega \cdot f\right)}{\omega^6 \cdot a + \omega^4 \cdot b + \omega^2 \cdot c + \frac{1}{R_L^2}} \end{aligned}} \tag{4.78}$$

with

$$a = 4L_S^2 C_{P1}^2 C'^2_{P2} \tag{4.79}$$

$$b = 4L_S^2 C'^2_{P2}\frac{1}{R_L^2} - 4L_S C_{P1} C'_{P2}\left(C_{P1} + C'_{P2}\right) \tag{4.80}$$

$$c = -4L_S C'_{P2}\frac{1}{R_L^2} + \left(C_{P1} + C'_{P2}\right)^2 \tag{4.81}$$

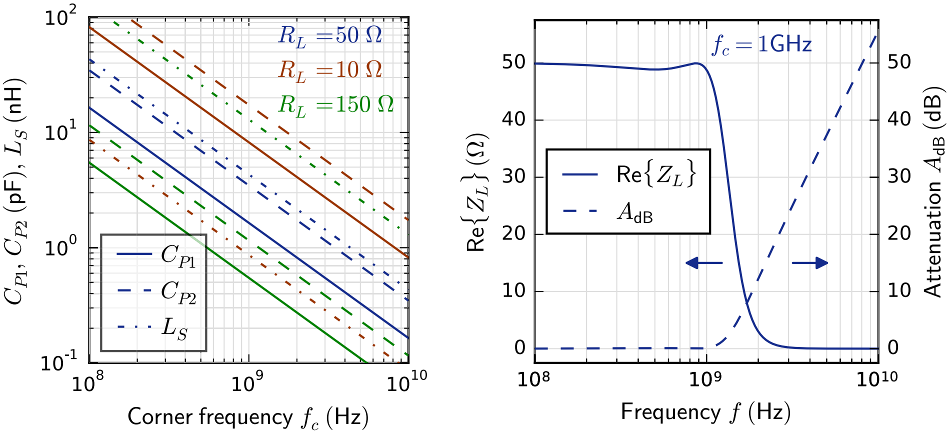

Figure 4.14.: Lumped element values C_{P1}, C_{P2} and L_P as a function of corner frequency $f_c = \frac{\omega_c}{2\pi}$ for a third order Chebyshev low-pass filter with $R_{\mathrm{dB}} = 0.1\,\mathrm{dB}$ (left) and real part of the input impedance Z_L and attenuation A_{dB} of that filter with $f_c = 1\,\mathrm{GHz}$ as a function of frequency (right)

$$d = -8L_S^2 C_{P1}^2 C'_{P2} \tag{4.82}$$

$$e = -4L_S^2 C'_{P2} \frac{1}{R_L^2} + 4L_S C_{P1} C'_{P2} + 2L_S C_{P1}^2 \tag{4.83}$$

$$f = 2L_S \frac{1}{R_L^2} - C_{P1} - C'_{P2}. \tag{4.84}$$

The attenuation A_{dB} at the load R_L as a function of $Z_L(\omega)$ is then

$$\boxed{A_{\mathrm{dB}}(\omega) = 10\log_{10} \frac{R_L}{\mathrm{Re}\{Z_L(\omega)\}}}. \tag{4.85}$$

In Fig. 4.14 (left) the lumped element values of a third order Chebyshev low-pass filter with $R_{\mathrm{dB}} = 0.1\,\mathrm{dB}$ are shown as a function of corner frequency $f_c = \frac{\omega_c}{2\pi}$. Fig. 4.14 (right) depicts the input impedance and the attenuation of that filter with $f_c = 1\,\mathrm{GHz}$ and $R_L = 50\,\Omega$ as a function of frequency.

The total harmonic distortion THD of a CMCD PA with this filter can be calculated with equation 4.48

$$P_{out}(n) = \frac{1}{2}\left(\hat{i}_{diff}(n)\right)^2 \cdot \mathrm{Re}\{Z_L(\omega)\} \tag{4.86}$$

and, therefore,

$$P_{out}(n) \sim \frac{1}{n^2} \cdot \mathrm{Re}\{Z_L(\omega)\} \tag{4.87}$$

and $\omega = n\omega_s$ as a function of the switching frequency by

$$\boxed{\mathrm{THD}(\omega_s) = \frac{\sum_{n=3,5,7,\ldots}^{\infty} P_{out}(n)}{P_{out}(1)} = \frac{\sum_{n=3,5,7,\ldots}^{\infty} \frac{1}{n^2} \cdot \mathrm{Re}\{Z_L(n\omega_s)\}}{\mathrm{Re}\{Z_L(\omega_s)\}}}. \tag{4.88}$$

The efficiency factor η_{PO} is

$$\boxed{\eta_{PO}(\omega_s) = \frac{P_{out}(1)}{P_{out}} = \frac{\mathrm{Re}\{Z_L(\omega_s)\}}{\sum_{n=1,3,5,7,\ldots}^{\infty} \frac{1}{n^2} \cdot \mathrm{Re}\{Z_L(n\omega_s)\}}}. \tag{4.89}$$

Fig. 4.15 (left) depicts the total harmonic distortion and efficiency of the low-pass from Fig. 4.14 with ($f_c = 1$ GHz) as a function of switching frequency $f_s = \frac{\omega_s}{2\pi}$. Additionally, the efficiency has been scaled with the attenuation A_{dB} of the filter to depict the usable bandwidth:

$$\eta(\omega_s) = \eta_{PO}(\omega_s) \cdot 10^{-0.1 \cdot A_{\mathrm{dB}}(\omega_s)}. \tag{4.90}$$

For a maximum THD of -15 dB and a minimum efficiency of 90%, the percent bandwidth of this low-pass filter is $B_{\%} = 71\%$. In the middle of the band at 870 MHz the THD comes to -30 dB. A comparative band-pass filter (LC resonator, Fig. 4.15, right) only has a usable bandwidth of $B_{\%} = 30\%$.

To further increase the bandwidth for a given maximum THD, higher filter orders have to be implemented. In practice the THD is usually lower due to additional filtering effects and a non-ideal rectangular drain current waveform.

The inherent passband ripple of the Chebyshev low-pass adds some attenuation in the passband. However, for $R_{\mathrm{dB}} = 0.1$ dB, the attenuation A_{dB} only decreases the efficiency by maximum 2.5 percentage points.

The capacitor values calculated for low-pass filters in the GHz range are all in the field of picofarads, especially towards high-resistance loads of $>50\,\Omega$. However, high loads are desirable to minimize transistor losses as shown in Section 3.2.2. Therefore, the filter has to be implemented in a way that allows to avoid any inductive parasitic influence at the capacitors. Section 4.5.3 presents a design technique, for implementing low-parasitic differential low-pass filters on printed circuit boards (PCBs).

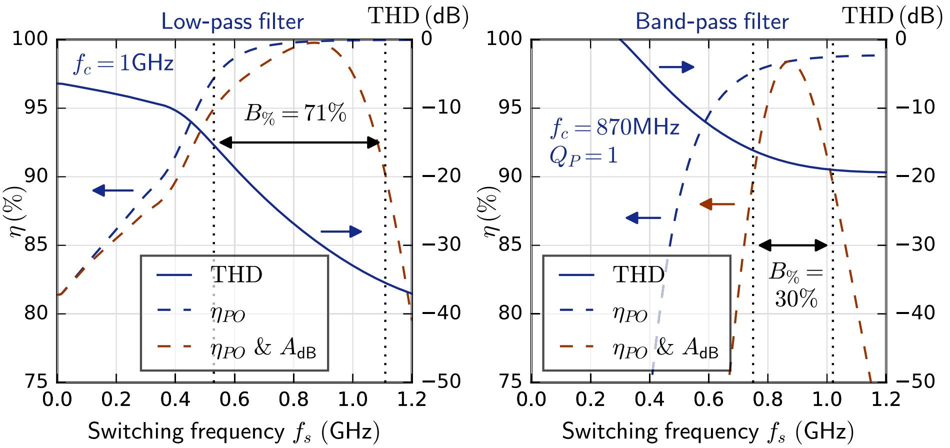

Figure 4.15.: Total harmonic distortion THD and efficiency η_{PO} as a function of switching frequency $f_s = \frac{\omega_s}{2\pi}$ for the low-pass filter from Fig. 4.14 with $f_c = 1$ GHz (left) and for a band-pass filter (LC resonator) with $f_c = 870$ MHz and $Q_P = 1$ (right). The bandwidths $B_{\%}$ of the filters are depicted for a maximum THD of -15 dB and a minimum efficiency of 90%. The term "η_{PO} & A_{dB}" means that the efficiency is weighted according to equation 4.90.

Higher Order Low-pass Filters

So far only filters with orders of $n = 2$ and $n = 3$ have been shown. Due to the necessity of a parallel (capacitive) element at the signal source (see Section 4.5.2), only low-pass filters with odd filter orders are permitted. A filter with an order of $n = 5$ would offer a 12 dB per octave and therefore 24 dB improved suppression of the third harmonic compared to a third order filter. However, two more reactive elements have to be added to raise the order to five and subsequently the passband loss due to parasitic resistances will increase. Fig. 4.1 has shown earlier that the total efficiency of the amplifier largely depends on the losses in the output network and therefore the output filter. Hence, the selection of filter order is a trade-off between harmonic suppression, i.e., distortion, and efficiency.

In Fig. 4.16 two filters with $n = 3$ and $n = 5$ are simulated and compared using ideal lumped elements and real models of high-quality surface mounted device (SMD) components provided by the *Modelithics* "CLR library" [44].

Aside from a slight frequency shift, the 5th order filter exhibits a 0.2 dB ($\approx 5\%$) higher loss at the shifted corner frequency $f_c = 900$ MHz compared to the 3rd order low-pass.

It has to be noted that the increase of efficiency due to improved harmonic matching (η_{PO} in equation 4.59 and 4.64) will not outweigh the additional passband losses.

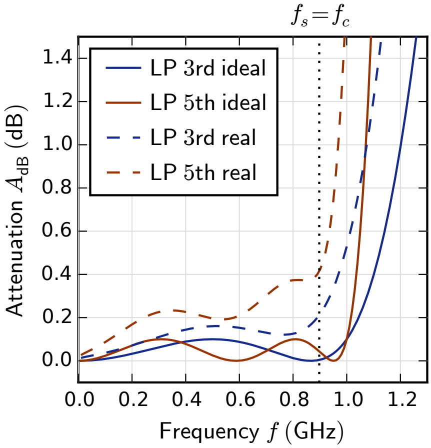

Figure 4.16.: Attenuation A_{dB} of two 3rd and 5th order low-pass filters with ideal and real elements compared on the frequency axis

4.5.3 Output Filter Implementation

PCB Implementation of Output Filters

The switched current sources at the current mode class-D amplifier generate a differential signal which has to be conveyed by a differential transmission line. Fig. 4.17 shows the two most popular implementations of differential transmission lines on a planar PCB. The PCB substrate itself is characterized by constant thickness h and relative permittivity or dielectric constant ϵ_r. The transmission line is either formed by two conductive strips on one side of the substrate with the width w, the slot distance s and conductor thickness t, or formed by two conductive traces on either sides of the substrate characterized by the width w and conductor thickness t. The reference or ground terminal, which completes the differential three-line system, is assumed to be at infinite distance. Therefore, the common mode impedance Z_{cc11} is assumed to be infinitely high and only a differential mode impedance Z_{dd11} is defined. This work does not focus on transmission line theory. To calculate the impedance of the proposed transmission lines, the reader is kindly referred to common literature (e.g., [45]) and software applications (e.g., *Keysight* ADS linecalc tool).

Fig. 4.18 depicts filter implementations with lumped SMD components using the example of an LC resonator and a 3rd order differential low-pass filter. On the top, the paralleled differential conductors are shown with the SMD components mounted horizontally on the surface. On the bottom, an alternative technique is shown using the stacked differential pair. The SMD components are vertically

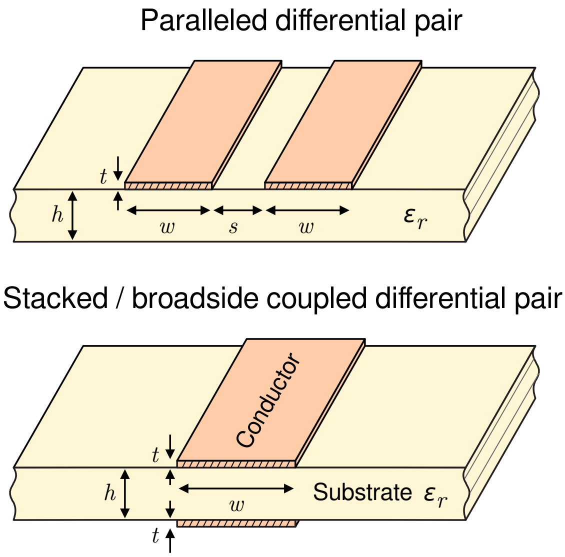

Figure 4.17.: Planar implementation of differential transmission lines: side by side paralleled or stacked pair of conductors

mounted by embedding them into the substrate. This can be done, for instance, by drilling a small hole in the PCB and mechanically fixing the components by soldering them. This way a low-parasitic connection between the conductors and the lumped elements can be implemented. Especially the capacitors will exhibit a low parasitic inductance, which would detune the filter and significantly lower efficiency (see Section 3.2.2 on how drain inductance influences efficiency).

Fig. 4.19 shows a cross section of the PCB with the vertically mounted and soldered SMD elements. To prevent the components from falling through the hole in the PCB in a standard, horizontal manufacturing process, in Fig. 4.20 a modification of the SMD capacitor cap is proposed. A collar added to the cap will secure the component in the vertical mounting position before soldering.

Selection of Transmission Line Layout and Technological Limits

Two transmission line implementations have been offered in this section. The selection in the design process is dependent on the substrate material and structure. In this section the selection is carried out using the example of a standard RF substrate, a two-layer *Rogers* RO4003C laminate with a height $h = 0.508\,\mathrm{mm}$ (0.02”) and relative permittivity $\epsilon_r = 3.55$. The height tolerance of this substrate is $\triangle h = \pm 0.038\,\mathrm{mm}$ (0.0015”) [46] and the conductor thickness is assumed to

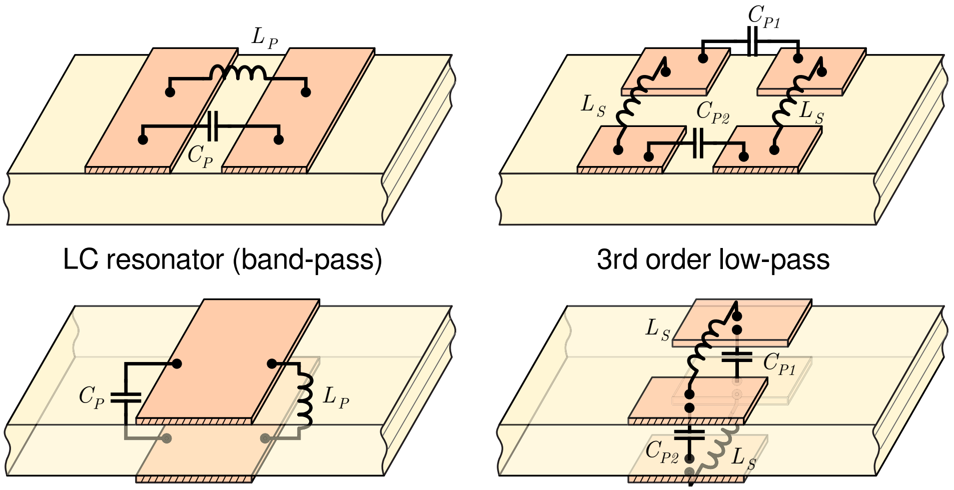

Figure 4.18.: Planar implementation of differential filters with lumped SMD components: surface-mounted on paralleled differential pair (top) and through-hole mounted on stacked differential pair (bottom)

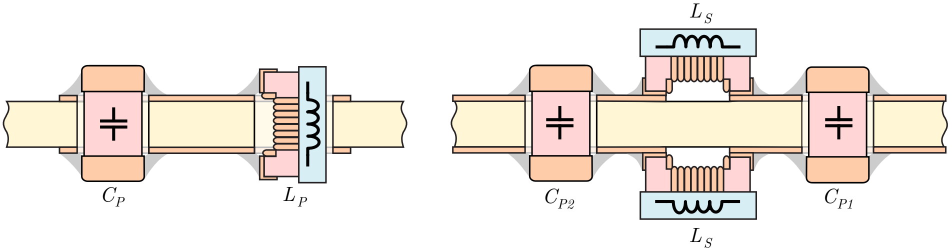

Figure 4.19.: Cross section of PCB with the through hole mounted SMD components

be $t = 35\,\mu\text{m}$. The following impedance calculations are conducted with EM simulations using *Keysight's* ADS Momentum.

A differential $50\,\Omega$ transmission line using the paralleled differential pair results in a conductor width of $w = 1.5\,\text{mm}$ and a slot width of $s = 13\,\mu\text{m}$. The major part of the electrical field component is located outside of the substrate, therefore the substrate thickness h only has little influence on the line impedance. On the other hand, the slot width is smaller than the conductor thickness $s \lesssim t$ (!) and, therefore, the design is very sensitive to manufacturing tolerances and might not be manufacturable at all.

A stacked (broad side coupled) differential pair $50\,\Omega$ transmission line results in a conductor width of $w = 1.5\,\text{mm}$. The major part of the electrical field component is located in the substrate. There is a big influence of the substrate

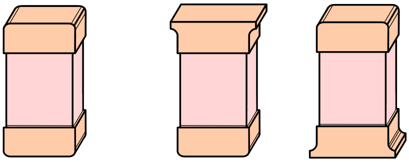

Figure 4.20.: Suggested modification of SMD capacitor cap with collar for fixation in vertical mounting position

thickness h and little influence of the conductor thickness t. The substrate thickness tolerance $\triangle t$ results in an impedance deviation of $\pm 10\%$ at 1 GHz. In the selection of a suitable substrate, the frequency-dependent dielectric loss (loss tangent $\tan\delta$) of the material has to be considered.

To sum up, on a standard RF substrate, the easiest way to implement a $50\,\Omega$ transmission line is by using a broadside coupled differential pair.

5 Optimized Output Balun

This chapter gives an overview of the common balun implementations suitable for differential PAs and presents optimized tapered baluns for wideband switched mode power amplifiers. Finally, a presentation of several CMCD demonstrator PAs consolidates the findings of this and earlier chapters.

The main contributions of this chapter are the analysis of baluns for switched mode PAs, the extension of a coupled line balun model with a phase shifting coefficient e_C*, the implementation and evaluation of tapered baluns and the presentation of a wideband and a high-power CMCD PA.*

5.1 Types of Baluns

The current mode class-D power amplifier has a differential output and a balun is required to attach a single-ended load, e.g., an antenna. The balun is a part of the output network, which has been described in terms of harmonic impedances in Table 4.1 in Section 4.3. Therefore, the following requirements apply for the balun as part of a CMCD PA; the term passband depicts the tuning range of the differential to single-ended mode transformer. The balun must have

- a minimum passband bandwidth as defined by the tuning range f_{L1} to f_{U1} of the differential PA (see Section 2.2),
- a high common mode impedance for the tuning range of the PA,
- a high common mode impedance for even harmonic frequencies of the PA (f_{Ln} to f_{Un} with $n \in \{2, 4, 6, ...\}$),
- a low insertion loss in the passband.

Meeting these requirements is quite challenging, because a real balun is an inherently asymmetric device and parasitic reactances usually gain influence towards higher frequencies.

In common literature, different balun implementations are often arranged according to technological aspects (e.g., lumped element vs. planar baluns, see [20] and [47]). In this work the baluns are categorized by their functional principle. On the one hand, there are delay line baluns, which implement the differential to single-ended mode conversion by phase shifting the signals. On the other hand, there are coupled line baluns, which achieve mode conversion by geometrically, thus electrically, separating the differential and common mode systems with a coupled line segment, eventually lifting the common mode impedance at the differential line end.

5.1.1 Delay Line Baluns

In delay line baluns the mode conversion is achieved by a 180° phase shift of one of the differential branches. The two (now) in-phase branches are then combined to the single-ended output. Fig. 5.1 shows a popular delay line balun implementation. A differential mode at port 1 is converted to a single-ended mode at port 2 by the 180° phase shifter. The 90° transmission lines are used to provide an open condition in common mode, which is needed in CMCD operation (see Table 4.1). They invert the common mode short circuit, which is caused by the 180° phase shifter. The delay lines can be implemented with, for example, planar (microstrip) lines, coaxial transmission lines or lumped elements [48].

Fig. 5.2 depicts the normalized differential and the common mode impedance of a delay line balun for the nth harmonic. The balun is implemented with ideal transmission lines. The fundamental is matched ($Z_{dd11}(1) = R'_L$ and $Z_{cc11}(1) \to \infty$). However, the delay line balun exhibits an inverting behavior for even-n harmonics. The common mode is not matched for proper CMCD operation ($Z_{cc11}(\text{even}\, n) \nrightarrow \infty$) and the bandwidth is quite small. Hence, this delay line balun is not suitable at the output of a CMCD power amplifier.

This limitation extends to all delay line baluns implemented with common (right-handed) transmission line elements. However, wideband implementations might be possible using a left-handed metamaterial (see [49, 50]), but are still restricted by the finite losses of the lumped elements in metamaterial phase shifters.

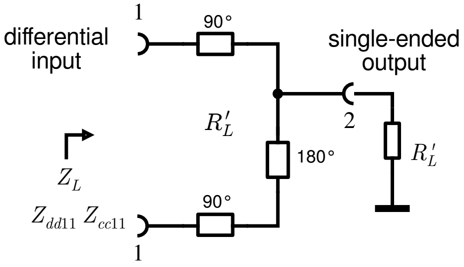

Figure 5.1.: Delay line balun configuration

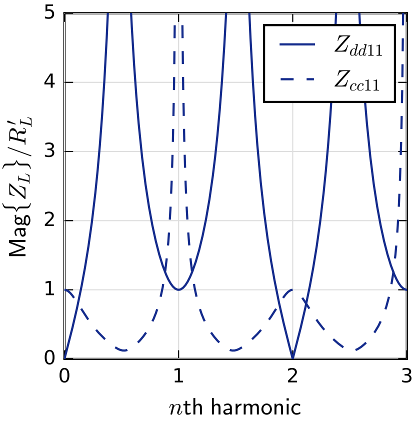

Figure 5.2.: nth harmonic differential (Z_{dd11}) and common mode (Z_{cc11}) impedance of an ideal delay line balun scaled to R'_L

5.1.2 Coupled Line Baluns

Introduction and Modeling

In coupled line baluns the mode conversion is implemented by one or more coupled line segments as shown in Fig. 5.3 (left). However, this model depicts the balun in a very limited and idealized way by a transmission line with the line impedance Z_d, the electrical length e and no ground coupling. In Fig. 5.3 (right) the coupled line model is extended according to [20] by adding the ground coupling of both transmission line elements with the common mode impedances Z_{c1} and Z_{c2}. Additionally, in this work a phase shifting coefficient e_c is added to the ground coupled elements to account for the different phase velocity (or effective permittivity) due to the material composition in the ground coupling path.

A popular implementation of a coupled line balun is the coaxial balun. A beneficial property of using a coaxial line as a transmission element for a balun is the shielded "inner" conductor, consequently increasing Z_{c1}. However, the "outer" conductor of the coax balun still has to be placed at optimum distance from the common ground to increase Z_{c2} as shown in [51]. This can result in a bulky construction. Nevertheless, coaxial baluns have been successfully implemented with high-efficiency CMCD PAs [9].

Planar implementations of double octave baluns in microstrip technology (with an infinite ground plane) are shown in [20], however they suffer from

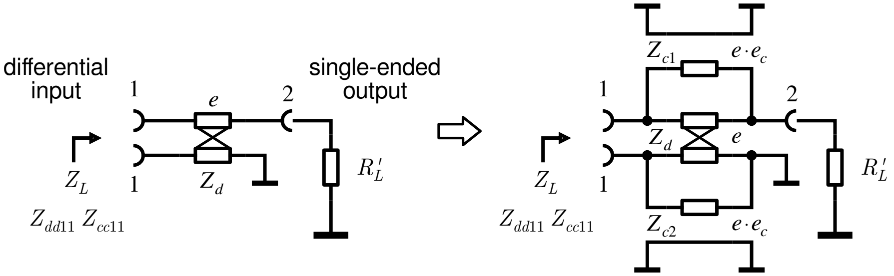

Figure 5.3.: Ideal coupled line balun (left) and coupled line balun with parasitic ground coupling (right)

optimization of the "inner" common mode impedance Z_{c1}. This results in gap widths between traces on the 10 µm scale and losses of $\geq$0.9 dB.

By discarding the infinite ground plane, a planar implementation of a coaxial balun can be designed in stripline technology (see Fig. 5.4 derived from Fig. 4.17) using a "purely" differential transmission line. A broadside coupled differential line is preferred to a paralleled pair of conductors due to common manufacturing constraints (e.g., tolerances), as shown in Section 4.5.3. Fig. 5.5 depicts a cross section of the balun. The common mode impedances Z_{c1} and Z_{c2} are both defined by the capacitive coupling (i.e., mechanical distance and dielectric properties) of the differential line to the global ground system, which is usually composed of the microstrip ground plane on a PCB and the (metallic) mounting plate of the PCB. Analytically this coupling is described by the coupling capacitances C_{c1} and C_{c2} in Fig. 5.5 for the common mode. The differential coupling is modeled with the capacitance C_d.

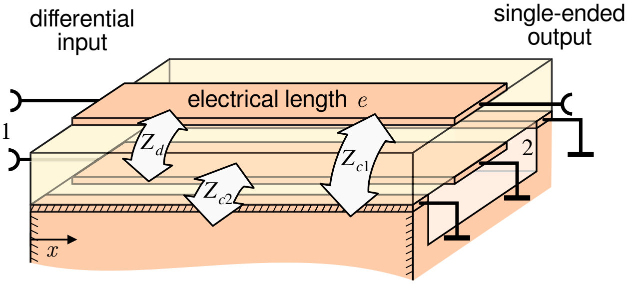

Figure 5.4.: Planar balun implemented with a differential transmission line with the line impedances from the equivalent circuit in Fig. 5.3 (right)

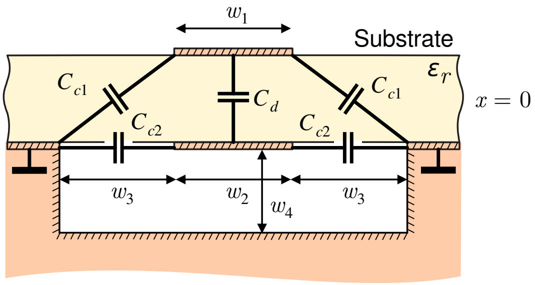

Figure 5.5.: Cross section of the planar balun in Fig. 5.4; the capacitors represent the differential and common mode line impedances.

Limits of Coupled Line Baluns

To get an insight into the properties and limits of coupled line baluns, the equivalent circuit from Fig. 5.3 (right) has to be evaluated. Analytically this can be done by using transmission line theory to compile the linear differential equations of the circuit and ultimately calculate the length-dependent impedance $Z_L\,(e)$. In this work the calculation is simplified by using a numerical simulator (*Keysight* ADS). For an analytical description of (coupled) transmission lines the reader is kindly referred to common literature (e.g., [45]).

Fig. 5.6 shows the differential and common mode input impedance of the equivalent circuit in Fig. 5.3 (right) as a function of electrical length e with the differential mode line impedance set to $Z_d = R'_L$. The common mode line impedances are combined to $Z_c = Z_{c1} = Z_{c2}$ and different values are depicted. The input impedances are scaled to Z_d. Upon looking at the figure, one can see two resonance points. For the differential mode input impedance (Z_{dd11}) a pole occurs at $e = 90°$ (and odd multiples of $90°$), for the common mode (Z_{cc11}) a zero point occurs at $e = 0°$ and $e = 180°$ (and even multiples of $180°$). As expected from theory (shown in Section 4.2), low values of Z_c detune the differential mode and reduce the common mode input impedance Z_{cc11}.

In Fig. 5.7 the balun circuit is evaluated for individual common mode line impedances Z_{c1} and Z_{c2} scaled to Z_d. $Z_{c1/2} = 5 \cdot Z_d$ is used as a default. While Z_{dd11} appears to be more sensitive to any changes of Z_{c1} compared to Z_{c2}, Z_{cc11} is more sensitive to lowering Z_{c1} compared to Z_{c2}.

At this point the balun model is evaluated for different shifting coefficients e_c. Fig. 5.8 shows Z_{dd11} and Z_{cc11} for $e_c = 1$, $e_c = 2/3$ (shorter common mode path) and $e_c = 3/2$ (longer common mode path).

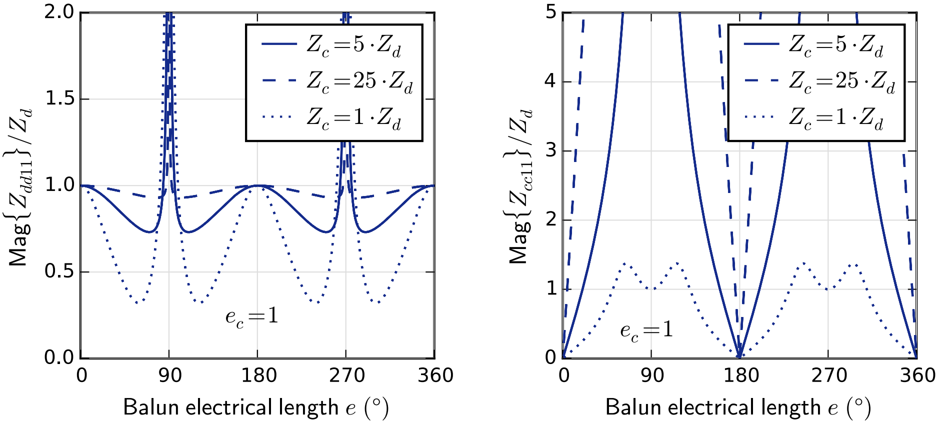

Figure 5.6.: Differential (Z_{dd11}) and common mode (Z_{cc11}) input impedance of the real coupled line balun depicted in Fig. 5.3 as a function of electrical length e with $Z_c = Z_{c1} = Z_{c2}$ and $Z_d = R'_L$. The input impedances are scaled to Z_d and the phase shifting coefficient e_c is set to 1.

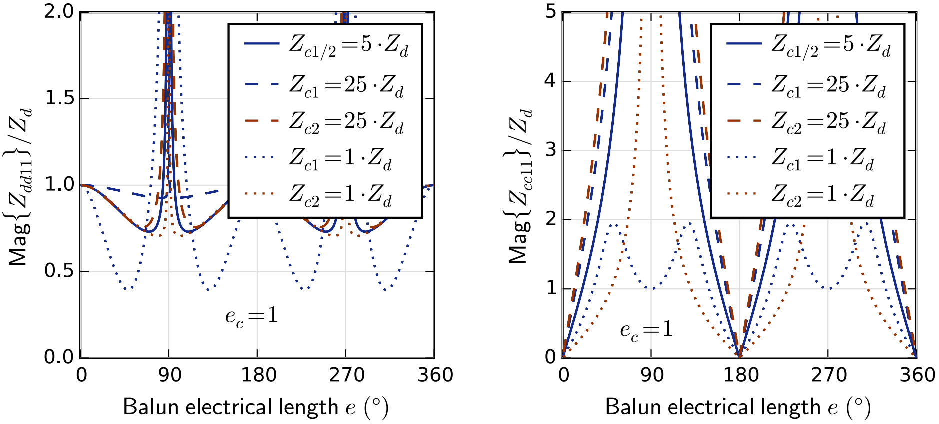

Figure 5.7.: Differential (Z_{dd11}) and common mode (Z_{cc11}) input impedance of the real coupled line balun as a function of electrical length e for different values of either Z_{c1} or Z_{c2}. $Z_{c1/2} = Z_d$ is used as a default, the input impedances are scaled to Z_d with $Z_d = R'_L$ and the phase shifting coefficient e_c is set to 1.

The common mode line impedance is set to $Z_c = Z_{c1} = Z_{c2} = 5 \cdot Z_d$. As for the common mode, the resonances of Z_{cc11} are shifted by a factor of $1/e_c$ on the e-axis. As for the differential mode, an additional resonance of Z_{dd11} shows up. Two resonances appear equally spaced and shifted by a factor of $1/e_c$ on the e-axis.

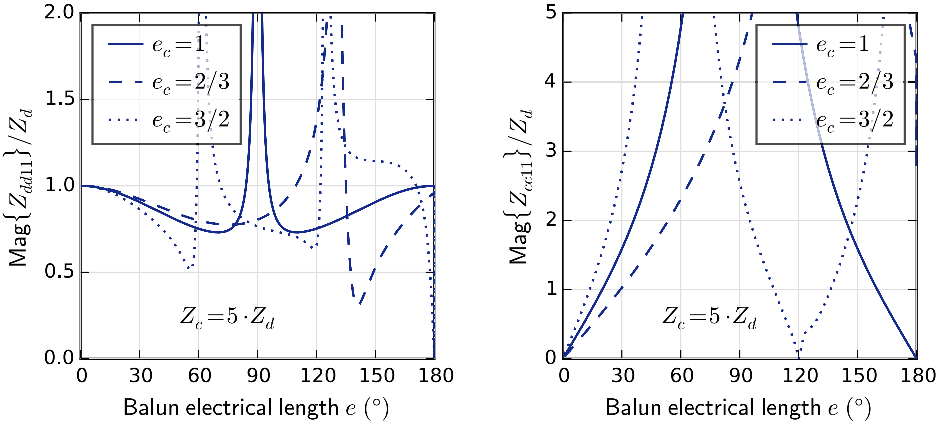

Figure 5.8.: Differential (Z_{dd11}) and common mode (Z_{cc11}) input impedance of the real coupled line balun as a function of electrical length e for different values of the phase shifting coefficient e_c. The input impedances are scaled to Z_d with $Z_d = R'_L$ and Z_c is set to $Z_c = Z_{c1} = Z_{c2} = 5 \cdot Z_d$.

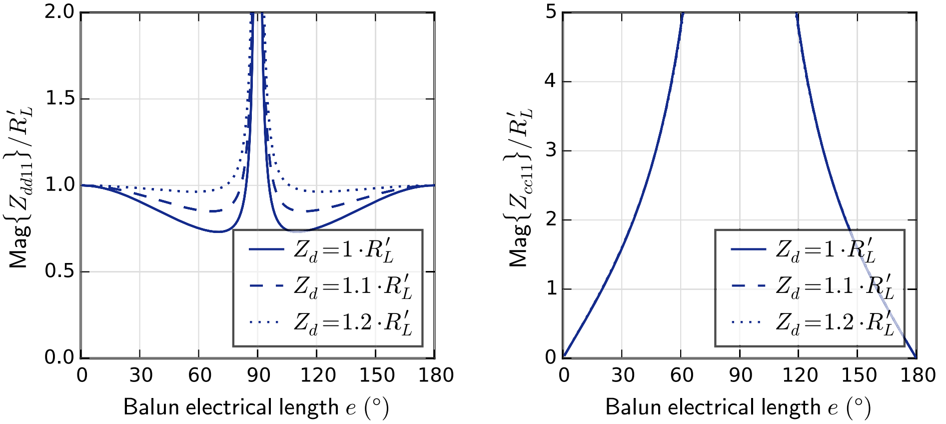

Figure 5.9.: Differential (Z_{dd11}) and common mode (Z_{cc11}) input impedance of the real coupled line balun as a function of electrical length e for different values of differential line impedance Z_d. The input impedances are scaled to R'_L and Z_c is set to $Z_c = Z_{c1} = Z_{c2} = 5 \cdot Z_d$.

Finally, the balun model is evaluated for different differential line impedances Z_d. Fig. 5.9 depicts Z_{dd11} and Z_{cc11} for $e_c = 1$. The common mode line impedance is set to $Z_c = Z_{c1} = Z_{c2} = 5 \cdot Z_d$. Scaling up Z_d reduces the dependency of the differential impedance (Z_{dd11}) on the balun length. In other words, the balun is matched for a broader range of electrical lengths, which directly translates into a broader bandwidth of the balun. Meanwhile the common mode impedance (Z_{cc11}) remains untouched.

Evaluation of the Balun Model

To verify the accuracy of the proposed balun model, a real planar coupled line balun is simulated using an electro-magnetic (EM) simulator (*Keysight* ADS Momentum). The balun is based on the cross section given in Fig. 5.5. The dimensions are $w_1 = w_2 = 1.5\,\mathrm{mm}$ and $w_3 = 5\,\mathrm{mm}$. The depth of the cavity w_4 is neglected to simplify the calculation ($w_4 \rightarrow \infty$), however, it will be taken into consideration again later in Section 5.2.2. The used RF substrate is a two-layer *Rogers* RO4003C laminate with a height $h = 0.508\,\mathrm{mm}$ (0.02") and relative permittivity $\epsilon_r = 3.55$. The balun is designed using the *Keysight* application extension language (AEL) and the code is depicted in Appendix A.1.

The results are given in Fig. 5.10 as a function of electrical length e of the differential transmission line of the balun and are scaled to $R'_L = 50\,\Omega$. All EM simulations are executed at $f = 1\,\mathrm{GHz}$. The selected circuit model parameters are $Z_d = 1.13 \cdot 50\,\Omega$, $Z_{c1} = 290\,\Omega$, $Z_{c2} = 380\,\Omega$ and $e_c = 2/3$. For these values the circuit model shows a very good alignment with the EM simulation.

The reduced electrical length of the grounded transmission lines ($e_c = 2/3$) can be physically explained by the change of the effective permittivity ϵ_{eff} of the differential transmission line. The common mode path has a different material composition (substrate and air). Therefore, the phase shifting coefficient e_c can be interpreted with the velocity factor VF as

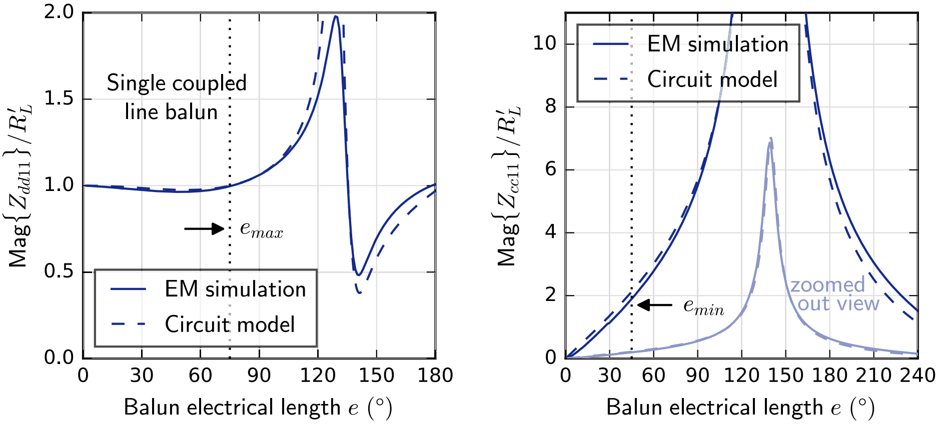

Figure 5.10.: Comparison of an EM simulated and circuit modeled coupled line balun from Fig. 5.3 and Fig. 5.5 with $w_1 = w_2 = 1.5\,\mathrm{mm}$ and $w_3 = 5\,\mathrm{mm}$. The circuit model proves to be very well aligned for $Z_d = 1.13 \cdot 50\,\Omega$, $Z_{c1} = 290\,\Omega$, $Z_{c2} = 380\,\Omega$ and $e_c = 2/3$.

$$e_c \geq \mathrm{VF} = \frac{1}{\sqrt{\epsilon_{eff}}}, \tag{5.1}$$

with $e_c = 1$ being the phase shifting in a homogeneous medium. The resonances appear from the abrupt balun-to-microstrip line transition.

Coupled Line Baluns for CMCD PAs

The maximum bandwidth of a differential class-D PA with a third harmonic impedance match is calculated in equation 2.5 by

$$B_{\%,classD} = 2 \cdot \frac{f_{L3} - \frac{1}{3} f_{L3}}{f_{L3} + \frac{1}{3} f_{L3}} = 100\% \tag{5.2}$$

and defines the minimum range of balun matching for the fundamental frequency in differential mode (Z_{dd11}) according to the ideal harmonic matching conditions in Table 4.1. The matching range for the common mode (Z_{cc11}) extends from the fundamental to even order multiples of that frequency, i.e., an infinitely high frequency range. However, matching of the fundamental and the second harmonic can be assumed to be sufficient for reaching a relatively good efficiency according to Fig. 4.6. The necessary percent bandwidth of the common mode (Z_{cc11}) is then calculated with f_{U2} as the upper and f_{L1} as the lower limit by

$$B_{\%,com} = 2 \cdot \frac{2 f_{L3} - \frac{1}{3} f_{L3}}{2 f_{L3} + \frac{1}{3} f_{L3}} \approx 143\%. \tag{5.3}$$

A useful operating range of the balun is limited at the lower edge by the electrical length e_{min} or the lower edge frequency f_{min} and at the upper edge by the electrical length e_{max} or the upper edge frequency f_{max}. The percent bandwidth $B_{\%}$ can be calculated from e_{min} and e_{max} by

$$B_{\%} = 2 \cdot \frac{f_{max} - f_{min}}{f_{max} + f_{min}}, \tag{5.4}$$

with $f_{max} \sim e_{max}$ and $f_{min} \sim e_{min}$ to

$$\boxed{B_{\%} = 2 \cdot \frac{e_{max} - e_{min}}{e_{max} + e_{min}}}. \tag{5.5}$$

For the balun in Fig. 5.10 the phase range for the differential mode extends from $e_{min} = 0°$ to $e_{max} \approx 75°$. The percent bandwidth is then $B_{\%} = 200\%$ and the differential mode is therefore always matched. However, when considering a minimum common mode matching of $Z_{cc11}/Z_d = 2$ to achieve a good efficiency of $> 90\%$ (see Fig. 4.6), the minimum electrical length of the balun rises to $e_{min} \approx 45°$. The differential mode percent bandwidth for this balun is then reduced to $B_{\%} \approx 50\%$. This would not suffice to cover the 100% bandwidth of an ideal CMCD PA (as shown in Section 2.2). The same applies to the common mode with $e_{min} \approx 45°$ and $e_{max} \approx 220°$ and therefore $B_{\%} \approx 132\%$. In order to improve the bandwidth of the balun, either the common mode impedances Z_{c1} and Z_{c2} have to be optimized, or the differential mode resonances have to be shifted or mitigated.

5.2 Tapered Coupled Line Baluns

5.2.1 Introduction and Modeling of Tapered Baluns

The simple coupled line balun shown in Section 5.1.2 is limited in bandwidth by parasitic resonances. These resonances physically appear from the abrupt balun-to-microstrip line transition. In fact, a microstrip line can be described by Fig. 5.5 with $w_3 \to 0$. Hence, the line capacitances shift to $C_{c2} \to \infty$ and $C_{c1} \to 0$ with $C_d \to 1/\omega R'_L$. In the circuit model in Fig. 5.3 this translates with $Z_d \to R'_L$ to $Z_{c1} \to \infty$ and $Z_{c2} = 0$, ultimately leading to reflections and resonances.

A common way to suppress effects caused by this abrupt transition is to smoothen the transition by tapering it [52–54]. To describe such a tapered balun, the equivalent circuit of Fig. 5.3 is extended to k sections in Fig. 5.11. Each section is individually characterized by a differential line impedance $Z_{d,k}$, two common mode line impedances $Z_{c1,k}$ and $Z_{c2,k}$ and a phase shifting coefficient $e_{c,k}$. A continuous transition is realized with $k \to \infty$ sections.

Fig. 5.12 shows a planar two-stage tapered balun, the simplest implementation of a tapered structure. The line impedances from the equivalent circuit in Fig. 5.11

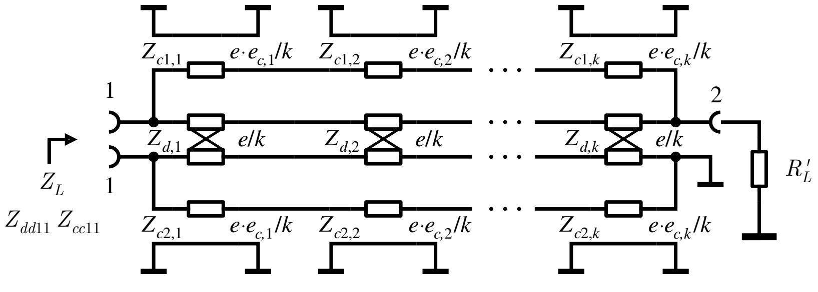

Figure 5.11.: Equivalent circuit of a tapered coupled line balun

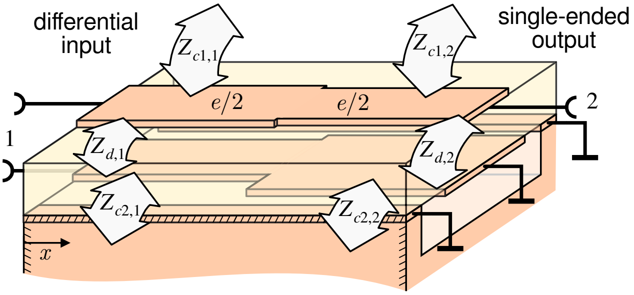

Figure 5.12.: Planar two-stage tapered balun implemented with differential transmission lines with the line impedances from the equivalent circuit in Fig. 5.11

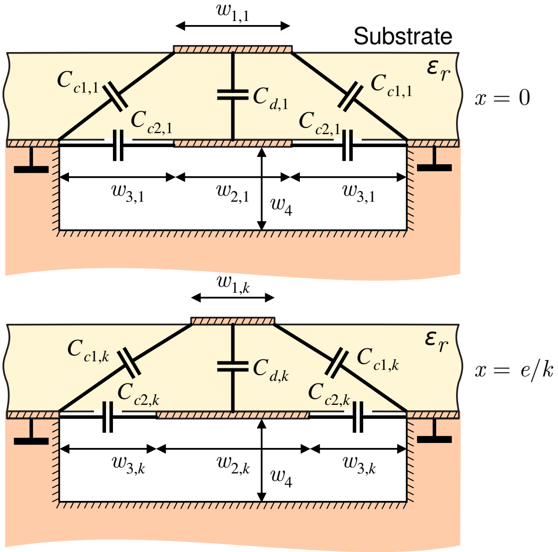

Figure 5.13.: Cross section of the planar tapered balun in 5.12; the capacitors represent the differential and common mode line impedances.

are depicted. The cross section of the planar taper in Fig. 5.13 shows the capacitors which represent the line impedances and reveals the influences from tapering the balun. A decrease of the top conductor width w_1 will also decrease C_{c1}, i.e., increase the line impedance Z_{c1}. An increase of the bottom conductor width w_2 in combination with a decrease of width w_3 will increase C_{c2}, i.e., decrease the line impedance Z_{c2}. Additionally less electrical field is submerged to open space and the effective permittivity therefore rises, i.e., the phase shifting constant e_c increases towards unity.

The proposed planar two-stage balun is implemented and simulated using an electro-magnetic (EM) simulator (*Keysight* ADS Momentum). The dimensions are $w_{1,1} = w_{2,1} = 1.5\,\mathrm{mm}$ and $w_{3,1} = 5\,\mathrm{mm}$ for the first section ($k = 1$) and $w_{1,2} = 1.2\,\mathrm{mm}$, $w_{2,2} = 3\,\mathrm{mm}$ and $w_{3,2} = 4.25\,\mathrm{mm}$ for the second section ($k = 2$). The depth of the cavity w_4 is again neglected to simplify the calculation ($w_4 \to \infty$). Just like in Section 5.1.2, the RF substrate used is a two-layer *Rogers* RO4003C laminate. The AEL code is depicted in Appendix A.1.

Fig. 5.14 shows the results, which are given as a function of electrical length e of the differential transmission line and are scaled to $R'_L = 50\,\Omega$. All EM simulations are executed at $f = 1\,\mathrm{GHz}$. The selected circuit model parameters (see Fig. 5.11) for the first section are identical to those in the single line balun ($Z_{d,1} = 1.13 \cdot 50\,\Omega$, $Z_{c1,1} = 290\,\Omega$, $Z_{c2,1} = 380\,\Omega$ and $e_{c,1} = 2/3$, see Fig. 5.10). For the second section the parameters are $Z_{d,2} = 1.07 \cdot 50\,\Omega$, $Z_{c1,2} = Z_{c1,1} \cdot 2$, $Z_{c2,2} = Z_{c2,1}/2$ and $e_{c,2} = 0.58$. For these values the circuit model shows a good alignment with the EM simulation up to the first resonance of the differential mode and the whole common mode (Fig. 5.14). As expected from the capacitor model in Fig. 5.13, the common mode line impedance $Z_{c1,2}$ increases and $Z_{c2,2}$ decreases.

The single line balun depicted earlier in Section 5.1.2 is printed for reference in Fig. 5.14. In comparison with the single line balun, the two-stage taper shows a reduction and a shift of the differential mode resonances towards higher balun length e. Additionally, the common mode impedance Z_{cc11} is shifted towards higher e, but *less* than the differential mode resonances.

For a minimum common mode matching of $Z_{cc11}/Z_d = 2$, in order to achieve a good efficiency of $> 90\%$ (see Fig. 4.6), the phase range in differential mode extends from $e_{min} \approx 50°$ to $e_{max} \approx 100°$. The differential mode percent bandwidth for this balun is then $B_{\%} \approx 67\%$. This is still not sufficient to cover the 100% bandwidth of an ideal CMCD PA, however, it is better than the $B_{\%} \approx 50\%$ of the single line balun. Yet this example unveils the advantages of even the simplest tapered balun implementation.

To sum up, the use of an equivalent circuit for modeling the (tapered) baluns (see Fig. 5.11) reveals the physical origin of the resonances in differential and common mode excitation. Stacked transmission line elements with individual common and differential mode line impedances and electrical lengths are used to describe the balun. This model scales quite well for different electrical lengths (i.e., different frequencies). However, it does not account for higher modes of propagation, which could, for instance, appear on the broadside coupled stripline of the planar balun, or electromagnetic radiation in electrically long baluns. Nevertheless, common balun implementations for switched mode power

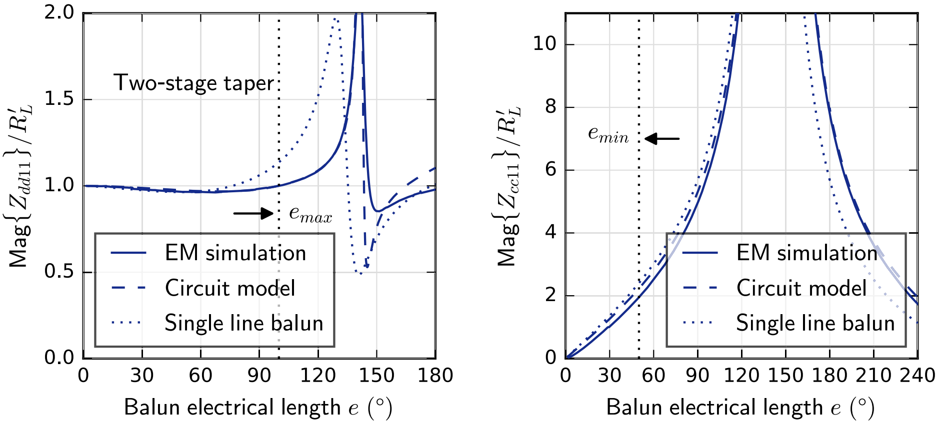

Figure 5.14.: Comparison of an EM simulated and circuit modeled two-stage tapered balun from Fig. 5.12 and Fig. 5.13 with $w_{1,1} = w_{2,1} = 1.5\,\mathrm{mm}$ and $w_{3,1} = 5\,\mathrm{mm}$ (first section) and $w_{1,2} = 1.2\,\mathrm{mm}$, $w_{2,2} = 3\,\mathrm{mm}$ and $w_{3,2} = 4.25\,\mathrm{mm}$ (second section). The circuit model proves to be well aligned for $Z_{d,1} = 1.13 \cdot 50\,\Omega$, $Z_{c1} = 290\,\Omega$, $Z_{c2} = 380\,\Omega$, $e_{c,1} = 2/3$ and $Z_{d,2} = 1.07 \cdot 50\,\Omega$, $Z_{c1,2} = Z_{c1,1} \cdot 2$, $Z_{c2,2} = Z_{c2,1}/2$ and $e_{c,2} = 0.58$. The single line balun depicted earlier is printed for reference.

amplifier applications can be described by the model in terms of impedance matching and bandwidth properties as a first approximation (e.g., in a circuit simulator). After implementing the power amplifier with the balun model, the actual balun design can then be verified and optimized using an EM simulator.

5.2.2 *Implementation of Tapered Baluns*

There are several ways to implement tapers and tapered baluns and a few of them have been discussed in literature before [52–55], including optimized solutions [56]. In this work two taper transitions, a linear taper and an exponential taper, are examined.

Calculation of Tapered Transitions

In an exponential taper of the length l, the line impedance $Z(x)$ changes in an exponential fashion from Z_0 at $x = 0$ to Z_l at $x = l$. This can be written as

$$Z\left(x\right) = Z_0 \cdot e^{ax} \qquad 0 \leq x \leq l \tag{5.6}$$

$$a = \frac{1}{l} \ln \left(\frac{Z_l}{Z_0} \right). \tag{5.7}$$

As for the linear taper, the line impedance $Z\left(x\right)$ at the position x on the taper is

$$Z\left(x\right) = Z_0 \left(\frac{x}{l} \cdot \frac{Z_l - Z_0}{Z_0} + 1 \right). \quad 0 \leq x \leq l \tag{5.8}$$

Fig. 5.15 (left) visualizes the two taper transitions.

The reflection coefficient $\Gamma\left(\beta\right)$ of a tapered line as a function of phase constant β is approximated in [55] to

$$\Gamma\left(\beta\right) = \frac{1}{2} \int\limits_0^l e^{-2j\beta x} \frac{\mathrm{d}}{\mathrm{d}x} \ln \left(\frac{Z\left(x\right)}{Z_0} \right) \mathrm{d}x \tag{5.9}$$

with

$$\beta = \frac{2\pi}{\lambda} = \frac{2\pi f \sqrt{\epsilon_{\mathit{eff}}}}{c_0}. \tag{5.10}$$

Now $\Gamma\left(\beta\right)$ can be calculated for the exponential taper to

$$\begin{aligned}
\Gamma\left(\beta\right) &= \frac{1}{2} \int\limits_0^l e^{-2j\beta x} \frac{\mathrm{d}}{\mathrm{d}x} \left(\ln e^{ax}\right) \mathrm{d}x = \frac{\ln\left(Z_l/Z_0\right)}{2l} \int\limits_0^l e^{-2j\beta x} \mathrm{d}x \\
&= \frac{\ln\left(Z_l/Z_0\right)}{2l} \frac{1}{-2j\beta} \left[e^{-2j\beta l} - e^{-2j\beta 0} \right] \\
&= \frac{\ln\left(Z_l/Z_0\right)}{2l} \frac{1}{-2j\beta} \left[e^{-2j\beta l} - 1 \right] \\
&= \frac{\ln\left(Z_l/Z_0\right)}{2l} \frac{1}{-2j\beta} \left[-e^{-j\beta l} \left(2j \sin\left(\beta l\right) - e^{j\beta l} \right) - 1 \right] \\
&= \frac{\ln\left(Z_l/Z_0\right)}{2} \cdot e^{-j\beta l} \cdot \frac{\sin\left(\beta l\right)}{\beta l}
\end{aligned} \tag{5.11}$$

and for the linear taper to

$$\begin{aligned}
\Gamma(\beta) &= \frac{1}{2}\int\limits_0^l e^{-2j\beta x}\frac{\mathrm{d}}{\mathrm{d}x}\ln\left(\frac{Z(x)}{Z_0}\right)\mathrm{d}x \\
&= \frac{1}{2}\int\limits_0^l e^{-2j\beta x}\frac{\mathrm{d}}{\mathrm{d}x}\ln\left(\frac{x}{l}\cdot\frac{Z_l-Z_0}{Z_0}+1\right)\mathrm{d}x \\
&= \frac{1}{2}\int\limits_0^l e^{-2j\beta x}\frac{1}{\frac{x}{l}\cdot\frac{Z_l-Z_0}{Z_0}+1}\cdot\frac{Z_l-Z_0}{l\cdot Z_0}\mathrm{d}x \\
&= \frac{1}{2}\left(Z_l-Z_0\right)\int\limits_0^l e^{-2j\beta x}\frac{1}{x\left(Z_l-Z_0\right)+l\cdot Z_0}\mathrm{d}x \\
&= \frac{1}{2}\left(Z_l-Z_0\right)\left[\frac{e^{-2j\beta x}\cdot\mathrm{Ei}\left(-2j\beta\left(\frac{Z_l-Z_0}{l\cdot Z_0}+x\right)\right)}{Z_l-Z_0}\right]_{x=0}^{x=l} \\
&= \frac{1}{2}e^{-2j\beta x}\left[\mathrm{Ei}\left(-2j\beta\left(\frac{Z_l-Z_0}{l\cdot Z_0}+l\right)\right)-\mathrm{Ei}\left(-2j\beta\left(\frac{Z_l-Z_0}{l\cdot Z_0}\right)\right)\right]
\end{aligned} \tag{5.12}$$

with Ei $(\cdot)$ the exponential integral, which is defined by

$$\mathrm{Ei}(z) = -\int\limits_{-z}^{\infty}\frac{e^{-t}}{t}\mathrm{d}t. \tag{5.13}$$

Fig. 5.15 (right) shows the reflection coefficients $\Gamma(\beta)$ of both tapers (normed to $2/\ln(Z_l/Z_0)$) as a function of length per wavelength $\beta \cdot l$ (i.e., frequency) for $Z_0 = 50\,\Omega$ and $Z_l = 100\,\Omega$. One can see that both tapers show a lower cutoff frequency. A first minimum of $\Gamma(\beta)$ is reached at $\beta \cdot l = \pi$ or $l = \frac{\lambda}{2}$. For higher $\beta \cdot l$, peaks of decreasing reflection Γ appear. The exponential taper shows a slightly improved behavior in comparison with the linear taper. Optimized taper transitions with equal ripple of Γ exist [56], but have higher cutoff frequencies [55].

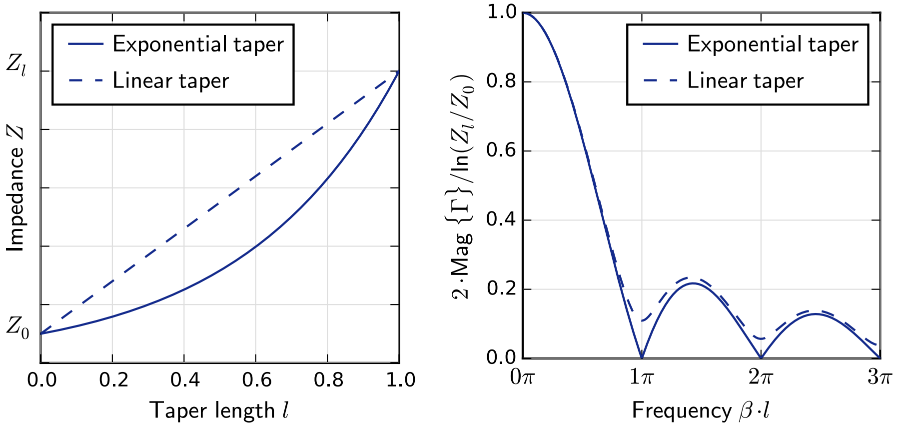

Figure 5.15.: Visualization of the two taper transitions (left) and reflection coefficients as a function of frequency $\beta \cdot l$ for $Z_0 = 50\,\Omega$ and $Z_l = 100\,\Omega$.

EM Simulation of Tapered Baluns

An electro-magnetic (EM) simulator (*Keysight* ADS Momentum) is used to calculate the continuous transitions of tapered baluns. Fig. 5.16 shows the three implemented and simulated balun designs with their dimensions. The balun length is composed of the length of the taper l and the offset line d. The width w_d defines the differential input line and the width w_s the microstrip output line. The maximum width of the taper is w_b. The dimension s defines a slot at the differential input. Ideally this slot is infinitely large. However, in a real push-pull class-D amplifier design with single-ended transistors, the slot is determined by the size of the transistor package and, more precisely, the distance of the output-pin (e.g., drain) to the ground-pin (e.g., source).

In the linear taper in Fig. 5.16, the top conductor strip varies from w_d to w_s in a linear fashion as well as the bottom conductor strip from w_d to w_b:

$$w(x) = w_d \left(\frac{x}{l} \cdot \frac{w_b - w_d}{w_d} + 1 \right). \quad 0 \le x \le l \tag{5.14}$$

The AEL code of the balun is depicted in Appendix A.1.

The exponential taper in Fig. 5.16 has an exponentially tapered bottom conductor with the width

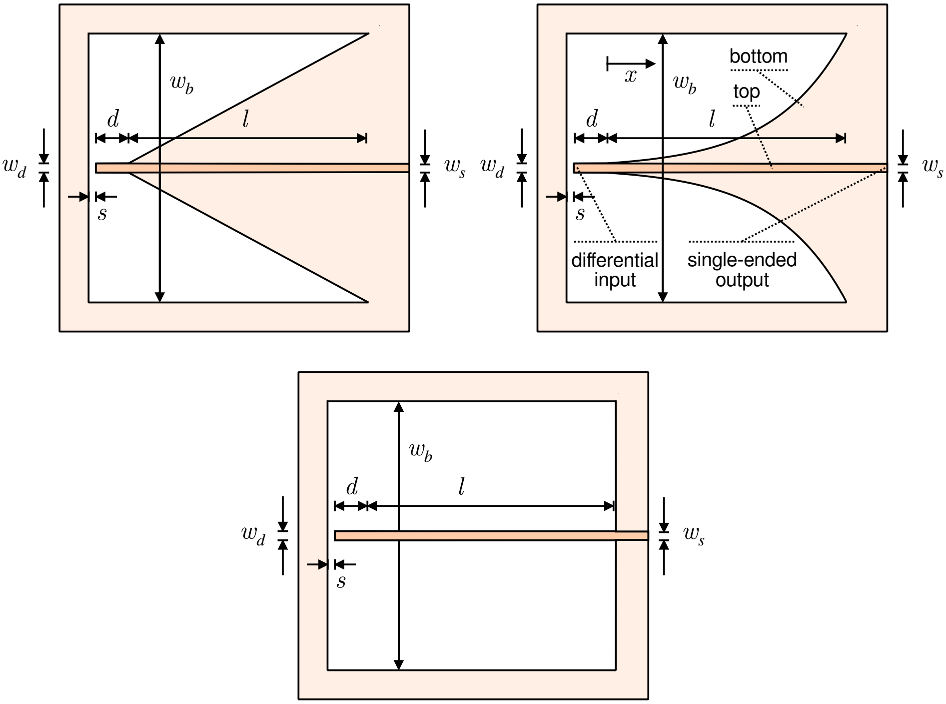

Figure 5.16.: Two different implementations of a tapered balun - a linear taper and an exponential taper. A single line balun is displayed for reference.

$$w(x) = w_d \cdot e^{ax} \qquad\qquad 0 \leq x \leq l \tag{5.15}$$

$$a = \frac{1}{l} \ln\left(\frac{w_b}{w_d}\right). \tag{5.16}$$

The top conductor is shaped exponentially in the same way as depicted in the AEL code in Appendix A.1. In addition to the two tapered implementations, a single line balun with a fixed width of w_d is simulated for reference. The AEL code can be found in the Appendix as well.

The RF substrate used in the simulations is once again a two-layer *Rogers* RO4003C laminate with a height $h = 0.508\,\mathrm{mm}$ (0.02") and relative permittivity $\epsilon_r = 3.55$.

Fig. 5.17 shows the EM simulation results of the tapered baluns in comparison. The dimensions of the different baluns are $w_d = 1.25\,\mathrm{mm}$, $w_s = 1.15\,\mathrm{mm}$, $w_b = 45\,\mathrm{mm}$, $d = 0\,\mathrm{mm}$ and $s = 1\,\mathrm{mm}$, resulting in a $Z_{d,1} \approx 50\,\Omega$ for the differential side and a $Z_{d,k} \approx 50\,\Omega$ for the single-ended microstrip side. The input impedances Z_{dd11} and Z_{cc11} are depicted as a function of electrical length e in Fig. 5.17 and are normalized (scaled to $R_L' = 50\,\Omega$). The depth of the cavity w_4 is neglected ($w_4 \rightarrow \infty$, compare Fig. 5.5). All EM simulations are executed at $f = 1\,\mathrm{GHz}$.

The 90-degree resonance shown earlier in Section 5.1.2 is observed for the line balun. The tapers entirely suppress this resonance (strictly speaking they move it towards very high electrical lengths) with the exponential taper having a slightly more flat differential mode input impedance Z_{dd11}. As for the common mode impedance Z_{cc11}, the line balun has the highest suppression for low lengths e. The exponential taper is slightly worse, but still superior to the linear taper. However, both tapers outperform the line balun in bandwidth due to the very flat behavior in differential mode.

This simulation shows a similar behavior of the tapered and (single) line baluns in comparison as depicted earlier in Fig. 5.14 in Section 5.2.1. The common mode impedance Z_{cc11} of the tapers is shifted towards higher e. Yet it is shifted *less* than the differential mode resonances (which are not visible for the tapers, because they are shifted towards very high electrical lengths). This confirms the

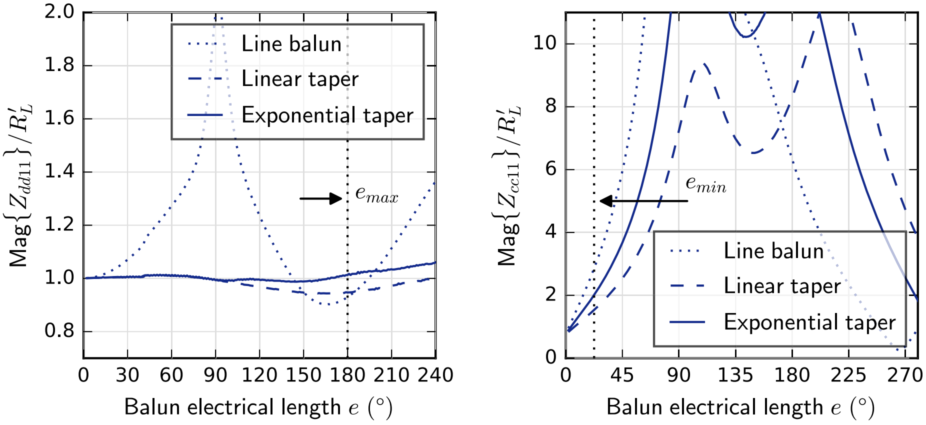

Figure 5.17.: Differential (Z_{dd11}) and common mode (Z_{cc11}) input impedance of different tapered balun implementations as shown in Fig. 5.16 in comparison. The dimensions are $w_d = 1.25\,\mathrm{mm}$, $w_s = 1.15\,\mathrm{mm}$, $w_b = 45\,\mathrm{mm}$, $d = 0\,\mathrm{mm}$, $s = 1\,\mathrm{mm}$ and $w_4 \rightarrow \infty$. The impedances are plotted as a function of electrical length e of the baluns and the input impedances are scaled to $R_L' = 50\,\Omega$.

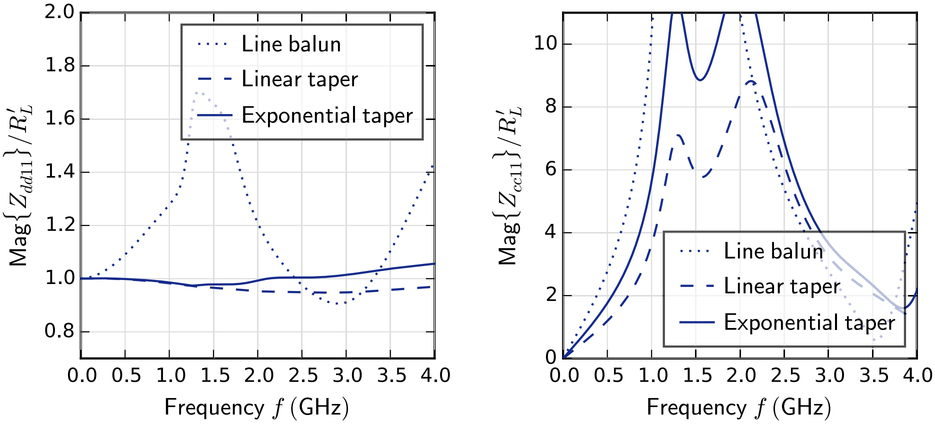

Figure 5.18.: Input impedances of different tapered balun implementations as a function of frequency f for a balun length $l = 30\,\mathrm{mm}$. The implementations and dimensions are shown in Fig. 5.16 and Fig. 5.17. The input impedances are scaled to R'_L.

earlier findings of Section 5.2.1: the simplified two-stage taper exhibits the same bandwidth enhancing properties as the continuously tapered baluns shown here.

For the exponential taper in Fig. 5.17 and a minimum common mode matching of $Z_{cc11}/Z_d = 2$, in order to achieve a good efficiency of >90% (see Fig. 4.6), the phase range in differential mode extends from $e_{min} \approx 22.5°$ to $e_{max} \approx 180°$. The differential mode percent bandwidth for this balun is then $B_{\%} \approx 156\%$, enough to cover the 100% bandwidth of an ideal CMCD PA.

As for the common mode, the minimum length is $e_{min} \approx 22.5°$ and maximum length is $e_{max} \approx 270°$ for $Z_{cc11}/Z_d = 2$. This results in $B_{\%} \approx 169\%$ which is larger than $B_{\%,com} \approx 143\%$ to match at least the fundamental and the second harmonic for the entire bandwidth (see Section 5.1.2).

Fig. 5.18 shows EM simulations for a fixed balun length $l = 30\,\mathrm{mm}$ as a function of frequency. The results are similar to those depicted earlier in the more generalized approach in Fig. 5.17 and demonstrate similar bandwidths for the common and the differential mode.

Finally, the exponentially tapered balun is examined for different slot widths s in Fig. 5.19 and different balun widths w_b in Fig. 5.20. As mentioned earlier, the slot width is defined by the pin distances of the transistor packages at the balun input. The simulation shows that the slot width has only a minor influence on the balun performance. The balun width, however, defines the common mode line impedances ($Z_{c1,k}$ and $Z_{c2,k}$, see Fig. 5.11), which for the tapered case do not only influence the height of the common mode suppression Z_{cc11}, but also

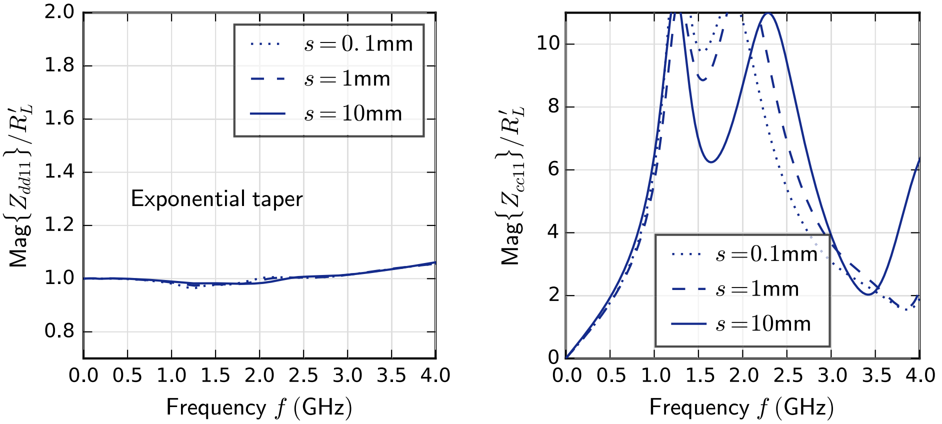

Figure 5.19.: Input impedances of an exponentially tapered and $l = 30$ mm long balun for different slot widths s as a function of frequency. The input impedances are scaled to R_L'.

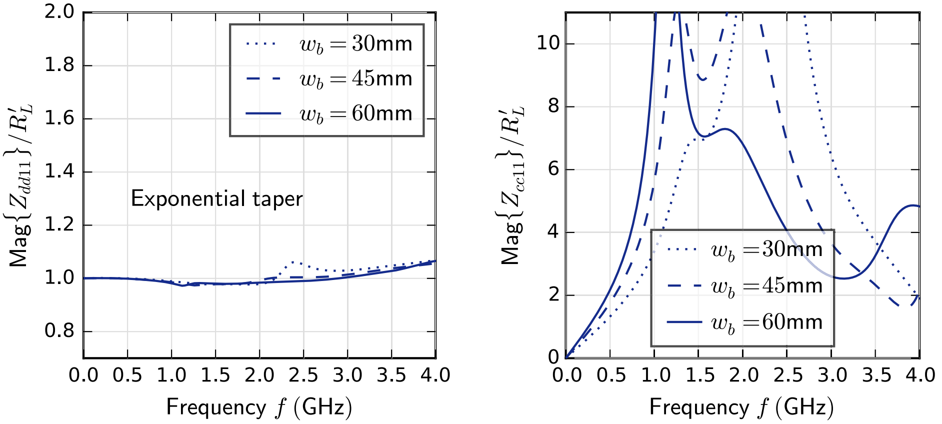

Figure 5.20.: Input impedances of an exponentially tapered and $l = 30$ mm long balun for different balun widths w_b as a function of frequency. The input impedances are scaled to R_L'.

the phase angle and therefore the position of the peak Z_{cc11} on the frequency scale. As a rule of thumb, exponentially tapered baluns for broadband matched current mode class-D PAs should be designed in an approximately square shape.

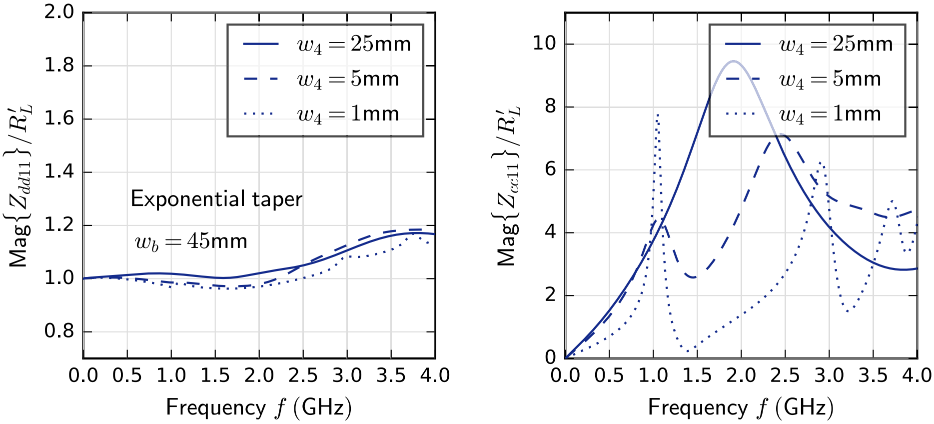

Figure 5.21.: Input impedances of an exponentially tapered balun for different balun cavity depths w_4 as a function of frequency. The dimensions are $w_d = 1.25\,\text{mm}$, $w_s = 1.15\,\text{mm}$, $w_b = 45\,\text{mm}$, $d = 0\,\text{mm}$, $s = 1\,\text{mm}$ and $l = 30\,\text{mm}$. The input impedances are scaled to $R'_L = 50\,\Omega$ and calculated using the FEM simulator of *Keysight* ADS.

3D FEM Simulation of the Balun Cavity

So far the depth of the cavity w_4 under the PCB has been neglected ($w_4 \to \infty$, compare Fig. 5.4 and Fig. 5.5). To get a full picture of the balun in a volumetric environment, the cavity has to be included in simulation. Unfortunately, the Momentum Microwave EM simulator of *Keysight* ADS is limited to planar problems. However, ADS has a Finite Element Method (FEM) EM simulator option, which can solve volumetric problems at the cost of additional simulation time.

Fig. 5.21 shows the input impedances of the balun for different balun cavity depths w_4. A finite depth slightly detunes the differential mode line impedance (Fig. 5.21, left). This problem can be solved by readjusting the width w_d of the differential input. Additionally, the cavity impairs the common mode suppression Z_{cc11} and a common mode "dip" appears in Fig. 5.21 for low w_4. Therefore, the cavity depth has to be taken into account in a practical implementation. In PA design, however, as long as a minimum common mode impedance (e.g., $Z_{cc11}/Z_d = 2$, see Fig. 4.6) is maintained, a ripple of Z_{cc11} is allowed and will not impair the overall performance of a CMCD amplifier. For this particular balun, a 5 mm deep pocket (e.g., in the heat sink) would be more than sufficient to maintain $Z_{cc11}/Z_d > 2$.

5.2.3 Impedance Transformation with Tapered Baluns

So far it has been assumed that the differential input impedance Z_{dd11} is equal to the load impedance R'_L resulting in an almost constant differential line impedance: $Z_{d,1} \approx Z_{d,k}$. However, in most amplifier designs, the optimum transistor output impedance differs from the load impedance. A matched device impedance is usually desired to achieve an optimum gain and output power. Wideband transformer networks are often implemented with planar tapered lines, therefore, the use of the already available tapered balun comes in handy.

With the transformation ratio $1 : k$ (see Section 2.3.1) and

$$Z_{dd,11} = R_L = k \cdot R'_L \tag{5.17}$$

only transformation of real loads is considered; the reactive parasitics of the transistors are absorbed by the output filter (see Section 4.5).

The transformation is implemented by changing the first element of the differential line $Z_{d,1}$ from $Z_{d,1} \gtrsim R'_L$ to $Z_{d,1} \gtrsim k \cdot R'_L$. A slight deviation from the ideal $Z_{d,1}$ ('$\gtrsim$' instead of '$=$' sign) occurs from the finite common mode line impedance (compare Fig. 5.9).

In Fig. 5.22 and Fig. 5.23, three different transformation ratios are considered for an exponential taper from Fig. 5.16: The dimensions of the differential input are $w_d = 1.25\,\text{mm}$ ($k = 1$), $w_d = 2.5\,\text{mm}$ ($k = \frac{1}{2}$) and $w_d = 5\,\text{mm}$ ($k = \frac{1}{4}$).

One can see that tapers have a lower cutoff length (Fig. 5.22) or frequency (Fig. 5.23), which complies with the calculation made in Section 5.2.2. In spite of the fact that the common mode remains nearly untouched, the differential mode bandwidth of this balun is considerably limited.

Assuming a minimum length $e_{min} \approx 90°$ and a maximum length $e_{max} \approx 180°$, the bandwidth is reduced to $B_{\%} \approx 66\%$. Additionally, due to the lower cutoff length in differential mode, the transforming balun is longer than its non-transforming counterpart.

A general design limitation of wideband power amplifiers holds true for push-pull switched mode PAs. The active devices should be selected (or even designed) to match the optimum load impedance as good as possible (see equation 2.18 for the class-D case).

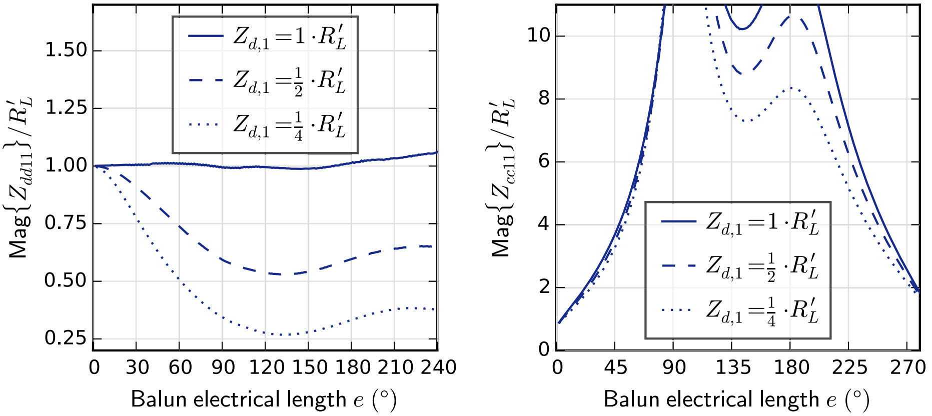

Figure 5.22.: Impedance transformation with two exponentially tapered baluns with $Z_{d,1} = R_L = \frac{1}{2} \cdot R'_L$, i.e., $k = \frac{1}{2}$ (see Fig. 2.6) and $Z_{d,1} = R_L = \frac{1}{4} \cdot R'_L$, i.e., $k = \frac{1}{4}$. The non-transforming ($k = 1$) taper is printed for reference. The dimensions are $w_d = 2.5\,\text{mm}$ ($k = \frac{1}{2}$), $w_d = 5\,\text{mm}$ ($k = \frac{1}{4}$), $w_s = 1.15\,\text{mm}$, $w_b = 45\,\text{mm}$, $d = 0\,\text{mm}$ and $s = 1\,\text{mm}$. The impedances are plotted as a function of electrical length e of the baluns and the input impedances are scaled to R'_L.

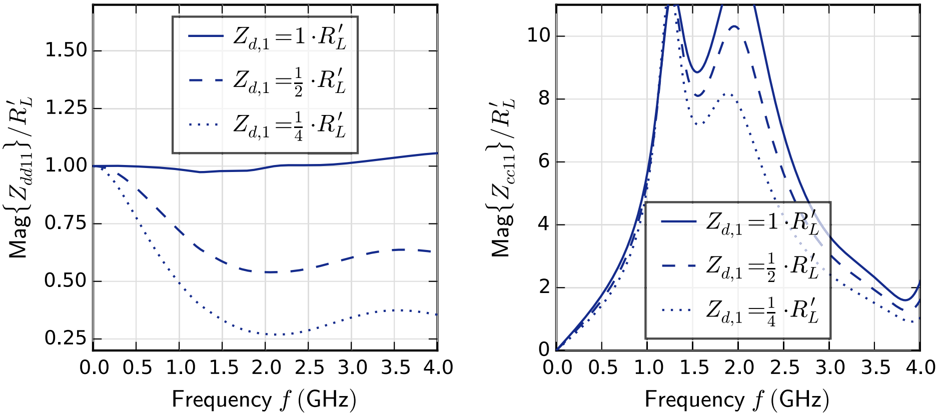

Figure 5.23.: Impedance transformation with two exponentially tapered baluns with $Z_{d,1} = R_L = \frac{1}{2} \cdot R'_L$, i.e., $k = \frac{1}{2}$ and $Z_{d,1} = R_L = \frac{1}{4} \cdot R'_L$, i.e., $k = \frac{1}{4}$ as a function of frequency f for a balun length $l = 30\,\text{mm}$. The non-transforming ($k = 1$) taper is printed for reference. The implementations and dimensions are shown in Fig. 5.16 and Fig. 5.22. The input impedances are scaled to R'_L.

5.3 Class-D Demonstrator PA

This section consolidates the findings of earlier chapters to design prototypes of current mode class-D amplifiers. On the basis of low-power, high-speed GaAs transistors, which represent almost ideal RF switches, optimized output networks and baluns are implemented, as depicted in Chapters 4 and 5. The resulting current mode class-D PAs exhibit both large bandwidth and high power-added efficiency PAE. Finally, a high-power PA is presented to demonstrate the scalability of the design methods shown in this work.

The operating frequency of the presented PAs is $f_s = 869\,\mathrm{MHz}$, which is part of the 863 to 870 MHz band for short range devices (SRD860) and is released for unlicensed use in Europe [57]. In order to demonstrate the wideband capabilities of the CMCD concept, a prototype is designed to cover not only the SRD860 band at high efficiency, but also the 700 MHz and 800 MHz television (TV) whitespace, which has been recently assigned for fourth generation (4G) long term evolution (LTE) mobile services [5, 6].

5.3.1 Device Selection and Implementation

The transistor used for the demonstrator is a 100 mW GaAs E-pHEMT from *Avago/Broadcom* the ATF-541M4. The “E” in E-pHEMT stands for enhancement mode, which means the transistor is normally off and is biased with positive gate voltages. According to the data sheet of the ATF-541M4 [33], the maximum drain-source voltage is given with $V_{DS,max} = 5\,\mathrm{V}$ and the maximum drain current is $I_{D,max} = 120\,\mathrm{mA}$. With equation 2.18 the optimum load impedance R_L of a CMCD PA using this transistor is

$$R_L = \frac{\pi^2}{4} \cdot \frac{V_{DC}}{I_{DC}} = \frac{\pi}{2} \cdot \frac{V_{DS,max}}{I_{D,max}} \approx 65\,\Omega. \tag{5.18}$$

This is relatively close to $50\,\Omega$ and, therefore, allows for a broadband match to a $50\,\Omega$ load. According to equation 2.20 the expected peak output power calculates to

$$P_{out} = \frac{\pi^2}{2} \cdot \frac{V_{DC}^2}{R_L} = \frac{1}{2} \cdot \frac{V_{DS,max}^2}{R_L} \approx 192\,\mathrm{mW}. \tag{5.19}$$

The transistor is shipped in a low parasitic package, which is important for minimizing inductive losses in switched mode operation (see Section 3.2.2). Finally *Avago/Broadcom* provides a nonlinear ADS model of the ATF-541M4 (see data sheet [33]), which enables large-signal simulations to be performed.

The substrate used for the demonstrator PAs is a standard two-layer *Rogers* RO4003C laminate with a height $h = 0.508\,\mathrm{mm}$ and relative permittivity $\epsilon_r = 3.55$ [46]. It is relatively inexpensive, but still offers stable properties, enabling a repeatable design.

The selection of the radio frequency chokes is crucial for the design of the DC supply network, which has to provide a high-impedance RF rejection and a low-impedance DC supply of the switched transistors. The minimum value of the radio frequency choke is defined by the lowest switching frequency. According to equation 4.34 the minimum value L_{RFC} at $f_s = 690\,\mathrm{MHz}$ (lower edge of the 700 MHz TV whitespace [6]) and $R_L = 50\,\Omega$ calculates to

$$L_{RFC} \geq \frac{8}{\pi^2}\frac{1}{f_s}R_L \approx 59\,\mathrm{nH}. \tag{5.20}$$

Section 4.4.3 shows high-quality wire-wound inductors, which offer good fundamental and harmonic rejection. Conical inductors have a superior broadband performance at a much higher cost [38]. This work uses the *Coilcraft* 1008HQ series and the *Coilcraft* conical inductor BCL-531JL.

In Section 4.5 two output filter implementations, a band-pass (LC resonator) and a low-pass filter, have been introduced for the odd harmonic termination of the CMCD power amplifier. Consequently, two amplifiers are designed implementing either type of output filter.

According to equation 4.43 the Q factor of an LC resonator filter for a percent bandwidth $B_{P\%} = 100\%$ calculates to

$$Q_P = \frac{1}{B_{P\%}} = 1. \tag{5.21}$$

This relatively low Q factor still offers a good efficiency $\eta_{PO} = 98\%$, however, the THD of -18 dB might be unacceptable (see Fig. 4.11). With equation 4.41, $f_s = 869\,\mathrm{MHz}$ and a load resistance $R_L \approx R_P = 50\,\Omega$, this results in the component values

$$L_P = \frac{R_L}{2\pi f_s} = 9.16\,\mathrm{nH}, \tag{5.22}$$

$$C'_P = \frac{1}{2\pi f_s R_L} = 3.66\,\mathrm{pF}. \tag{5.23}$$

Finally the drain-to-source capacitance $C_{DS} \approx 0.27\,\mathrm{pF}$ of the ATF-541M4 [33] has to be subtracted from C'_P to calculate the lumped element value of C_P:

$$C_P = C'_P - C_{DS} = 3.39\,\text{pF}. \tag{5.24}$$

As for the low-pass output filter, the design equations for a 3rd order filter derived in Section 4.5.2 are used. The corner frequency $f_c = \frac{\omega_c}{2\pi} = 900\,\text{MHz}$ is placed slightly above the highest operating frequency of 870 MHz. For a Chebyshev passband ripple $R_{\text{dB}} = 0.1\,\text{dB}$ and $R_L = 50\,\Omega$, the lumped element values are

$$C_{P1} = 1.82\,\text{pF} \tag{5.25}$$

$$C'_{P2} = 3.85\,\text{pF} \tag{5.26}$$

$$L_S = 4.80\,\text{nH}. \tag{5.27}$$

The lumped element value C_{P2} is calculated to

$$C_{P2} = C'_{P2} - C_{DS} = 3.58\,\text{pF}. \tag{5.28}$$

The expected THD is -30 dB at $f_s = 869\,\text{MHz}$ (Equation 4.88).

Section 4.5.3 shows that an implementation of a paralleled differential transmission line on a standard RF substrate is not applicable due to very narrow slot widths that are difficult to manufacture. Therefore, the output filters are implemented using broadside coupled differential transmission lines, as previously shown in Fig. 4.19. In order to minimize parasitics, the switching transistor terminals have to be placed as close to the filter terminals as possible. This can be done by placing the transistors on either side of the substrate. Fig. 5.24 illustrates this idea by showing a cross section of a CMCD PA core with a low-pass output filter.

Finally the output balun is designed. As shown in Section 5.2.2, with the purpose of maximizing the bandwidth, an exponentially tapered balun is implemented. A non-tapered section of the length d is added to the balun, in order to account for the output filter and the DC supply network. Fig. 5.25 illustrates the amplifier implementation. The balun width w_b and length l are chosen for a good match of the differential mode ($Z_{dd11}/R'_L \approx 1$) in the passband of 690 MHz to 870 MHz and a good suppression of the common mode ($Z_{cc11}/R'_L > 2$) for the passband frequencies and the second harmonics. The output width w_s is designed for a 50 Ω single-ended load and the input width w_d for a 50 Ω differential source.

Table 5.1 shows the analytical estimation of the efficiency with the selected devices. The parasitics of the transistor are depicted in the data sheet [33]. $R_{DS,on}$ and τ are extracted from the ADS model of the transistor with a rectangular switch simulation at 1 GHz. Unfortunately R_c is not modeled or supplied. R_{RFC}

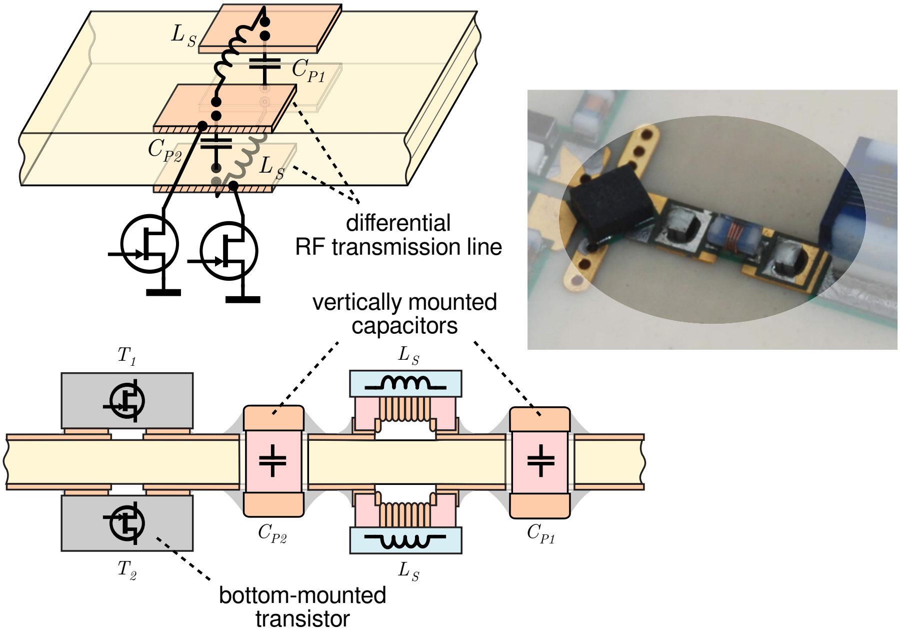

Figure 5.24.: Cross section of PCB with switching transistors mounted on either side of the board

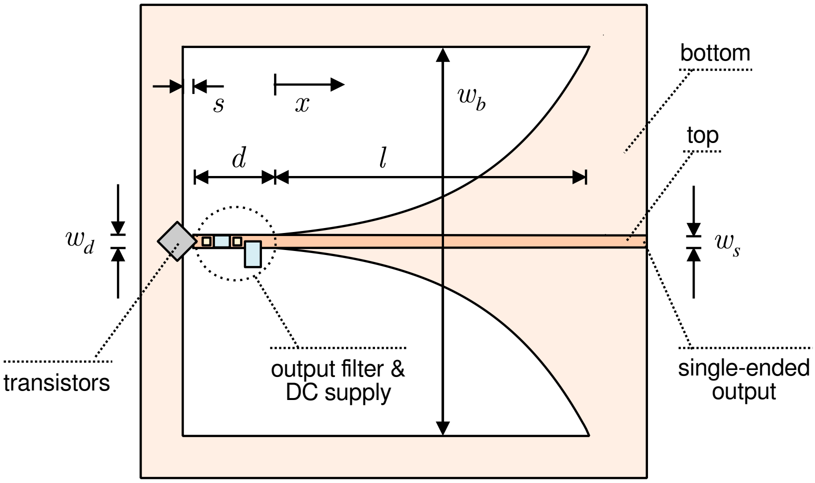

Figure 5.25.: Implementation of the CMCD PA with an exponentially tapered balun

Table 5.1.: Efficiency estimation of the implemented PA with LC resonator (CMCD A1)

Device	$f_s = 869\,\text{MHz}$, $R_L = 50\,\Omega$	
	Parasitic element	**Efficiency factor**
Transistor ATF-541M4 [33]	$R_{DS,on} = 0.25\,\Omega$ $C_{DS} = 0.27\,\text{pF}$ $R_c \to \infty$	$\eta_{TR} = 97.5\%$
	$\tau = 0.156 \cdot \pi$	$\eta_{TT} = 99.0\%$
	$L_D = 0.63\,\text{nH}$	$\eta_{LD} = 94.6\%$
Radio frequency choke	$R_{RFC} = 0.16\,\Omega$	$\eta_{RFC} = 99.2\%$
Output filter	$Q_P = 1$	$\eta_{PO} = 98.5\%$
	$R_V = 3.1\,\text{k}\Omega$	$\eta_{PP} = 98.4\%$
Balun	$R_{cc11}(2) \geq 2 \cdot R_L$	$\eta_{BI} = 97.2\%$
	$S_{sd21} = 0.2\,\text{dB}$	$\eta_{BL} = 95.5\%$
Total efficiency: $\eta \gtrsim \prod \eta_i = 81.5\%$		

is extracted from the data sheet of the RFC inductor (see Section 4.4.3). R_V of the resonator is determined with the *Modelithics* models of the lumped elements. The balun losses are simulated with the EM model in ADS. A common mode resistance of at least $R_{cc11}(1) > 2 \cdot R_L$ is the design value of the balun (compare Fig. 4.6).

The individual efficiency factors are calculated with the equations from Chapters 3 and 4. The resulting total efficiency is $\eta = 81.5\%$. As explained in Section 2.3.2, this is a lower bound value. On the other hand, there may always be additional, unconsidered loss mechanisms in reality. It is adequate for a first approximation of PA efficiency and an identification (and optimization) of critical components. As a rule of thumb, the individual efficiency factors should not fall below 90% for high-efficiency PA operation.

5.3.2 Simulation Setup

The presented design equations support the designer in choosing an amplifier concept and give start values for the subsequent nonlinear simulation. A simulation-based design methodology enables a first pass implementation of the class-D amplifier, provided all additional parasitic and material-specific properties are included in the model. Therefore, much effort has to be put into researching high-quality models and selecting suitable simulators.

This work utilizes large-signal transistor models provided by the manufacturers *Avago/Broadcom* [33] and *Wolfspeed*. Passive lumped elements are implemented using the *Modelithics* simulation library [44]. Finally, transmission lines and planar elements are modeled with an EM simulator.

Harmonic balance (HB) circuit simulation with *Keysight* ADS is used to simulate and optimize the design. EM simulation is conducted with *Keysight* ADS Momentum. The parametrized EM models of all critical components (e.g., the output balun) are generated and employed with the HB simulator.

The sophisticated output filters of the CMCD PAs presented in this work with vertically mounted SMD components on broadside coupled transmission lines are implemented with *Modelithics* simulation models. The SMD pads are de-embedded from the models using the “Sim_mode=2” option. As *Keysight* ADS Momentum unfortunately only offers uncalibrated ports to connect the *Modelithics* components, the question arises as to where to place the uncalibrated ports on the EM simulated SMD pads for an accurate simulation. *Modelithics* uses *Sonnet* EM Analysis to implement their models [44] and, therefore, *Sonnet* with so-called “auto-grounded” ports [58] is utilized to select the port location. As it turns out, the placement of the uncalibrated Momentum ports in the middle of the pad usually proves to be most accurate.

Fig. 5.26 shows an overview of the *Keysight* ADS simulation setup.

The time domain waveforms of the intrinsic drain-source voltages $v_{DS1}(t)$ and $v_{DS2}(t)$ and drain currents $i_{D1}(t)$ and $i_{D2}(t)$ are used to evaluate the loadlines at the transistor. A histogram function is used to plot the probability of a certain voltage-current combination on the loadline chart. Fig. 5.27 (left) shows this histogram.

The loadline is shifted towards the edges of the voltage-current plane, as one would expect in a high-efficiency operation. High voltages at low currents as well as low currents at high voltages have the highest probability and the transitions are fast, thus the transistors are in switched mode operation. The Python code used to extract this figure is shown below.

```
// Drain-source voltage (v_ds) and drain current (i_d)
plt.plot(v_ds, i_d)            // in time domain
plt.hist2d(v_ds, i_d, bins=40, cmin=1, zorder=3,
          cmap = plt.cm.bwr, norm=LogNorm())
```

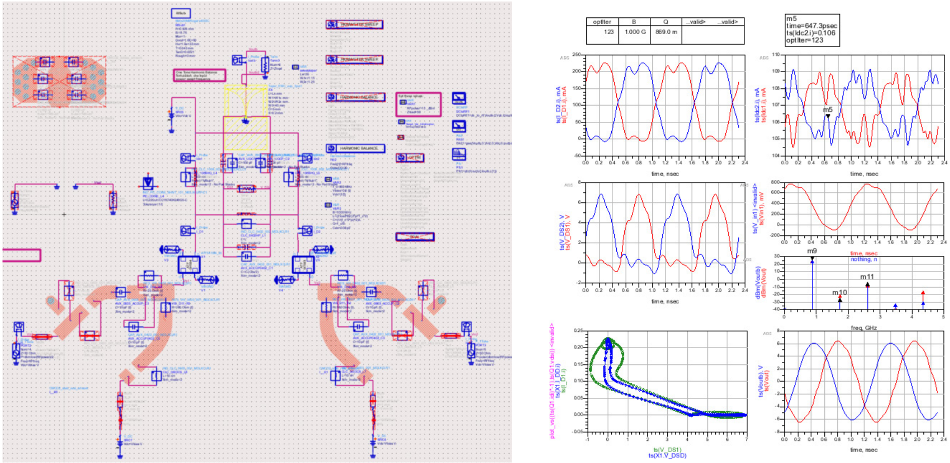

Figure 5.26.: *Keysight* ADS Simulation setup

To optimize the efficiency, a power-weighted histogram function is used with the Python code shown below.

```
// Drain-source voltage (v_ds) and drain current (i_d)
plt.plot(v_ds,i_d)                    // in time domain
gridx = np.linspace(min(v_ds),max(v_ds),41)
gridy = np.linspace(min(i_d),max(i_d),41)
H, xedges, yedges = np.histogram2d(v_ds, i_d,
                                   bins=[gridx, gridy])
H=np.log(H)
myextent = [xedges[0],xedges[-1],yedges[0],yedges[-1]]
v_ds_a, i_d_a = np.meshgrid (np.linspace(0,1,len(H)),
                             np.linspace(0,1,len(H)))
power = v_ds_a * i_d_a
plt.imshow(H.T*power,cmap = diverge_map(),origin=’low’,
           extent=myextent, interpolation=’nearest’,
           aspect=’auto’, zorder=3)
```

The probability function is weighted with a power loss function. Fig. 5.27 (right) shows this power-weighted histogram. The bins on the histogram that are equivalent to a high power loss are more prominent at this point.

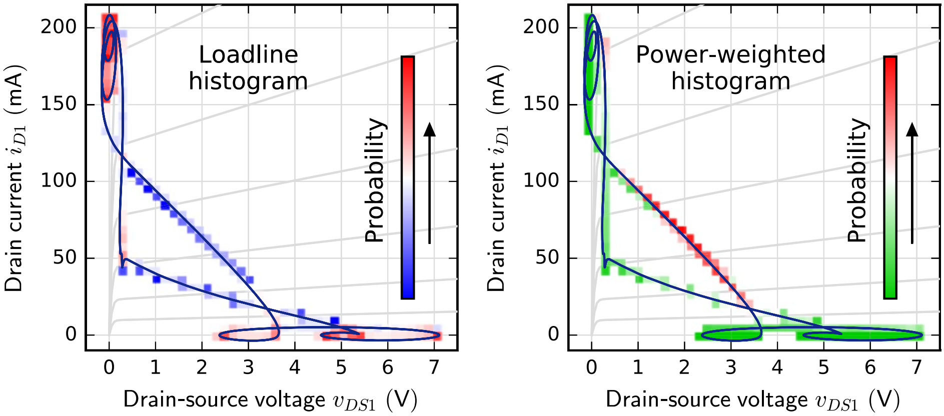

Figure 5.27.: Loadline with histogram of the CMCD A1 PA (left) and power-weighted histogram (right). The static I-V curves of the transistor are illustrated in the background.

5.3.3 Manufacturing

The accurate manufacturing of the power amplifier is crucial for achieving good repeatability in conjunction with the simulation model. A 6 mm thick gold plated brass mounting plate with SMA flange connectors is used to mechanically fix the PA board. The brass plate also houses the bias cabling and serves as a heat sink.

Vapor phase soldering of the board ensures a very accurate and repeatable positioning and puts low stress on the components.

The through hole mounted SMD components (see Fig. 4.19 in Section 4.5.3) are attached with much care. Precise cutouts, which are not plated-through, are placed in the PCB. The SMD components are fixed by a heat-proof tape on one side and kept from falling through while soldering the other side.

Two PA boards are manufactured, implementing the two types of differential output filters. Fig. 5.28 shows a picture of the manufactured power amplifier CMCD A1 with a band-pass filter (LC resonator). A picture of the low-pass implementation (CMCD A2) is depicted in Appendix A.2. A detail view of the differential output filters with the through hole mounted components is illustrated in Fig. 5.29.

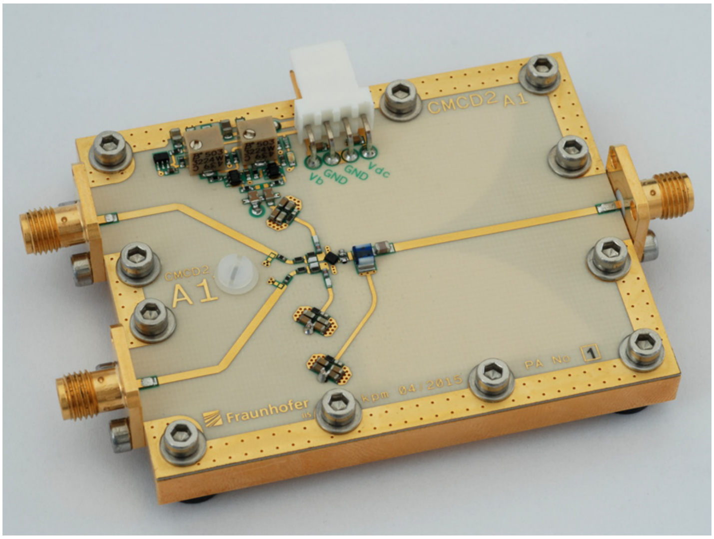

Figure 5.28.: Picture of the CMCD A1 PA (band-pass filter)

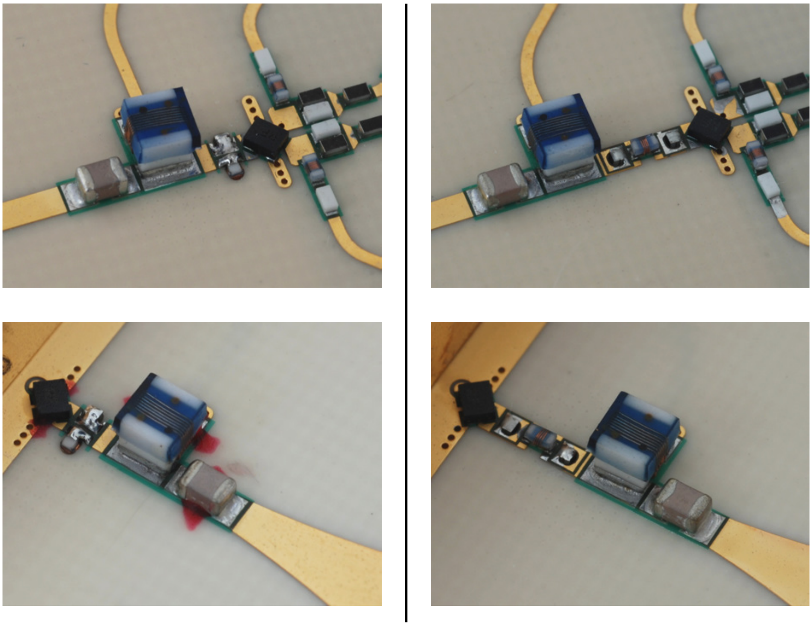

Figure 5.29.: Detail views of the differential output filters on top and bottom of the PCB. CMCD A1 PA (left) and CMCD A2 PA (right)

5.3.4 Measurement Setup and Results

Fig. 5.30 shows an overview of the fully automatic measurement setup. The *R&S* ZVA24 vector network analyzer is used as signal generator and as a measurement receiver. The differential input signal is generated in a so-called defined coherence mode, i.e., the signal sources have a fixed (and adjustable) phase and amplitude relationship. This way, the calibrated input signals P_{in1} and P_{in2} are provided with the total input power $P_{in} = P_{in1} + P_{in2}$. Power calibration is done with a *R&S* NRP-Z22 power sensor. The supply voltages V_{DC} (DC voltage) and V_{bias} (bias voltage) are provided by a *Keysight* N6705B DC power analyzer, which accurately measures the DC input power P_{DC}. The RF output power P_{out} of the DUT is determined by the port 2 measurement receiver of the ZVA24. The harmonic components of P_{out} are simultaneously recorded. Finally, the spectrum is monitored with a *R&S* FSP spectrum analyzer. A LAN connection is used to calculate drain efficiency η and PAE.

Even the smallest measurement errors can considerably distort the efficiency reading. The absolute measuring accuracy of the *R&S* NRP-Z22 power sensor is 0.085 dB at 20 to 25°C in a frequency range of 0.1 to 4 GHz [59]. This corresponds to an uncertainty of 2.0% in the efficiency measurement. The P_{DC} uncertainty is less than 0.1% as precision DC power modules are used in the *Keysight* N6705B [60]. Attenuators at the input and at the output of the DUT are used to reduce matching errors. An overall measurement uncertainty of 0.1 dB in absolute output power and 2.5% in efficiency is a realistic estimate.

Fig. 5.31 shows a measurement of the CMCD PA prototype A1 with a band-pass (LC resonator) output filter. The RF parameters output power P_{out}, gain G, the drain efficiency η and the power-added efficiency PAE are depicted as

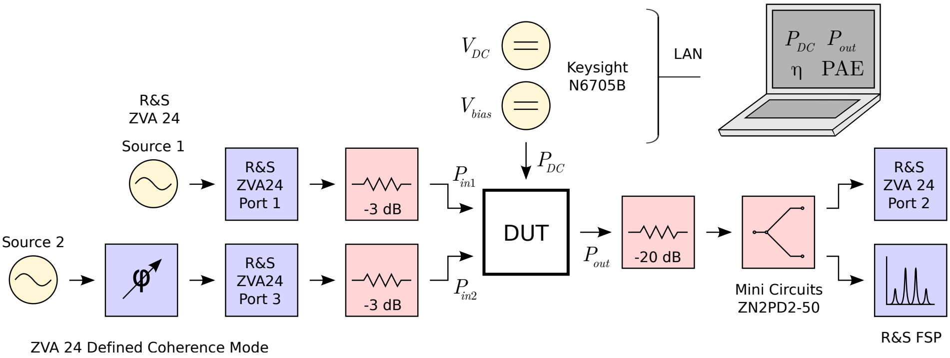

Figure 5.30.: Overview of the fully automatic measurement setup with phase coherent signal sources

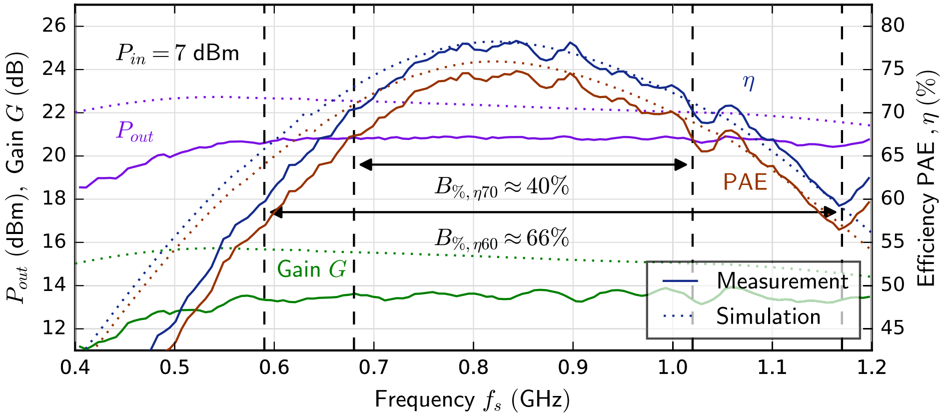

Figure 5.31.: CMCD PA A1 (band-pass filter): RF parameters as a function of frequency at $P_{in} = 7\,\mathrm{dBm}$

a function of input frequency. The input power is constant at $P_{in} = 7\,\mathrm{dBm}$. Additionally, the ADS simulation results are added to the figure. A peak drain efficiency $\eta = 77\%$ is demonstrated at $f_s = 840\,\mathrm{MHz}$.

A figure of merit is necessary to assess the bandwidth of the amplifier. In this work the bandwidth is calculated for a minimum efficiency of 0.9 times (or 90%) the peak efficiency. The same figure of merit has been used in Section 5.1.2 to determine the (high-efficiency) bandwidth of the balun. With a peak efficiency $\eta = 77\%$, the bandwidths below are calculated for a minimum efficiency of 70%. For the sake of comparison, the bandwidths with a minimum efficiency of 60% are noted as well.

The drain efficiency exceeds 70% (η_{70}) for a range of 680 MHz to 1020 MHz, which is only slightly lower than the simulation had predicted. The resulting bandwidth is

$$B_{\%,\eta70} = 2 \cdot \frac{1020 - 680\,\mathrm{MHz}}{1020 + 680\,\mathrm{MHz}} \approx 40\%. \tag{5.29}$$

The drain efficiency exceeds 60% (η_{60}) for a range of 590 MHz to 1170 MHz. The resulting bandwidth is

$$B_{\%,\eta60} = 2 \cdot \frac{1170 - 590\,\mathrm{MHz}}{1170 + 590\,\mathrm{MHz}} \approx 66\%. \tag{5.30}$$

The output power and gain deviate from the simulation by 2 dB in the high-efficiency region. This can be explained by additional losses in the input network,

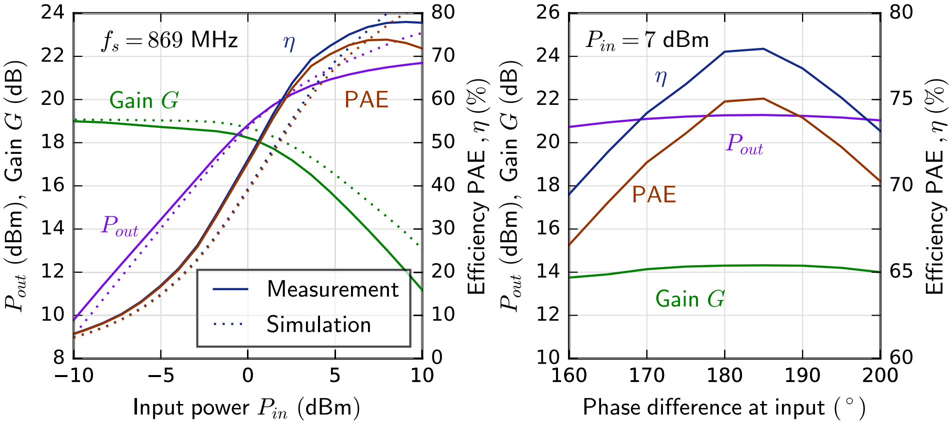

Figure 5.32.: CMCD PA A1 (band-pass filter): RF parameters as a function of input power and as a function of input phase at $f_s = 869\,\text{MHz}$

which were not covered by the simulation and an inaccurately modeled transconductance of the transistor in the compression region.

A power sweep of the PA at the operating frequency $f_s = 869\,\text{MHz}$ is depicted in Fig. 5.32 (left). The amplifier is stable in linear mode. As expected, the efficiency drastically decreases towards low output powers. The input phase sweep in Fig. 5.32 (right) demonstrates that the implemented PA is symmetric.

The measured total harmonic distortion at $f_s = 869\,\text{MHz}$ and $P_{in} = 7\,\text{dBm}$ is THD $= -26\,\text{dB}$. This is lower than the design value of -18 dB in Section 5.3.1. The deviation can be explained with the reduced harmonic content of the real current waveform (Fig. 5.26), which doesn't have an ideal rectangular shape. Furthermore, the insertion loss of the balun increases at high frequencies.

Fig. 5.33 depicts the RF parameters of the CMCD PA prototype A2 with a low-pass output filter as a function of input frequency.

The drain efficiency exceeds 70% (η_{70}) for a range of 500 MHz to 1010 MHz. The resulting bandwidth is

$$B_{\%,\eta 70} = 2 \cdot \frac{1010 - 500\,\text{MHz}}{1010 + 500\,\text{MHz}} \approx 68\%. \tag{5.31}$$

The drain efficiency exceeds 60% (η_{60}) for a range of 415 MHz to 1100 MHz. The resulting bandwidth is

$$B_{\%,\eta 60} = 2 \cdot \frac{1100 - 415\,\text{MHz}}{1100 + 415\,\text{MHz}} \approx 90\%. \tag{5.32}$$

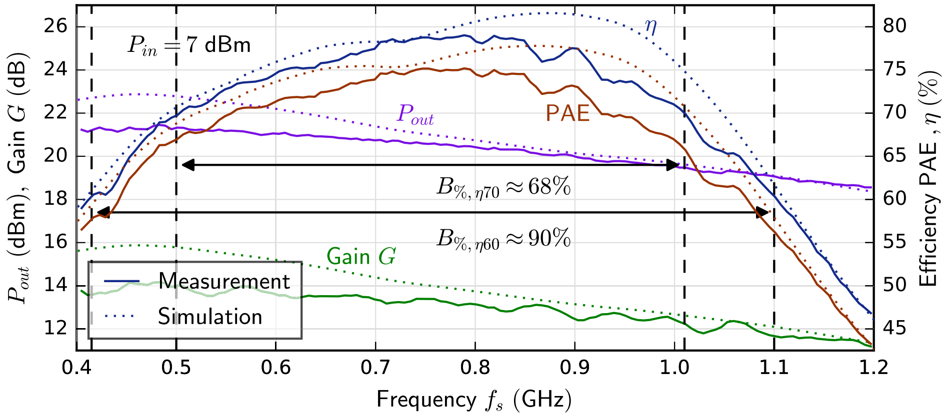

Figure 5.33.: CMCD PA A2 (low-pass filter): RF parameters as a function of frequency at $P_{in} = 7\,\text{dBm}$

A peak power-added efficiency PAE $= 75\%$ is maintained for a range of 700 MHz to 850 MHz.

Power sweeps of several frequencies of interest ($f_s = 869\,\text{MHz}$, $f_s = 690\,\text{MHz}$ and $f_s = 960\,\text{MHz}$) are shown in Fig. 5.34 (left). Once again, the input phase sweep in Fig. 5.34 (right) depicts a symmetric PA design.

The measured total harmonic distortion at $f_s = 869\,\text{MHz}$ and $P_{in} = 7\,\text{dBm}$ is THD $= -38\,\text{dB}$. This is lower than the design value of -30 dB in Section 5.3.1. The deviation coincides with the measurements of the A1 prototype.

The presented CMCD power amplifier does not only cover the SRD860 band and the 700 MHz and 800 MHz TV whitespace at a high efficiency, but also handles the industrial, scientific and medical (ISM) radio band at 915 MHz [61] and the Global System for Mobile Communications (GSM) radio band at up to 960 MHz [61]. For an octave bandwidth (500 MHz to 1 GHz) the PA maintains a drain efficiency $\eta > 70\%$ and a power-added efficiency PAE $> 67\%$.

Table 5.2 gives an overview of current state-of-the-art wideband PAs with similar operating frequencies. Single-ended class-F, -E and -J PAs are depicted as well as differential class-D PAs. The CMCD A2 PA has the highest 60%-bandwidth ($B_{\%,\eta60}$) and the highest 70%-bandwidth ($B_{\%,\eta70}$). For instance, compared to a single-ended wideband class-F PA ([16], $B_{\%,\eta70} = 51\%$), the CMCD A2 PA maintains high efficiency over a higher bandwidth ($B_{\%,\eta70} = 68\%$). This is only possible with a defined harmonic impedance space and this result underlines the potentials of differential switched mode power amplifiers.

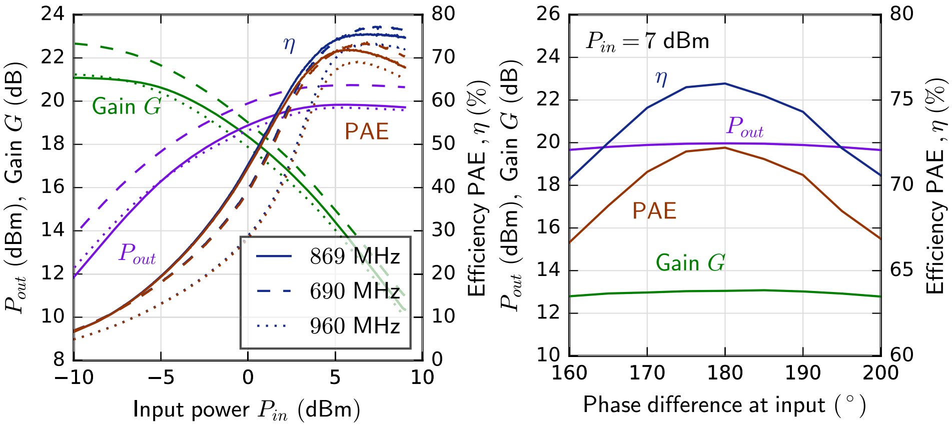

Figure 5.34.: CMCD PA A2 (low-pass filter): RF parameters as a function of input power and as a function of input phase at $f_s = 869\,\text{MHz}$

[62] presents a continuous class-F/F^{-1} mode PA with a phenomenal 60%-bandwidth ($B_{\%,\eta 60} = 84\%$). However, at higher efficiencies the bandwidth drops significantly because of the transition band between class-F and class-F^{-1} mode.

The class-D PA in [8] de-embeds the losses of the external wideband balun. In this work all balun losses are included in the measurements.

The class-D PA in [19] uses a bulky coaxial balun. To the knowledge of the author, this work is the first demonstration of a CMCD PA with a planar PCB-embedded balun.

Most of the PAs in Table 5.2 use GaN devices and operate at higher powers, than the GaAs demonstrator PA in this work. Unfortunately only few GaAs PAs have been published operating in class-F (e.g., [63]) and class-D (e.g., [8]) mode. Thus, to verify the scalability of the design, the next section offers a high-power 25 W demonstrator PA.

Table 5.2.: State-of-the-art wideband PAs

Reference	**Topology**	P_{out}(dBm)	$B_{\eta 60}$(GHz)	$B_{\%,\eta 60}$	$B_{\%,\eta 70}$
[64]	class-J GaN	40	1.5-2.7	60%	-
[65]	class-F GaN	40	1.8-3.3	59%	-
[16]	class-F GaN	40	0.5-1.1	77%	51%
[66]	class-E GaN	40-43	0.9-2.2	84%	56%
[62]	class-F/F^{-1} GaN	40	1.3-3.3	87%	44%
[17]	class-F GaN	41-42	1.3-2.5	63%	42%
[63]	class-F GaAs	22	0.55-0.99	57% (PAE)	-
[67]	class-F GaAs	31	1.3-2.1	47% (PAE)	-
[8]	class-D GaAs external balun	29	0.55-1.0	58%	38%
[19]	class-D GaN coax balun	44-46	0.5-1.2	82%	-
This work (CMCD PA A2)	**class-D GaAs planar balun**	**19-21**	**0.4-1.1**	90%	68%

5.3.5 High-Power Demonstrator PA

To verify the proposed design methods at high powers, a 25 W demonstrator PA is presented. This amplifier is based on the CMCD A1 design.

To scale up the output power, an unmatched GaN HEMT is used. The *Wolfspeed* CGH27030S [31] delivers up to 30 W peak power and can be operated over a wide range of supply voltages. It features an SMD plastic package and can therefore be mounted on either side of the PCB to minimize parasitic effects (compare Fig. 5.24).

The LC resonator output filter is tuned to $f_c = 635\,\mathrm{MHz}$. All passive SMD components are selected according to the necessary voltage and current ratings of the high-power operation.

Fig. 5.35 shows the implemented power amplifier. The high-power measurement setup in Fig. 5.36 employs a preamplifier and a mechanical phase shifter. Unfortunately, the defined coherence mode of the ZVA24 cannot be used. The internal self-calibration procedures of the ZVA24 might lead to improper phase relationships which could damage the transistors. A mechanical phase shifter ensures that the 180° phase condition is always met.

Fig. 5.37 (left) shows a measurement of the high-power CMCD PA prototype. The RF parameters output power P_{out}, gain G, the drain efficiency η and the

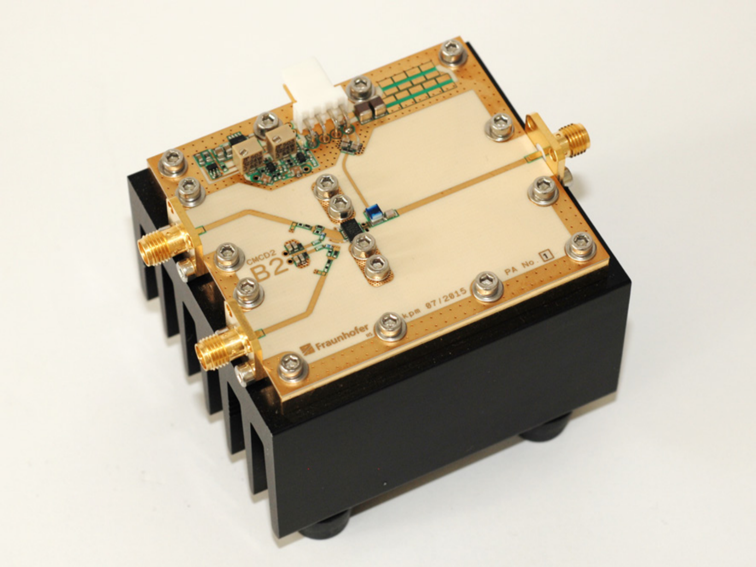

Figure 5.35.: Picture of the CMCD B2 PA (band-pass filter)

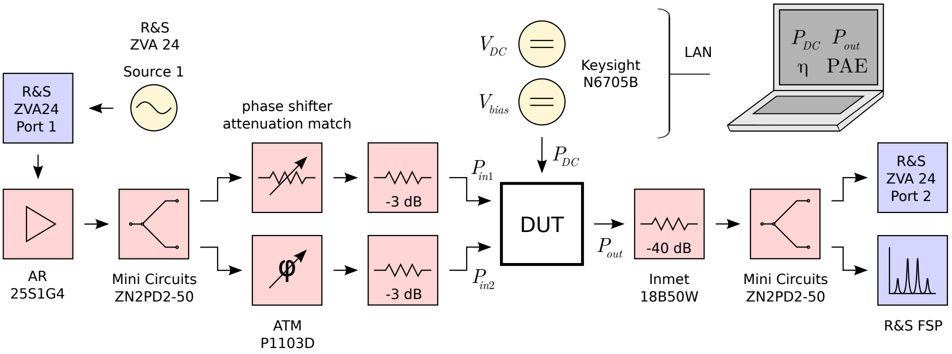

Figure 5.36.: Modified high-power measurement setup with mechanical phase shifter

power-added efficiency PAE are depicted as a function of input power P_{in} for three different drain voltages V_{DC}. The switching frequency is constant at $f_s = 635\,\text{MHz}$.

The peak drain efficiency is about 80% and the peak PAE is 72%. The drain voltage sweep in Fig. 5.37 (right) depicts efficient operation of the power amplifier for a wide range of output powers from $P_{out} = 7\,\text{W}$ up to $25\,\text{W}$. This amplifier could be used, for instance, as the core PA of an EER amplifier system. Table 5.3 gives an overview of current state-of-the-art high-power class-D PAs with similar operating frequencies.

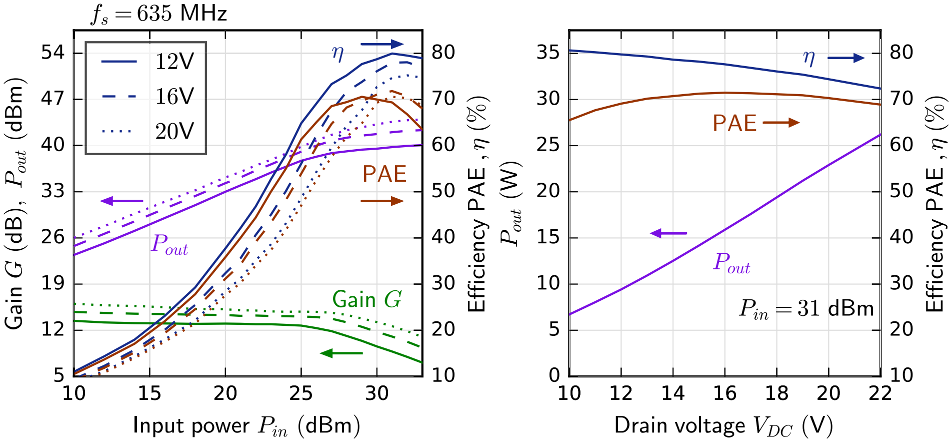

Figure 5.37.: CMCD PA B2: RF parameters as a function of input power and as a function of supply voltage V_{DC} at $f_s = 635\,\text{MHz}$

Table 5.3.: State-of-the-art high-power class-D PAs

Reference	**Topology**	P_{out}(dBm)	f_s(MHz)	η	PAE
[10]	class-D LdMOS planar balun	41	900	60%	58%
[68]	class-D LdMOS planar balun	43	1000	71%	69%
[69]	class-D GaN VMCD	35	470	77%	67%
[70]	class-D GaN external balun	36	860	64%	-
This work (CMCD PA B2)	**class-D GaN planar balun**	**42**	**635**	79%	72%

6 Antenna Integrated Amplifier

This chapter examines the integration of CMCD PAs into differential antennas. The use of an antenna as a differential load allows to drop the balun and thereby simplifies the PA-antenna interface. A description of different antenna types is followed by the presentation of an antenna integrated amplifier ("amplitenna"). Finally, the efficiency of the prototype is measured in an anechoic chamber.

The main contributions of this chapter are the analysis of antenna designs for CMCD PAs, the implementation of an antenna integrated CMCD PA and a measurement of the over-the-air (OTA) efficiency of this PA.

6.1 Motivation and Antenna Types

In many RF power amplifier applications, the RF signal is first amplified and then transmitted by an antenna. The antenna and the power amplifier are usually separate devices and are connected by a $50\,\Omega$ single-ended RF transmission line (Fig. 6.1). In many cases the antenna is actually composed of one or more differential antenna elements and a balun is used for attaching the single-ended input.

With a differential PA concept like the CMCD power amplifier, the PA-antenna interface can be simplified by dropping the single-ended path and the baluns and, eventually, integrating the power amplifier into the antenna. Fig. 6.1 visualizes this idea.

An antenna array, which is a set of multiple antenna elements, usually requires a feed network that distributes the input power to k individual elements at a defined power level $P_{out,k}$ and a phase angle φ_k. For efficiency sensitive applications, the design of the feed network is a compromise between power loss and bandwidth. Fig. 6.2 shows an alternative design approach, which allows to drop the feed network. The transmitter is now composed of k multiple CMCD PAs with k multiple antenna elements. The output power of each element is determined by the supply voltage $V_{DC,k}$ of the corresponding CMCD PA. The digital drive signal defines the phase angle φ_k.

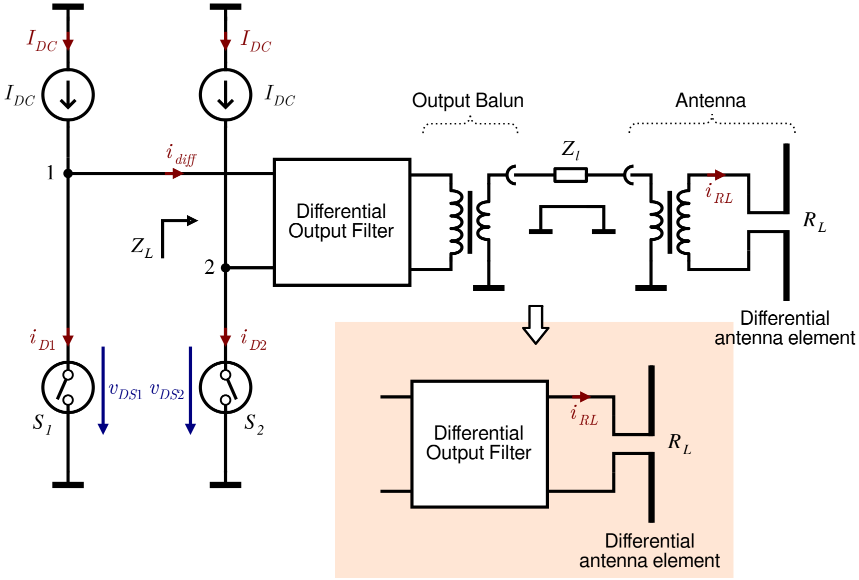

Figure 6.1.: Ideal current mode class-D amplifier with a differential antenna load

6.1.1 Antenna Design for CMCD PAs

In general, the properties of antennas can be subdivided into two main areas [71]. On the one hand, an antenna is defined by its spatial electro-magnetic field distribution. On the other hand, an antenna is defined by its electrical properties in terms of an input impedance. If the antenna is a part of a transmission system, it has to be matched to the output impedance of the power amplifier. The antenna input impedance $Z_{feed} = R_{feed} + jX_{feed}$ is the impedance at the input (or feed) terminals, which is transformed to three components in series at the antenna:

- a radiation resistance R_{rad}, which describes the emitted power in the far field (i.e., in the radiation zone or *Fraunhofer region*),
- a loss resistance R_{loss}, which describes ohmic losses,
- a reactance X_{rad}, which includes all electromagnetic energy saved in the (reactive) near field.

The radiation resistance is usually referred to the point of the current maximum on the antenna. If this current maximum appears at the input terminals (and losses are neglected), then input resistance and radiation resistance are equal: $R_{feed} = R_{rad}$. The same applies for the input reactance.

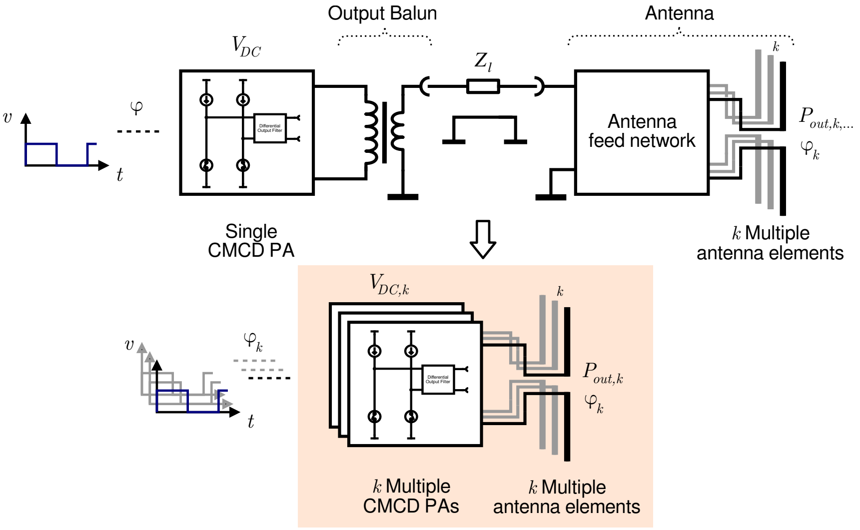

Figure 6.2.: Array of multiple antenna elements with a single common and with multiple individual CMCD power amplifiers

The spatial field distribution of an antenna is usually only used in the far field to calculate, for example, the directivity. For this purpose, the antenna reactance in the near field is neglected. However, a complete picture of the input impedance is required to design an antenna integrated amplifier according to Fig. 6.1. Resonant emitters are especially sensitive to reactive mismatch. The same applies to the output network of the harmonically tuned CMCD power amplifier.

All antenna parameters, including the input impedance, can be calculated from the exact current distribution on the antenna. This calculation is very elaborate even for relatively simple antenna structures. In fact, analytical solutions are often unavailable and electro-magnetic (EM) simulations using, for instance, finite element methods (FEM) are used to calculate the current distribution and the resulting input impedance. Based on this, the input impedance analysis in this work is restricted to a basic element, a thin linear dipole antenna.

The calculation of the spatial field distribution can be done using simplifications by neglecting the reactive near field. For further information the reader is kindly referred to common literature [71–73].

6.1.2 Thin Linear Dipole Antenna

Fig. 6.3 shows a cylindrical linear dipole antenna depicted in [72]. In opposition to a single-ended monopole, the dipole is a differential antenna and is, therefore, suitable for the CMCD power amplifier. The current source I_0 induces the current density $\mathbf{J}$ into the two cylindrical conductors with the height h and the diameter d. Due to the skin-effect at high frequencies, the current density $\mathbf{J}$ can be assumed to be a rotationally symmetric surface current $\mathbf{J}_F$ on the surface A' of the cylindrical conductors.

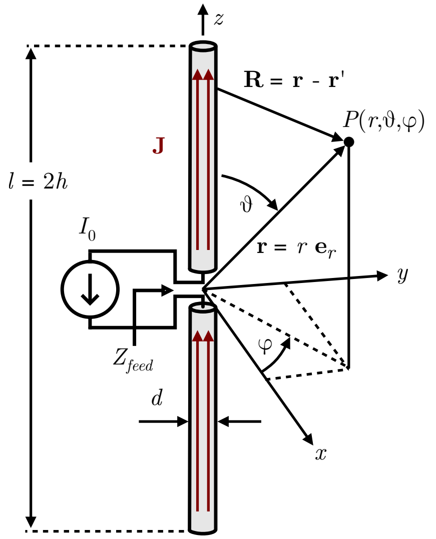

The antenna is called “thin” if

$$\frac{l}{d} = \frac{2h}{d} \geq 75$$

and

$$d \leq \frac{\lambda_0}{50}.$$

Figure 6.3.: A cylindrical linear dipole antenna

Calculation of the Far Field Components

The magnetic vector potential $\mathbf{A}(\mathbf{r})$ at a space point $\mathbf{r}$ with a source point $\mathbf{r}'$ can be calculated from the Maxwell equations [72] to

$$\mathbf{A}(\mathbf{r}) = \frac{1}{4\pi} \oiint_{A'} \mathbf{J}_F(\mathbf{r}') \frac{e^{-jk_0|\mathbf{r}-\mathbf{r}'|}}{|\mathbf{r}-\mathbf{r}'|} dA' \tag{6.1}$$

with $k_0 = \omega/c_0$ in free space.

The integration of the current density $\mathbf{J}_F$ at the cylindrical surface A' is quite elaborate. A reduction of the current density $\mathbf{J}_F$ to a one-dimensional current $I(z')$ would simplify the calculation. It is allowed, if the antenna is sufficiently thin. According to [72], a cylindrical linear dipole antenna is referred to as “thin” if the antenna length is considerably larger than the diameter

$$\frac{l}{d} = \frac{2h}{d} \geq 75 \tag{6.2}$$

and the diameter is considerably smaller than the wavelength in free space

$$d \leq \frac{\lambda_0}{50}. \tag{6.3}$$

In the far field of the antenna the field strengths are given by

$$\mathbf{H} = -jk_0 e_r \times \mathbf{A} \qquad \text{and} \qquad \mathbf{E} = -e_r \times Z_0 \mathbf{H} \tag{6.4}$$

with $k_0 = \omega / c_0$ and $Z_0 = \sqrt{\mu_0 / \epsilon_0}$ in free space [72]. With $|\mathbf{r}| \gg |\mathbf{r}'|$ in the far field the magnetic field of the thin antenna can be written as

$$Z_0 \mathbf{H}(\mathbf{r}) = -j\omega\mu_0 \frac{e^{-jk_0 r}}{4\pi r} \left(\mathbf{e}_r \times \mathbf{e}_z\right) \int\limits_{-h}^{h} I\left(z'\right) e^{jk_0 z' (\mathbf{e}_r \cdot \mathbf{e}_z)} dz'. \tag{6.5}$$

With $\mathbf{e}_r \cdot \mathbf{e}_z = \cos\vartheta$ and $\mathbf{e}_r \times \mathbf{e}_z = -\mathbf{e}_\varphi \sin\vartheta$ and the symmetry of the current $I(-z') = I(z')$, the far field components are

$$\boxed{E_\vartheta = Z_0 H_\varphi = -j\omega\mu_0 \frac{e^{-jk_0 r}}{2\pi r} \sin\vartheta \int\limits_{0}^{h} I\left(z'\right) \cos\left(k_0 z' \cos\vartheta\right) dz'}. \tag{6.6}$$

In practice the current distribution can be approximated by a standing sinusoidal wave [72] with

$$\boxed{I\left(z'\right) = \hat{I} \sin\left[k_0 \left(h - |z'|\right)\right]}. \tag{6.7}$$

With this assumption in mind, the far field components can be calculated [72] as a function of antenna height h and the spatial coordinates by

$$\boxed{E_\vartheta = Z_0 H_\varphi = jZ_0 \hat{I} \frac{e^{-jk_0 r}}{2\pi r} \frac{\cos\left(k_0 h \cos\vartheta\right) - \cos\left(k_0 h\right)}{\sin\vartheta}}. \tag{6.8}$$

Calculation of the Input Impedance

The radiated power P_{rad} of an antenna can be calculated [72] by integrating the Poynting vector $\mathbf{S}$ at the spherical surface element $d\mathbf{A} = \mathbf{e}_r r^2 \sin\vartheta d\vartheta d\varphi$ by

$$P_{rad} = \mathrm{Re}\left\{ \oiint_A \mathbf{S} \cdot d\mathbf{A} \right\} = \int_{\varphi=0}^{2\pi} \int_{\vartheta=0}^{\pi} S_r r^2 \sin\vartheta d\vartheta d\varphi. \tag{6.9}$$

The magnitude of the Poynting vector S_r is obtained from the far field components by

$$S_r = \frac{1}{2}\mathbf{e}_r \cdot \mathrm{Re}\left\{ E_\vartheta \times H_\varphi^* \right\} = \frac{1}{2Z_0} \left| E_\vartheta \right|^2 \tag{6.10}$$

and with 6.8 S_r is calculated to

$$S_r = \frac{Z_0 \left| \hat{I} \right|^2}{8\pi^2 r^2} \frac{\left[\cos\left(k_0 h \cos\vartheta\right) - \cos\left(k_0 h\right) \right]^2}{\sin^2\vartheta}. \tag{6.11}$$

The calculation of the radiation power P_{rad} is then reduced to the integration of the ϑ-component:

$$P_{rad} = \frac{Z_0 \left| \hat{I} \right|^2}{4\pi} \int_{\vartheta=0}^{\pi} \frac{\left[\cos\left(k_0 h \cos\vartheta\right) - \cos\left(k_0 h\right) \right]^2}{\sin\vartheta} d\vartheta. \tag{6.12}$$

The radiated power P_{rad} of a thin linear antenna can be given as a function of radiation resistance R_{rad} if a sinusoidal current distribution is assumed:

$$P_{rad} = \frac{\left| \hat{I} \right|^2}{2} R_{rad}. \tag{6.13}$$

Therefore, the radiation resistance can be given as a function of dipole height h by

$$\boxed{R_{rad} = \frac{Z_0}{2\pi} \int_{\vartheta=0}^{\pi} \frac{\left[\cos\left(k_0 h \cos\vartheta\right) - \cos\left(k_0 h\right) \right]^2}{\sin\vartheta} d\vartheta}. \tag{6.14}$$

Unfortunately the integral in 6.14 cannot be solved analytically. [73] offers an approximation

$$\begin{aligned} R_{rad} &= \frac{Z_0}{4\pi}\Bigg\{2\left[\gamma+\ln\left(2k_0h\right)-\mathrm{Ci}\left(2k_0h\right)\right] \\ &\quad +\sin\left(2k_0h\right)\left[\mathrm{Si}\left(4k_0h\right)-2\mathrm{Si}\left(2k_0h\right)\right] \\ &\quad +\cos\left(2k_0h\right)\left[\gamma+\ln\left(k_0h\right)+\mathrm{Ci}\left(4k_0h\right)-2\mathrm{Ci}\left(2k_0h\right)\right]\Bigg\} \end{aligned} \tag{6.15}$$

with $\gamma = 0.57721...$ the Euler–Mascheroni constant and the sine (Si) and cosine (Ci) integrals

$$\mathrm{Si}\left(x\right)=\int\limits_0^x \frac{\sin t}{t}dt \qquad \text{and} \qquad \mathrm{Ci}\left(x\right)=-\int\limits_x^\infty \frac{\cos t}{t}dt. \tag{6.16}$$

[73] also offers a solution for the antenna reactance X_{rad} as a function of antenna diameter $d = 2a$ and height h:

$$\begin{aligned} X_{rad} &= \frac{Z_0}{2\pi}\Bigg\{2\mathrm{Si}\left(2k_0h\right)+\cos\left(2k_0h\right)\left[2\mathrm{Si}\left(2k_0h\right)-\mathrm{Si}\left(4k_0h\right)\right]+ \\ &\quad +\sin\left(2k_0h\right)\left[\gamma+\ln\frac{\left(k_0a\right)^2}{k_0h}+\mathrm{Ci}\left(4k_0h\right)-2\mathrm{Ci}\left(2k_0h\right)\right]\Bigg\}. \end{aligned} \tag{6.17}$$

The reactance calculation is done using the EMF (electro-motive force) method, which is shown in [74]. It is based on the Lorentz reciprocity theorem, which states that two localized current densities J_1 and J_2 that produce the fields E_1 and E_2 at an angular frequency ω can be integrated over a volume V by

$$\int\limits_V J_1 \cdot E_2 dV = \int\limits_V J_2 E_1 dV. \tag{6.18}$$

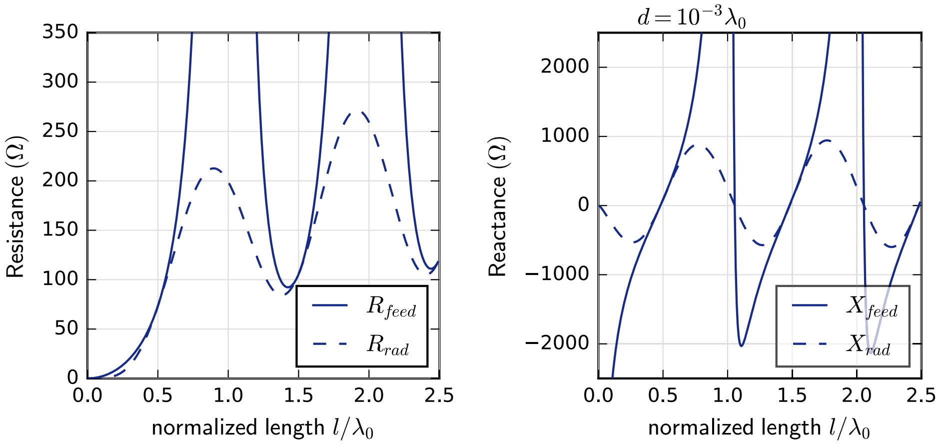

Figure 6.4.: Input- and radiation impedance of a thin linear dipole $d = 2a = 10^{-3}\lambda_0$ as a function of l/λ_0

Table 6.1.: Selected input impedances of a thin linear dipole

	Half-wave dipole	**Matched dipole**
Antenna length l	$\lambda_0/2$	$0.96 \cdot \lambda_0/2$
$Z_{feed} = R_{feed} + jX_{feed}$	$(73.1 + j42.5)\Omega$	$(73.1 + j0)\Omega$

Fig. 6.4 shows the input and radiation resistances and -reactances of a thin linear dipole $d = 2a = 10^{-3}\lambda_0$ as a function of normalized length l/λ_0. The input and radiation impedances differ at integer multiples of the wavelength. This happens due to a shift of the point of current maximum away from the input terminals. The radiation impedances are always defined for the point of the current maximum on the antenna. Table 6.1 depicts selected values of R_{feed} and X_{feed}. The half-wave dipole has an input resistance of 73.1Ω and is slightly inductive at +42.5Ω. This inductance can be compensated by slightly trimming the dipole length. At approximately $0.96 \cdot \lambda_0/2$ only a resistive input impedance is presented.

However, the reactance, in combination with a CMCD PA, can be absorbed by the output filter. At $f_s = 869\,\text{MHz}$, the input reactance of the half-wave dipole is equivalent to an inductance $L_{feed} = 7.78\,\text{nH}$. This value can be easily absorbed in the parallel inductance L_p of a practical LC resonator filter (compare Section 5.3.1).

Antenna Efficiency

The radiated power P_{rad} and the loss power P_{loss} are used to calculate the antenna efficiency η_{rad}. With Kirchhoff's current law, the antenna efficiency can be given as a function of radiation resistance and loss resistance by

$$\boxed{\eta_{rad} = \frac{P_{rad}}{P_{rad} + P_{loss}} = \frac{R_{rad}}{R_{rad} + R_{loss}}}. \tag{6.19}$$

According to [72], the ohmic resistance of a cylindrical wire at high frequencies with $a \gg \delta = 1/\sqrt{\pi f \mu_0 \kappa}$ (skin depth) is

$$R_{loss} = \frac{a}{2\delta} R_0 \tag{6.20}$$

with $R_0 = \frac{l}{\kappa \pi a^2}$ and the conductivity κ.

For example, a thin linear copper dipole ($\kappa = 58 \cdot 10^6\,\mathrm{S/m}$) of varying length with a diameter $d = 2a = 1\,\mathrm{mm}$ is calculated at $f = 900\,\mathrm{MHz}$. The loss resistance is

$$R_{loss} = \frac{l}{2a}\sqrt{\frac{f\mu_0}{\pi\kappa}} = 2.49\,\frac{\Omega}{\mathrm{m}} \cdot l. \tag{6.21}$$

Now η_{rad} can be calculated with R_{rad} from 6.15 and R_{loss}. Fig. 6.5 shows η_{rad} as a function of normalized length l/λ_0. The resistive losses slowly increase towards high lengths. However, short antennas have a very bad efficiency due to the low radiation impedance.

6.1.3 Wideband Antenna Implementations

A thin linear dipole antenna can be easily matched to a CMCD power amplifier. However, the antenna impedance in Fig. 6.4 shows steep impedance gradients. In other words, the dipole is sensitive to length and frequency variations. The resulting mismatch is likely to deteriorate output power (resistive mismatch) and efficiency (reactive detuning of the harmonic output filter).

The steep impedance gradients of the linear dipole originate from the resonant properties of this antenna. Thus, frequency independent (i.e., wideband) antenna implementations would be highly desirable.

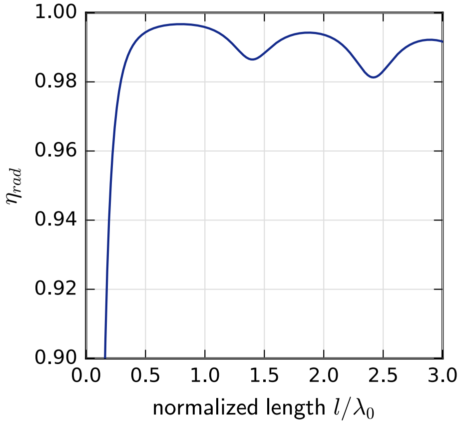

Figure 6.5.: Efficiency η_{rad} of a thin linear copper dipole with $d = 2a = 1\,\mathrm{mm}$ at $f = 900\,\mathrm{MHz}$ as a function of l/λ_0

Quality Factor Criterion for Wideband Antennas

The bandwidth of an antenna is often defined using the percent bandwidth (see 2.2) with

$$B_{\%} = 2 \cdot \frac{f_{max} - f_{min}}{f_{max} + f_{min}}. \tag{6.22}$$

The bandwidth and the antenna quality factor are linked with each other by equation 4.43

$$B_{\%} = \frac{1}{Q}.$$

Meanwhile, the thin linear dipole antenna can be modeled as a series LC circuit up to the first resonance with the quality factor

$$Q = \frac{1}{R'}\sqrt{\frac{L'}{C'}}.$$

Therefore, in order to increase the bandwidth $B_{\%}$, one should lower the Q factor, i.e., decrease the distributed inductance L' and increase the distributed capacitance C'. This can be done by increasing the diameter d of the dipole antenna. Practical implementations either use tubes or paralleled wires to increase the antenna diameter (Fig. 6.6). Conical caps are used at the input terminals to improve matching to the feed line.

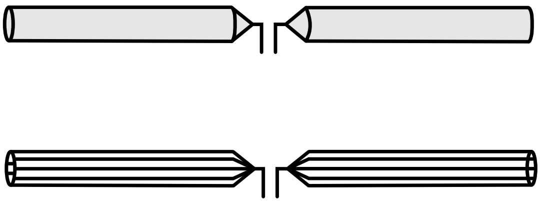

Figure 6.6.: Implementations of cylindrical thick dipole antennas with metal tubes (top) and paralleled wires (bottom)

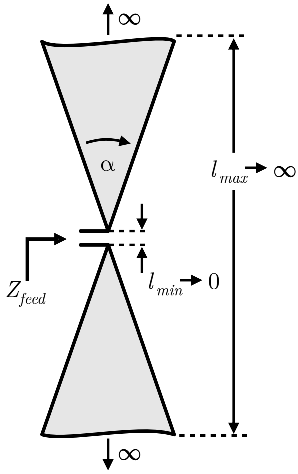

Figure 6.7.: Symmetrical "bow tie" antenna with infinite length

Angle Criterion for Wideband Antennas

The input impedance of an antenna depends on the geometrical shape in relation to the wavelength (for example in case of a thin linear dipole - the height of the radiating elements). Thus, the input impedance should stay constant provided that the geometry scales with the wavelength: the antenna is frequency-independent [72, 75]. Consequently, such an antenna has to be geometrically specified *only* in terms of angles and not in terms of absolute lengths.

Fig. 6.7 shows a so-called "bow tie" antenna. This planar dipole antenna consists of two tapered, conductive shields of infinite length. The symmetrical antenna is fully defined by the angle α. It is assumed that the antenna length is $l_{max} \to \infty$ and the input terminal spacing is $l_{min} \to 0$. With this assumption the antenna is independent of frequency.

The input impedance of the infinitesimally long "bow tie" dipole can be expressed [76] by

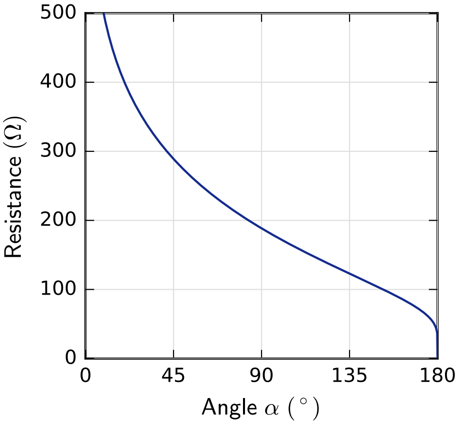

Figure 6.8.: Input resistance of the infinitesimally long “bow tie” dipole as a function of taper angle α

$$Z_{feed} = \frac{Z_0}{2} \frac{K\left(\cos\frac{\alpha}{2}\right)}{K\left(\sin\frac{\alpha}{2}\right)}, \tag{6.23}$$

with $K(x)$ being the complete elliptic integral of the first kind

$$K(x) = \int_0^{\varphi=\pi/2} \frac{d\varphi}{\sqrt{1 - x^2 \sin^2\varphi}}. \tag{6.24}$$

As Fig. 6.8 shows, the input impedance is real, i.e., it is an input resistance. The antenna can be described as an infinitesimally long waveguide, which is independent of frequency. In a real implementation the lower frequency limit f_{min} is usually limited by the maximum antenna length l_{max} being approximately half the wavelength λ_0 [72] with

$$f_{min} \gtrsim \frac{\lambda_0}{2} = \frac{c_0}{2 l_{max}}, \tag{6.25}$$

meanwhile the upper frequency limit f_{max} is defined by the input terminal spacing l_{min}. Reflections at the finite antenna distort Z_{feed}. The reader is kindly referred to [72], which offers equations for the finite “bow tie” dipole.

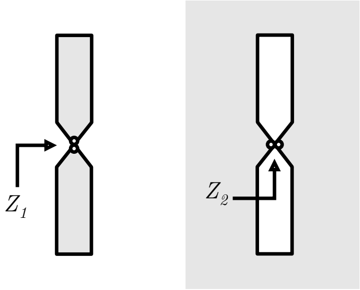

Figure 6.9.: Babinet's principle states that two complementary antennas have the same properties

Babinet's Principle for Wideband Antennas

The Babinet's principle is a theorem from optics. It states that the sum of two fields, which are shielded by two complementary screens, is equal to the field without any screen. The theorem can be transferred into the electro-magnetic world with electric and magnetic screens by

$$E_e + E_m = E_0 \tag{6.26}$$

with E_e and E_m being the fields with electric and magnetic screens and E_0 being the field without a screen. A magnetic screen can be implemented by inverting voltages and currents in a conductive shield, thus designing a complementary shape. Fig. 6.9 shows two complementary antennas with the input impedances Z_1 and Z_2. With Babinet's principle, the planar dipole (Z_1) has the same radiation characteristics as the slot antenna (Z_2). According to [77], the input impedances are related to the intrinsic impedance of the medium Z_0 by

$$Z_1 Z_2 = \left(\frac{Z_0}{2}\right)^2 . \tag{6.27}$$

Consequently, an antenna is a wideband antenna, if its complementary structure is a wideband antenna too.

If the input impedances of the complementary antennas are identical with

$$Z_1 = Z_2 = Z_0/2, \tag{6.28}$$

the so-called Mushiake relationship, and

$$Z_0/2 \approx 188\,\Omega \tag{6.29}$$

in free space, then the antenna is called self-complementary [77]. A self-complementary antenna has a frequency- and shape-independent input impedance. For the symmetrical, planar "bow tie" (Fig. 6.7) this is the case for $\alpha = 90°$ with the input impedance

$$Z_{feed} = Z_0/2. \tag{6.30}$$

[77] presents more implementations of self-complementary structures. For example, the wideband nature of log-periodic antennas is based on self-complementarity.

6.2 Implementation of an "Amplitenna"

6.2.1 Definition

The term "amplitenna" is a made-up word combining the terms "antenna" and "amplifier". Therefore, an "amplitenna" does not only merge the amplifier and the antenna (e.g., on one PCB) from a system perspective, but also combines them on a nonlinear circuit level. This allows parasitic properties of the linear antenna to be absorbed by the nonlinear PA circuit and vice versa.

A typical feature of an "amplitenna" would be either a missing or a very short output transmission line that connects the PA output and the radiating antenna elements (compare Fig. 6.1).

6.2.2 Implementation and Antenna Design

The antenna type implemented in this work is a symmetrical, differential "bow tie" antenna, which has been presented earlier in Section 6.1.3. The wideband nature of this antenna implementation does not only increase the bandwidth of the whole "amplitenna" (taking advantage of the wideband CMCD PA), but also enables a robust, first pass design.

Fig. 6.10 shows the implemented antenna. The two radiating elements are positioned on opposite sides of the PCB. The definition of the angle α enables a compact, rectangular design of the board. The antenna input terminals are w_f wide and b_f long. A d long feed line is used to connect the transistors to the antenna input. The feed line reduces coupling of the antenna to the amplifier board, by raising the common mode impedance at the transistor reference plane. Just like in the CMCD demonstrators in Section 5.3, the feed line is also used to implement the lumped element output filter of the CMCD PA.

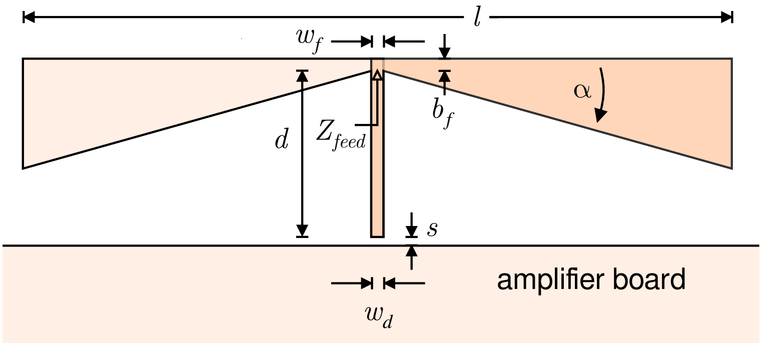

Figure 6.10.: Symmetrical, differential "bow tie" antenna

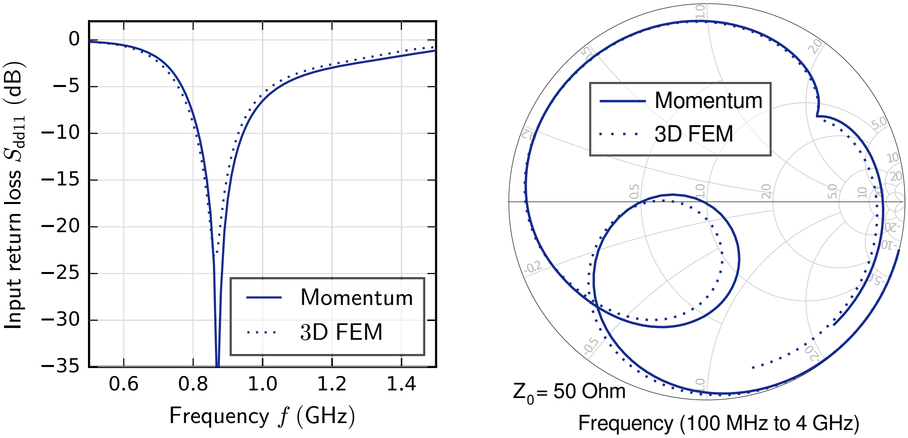

Figure 6.11.: Simulation of the antenna input impedance in differential mode with *Keysight's* ADS Momentum and ADS 3D FEM in comparison

Fig. 6.11 depicts a simulation of the antenna input impedance based on the following geometric properties: $l = 129\,\mathrm{mm}$, $\alpha = 17°$, $w_f = 2.6\,\mathrm{mm}$, $b_f = 2.3\,\mathrm{mm}$, $d = 21.4\,\mathrm{mm}$, $w_d = 1.25\,\mathrm{mm}$ and $s = 0.2\,\mathrm{mm}$. The simulation is done using *Keysight's* ADS Momentum and is verified with the ADS 3D Finite Element Method (FEM) EM simulator. With ADS Momentum the antenna simulation and the large-signal PA simulation can be combined. This simplifies the design and enables optimization.

Finally, Fig. 6.12 shows the input impedance in differential mode and in common mode. The antenna is matched to the load impedance of the CMCD PA $Z_L = 50\,\Omega$ at 870 MHz. The third harmonic in differential mode is relatively high-impedance and has to be lowered, for instance, by a lumped element output filter

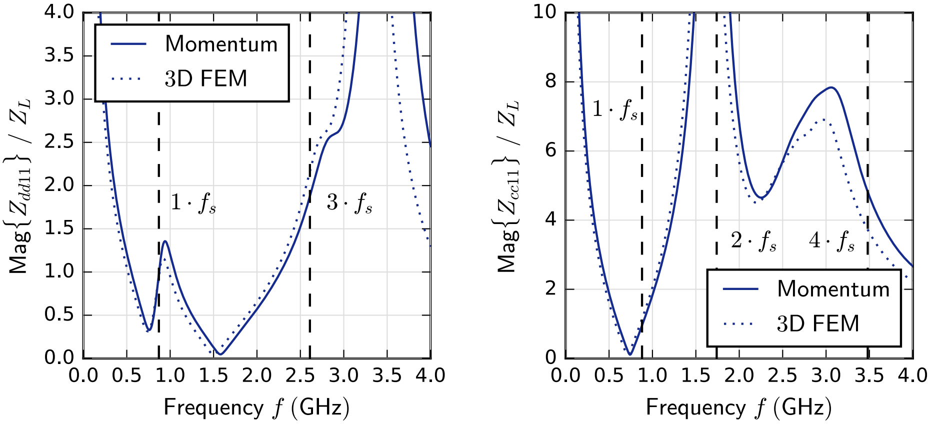

Figure 6.12.: Differential (Z_{dd11}) and common mode (Z_{cc11}) input impedance of the "bow tie" antenna as a function of frequency simulated with ADS Momentum and ADS 3D FEM

to provide a harmonic short (see Table 4.1). In common mode two even harmonics are high-impedance. The fundamental impedance is $\text{Mag}\{Z_{cc11}(1)\} \approx Z_L$, which according to Fig. 4.6 corresponds to an efficiency of 80%. However, the simulated efficiency is higher due to the highly reactive nature of Z_{cc11}.

The bandwidth of the antenna is not very large due to the small angle of the "bow tie" ($\alpha = 17°$), which, according to Babinet's principle for wideband antennas (see Section 6.1.3), should be in the range of 90°. However, compared to an "ideal" dipole, the bandwidth is increased (visible by the loop in the Smith chart in Fig. 6.11). This enables a robust design of an "amplitenna" demonstrator.

6.2.3 "Amplitenna" Demonstrator

A low-power "amplitenna" demonstrator is designed based on the CMCD wideband core in Section 5.3 and Fig. 5.24. The large-signal simulation is done with *Keysight's* ADS using an S-parameter based EM model of the antenna. To calculate the RF parameters of the "amplitenna", the radiated output power P_{rad} has to be determined. The radiated output power is equal to the output power of the PA P_{out} minus the loss power of the antenna:

$$P_{rad} = P_{out} - P_{loss}. \tag{6.31}$$

Unfortunately it is not possible to access the radiated power in the HB circuit simulation of ADS. Therefore, the RF output power P_{out} has to be calculated

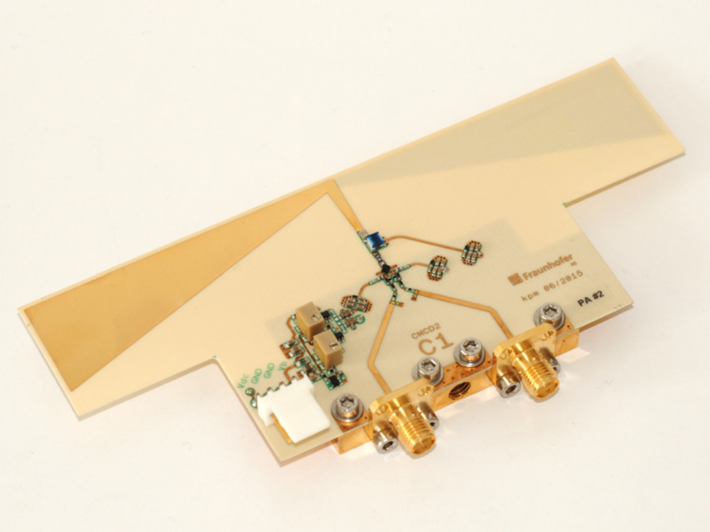

Figure 6.13.: Picture of the implemented "amplitenna" (CMCD PA C1)

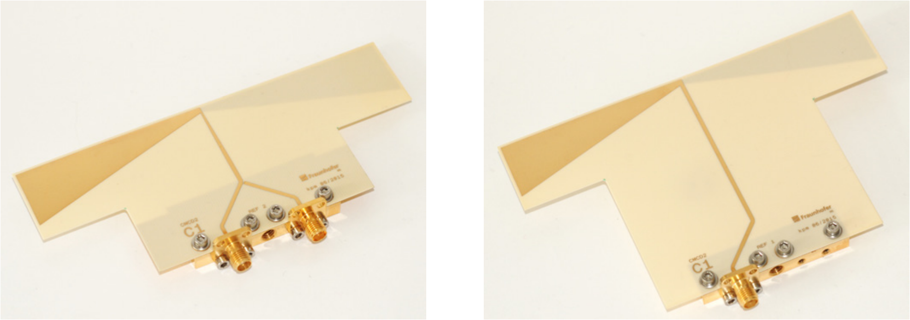

Figure 6.14.: Pictures of the CMCD C1 reference antennas with differential (left) and single-ended inputs (right)

from the voltage and current waveforms at the PA-antenna interface and losses at the antenna are included with the radiation efficiency η_{rad} from 6.19.

$$P_{rad} = P_{out} \cdot \eta_{rad} \tag{6.32}$$

The simulated radiation efficiency of the implemented "bow tie" antenna (see Fig. 6.10) is $\eta_{rad} = 97.9\%$ at $f = 870\,\text{MHz}$.

Fig. 6.13 shows a photo of the implemented "amplitenna" (CMCD PA C1). For calibration purposes two reference antennas with differential and single-ended SMA flange connector inputs are designed (Fig. 6.14).

6.3 OTA Efficiency Measurement

In order to fully characterize the implemented "amplitenna", the radiated power P_{rad} has to be determined to calculate the efficiency by

$$\eta = \frac{P_{rad}}{P_{DC}} \qquad\qquad \text{PAE} = \frac{P_{rad} - P_{in}}{P_{DC}}. \tag{6.33}$$

This section presents an over-the-air (OTA) measurement in an anechoic chamber, in order to quantify the radiated power P_{rad}.

6.3.1 Measurement Setup

An antenna commonly distributes power in a non-uniform way in all three dimensions. This distribution of power is described by the radiation pattern of the antenna in terms of spherical coordinate angles ϑ and φ. Several methods exist for determining the radiated power P_{rad} of an antenna, namely:

1. Absolute measurement of P_{rad} by a spherical integration of the power density,
2. relative measurement of the "amplitenna" gain with a passive reference antenna and calculation of P_{rad},
3. absolute measurement of maximum power density and calculation of P_{rad} with the directivity D from a simulation.

To measure the absolute radiation power P_{rad} of an antenna, the Poynting vector $\mathbf{S}$ has to be integrated at the spherical surface element $d\mathbf{A}$:

$$\boxed{P_{rad} = \text{Re}\left\{ \oiint_{A} \mathbf{S} \cdot d\mathbf{A} \right\} = \int_{\varphi=0}^{2\pi} \int_{\vartheta=0}^{\pi} S_r\left(\vartheta, \varphi\right) r^2 \sin\vartheta d\vartheta d\varphi}.$$

$S_r\left(\vartheta, \varphi\right)$ is the angle-dependent power density, which is evaluated at a distance r.

This absolute measurement method does not require a calibration with reference antennas or inclusion of simulation data. Measurement inaccuracies arise from the fact that parts of the antenna will be shadowed by the antenna mount during measurement, which is illustrated in Fig. 6.15. The method in question will therefore predict a lower bound for the radiation power and the PA efficiency. In opposition to anechoic chambers, electromagnetic reverberation chambers

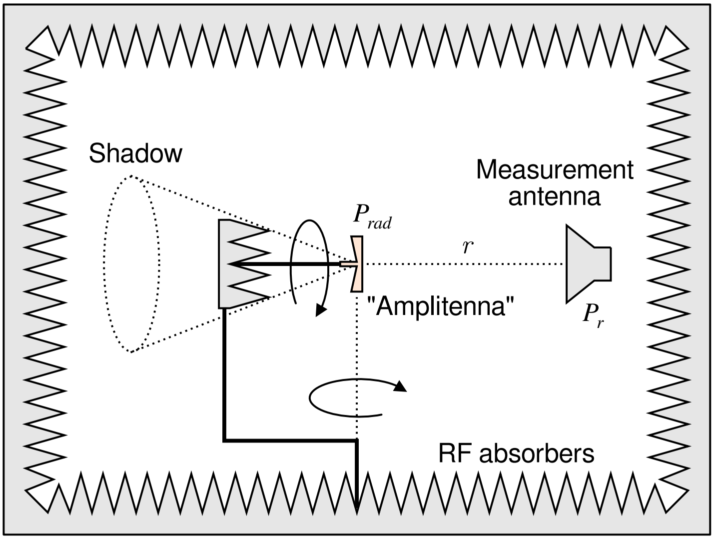

Figure 6.15.: Measurement setup in an anechoic chamber

can be used [78] to measure the radiated power P_{rad} of a DUT. The reflective surface of an electromagnetic reverberation chamber and the usage of a mechanical “mode stirrer” eliminates shadowed areas. Electromagnetic reverberation chambers are often used in electromagnetic compatibility (EMC) measurements to determine the absolute interference power of a DUT.

A relative measurement of the “amplitenna” gain G can be used to determine P_{rad} by

$$P_{rad} = G \cdot P_{in} = G \cdot (P_{in1} + P_{in2}), \qquad (6.34)$$

with the known input power P_{in}.

The received power at a randomly positioned measurement antenna $P_{r,PA}$ is

$$P_{r,PA} = P_{rad} \cdot A = G \cdot P_{in} \cdot A, \qquad (6.35)$$

with A the path loss due to the distance to and the radiation pattern of the DUT.

A second measurement determines the received power $P_{r,ref}$ with a geometrically identical reference antenna (Fig. 6.14, left) instead of the DUT. The gain of this passive reference antenna is $G = 1$:

$$P_{r,ref} = P_{rad} \cdot A = P_{in} \cdot A. \qquad (6.36)$$

This said, G of the DUT can be calculated by

$$\begin{aligned}\frac{P_{r,PA}}{P_{r,ref}} &= \frac{G \cdot P_{in} \cdot A}{P_{in} \cdot A}, \\ G &= \frac{P_{r,PA}}{P_{r,ref}}. \end{aligned} \tag{6.37}$$

P_{rad} is then

$$\boxed{P_{rad} = \frac{P_{r,PA}}{P_{r,ref}} \cdot P_{in}}. \tag{6.38}$$

This method does not require an elaborate integration of the angle-dependent power density. However, the reference antenna has to have the same radiation pattern as the "amplitenna". Additional measurement inaccuracies arise from positioning errors of reference antenna and DUT and from losses in the feed lines of the reference antenna.

Finally, a method is presented which uses simulation data to determine P_{rad}. The power can be calculated with an absolute measurement of maximum power density and the directivity D of the antenna acquired from a simulation.

The directivity D of an antenna is a measure used to define this power distribution and is given in [72] as a function of power density $S_r(\vartheta, \varphi)$ by

$$D = \frac{\text{maximum power density}}{\text{mean power density}} = \frac{(S_r(\vartheta, \varphi))_{max}}{\langle S_r(\vartheta, \varphi)\rangle}. \tag{6.39}$$

The mean power density $\langle S_r(\vartheta, \varphi)\rangle$ is equal to the power density of a sphere and is independent of ϑ and φ. It corresponds to the magnitude of the Poynting vector $\mathbf{S}$ with

$$\langle S_r(\vartheta, \varphi)\rangle = S_r. \tag{6.40}$$

As shown in 6.9, the radiation power P_{rad} can be calculated from the Poynting vector by integrating the spherical surface element $d\mathbf{A}$:

$$\begin{aligned} P_{rad} &= \mathrm{Re}\left\{ \oint\!\!\!\oint_A \mathbf{S} \cdot d\mathbf{A} \right\} = \int_{\varphi=0}^{2\pi} \int_{\vartheta=0}^{\pi} S_r r^2 \sin\vartheta d\vartheta d\varphi, \\ &= 4\pi r^2 S_r. \end{aligned} \tag{6.41}$$

The radiation power can then be given as a function of directivity D, distance r and maximum power density with

$$\boxed{P_{rad} = 4\pi r^2 \frac{(S_r(\vartheta, \varphi))_{max}}{D}}. \tag{6.42}$$

The maximum power density has to be found by positioning the DUT in an anechoic chamber. The directivity can be easily acquired from simulation. Partial shadowing of the antenna is allowed as long as the electrical boresight is not masked. However, simulation inaccuracies can distort the result.

Table 6.2 on the following page sums up the three over-the-air measurement methods.

Table 6.2.: Summary of over-the-air P_{rad} measurement methods

Method	Input quantities	Evaluation
1: Absolute measurement of P_{rad} by spherical integration	• Measured angle-dependent power density $S_r(\vartheta, \varphi)$ • Measured distance r	⊕ No calibration required ⊕ Direct measurement of absolute power ⊖ Power error due to shadowing by the antenna mount ⊖ Long, time-consuming measurement
2: Relative gain measurement with reference antenna	• Measured power with reference antenna $P_{r,ref}$ • Measured power with "amplitenna" $P_{r,PA}$	⊕ Quick measurement ⊖ Reference antenna required ⊖ Potential positioning errors
3: Simulation of directivity and measurement of maximum power density	• Measured maximum power density $(S_r(\vartheta, \varphi))_{max}$ • Measured distance r • Simulated directivity D	⊕ Quick measurement ⊖ Simulation data required

6.3.2 Measurement Results

Relative Gain Measurement (Method 2)

Due to the difficulties of an absolute P_{rad} measurement (time-consuming, shadowing error), only the second method of Table 6.2 (relative measurement of the “amplitenna” gain with a reference antenna) is used. The third method (absolute measurement of maximum power density and calculation of P_{rad} with the directivity D) is applied additionally to verify the measurement.

Fig. 6.16 depicts the “amplitenna” measurement setup in an anechoic chamber. A *R&S* ZVA40 vector network analyzer is used as signal generator and as a measurement receiver. The differential input signal is generated with a balun ZFSCJ-2-4-S+ from *Minicircuits*. The input powers P_{in1} and P_{in2} are calibrated using a power meter *R&S* NRP-Z22. Attenuators at the input are used to reduce matching errors. The supply voltages V_{DC} (DC voltage) and V_{bias} (bias voltage) are provided by a *Keysight* N6705B DC power analyzer, which accurately measures the DC input power P_{DC}. P_{DC} excludes the ohmic losses of the supply cables.

Fig 6.17 shows photos of the “amplitenna” in the anechoic chamber at *Fraunhofer IIS.*

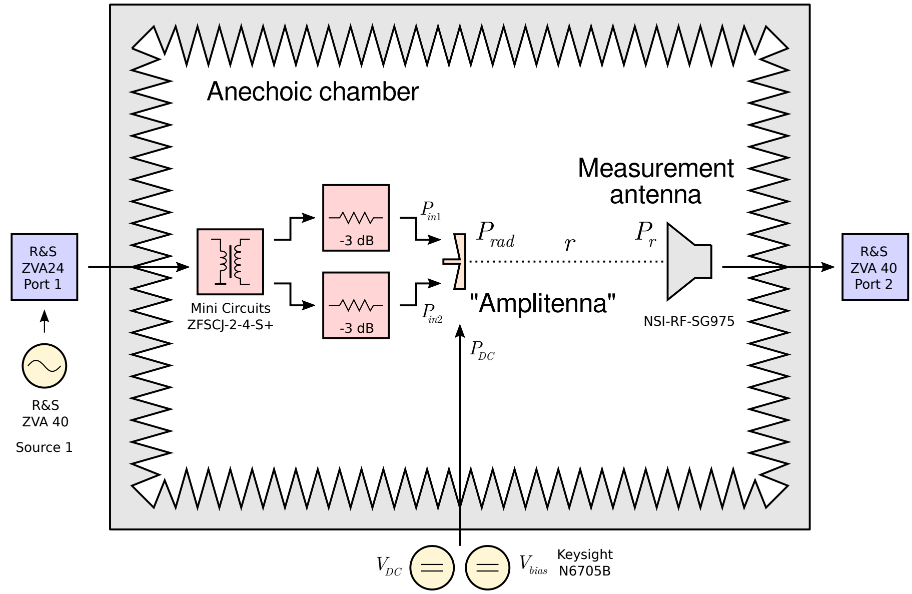

Figure 6.16.: “Amplitenna” measurement setup in an anechoic chamber

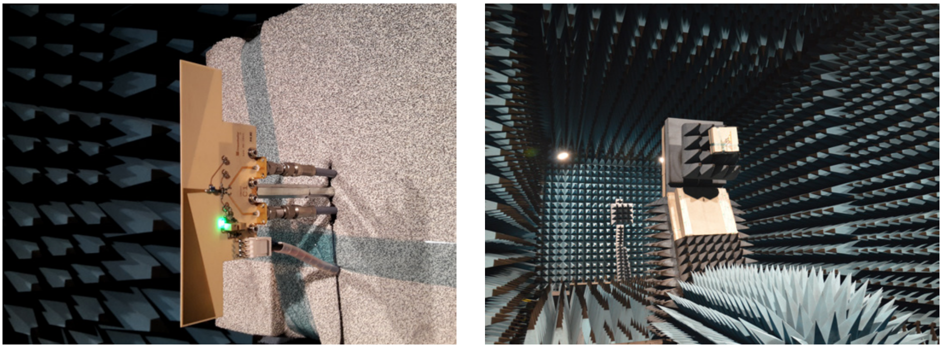

Figure 6.17.: Photos of the “amplitenna” in the anechoic chamber at *Fraunhofer IIS*

The relative gain measurement (method 2 of Table 6.2) is done with the reference antenna in Fig. 6.14 (left), which has a differential input and is geometrically identical to the “amplitenna”.

Instead of the absolute power $P_{r,ref}$, the forward gain $S_{21,ref}$ is measured. It includes all the cable losses and avoids matching errors at the antenna input. Afterwards, the input powers P_{in1} and P_{in2} are calibrated with the power meter. The difference due to the balun imbalance is 0.1 dB, which is acceptable.

At $f = 870\,\mathrm{MHz}$ the forward gain of the reference antenna is $S_{21,ref} = -48.11\,\mathrm{dB}$. With $P_{in} = P_{in1} + P_{in2} = 6.3\,\mathrm{dBm} = 4.3\,\mathrm{mW}$, the forward gain of the “amplitenna” is $S_{21,PA} = -36.13\,\mathrm{dB}$. P_{rad} is then

$$P_{rad} = 10^{0.1\cdot\left(S_{21,PA}-S_{21,ref}\right)} \cdot P_{in} = 67.8\,\mathrm{mW}. \tag{6.43}$$

The measured DC power is $P_{DC} = 86\,\mathrm{mW}$ and the efficiency is, therefore,

$$\eta = \frac{P_{rad}}{P_{DC}} = 78.8\%. \tag{6.44}$$

Power Density Measurement (Method 3)

To verify the previous measurements, method 3 of Table 6.2 is used. To accurately determine the directivity in simulation, the FEM simulator of *Keysight’s* ADS is used. The absorbers of the antenna mount (Fig. 6.17) are included in the simulation. Unfortunately the maximum directivity of the simulated “amplitenna” is at the back ($\varphi = 270°$, Fig. 6.18), which is inaccessible due to the antenna mount. Therefore, the second local directivity maximum at $\varphi = 90°$ with $D = 1.087\,\mathrm{dBi}$ is used.

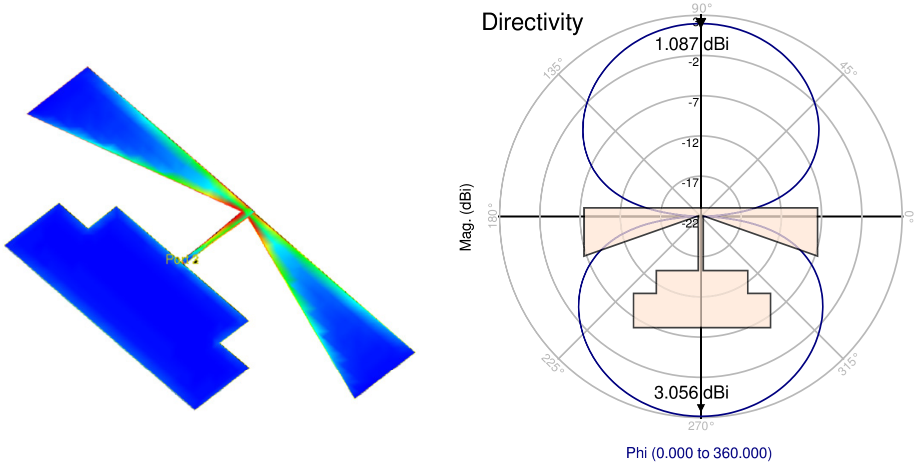

Figure 6.18.: ADS Momentum far field simulation of the implemented antenna

The distance between measurement antenna and DUT is acquired with a *Leica* "DISTO plus laser rangefinder" and is $r = 3.194\,\mathrm{m}$. The maximum power density $(S_r(\vartheta,\varphi))_{max}$ at the measurement antenna is calculated from the power P_r. P_r is directly measured at the *NSI* RF-SG975 standard gain horn with a power meter *R&S* NRP-Z22 after repositioning the antenna to the maximum power. With $P_r = -9.53\,\mathrm{dBm}$ and with the measurement antenna gain at 870 MHz (13.3 dB) the maximum power density is [72]

$$(S_r(\vartheta,\varphi))_{max} = P_r \cdot \frac{4\pi}{\lambda_0^2} \cdot \frac{1}{\text{measurement antenna gain}} = 0.551\,\frac{\mathrm{mW}}{\mathrm{m}^2}. \quad (6.45)$$

With equation 6.42 the radiation power P_{rad} can be calculated by

$$\begin{aligned} P_{rad} &= 4\pi r^2 \frac{(S_r(\vartheta,\varphi))_{max}}{D} \\ &= 4\pi \cdot (3.194\,\mathrm{m})^2 \frac{0.551\,\frac{\mathrm{mW}}{\mathrm{m}^2}}{10^{(0.1\cdot 1.087\,\mathrm{dBi})}} = 55.0\,\mathrm{mW} = 17.4\,\mathrm{dBm}. \end{aligned} \quad (6.46)$$

The input power used in this measurement was $P_{in} = 6.3\,\mathrm{dBm}$. The expected radiated power at this point (relative gain, method 2) is $P_{rad} = 67.8\,\mathrm{mW} = 18.3\,\mathrm{dBm}$.

Summary and Evaluation of the Measurements

Fig. 6.19 (left) shows the measurement of the "amplitenna" as a function of input power at 870 MHz. The results of both measurement methods are depicted. On the right side, the simulation results are plotted for comparison. As Section 6.2.3 suggests, the radiated output power is calculated from the voltage and current waveforms at the PA-antenna interface and the radiation efficiency $\eta_{rad} = 97.9\%$ of the antenna.

The difference between the results of method 3 ($P_{rad} = 17.4\,\mathrm{dBm}$) and 2 ($P_{rad} = 18.3\,\mathrm{dBm}$) is 0.9 dB.

Method 3 is a lower bound measurement, because the absolute value of power density is lowered by

- additional connector losses at the measurement antenna,
- mechanical adjustment errors
- and the linear polarization of the measurement antenna.

The absolute accuracy of the *R&S* NRP-Z22 power sensor is 0.085 dB [59] and includes connector mismatch losses. The measured power level is stable within ±5° of mechanical readjustment. The cross-polarized power is 30 dB below the measured linear level. However, the gain of the *NSI* RF-SG975 standard gain horn is only specified with ±0.5 dB [79].

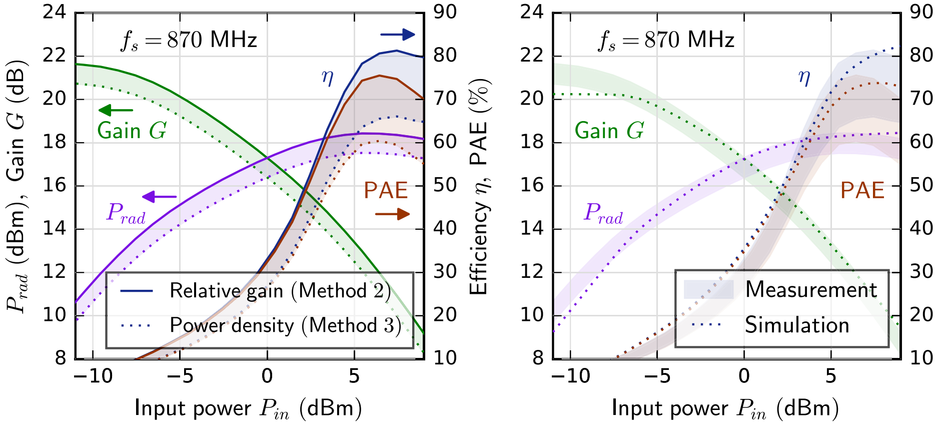

Figure 6.19.: Measurement of the "amplitenna" (CMCD PA C1): Radiated output power, gain and efficiency as a function of input power at $f_s = 870\,\mathrm{MHz}$. The results of the relative gain measurement (method 2) and the power density measurement (method 3) are depicted. The ADS simulation is plotted for comparison.

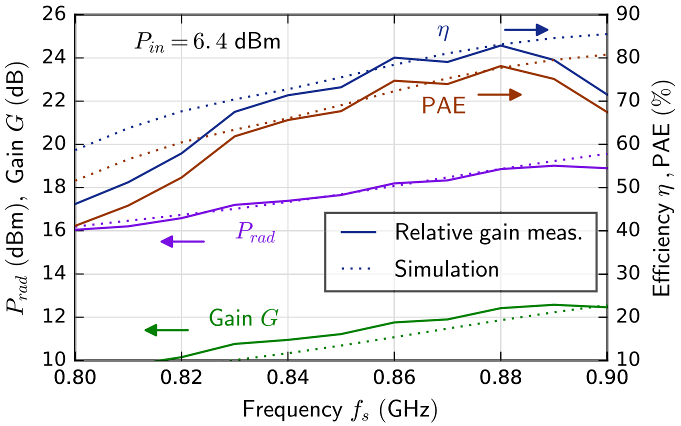

Figure 6.20.: Measurement of the "amplitenna" (CMCD PA C1): Radiated output power, gain and efficiency as a function of frequency at $P_{in} = 6.3$ dBm. The ADS simulation is plotted for comparison.

Method 2 is an upper bound measurement, because the relative gain is raised by the mismatch of reference antenna.

Even though S-parameters are measured, the 3 dB attenuators at the input "hide" the reflected power. Within ±30 MHz the simulation predicts an input return loss of $<$-13 dB, that is, the mismatch error should be $<$5% or 0.2 dB. Additional errors potentially appear from the mechanical repositioning while changing the antennas. However, the power density measurement has shown that the gain gradient of the antennas is low enough. Eventually, even though the reference antenna and the "amplitenna" have the same physical dimensions, the directivity in simulation differs by 0.35 dB.

The 0.9 dB difference of the two measurement methods is within the scope of the combined errors from the standard gain horn, the power meter, the reference antenna mismatch and the directivity deviation of the reference antenna.

Unfortunately, it was not possible to perform a wideband frequency sweep because of the mismatch issue. Fig. 6.20 depicts a narrowband frequency sweep of the "amplitenna".

The presented measurements demonstrate a high-efficiency switched mode operation of the PA with a seamlessly integrated differential antenna. It has to be noted that the measurements already include the radiation efficiency (97.9% in simulation) of the antenna. The drain efficiency at the PA interface is therefore 2.1% higher.

7 Conclusions and Outlook

7.1 Conclusions

The design of a fully digital RF power amplifier is a long-cherished wish. Agile and low-cost software-defined radio transmitters can only be implemented, if the digital domain is moved further towards the analog RF interface. This work has achieved important progress towards this goal. The main aim of this work was

- to motivate the use of differential (i.e., push-pull) architectures for switched mode PAs
- and to present solutions for flexible, efficient and wideband switched mode amplifiers.

After an introduction to the bandwidth-enhancing properties of differential PA architectures, the differential current mode class-D (CMCD) switched mode PA concept has been introduced and analyzed. This PA can be designed for bandwidths of up to 100%, in comparison to a single-ended inverse class-F PA (40%) with second and third harmonic output termination.

The switched mode operation of RF transistors was not the main focus of this work. However, an overview of RF transistor technologies, losses in switched mode operation and stability has been given in accordance with the state of the art.

One of the main contributions of this work is the output network analysis of the differential CMCD PA. The ideal harmonic output impedances were calculated in common and differential mode. Usually, the common mode is inherently terminated by the symmetry of the PA. However, the output balun and the output filter distort this symmetry. The imbalance of the output network has been analytically evaluated and the efficiency degradation of a finite common mode impedance has been calculated.

The output filter has to provide a differential short for the odd harmonic frequencies of the switched currents. Two output filter implementations, a band-pass filter (LC resonator) and a low-pass filter, have been calculated and optimized for CMCD PAs. Furthermore, a low parasitic PCB implementation with vertically mounted SMD components has been offered.

The output balun is one of the key components of a differential PA. Its passband defines the bandwidth of the PA and its symmetry and insertion loss have a major influence on the efficiency. To begin with, baluns have been subdivided into two functional principles, delay line baluns and coupled line baluns. While delay line baluns suffer from the narrowband implementation of technically feasible 180° phase shifters, coupled line baluns can be implemented for high bandwidths. An improved circuit model of a planar coupled line balun has been developed and verified by EM simulations. Furthermore, the bandwidth limits of planar broadside coupled line baluns have been identified. It has been shown, that a simple coupled line balun cannot cover the 100% bandwidth of an ideal CMCD PA. Therefore, an improved tapered balun, which can cover 100% bandwidth, has been developed and analyzed.

Finally, several CMCD demonstrator PAs have been presented. The PAs are all implemented with a tapered coupled line balun. The output filter has been embedded in the balun using vertically mounted SMD components. A low-power (100 mW) PA maintains a drain efficiency of $>70\%$ and a power-added efficiency (PAE) of $>67\%$ for an octave bandwidth (500 MHz to 1 GHz, 68% bandwidth). The peak drain efficiency is about 78%, the peak PAE is 75%. The drain efficiency is over 60% for a range of 415 MHz to 1100 MHz, which corresponds to a bandwidth of 90%. Compared to a single-ended wideband class-F PA ([16], 51% bandwidth at 70% drain efficiency), this differential class-D PA maintains high efficiency over a higher bandwidth (68% bandwidth at 70% drain efficiency). This is only possible with a defined harmonic impedance space and it underlines the potentials of differential switched mode power amplifiers. Table 5.2 in Section 5.3 gives a detailed overview of state-of-the-art single-ended and differential PAs.

To verify the proposed design methods for CMCD PAs at high powers a 25 W demonstrator PA is presented. The measured peak drain efficiency of this PA is about 80% and the peak PAE is 72% at 635 MHz. For an output power range of 7 W to 25 W the PA maintains high efficiency. Therefore, this amplifier could be used, e.g., as the core PA of an EER amplifier system.

In many RF power amplifier applications, the RF signal is amplified and afterwards transmitted by an antenna. Quite a few antennas are implemented as a differential load and baluns are needed to connect the PA and the antenna with a 50 Ω single-ended RF transmission line. The use of an antenna as a differential load allows to drop the balun and simplifies the PA-antenna interface.

Therefore, several wideband antenna implementations have been offered in this work and an antenna integrated amplifier, the so-called “amplitenna”, has been designed. This 100 mW prototype has then been measured over-the-air in an anechoic chamber. The radiated output power has been assessed by a measurement of the relative gain with a passive reference antenna and, for reference, by an absolute measurement of the power density. The two measurements differ in 0.9 dB, which is within the accuracy of the setup. A comparison shows that the relative gain measurement will give an upper bound for the radiated power, whereas the absolute power measurement outputs a lower bound. The peak efficiency is within a range of 67% to 81% at 870 MHz.

Most PA designs are characterized and compared with ideal, wideband 50 Ω loads. In this work, the effective radiated power of an "amplitenna" has been quantified. The measured efficiency includes the radiation efficiency (97.9%) of the antenna. The presented measurements demonstrate a high-efficiency switched mode operation of the PA with a seamlessly integrated differential antenna.

The findings of this thesis can help the PA designer to better understand the operating principle of harmonically terminated differential PAs. The design techniques proposed in this work can assist engineers in building PAs with improved performance, such as enhanced efficiency and bandwidth.

7.2 Outlook

A complete examination of the topic is beyond the scope of this work and further research is needed.

Miniaturization of the balun at higher frequencies: At an operating frequency of about 500 MHz, the planar tapered coupled line balun designed in this work needs about 20 cm^2 of PCB area. This is quite small for a high-power PA. However, future wideband telecommunication systems (e.g., 5G) use a network of denser base stations at higher frequencies and lower RF powers. Fortunately, the presented coupled line baluns scale down with frequency. It would be interesting to design a hybrid or an integrated balun for high frequencies, for example, at X-band.

Miniaturization of the balun at lower frequencies: At frequencies below a few hundred megahertz the balun becomes very large. The common mode impedance of the balun can be raised with magnetic materials in much the same way as a common mode choke. Future work could investigate different magnetic materials and core designs to optimize the low frequency response.

Balun with impedance transformer: The application of the tapered balun as an impedance transformer for, for instance, low-resistance high-power transistors has been shown. However, a practical demo is required to verify the simulation.

Advanced filters with vertical SMDs: Vertically PCB-embedded SMD components enable the design of low parasitic filters. It would be interesting to apply this technique for designs, which require a high stopband attenuation, for example, superhet receivers.

Wideband high-power PA: A 25 W push-pull PA with a planar tapered balun has been designed in this work to verify the harmonic termination of the output network at a high power. This prototype has not been optimized for a wide bandwidth with a low-pass output filter so far.

Linear and wideband amplification: This work has focused on high-efficiency switched mode operation and PA linearity was not covered within the scope of the research. However, all presented PAs can be operated in a linear region at reduced efficiency. The 25 W prototype has a high efficiency for a wide range of supply voltages and could be used in an EER amplifier system. Advanced pre-distortion concepts could take advantage of the separate input ports to further improve the bandwidth and the linearity. A hybrid PA system with a CMCD core PA, a supply voltage modulator (for EER) and a digital pre-distorter would allow efficient, linear PA operation across a large bandwidth.

To sum up, this thesis can be used as a starting point for further research in order to design advanced amplifier systems to progress towards a fully digital RF power amplifier.

A Appendix

A.1 Keysight ADS AEL Scripts

To verify the accuracy of the proposed balun circuit models and to simulate the tapered transitions an electro-magnetic (EM) simulator (*Keysight* ADS Momentum) is used in this work. The baluns are designed using the *Keysight* application extension language (AEL) and the code is depicted below.

AEL Script of the Broadside Coupled Differential Line

```
// Measurement of odd and even mode impedances of a
// broadside coupled differential (top-bottom) line

// L:  Length of the line
// W1: Width of the top line
// W2: Width of the bottom line
// W3: Bottom line to ground separation

defun diff_line_art(L, W1,W2,W3)
{
  de_set_global_db_factor(); // Sets the simulator
                // units to layout user unit
                // conversion factor used during
                // rendering of AEL artwork objects.
  de_set_layer(1);

  de_draw_port(0, 0, -90.0); // Input top
  de_draw_port(L, 0, 90.0);  // Output top

  de_add_polygon();
    de_add_point(0,(W1)/2*1000);
    de_add_point(0,(-W1)/2*1000);
    de_add_point(L*1000,(-W1)/2*1000);
    de_add_point(L*1000,(W1)/2*1000);
  de_end();
```

```
// Alternative to polygon:
// de_add_rectangle(0,(W1)/2*1000,L*1000,
//                  (-W1)/2*1000);
de_set_layer(2);

de_draw_port(0, 0, -90.0); // Input bottom
de_draw_port(L, 0, 90.0);  // Output bottom

// all ports for ground on bottom side:
de_draw_port(0, ((W2/2)+W3), -90.0);
de_draw_port(0, ((-W2/2)-W3), -90.0);
de_draw_port(L/4, ((W2/2)+W3), -90.0);
de_draw_port(L/4, ((-W2/2)-W3), -90.0);
de_draw_port(L/2, ((W2/2)+W3), -90.0);
de_draw_port(L/2, ((-W2/2)-W3), -90.0);
de_draw_port(3*L/4, ((W2/2)+W3), -90.0);
de_draw_port(3*L/4, ((-W2/2)-W3), -90.0);
de_draw_port(L, ((W2/2)+W3), 90.0);
de_draw_port(L, ((-W2/2)-W3), 90.0);

de_add_polygon();
  de_add_point(0,(W2)/2*1000);
  de_add_point(0,(-W2)/2*1000);
  de_add_point(L*1000,(-W2)/2*1000);
  de_add_point(L*1000,(W2)/2*1000);
de_end();

de_add_polygon();
  de_add_point(0,(W2/2+W3)*1000);
  de_add_point(0,20);
  de_add_point(L*1000,20);
  de_add_point(L*1000,((W2/2)+W3)*1000);
de_end();

de_add_polygon();
  de_add_point(0,(-W2/2-W3)*1000);
  de_add_point(0,-20);
  de_add_point(L*1000,-20);
  de_add_point(L*1000,((-W2/2)-W3)*1000);
```

```
  de_end();
}
```

AEL Script of the Broadside Coupled Differential Two Stepped Line

```
// Measurement of odd and even mode impedances
// of a broadside coupled differential (top-bottom)
// two stepped line

// L:  Length of the line
// W1: Width of the first top line
// W2: Width of the first bottom line
// W12: Width of the second top line
// W22: Width of the second bottom line
// W3: Bottom line to ground separation

defun diff_line_step_art(L, W1,W2,W3,W12,W22)
{
  de_set_global_db_factor(); // Sets the simulator
                // units to layout user unit
                // conversion factor used during
                // rendering of AEL artwork objects.
  de_set_layer(1);

  de_draw_port(0, 0, -90.0); // Input top
  de_draw_port(L, 0, 90.0);  // Output top

  de_add_polygon();
    de_add_point(0,(W1)/2*1000);
    de_add_point(0,(-W1)/2*1000);
    de_add_point((L*1000)/2,(-W1)/2*1000);
    de_add_point((L*1000)/2,(W1)/2*1000);
  de_end();

  de_add_polygon();
    de_add_point((L*1000)/2,(-W12)/2*1000);
    de_add_point((L*1000)/2,(W12)/2*1000);
    de_add_point((L*1000),(W12)/2*1000);
   de_add_point((L*1000),(-W12)/2*1000);
```

```
de_end();

de_set_layer(2);

de_draw_port(0, 0, -90.0); // Input bottom
de_draw_port(L, 0, 90.0);  // Output bottom

// all ports for ground on bottom side:
de_draw_port(0, ((W2/2)+W3), -90.0);
de_draw_port(0, ((-W2/2)-W3), -90.0);
de_draw_port(L/4, ((W2/2)+W3), -90.0);
de_draw_port(L/4, ((-W2/2)-W3), -90.0);
de_draw_port(L/2, ((W2/2)+W3), -90.0);
de_draw_port(L/2, ((-W2/2)-W3), -90.0);
de_draw_port(3*L/4, ((W2/2)+W3), -90.0);
de_draw_port(3*L/4, ((-W2/2)-W3), -90.0);
de_draw_port(L, ((W2/2)+W3), 90.0);
de_draw_port(L, ((-W2/2)-W3), 90.0);

de_add_polygon();
  de_add_point(0,(W2)/2*1000);
  de_add_point(0,(-W2)/2*1000);
  de_add_point((L*1000)/2,(-W2)/2*1000);
  de_add_point((L*1000)/2,(W2)/2*1000);
de_end();

de_add_polygon();
  de_add_point((L*1000)/2,(-W22)/2*1000);
  de_add_point((L*1000)/2,(W22)/2*1000);
  de_add_point(L*1000,(W22)/2*1000);
  de_add_point(L*1000,(-W22)/2*1000);
de_end();

de_add_polygon();
  de_add_point(0,(W2/2+W3)*1000);
  de_add_point(0,20);
  de_add_point(L*1000,20);
  de_add_point(L*1000,((W2/2)+W3)*1000);
de_end();
```

```
    de_add_polygon();
      de_add_point(0,(-W2/2-W3)*1000);
      de_add_point(0,-20);
      de_add_point(L*1000,-20);
      de_add_point(L*1000,((-W2/2)-W3)*1000);
    de_end();
  }
```

AEL Script of the Linear Coupled Line Balun

```
// Linear coupled line balun for a CMCD
// power amplifier

// L:  Length of the taper
// W1 = Ws: Width of the microstrip top output line
// W2 = Wd: Width of the differential top and bottom
//          input lines
// W3 = Wb: Width of the entire balun
// D:  Linear differential line offset at the input
// S:  Slot width at the input

defun Taper_art_line_3port(L, W1,W2,W3, D, S)
{
  de_set_global_db_factor();
  de_set_layer(1);

  de_draw_port(-D+0.0001, W3/2, -90.0); // simulator
                                         // units
  de_draw_port(L-0.0001+0.004, W3/2, 90.0);

  de_add_polygon();
    de_add_point(0,(W3-W2)/2*1000); // user units
    de_add_point(0,(W3+W2)/2*1000);
    de_add_point(L*1000,(W3+W1)/2*1000);
    de_add_point(L*1000,(W3-W1)/2*1000);
  de_end();

  de_add_rectangle(-D*1000,(W3-W2)/2*1000, 0,
```

```
                    (W3+W2)/2*1000);
                    // diff port top
  de_add_rectangle(L*1000,(W3-W1)/2*1000,
                    L*1000+4,(W3+W1)/2*1000);
                    // small area at the output
  de_set_layer(2);

  de_draw_port(-D+0.0001, W3/2, -90.0);
  de_draw_port(L-0.0001+0.004, W3/2, 90.0);
  de_draw_port(-D-S-0.0001, W3/2, 90.0);
  de_draw_port(-D-S-0.0001, W3/2, 90.0);

  de_add_polygon();
    de_add_point(0,(W3-W2)/2*1000);
    de_add_point(0,(W3+W2)/2*1000);
    de_add_point(L*1000,(W3+W1)/2*1000);
    de_add_point(L*1000,(W3-W1)/2*1000);
  de_end();

  de_add_rectangle(-D*1000,(W3-W2)/2*1000, 0,
                    (W3+W2)/2*1000);
                    // diff port bottom
  de_add_rectangle((-D-S)*1000,0, L*1000,4);
                    // small area top
  de_add_rectangle((-D-S)*1000,W3*1000-4,
                    L*1000,W3*1000);
                    // small area bottom
  de_add_rectangle(-40,0, (-D-S)*1000,W3*1000);
                    // big area at the input
  de_add_rectangle(L*1000,0, L*1000+4,W3*1000);
                    // small area at the output
}
```

AEL Script of the Linear Tapered Coupled Line Balun

```
// Linear tapered coupled line balun for a CMCD
// power amplifier

// L:  Length of the taper
```

```
// W1 = Ws: Width of the microstrip top output line
// W2 = Wd: Width of the differential top and bottom
//          input lines
// W3 = Wb: Width of the entire balun
// D:  Linear differential line offset at the input
// S:  Slot width at the input

defun Taper_art_3port_v2(L, W1,W2,W3, D, S)
{
  de_set_global_db_factor();
  de_set_layer(1);

  de_draw_port(-D+0.0001, W3/2, -90.0); // simulator
                                         // units
  de_draw_port(L-0.0001+0.004, W3/2, 90.0);

  de_add_polygon();
    de_add_point(0,(W3-W2)/2*1000); // user units
    de_add_point(0,(W3+W2)/2*1000);
    de_add_point(L*1000,(W3+W1)/2*1000);
    de_add_point(L*1000,(W3-W1)/2*1000);
  de_end();

  de_add_rectangle(-D*1000,(W3-W2)/2*1000, 0,
                   (W3+W2)/2*1000);
                   // diff port top
  de_add_rectangle(L*1000,(W3-W1)/2*1000,
                   L*1000+4,(W3+W1)/2*1000);
                   // small area at the output
  de_set_layer(2);

  de_draw_port(-D+0.0001, W3/2, -90.0);
  de_draw_port(L-0.0001+0.004, W3/2, 90.0);
  de_draw_port(-D-S-0.0001, W3/2, 90.0);
  de_draw_port(-D-S-0.0001, W3/2, 90.0);

  de_add_polygon();
    de_add_point(0,(W3-W2)/2*1000);
    de_add_point(0,(W3+W2)/2*1000);
```

```
      de_add_point(L*1000,W3*1000);
      de_add_point(L*1000,0);
    de_end();

    de_add_rectangle(-D*1000,(W3-W2)/2*1000, 0,
                     (W3+W2)/2*1000);
                     // diff port bottom
    de_add_rectangle((-D-S)*1000,0, L*1000,4);
                     // small area top
    de_add_rectangle((-D-S)*1000,W3*1000-4,
                     L*1000,W3*1000);
                     // small area bottom
    de_add_rectangle(-40,0, (-D-S)*1000,W3*1000);
                     // big area at the input
    de_add_rectangle(L*1000,0, L*1000+4,W3*1000);
                     // small area at the output
  }
```

AEL Script of the Exponentially Tapered Coupled Line Balun

```
  // Exponentially tapered coupled line balun for a
  // CMCD power amplifier

  // L:  Length of the taper
  // W1 = Ws: Width of the microstrip top output line
  // W2 = Wd: Width of the differential top and bottom
  //          input lines
  // W3 = Wb: Width of the entire balun
  // D:  Linear differential line offset at the input
  // S:  Slot width at the input
  defun Taper_art_exp_3port(L, W1,W2,W3, D, S)
  {
    decl N;
    N=100;    // N is restricted to < 100 due to
    L=L+L/N;  // constraints of the polygon function
              // in ADS
    decl i=0; decl x={0::L/N::L};
    decl y1={0::L/N::L};
    decl y2={0::L/N::L};
```

```
decl y3={0::L/N::L};
decl y4={0::L/N::L};
for (i=0;i<N;i++){
  y1[i]=W2/2*exp(1/L*ln(W3/W2)*x[i])+W3/2;
  y2[i]=-W2/2*exp(1/L*ln(W3/W2)*x[i])+W3/2;
  y3[i]=-W2/2*exp(1/L*ln(W1/W2)*x[i])+W3/2;
  y4[i]=W2/2*exp(1/L*ln(W1/W2)*x[i])+W3/2;
}

de_set_global_db_factor();
de_set_layer(1);

de_draw_port(-D+0.0001, W3/2, -90.0); // simulator
                                      // units
de_draw_port(L-L/N-0.0001+0.004, W3/2, 90.0);
de_add_polygon();
  for (i=0;i<N;i++)  de_add_point(x[i]*1000,
                                  y3[i]*1000);
  for (i=N-1;i>=0;i--)  de_add_point(x[i]*1000,
                                     y4[i]*1000);
de_end();

de_add_rectangle(-D*1000,(W3-W2)/2*1000, 0,
                 (W3+W2)/2*1000);
                 // diff port top
de_add_rectangle((L-L/N)*1000,(W3-W1)/2*1000,
                 (L-L/N)*1000+4,
                 (W3+W1)/2*1000);
                 // small area at the output
de_set_layer(2);

de_draw_port(-D+0.0001, W3/2, -90.0);
de_draw_port(L-L/N-0.0001+0.004, W3/2, 90.0);
de_draw_port(-D-S-0.0001, W3/2, 90.0);
de_draw_port(-D-S-0.0001, W3/2, 90.0);

de_add_polygon();
  for (i=0;i<N;i++) de_add_point(x[i]*1000,
                                 y1[i]*1000);
```

```
      for (i=N-1;i>=0;i--)  de_add_point(x[i]*1000,
                                         y2[i]*1000);
    de_end();

    de_add_rectangle(-D*1000,(W3-W2)/2*1000, 0,
                     (W3+W2)/2*1000);
                     // diff port bottom
    de_add_rectangle((-D-S)*1000,0, (L-L/N)*1000,4);
                     // small area top
    de_add_rectangle((-D-S)*1000,W3*1000-4,
                     (L-L/N)*1000,W3*1000);
                     // small area bottom
    de_add_rectangle(-40,0, (-D-S)*1000,W3*1000);
                     // big area at the input
    de_add_rectangle((L-L/N)*1000,0,
                     (L-L/N)*1000+4,W3*1000);
                     // small area at the output
  }
```

A.2 Additional Pictures of the PAs and the Measurement Setup

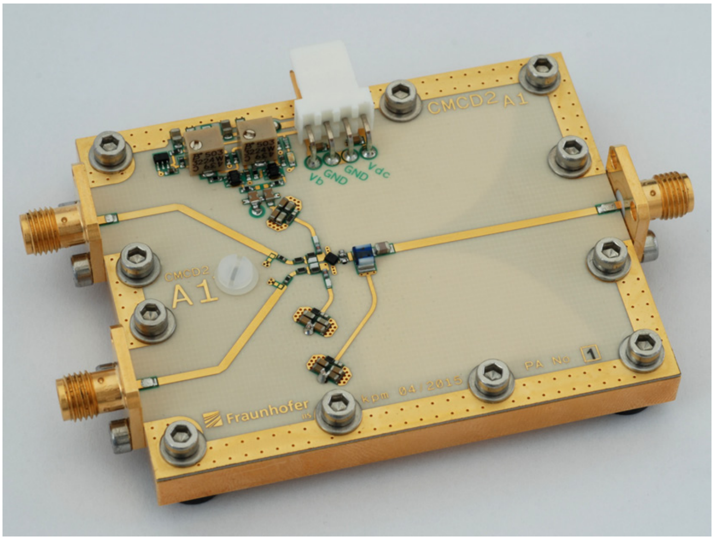

Figure A.1.: Picture of the CMCD A1 PA (band-pass filter)

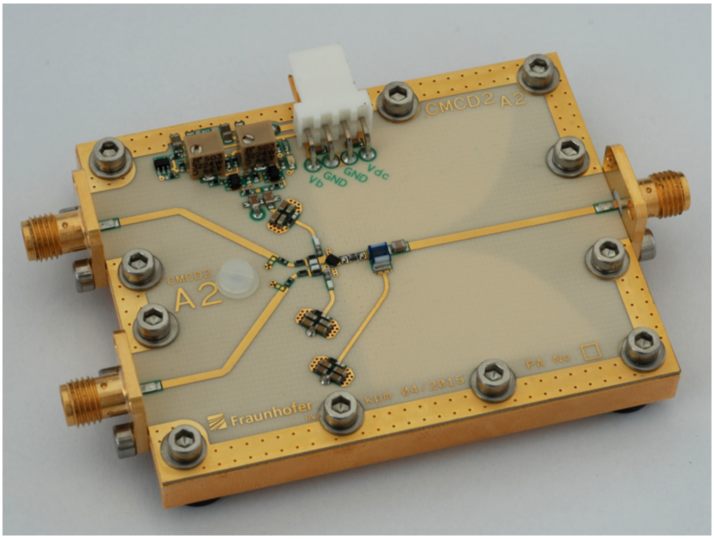

Figure A.2.: Picture of the CMCD A2 PA (low-pass filter)

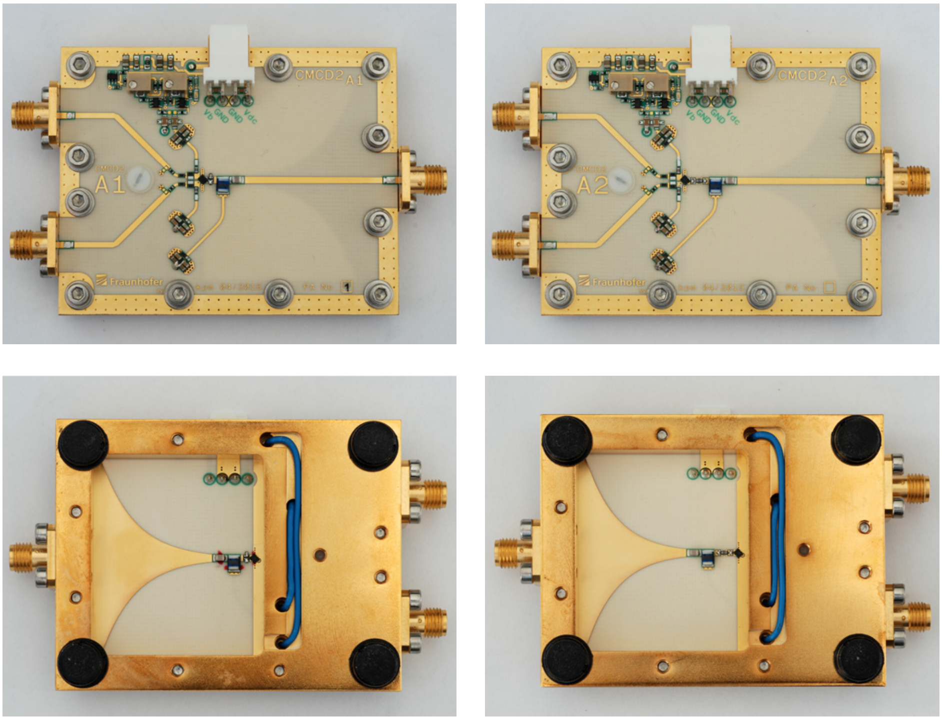

Figure A.3.: Top and bottom views of the manufactured power amplifiers CMCD A1 PA (left) and CMCD A2 PA (right)

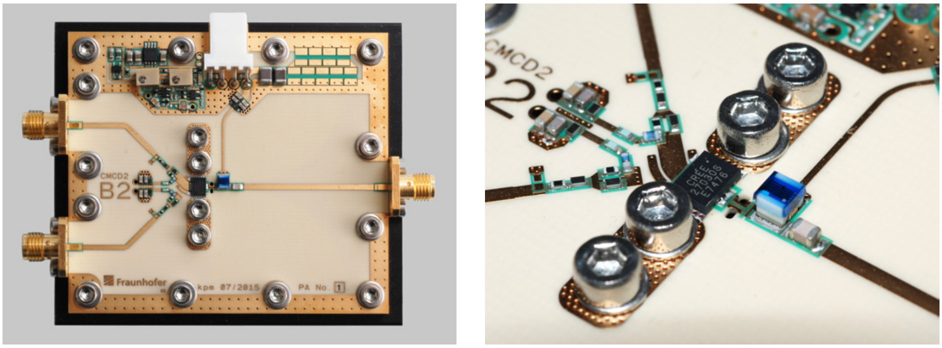

Figure A.4.: Top and detailed views of the manufactured power amplifier CMCD B2 PA

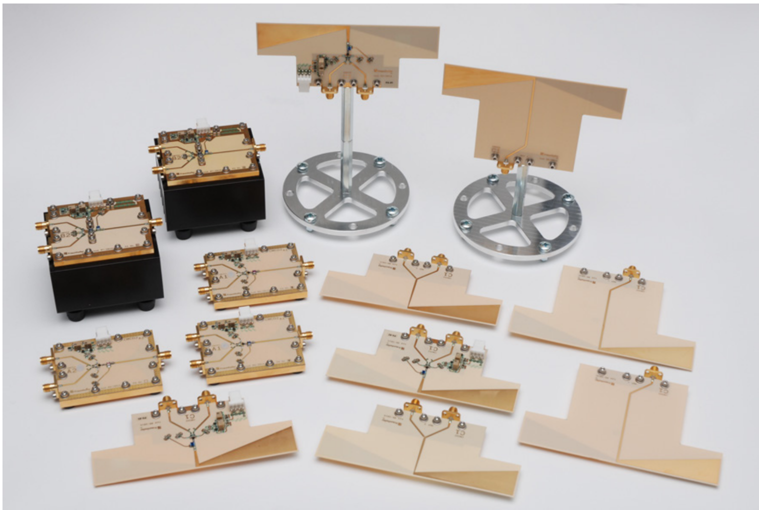

Figure A.5.: Overview of the manufactured boards

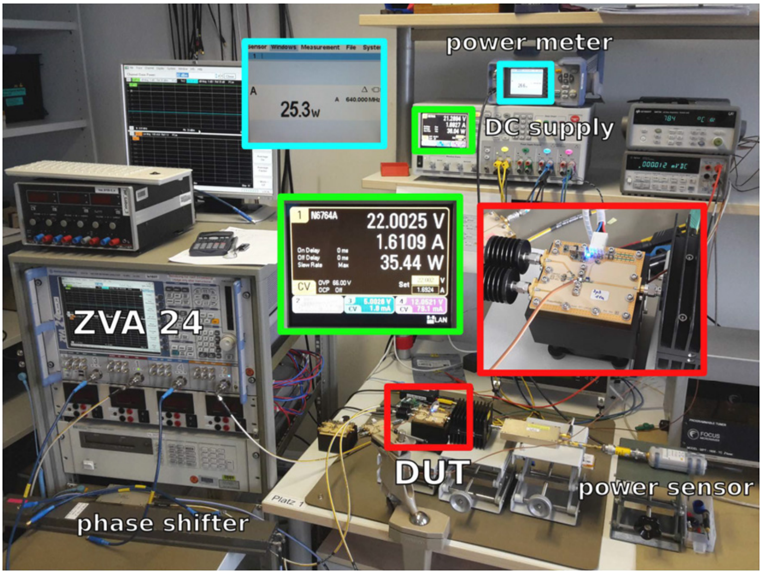

Figure A.6.: Photo of the measurement setup for the CMCD B2 PA

List of Tables and Figures

List of Tables

List of Figures

Color codes used in figures depicting voltages and currents:

- voltage: 🟦
- current: 🟫

Color codes used in figures depicting efficiencies, gain and output power:

- drain efficiency: 🟦
- power-added efficiency: 🟫
- gain: 🟩
- output power: 🟪

List of Acronyms and Symbols

Acronyms:

2-DEG	two-dimensional Electron Gas
4G	Fourth generation
5G	Fifth generation
ADC	Analog-to-Digital Converter
ADS	Advanced Design System
AEL	Application Extension Language
BJT	Bipolar Junction Transistor
BW	Bandwidth
CA	Carrier Aggregation
CMCD	Current Mode Class-D
CPM	Continuous Phase Modulation
DAC	Digital-to-Analog Converter
DC	Direct Current
DPD	Digital Pre-Distortion
DUT	Device Under Test
DVB-T2	Digital Video Broadcasting – Terrestrial, 2nd generation
EER	Envelope Elimination and Restoration
EM	Electromagnetic
EMC	Electromagnetic compatibility
E-pHEMT	Enhancement Mode Pseudomorphic High Electron Mobility Transistor
ETSI	European Telecommunications Standards Institute
FDMA	Frequency-Division Multiple Access
FEM	Finite Element Method
FET	Field Effect Transistor
FM	Frequency Modulation
FPGA	Field Programmable Gate Array
FSK	Frequency Shift Keying
GaAs	Gallium Arsenide
GaN	Gallium Nitride

GMSK	Gaussian Minimum Shift Keying
GSM	Global System for Mobile Communication
HBT	Heterojunction Bipolar Transistor
HEMT	High Electron Mobility Transistor
IMD	Intermodulation Distortion
IoT	Internet of Things
ISM	Industrial, Scientific and Medical
LAN	Local Area Network
LDMOS	Lateral Diffused Metal Oxide Semiconductor
LINC	LInar amplification with Nonlinear Components
LP	Low-pass
LTE	Long Term Evolution
MESFET	Metal-semiconductor FET
MOS	Metal Oxide Semiconductor
MOSFET	Metal Oxide Semiconductor Field-Effect Transistor
MSK	Minimum Shift Keying
OFDM	Orthogonal Frequency Division Multiplexing
OTA	Over The Air
PA	Power Amplifier
PAE	Power-Added Efficiency
PAPR	Peak to Average Power Ratio
PCB	Printed Circuit Board
pHEMT	Pseudomorphic High Electron Mobility Transistor
PMSE	Program Making and Special Events
QAM	Quadrature Amplitude Modulation
RF	Radio Frequency
RFC	Radio Frequency Choke
UHF	Ultra High Frequency
VMCD	Voltage Mode Class-D
VSWR	Voltage Standing Wave Ratio
ZCS	Zero Current Switching
SMD	Surface Mounted Device
SRD	Short Range Devices
TDR	Time Domain Reflectometry
TV	Television
ZVS	Zero Voltage Switching

Symbols:

α	Angle defining a bow tie antenna
β, γ	Auxiliary variables for calculating the low-pass output filter; also: phase constant β
Γ	Reflection coefficient
Γ_{max}	Maximum reflection coefficient for stability
Γ_S	Input matching of an amplifier
Γ_L	Output matching of an amplifier
δ	Skin depth
ϵ_0	Vacuum permittivity
ϵ_{eff}	Effective permittivity
ϵ_r	Relative permittivity
η	Drain efficiency of the amplifier
η_{60}	Drain efficiency that is higher than 60%
η_{70}	Drain efficiency that is higher than 70%
η_{BI}	Losses due to the imbalance of the output network (including the balun)
η_{BL}	Losses in the balun
η_i	Individual loss efficiencies of the components in the CMCD PA
η_{ideal}	Drain efficiency for ideal conditions (without parasitic losses)
η_{LD}	Losses due to the parasitic drain inductance
η_{PP}	Losses due to the parasitic resistance in the output filter
η_{PO}	Losses due to higher harmonic power in the output signal
$\eta_{PO,LP2}$	Losses due to higher harmonic power in the output signal with a second order low-pass output filter
$\eta_{PO,LP3}$	Losses due to higher harmonic power in the output signal with a third order low-pass output filter
η_{rad}	Antenna efficiency
η_{RFC}	Resistive losses of the real RFCs
η_{TR}	Losses due to the parasitic on-resistance and drain-to-source capacitance of the transistor
η_{TT}	Losses due to the limited transition time of the transistor

ϑ	Polar angle
κ	Electrical conductivity of a material
λ	Wavelength
λ_0	Wavelength in vacuum
μ_0	Vacuum permeability
τ	Rise and fall time of the drain current
φ	Azimuthal angle
φ_k	Phase angle at each antenna element
ω_c	Angular resonance frequency of the output resonator; also: corner frequency of the low-pass output filter
ω_c'	Normalized corner frequency of the low-pass output filter
ω_s	Angular switching frequency
a	Incident wave; also: radius of a cylindrical linear dipole antenna
$\mathbf{A}$	Magnetic vector potential; also: spherical surface
A	Path loss due to the distance to and the radiation pattern of the DUT antenna
A'	Surface of a cylindrical linear dipole antenna
A_{dB}	Attenuation of the output filter
a_i, b_i	Filter coefficients of the low-pass output filter
a_k, d_k	Auxiliary variables for calculating the low-pass output filter
a_m	Incident modal wave
$a_{1/2/3}$	Incident waves at the balun
a_{d1}	Differential mode stimulus at the differential input of the balun
a_{c1}	Common mode stimulus at the differential input of the balun
a_{s2}	Single-ended stimulus at the single-ended output of the balun
b	Reflected wave
b_f	Length of the antenna input terminals
b_m	Reflected modal wave
$b_{1/2/3}$	Reflected waves at the balun
B	Bandwidth
$B_{\eta 60}$	Bandwidth with a drain efficiency that is higher than 60%

$B_{\%}$	Percent bandwidth
$B_{\%,\eta 70}$	Percent bandwidth with a drain efficiency that is higher than 70%
$B_{\%,\eta 60}$	Percent bandwidth with a drain efficiency that is higher than 60%
$B_{\%,\mathrm{PAE70}}$	Percent bandwidth with a power-added efficiency that is higher than 70%
$B_{\%,classD}$	Maximum class-D power amplifier bandwidth
$B_{\%,classF}$	Maximum class-F power amplifier bandwidth
$B_{\%,com}$	Percent bandwidth of the common mode
B_P	3 dB bandwidth of the LC resonator, which is given as a function of the loaded Q factor Q_P
$B_{P\%}$	3 dB percent bandwidth of the LC resonator
B_{max}	Maximum bandwidth of an amplifier
c	Midpoint of the stability circle in the Smith chart
c_0	Speed of light in vacuum
C'	Distributed capacitance
C_1	Shunt capacitance of the proposed input stabilization network
C_2	Parallel capacitance of the proposed input stabilization network
C_{c1}, C_{c2}	Common mode coupling capacitances
$C_{c1,k}$, $C_{c2,k}$	Common mode coupling capacitances of the tapered balun
C_d	Differential mode coupling capacitances
$C_{d,k}$	Differential mode coupling capacitances of the tapered balun
C_{DS}	Drain-to-source capacitance of a FET
C_{GS}	Gate-to-source capacitance of a FET
C_{GD}	Gate-to-drain capacitance of a FET
C_P	Capacitance of the LC resonator output filter
C'_P	Combined capacitance $C'_P = C_P + C_{DS}$
C_{P1}, C_{P2}	Parallel capacitors of the third order low-pass filter
C'_{P2}	Combined capacitance $C'_{P2} = C_{P2} + C_{DS}$
C_S	Series capacitance of the proposed input stabilization network

d	Length of the offset line in the tapered balun and the “amplitenna”; also: thickness/diameter of a cylindrical linear dipole antenna
D	Directivity of an antenna; also: drain terminal of a FET
e	Electrical length in degrees
e_c	Phase shifting coefficient
$e_{c,k}$	Phase shifting coefficients of the tapered balun
e_{max}	Upper edge of the electrical length
e_{min}	Lower edge of the electrical length
e_r, e_z, e_φ	Unit vectors
$\mathbf{E}$	Unit matrix; also: Electric field
E_ϑ	ϑ-component of the electric field
E_0, E_e, E_m	Fields without, with electric and with magnetic screen
$E_{RF,1}$	Fundamental energy of half an RF cycle
E_{LD}	Magnetic energy saved in the inductance L_D
E_{RFC}	Magnetic energy saved in the inductor L_{RFC}
f	Frequency
f_{Ln}	Lower edge of the nth harmonic output filter
f_{Un}	Upper edge of the nth harmonic output filter
f_c	Resonance frequency of the output resonator; also: corner frequency of the low-pass output filter
f_s	Switching frequency
f_{max}	Maximum transmission frequency (e.g., of an amplifier)
f_{min}	Minimum transmission frequency (e.g., of an amplifier)
G	Power gain of the amplifier; also gate terminal of a FET
g_0	Normalized load resistance of the low-pass output filter
g_k	Normalized element values of the low-pass output filter
G_{LP}	Magnitude of the low-pass transfer function $G_{LP}(\omega) = \lvert H_{LP}(j\omega)\rvert$

h	Thickness of the PCB substrate; also: height of a dipole antenna
$\mathbf{H}$	Magnetic field
E_{φ}	φ-component of the magnetic field
H_{LP}	General transfer function of a passive low-pass filter
H_{LP2}	Transfer function of the second order low-pass output filter
H_{LP3}	Transfer function of the third order low-pass output filter
i	Current
I	One-dimensional current at a thin antenna
$\hat{I}$	Amplitude of a one-dimensional current at a thin antenna
I_0	Current source at a cylindrical linear dipole antenna
i_{com}	Common mode output current at the CMCD PA
$\hat{i}_{com}$	nth harmonic amplitude of the common mode current at the CMCD PA
$i_{D1/2}$	Drain currents at the CMCD PA
$\hat{i}_{D1/2}$	nth harmonic amplitude of the drain currents at the CMCD PA
$I_{D,max}$	Peak drain current at the switches of the CMCD PA
I_{DC}	Constant supply current at the CMCD PA supply terminals
i_{diff}	Differential output current of the CMCD PA (difference of i_{D1} and i_{D2})
i_{RL}	Load current at the load resistance R_L
$\hat{i}_{RL}$	Amplitude of the load current at the load resistance R_L
$\mathbf{J}$	Current density at a cylindrical linear dipole antenna
$\mathbf{J}_F$	Surface current at a cylindrical linear dipole antenna
k	Impedance transformation ratio of the output balun; also: running index
k_0	Angular wavenumber
k_{0e}	Even-mode coupling constant representing coupling in the differential network

k_{0o}	Odd-mode coupling constant representing coupling in the differential network
l	Length of the taper; also: length of a dipole antenna
l_{max}	Maximum dimension of an arbitrary antenna
l_{min}	Minimum dimension of an arbitrary antenna
L'	Distributed inductance
L_1	Shunt inductance of the proposed input stabilization network
L_G	Bond wire inductance at the gate terminal of a FET
L_D	Package parasitic drain (and source) inductance
L_P	Inductance of the LC resonator output filter
L_{RFC}	Inductance of a radio frequency choke
L_S	Series inductor of the third order low-pass filter; also: package parasitic source inductance
$\mathbf{M}_{1,2}$	Conversion matrices, which represent the relationship of differential mode and common mode impedances
n	nth harmonic; also: filter order
PAE	Power-Added Efficiency of the amplifier
PAE_{70}	Power-Added Efficiency that is higher than 70%
P_{com}, P_{diff}	Powers absorbed into the impedances Z_{com} and Z_{diff}
P_{DC}	DC delivered power
P_{in}	Total RF power supplied from the source
$P_{in1/2}$	RF power supplied from the source at the individual, differential inputs
$P_{in,on}$	Total RF input power necessary for transistor compression
P_{LD}	Power loss at the inductance L_D at the switching frequency f_s
P_{loss}	General loss power
$P_{loss,i}$	Individual loss powers of the components in the CMCD PA
P_{out}	RF power delivered to load
$P_{out,k}$	RF power at each antenna element
$P_{out}(1)$	Fundamental RF power delivered to load

P_{rad}	Radiated power of an antenna
P_r	Received power at a measurement antenna with the distance r
$P_{r,PA}$	Received power from "amplitenna"
$P_{r,ref}$	Received power from reference antenna
$P_{T,loss}$	Power loss at the transistor due to voltage-current overlap
$P_{T,loss,1}$	Power loss at the first transistor
Q_{LP}	Pole quality factor of the second order low-pass output filter
Q_P	Loaded quality factor of the LC resonator
r	Radius of the stability circle in the Smith chart; also: radial distance
$\mathbf{r}$	Space point
$\mathbf{r}'$	Source point
R'	Distributed resistance
R_0	Reference resistance for calculating the low-pass output filter; also: DC resistance of a cylindrical wire
R_1	Shunt resistance of the proposed input stabilization network
R_2	Parallel resistance of the proposed input stabilization network
R_C	Off-resistance of a FET in switched mode (in parallel to C_{DS})
R_{cc11}	Common mode input resistance of the output network to calculate η_{BI}
R_{dB}	Chebyshev passband ripple
R_D, R_G, R_S	Drain, gate and source bulk resistances of a FET
$R_{DS,on}$	On-resistance of the FET in switched mode
R_{DS}	General drain-to-source resistance of a FET
R_{feed}	Antenna input resistance
R_{GD}	Loss resistance of C_{GD}
R_{GS}	Loss resistance of C_{GS}
R_{in}	Resistance of the signal source
R_L	Differential load resistance of the CMCD PA
R'_L	Single-ended load resistance of the CMCD PA
R_{loss}	Antenna loss resistance

R_P	Combined parallel resistance $R_P = \frac{1}{\frac{1}{R_L}+\frac{1}{R_V}}$ to calculate Q_P
R_{rad}	Antenna radiation resistance
R_{RFC}	Parasitic series resistance of L_{RFC}
R_V	Loss resistance of the reactive components in the LC resonator output filter
s	Complex number frequency parameter; also: slot distance of the differential line / of the balun and antenna input terminals
$\mathbf{S}$	3x3 scattering matrix of a balun; also: Poynting vector
$\mathbf{S}_m$	Modal representation of the 3x3 scattering matrix of a balun
$S_{11,12,\ldots,33}$	Scattering parameters of a balun
$S_{21,ref}$	Forward gain of the reference antenna
$S_{21,PA}$	Forward gain of the “amplitenna”
$S_{dd11,cc11,ss22}$	Modal scattering parameters of a balun describing the reflection quantity of differential, common and single-ended signals
$S_{dc11,cd11}$	Modal scattering parameters of a balun describing the conversion of modes at the differential port during reflection
$S_{ds12,sd21,cs12,sc21}$	Modal scattering parameters of a balun describing the conversion of single-ended to mixed modes and vice versa during transmission between the two balun ports
S_r	Magnitude of the Poynting vector
S	Source terminal of a FET
S_1, S_2	Switches at the CMCD representing the transistors
T_1, T_2	Transistors at the CMCD PA
t	Time; also: conductor thickness
T_s	Switching period
THD	Total harmonic distortion of the amplifier with the output network
THD_{LP2}	Total harmonic distortion of the amplifier with a second order low-pass output filter

THD_{LP3}	Total harmonic distortion of the amplifier with a third order low-pass output filter
v	Voltage
V	Volume
V_{bias}	Bias voltage at the transistors
v_{com}	Common mode output voltage at the CMCD PA
$\hat{v}_{com}$	nth harmonic amplitude of the common mode voltage at the CMCD PA
V_{DC}	DC supply voltage of the CMCD PA
$V_{DC,k}$	DC supply voltage of each individual CMCD PA for multiple antenna elements
v_{diff}	Differential output voltage of the CMCD PA
$\hat{v}_{\mathit{diff}}$	Amplitude of the differential output voltage of the CMCD PA
$v_{DS1/2}$	Drain-source voltages at the CMCD PA
$V_{DS,max}$	Peak drain current at the switches of the CMCD PA
$v_{in1/2}$	180° phase delayed input voltages of the CMCD PA
$\hat{v}_{in,rect}$	Amplitude of a rectangular input voltage
$\hat{v}_{in,sin}$	Amplitude of a sinusoidal input voltage
VF	Velocity Factor of a transmission medium
VSWR_{max}	Worst-case VSWR of an antenna
w	Width of a conductive trace
w_1, w_2, w_3	Widths of the conductive traces of the single line balun
w_4	Depth of the cavity below the balun
$w_{1,k}$; $w_{2,k}$; $w_{3,k}$	Widths of the conductive traces of the tapered balun
w_b	Maximum width of the tapered line
w_d	Width of the differential input line
w_f	Width of the antenna input terminals
w_s	Width of the single-ended microstrip output line
X_{feed}	Antenna input reactance
X_{rad}	Antenna reactance
z'	z-coordinate symmetrical to the antenna feed

$\mathbf{Z}_m$	Mixed-mode impedances
Z_0	Reference impedance (e.g., $50\,\Omega$); also: impedance of the medium (e.g., $377\,\Omega$ in free space)
Z_{0e}	Even-mode impedance
Z_{0o}	Odd-mode impedance
Z_1, Z_2	Input impedances of two complementary antennas
Z_c	Common mode impedance
Z_{c1}, Z_{c2}	Common mode impedances of the balun model
$Z_{c1,k}$; $Z_{c2,k}$	Individual common mode impedances of the tapered balun
Z_{cc11}	Common mode input impedance of the output network / balun
Z_{com}, Z_{diff}	Lumped element representation of the mixed mode load impedance Z_L
Z_d	Differential mode impedance
$Z_{d,k}$	Individual differential mode impedances of the tapered balun
Z_{dd11}	Differential mode input impedance of the output network / balun
Z_{feed}	Antenna input impedance
Z_L	Load impedance of the output network of the CMCD PA

Bibliography

References

[1] S. C. Cripps. *RF Power Amplifiers for Wireless Communications*. Artech House, 2006.

[2] R. Rahman, E. Perrins, and M. Green. “Power efficient uplink LTE with CPM-SC-IFDMA”. In: *2011 - MILCOM 2011 Military Communications Conference*. Nov. 2011, pp. 507–512. DOI: `10.1109/MILCOM.2011.6127721`.

[3] 3rd Generation Partnership Project (3GPP). *Physical layer aspects for E-UTRA, 3GPP TR 25.814*. 2006. URL: `http://3gpp.org` (visited on 03/30/2017).

[4] **M. Kamper**, G. Ulbricht, R. Weigel, and G. Fischer. “Comparison of class A and class D RF amplifier operation with focus on reverse intermodulation and efficiency performance”. In: *Microwave Integrated Circuits Conference (EuMIC), 2011 European*. Oct. 2011, pp. 272–275.

[5] J. Ribadeneira-Ramírez, G. Martínez, D. Gómez-Barquero, and N. Cardona. “Interference Analysis Between Digital Terrestrial Television (DTT) and 4G LTE Mobile Networks in the Digital Dividend Bands”. In: *IEEE Transactions on Broadcasting* 62.1 (Mar. 2016), pp. 24–34. ISSN: 0018-9316. DOI: `10.1109/TBC.2015.2492465`.

[6] Bundesnetzagentur, ed. *Vernetzt Ausgabe 1/2015* 01 (2015). German. URL: `http://www.bundesnetzagentur.de/SharedDocs/Downloads/DE/Allgemeines/Bundesnetzagentur/Publikationen/VERNETZT/VERNETZT2015_01.pdf` (visited on 03/30/2017).

[7] G. Kilian et al. “Increasing Transmission Reliability for Telemetry Systems Using Telegram Splitting”. In: *IEEE Transactions on Communications* 63.3 (Mar. 2015), pp. 949–961. ISSN: 0090-6778. DOI: `10.1109/TCOMM.2014.2386859`.

[8] Tsai-Pi Hung et al. “Design of high-efficiency current-mode class-D amplifiers for wireless handsets”. In: *IEEE Trans. Microw. Theory Techn.* 53.1 (2005), pp. 144–151. DOI: `10.1109/TMTT.2004.839327`.

[9] H. Kobayashi, J.M. Hinrichs, and P.M. Asbeck. “Current-mode class-D power amplifiers for high-efficiency RF applications”. In: *IEEE Trans. Microw. Theory Techn.* 49.12 (Dec. 2001), pp. 2480–2485. DOI: `10.1109/22.971639`.

[10] A. Long, Jingshi Yao, and S. I. Long. “A 13 W current mode class D high efficiency 1 GHz power amplifier”. In: *Proc. MWSCAS-2002 Circuits and Systems The 2002 45th Midwest Symp.* 2002. DOI: `10.1109/MWSCAS.2002.1187146`.

[11] H. M. Nemati, C. Fager, M. Thorsell, and H. Zirath. “High-Efficiency LDMOS Power-Amplifier Design at 1 GHz Using an Optimized Transistor Model”. In: *IEEE Transactions on Microwave Theory and Techniques* 57.7 (2009), pp. 1647–1654. DOI: `10.1109/TMTT.2009.2022590`.

[12] C. Y. Hang, Y. Qian, and T. Itoh. “High efficiency S-band class AB push-pull power amplifier with wideband harmonic suppression”. In: *2001 IEEE MTT-S International Microwave Symposium Digest (Cat. No.01CH37157).* Vol. 2. May 2001, 1079–1082 vol.2. DOI: `10.1109/MWSYM.2001.967079`.

[13] R. M. Smith et al. “A Novel Formulation for High Efficiency Modes in Push-Pull Power Amplifiers Using Transmission Line Baluns”. In: *IEEE Microwave and Wireless Components Letters* 22.5 (May 2012), pp. 257–259. ISSN: 1531-1309. DOI: `10.1109/LMWC.2012.2191273`.

[14] A. N. Stameroff, A. V. Pham, and R. E. Leoni. “High efficiency push-pull inverse class F power amplifier using a balun and harmonic trap waveform shaping network”. In: *2010 IEEE MTT-S International Microwave Symposium.* May 2010, pp. 521–525. DOI: `10.1109/MWSYM.2010.5517720`.

[15] P. Saad, M. Thorsell, K. Andersson, and C. Fager. “Investigation of Push-Pull Microwave Power Amplifiers Using an Advanced Measurement Setup”. In: *IEEE Microwave and Wireless Components Letters* 23.4 (Apr. 2013), pp. 220–222. ISSN: 1531-1309. DOI: `10.1109/LMWC.2013.2249502`.

[16] V. Carrubba et al. “A novel highly efficient broadband continuous class-F RFPA delivering 74% average efficiency for an octave bandwidth”. In: *2011 IEEE MTT-S International Microwave Symposium.* June 2011, pp. 1–4. DOI: `10.1109/MWSYM.2011.5972701`.

[17] M. Yang, J. Xia, Y. Guo, and A. Zhu. “Highly Efficient Broadband Continuous Inverse Class-F Power Amplifier Design Using Modified Elliptic Low-Pass Filtering Matching Network”. In: *IEEE Transactions on Microwave Theory and Techniques* 64.5 (May 2016), pp. 1515–1525. ISSN: 0018-9480. DOI: `10.1109/TMTT.2016.2544318`.

[18] R. M. Smith et al. “A 40W push-pull power amplifier for high efficiency, decade bandwidth applications at microwave frequencies”. In: *Microwave Symposium Digest (MTT), 2012 IEEE MTT-S International.* June 2012, pp. 1–3. DOI: `10.1109/MWSYM.2012.6259418`.

[19] R. M. H. Smith and S. C. Cripps. “Broadband push-pull power amplifier design at microwave frequencies”. In: *2016 46th European Microwave Conference (EuMC).* Oct. 2016, pp. 1353–1356. DOI: `10.1109/EuMC.2016.7824603`.

[20] T. Canning, J.R. Powell, and S.C. Cripps. “Optimal Design of Broadband Microwave Baluns Using Single-Layer Planar Circuit Technology”. In: *Microwave Theory and Techniques, IEEE Transactions on* 62.5 (May 2014), pp. 1183–1191. ISSN: 0018-9480. DOI: `10.1109/TMTT.2014.2311417`.

[21] S. K. Dhar, O. Hammi, M. S. Sharawi, and F. M. Ghannouchi. “Power amplifier based integrated and miniaturized active antenna”. In: *2015 9th European Conference on Antennas and Propagation (EuCAP).* May 2015, pp. 1–4.

[22] V. Radisic, Yongxi Qian, and T. Itoh. “Class F power amplifier integrated with circular sector microstrip antenna”. In: *1997 IEEE MTT-S International Microwave Symposium Digest.* Vol. 2. June 1997, 687–690 vol.2. DOI: `10.1109/MWSYM.1997.602884`.

[23] Younkyu Chung et al. “AlGaN/GaN HFET power amplifier integrated with microstrip antenna for RF front-end applications”. In: *IEEE Transactions on Microwave Theory and Techniques* 51.2 (Feb. 2003), pp. 653–659. ISSN: 0018-9480. DOI: `10.1109/TMTT.2002.807685`.

[24] John L. B. Walker. *High-Power GaAs FET Amplifiers (Artech House Microwave Library (Hardcover)).* Artech House Publishers, 1993. ISBN: 0890064792.

[25] F. H. Raab. “Maximum efficiency and output of class-F power amplifiers”. In: *IEEE Transactions on Microwave Theory and Techniques* 49.6 (June 2001), pp. 1162–1166. ISSN: 0018-9480. DOI: `10.1109/22.925511`.

[26] Julius Edgar Lilienfeld. “Method and apparatus for controlling electric currents”. US1745175. 1930.

[27] Peter Aaen, Jaime A. Plá, and John Wood. *Modeling and Characterization of RF and Microwave Power FETs.* Cambridge Books Online. Cambridge University Press, 2007. ISBN: 9780511541124. URL: `http://dx.doi.org/10.1017/CBO9780511541124`.

[28] A. Katz and M. Franco. “GaN Comes of Age”. In: *Microwave Magazine, IEEE* 11.7 (Dec. 2010), S24–S34. ISSN: 1527-3342. DOI: `10.1109/MMM.2010.938583`.

[29] A. Samulak. “System Analyses of Class-S Power Amplifier”. PhD Thesis. Universität Erlangen-Nürnberg, 2010.

[30] Stephan Maroldt. “Gallium Nitride Based Transistors for High-Efficiency Microwave Switch-Mode Amplifiers”. PhD Thesis. Albert-Ludwigs Universität Freiburg im Breisgau, 2010.

[31] Wolfspeed. *CGH27030S; 30 W RF Power GaN HEMT; Data Sheet*. Wolfspeed. May 2015.

[32] Z. Yusoff et al. “Linearity improvement in RF power amplifier system using integrated Auxiliary Envelope Tracking system”. In: *Microwave Symposium Digest (MTT), 2011 IEEE MTT-S International*. June 2011, pp. 1–4. DOI: `10.1109/MWSYM.2011.5972769`.

[33] Avago. *ATF-541M4; Low Noise Enhancement Mode Pseudomorphic HEMT; Data Sheet*. Avago. Nov. 2006.

[34] A. Suarez. “Check the Stability: Stability Analysis Methods for Microwave Circuits”. In: *Microwave Magazine, IEEE* 16.5 (June 2015), pp. 69–90. ISSN: 1527-3342. DOI: `10.1109/MMM.2015.2410951`.

[35] C. Musolff, **M. Kamper**, Z. Abou-Chahine, and G. Fischer. “Linear and Efficient Doherty PA Revisited”. In: *Microwave Magazine, IEEE* 15.1 (Jan. 2014), pp. 73–79. ISSN: 1527-3342. DOI: `10.1109/MMM.2013.2288713`.

[36] C. Musolff, **M. Kamper**, Z. Abou-Chahine, and G. Fischer. “A Linear and Efficient Doherty PA at 3.5 GHz”. In: *Microwave Magazine, IEEE* 14.1 (Jan. 2013), pp. 95–101. ISSN: 1527-3342. DOI: `10.1109/MMM.2012.2226998`.

[37] C. Musolff, **M. Kamper**, and G. Fischer. “Linear Doherty PA at 5 GHz”. In: *Microwave Magazine, IEEE* 16.1 (Feb. 2015), pp. 89–93. ISSN: 1527-3342. DOI: `10.1109/MMM.2014.2367862`.

[38] T.A. Winslow. “Conical inductors for broadband applications”. In: *Microwave Magazine, IEEE* 6.1 (Mar. 2005), pp. 68–72. ISSN: 1527-3342. DOI: `10.1109/MMW.2005.1418000`.

[39] **M. Kamper** and G. Fischer. “Optimized output baluns for wideband differential class D PAs”. In: *2017 IEEE Topical Conference on RF/Microwave Power Amplifiers for Radio and Wireless Applications (PAWR)*. Jan. 2017, pp. 84–87. DOI: `10.1109/PAWR.2017.7875580`.

[40] **M. Kamper**, D. Kondakov, and G. Fischer. "Optimized Output Baluns for Current Mode Class D Power Amplifiers". In: *Microwave Conference (GeMIC), 2014 German*. Mar. 2014, pp. 1–4.

[41] A. Huynh, P. Hakansson, and Shaofang Gong. "Mixed-mode S-parameter conversion for networks with coupled differential signals". In: *Microwave Conference, 2007. European*. Oct. 2007, pp. 238–241. DOI: `10.1109/EUMC.2007.4405170`.

[42] Engineering Staff Analog Devices Inc. *Linear Circuit Design Handbook*. Oxford: Elsevier Science & Technology Books, 2008. ISBN: 978-0-750-68703-4.

[43] G.L. Matthaei, L. Young, and E.M.T. Jones. *Microwave filters, impedance-matching networks, and coupling structures*. Artech House microwave library Bd. 1. McGraw-Hill, 1964.

[44] L. Dunleavy et al. "Advances in linear and non-linear modeling for improved microwave design". In: *Wireless and Microwave Technology Conference (WAMICON), 2012 IEEE 13th Annual*. Apr. 2012, pp. 1–5. DOI: `10.1109/WAMICON.2012.6208478`.

[45] R. Mongia, I.J. Bahl, P. Bhartia, and S.J. Hong. *RF and Microwave Coupled-line Circuits*. Artech House microwave library. Artech House, 2007. ISBN: 9781596931565.

[46] Rogers Corporation. *Product Selector Guide*. Rogers Corporation. Jan. 2016.

[47] J.W. Duncan and V.P. Minerva. "100:1 Bandwidth Balun Transformer". In: *Proceedings of the IRE* 48.2 (Feb. 1960), pp. 156–164. ISSN: 0096-8390. DOI: `10.1109/JRPROC.1960.287458`.

[48] Tze-Min Shen, Chin-Ren Chen, Ting-Yi Huang, and Ruey-Beei Wu. "Design of lumped rat-race coupler in multilayer LTCC". In: *Microwave Conference, 2009. APMC 2009. Asia Pacific*. Dec. 2009, pp. 2120–2123. DOI: `10.1109/APMC.2009.5385258`.

[49] M.A. Antoniades and G.V. Eleftheriades. "A broadband Wilkinson balun using microstrip metamaterial lines". In: *Antennas and Wireless Propagation Letters, IEEE* 4 (2005), pp. 209–212. ISSN: 1536-1225. DOI: `10.1109/LAWP.2005.851005`.

[50] Chao-Hsiung Tseng and Chih-Lin Chang. "Microwave push-pull power amplifier using metamaterial-based baluns". In: *Microwave Conference, 2008. APMC 2008. Asia-Pacific*. Dec. 2008, pp. 1–4. DOI: `10.1109/APMC.2008.4958290`.

[51] R.M. Smith et al. “A design methodology for the realization of multi-decade baluns at microwave frequencies”. In: *Microwave Symposium Digest (MTT), 2011 IEEE MTT-S International*. June 2011, pp. 1–4. DOI: `10.1109/MWSYM.2011.5972702`.

[52] B. Climer. “Analysis of suspended microstrip taper baluns”. In: *IEE Proceedings H - Microwaves, Antennas and Propagation* 135.2 (Apr. 1988), pp. 65–69. ISSN: 0950-107X. DOI: `10.1049/ip-h-2.1988.0015`.

[53] P. Pramanick and P. Bhartia. “A generalized theory of tapered transmission line matching transformers and asymmetric couplers supporting non-TEM modes”. In: *IEEE Transactions on Microwave Theory and Techniques* 37.8 (Aug. 1989), pp. 1184–1191. ISSN: 0018-9480. DOI: `10.1109/22.31077`.

[54] Manuel Vicente-Lozano, Francisco Ares-Pena, and Eduardo Moreno-Piquero. “Synthesis of tapered transmission lines with characteristic impedance optimization”. In: *Microwave and Optical Technology Letters* 24.4 (2000), pp. 277–281. ISSN: 1098-2760. DOI: `10.1002/(SICI)1098-2760(20000220)24:4<277::AID-MOP20>3.0.CO;2-P`.

[55] R.E. Collin. *Foundations for Microwave Engineering*. IEEE Press Series on Electromagnetic Wave Theory. Wiley, 2001. ISBN: 9780780360310.

[56] R. W. Klopfenstein. “A Transmission Line Taper of Improved Design”. In: *Proceedings of the IRE* 44.1 (Jan. 1956), pp. 31–35. ISSN: 0096-8390. DOI: `10.1109/JRPROC.1956.274847`.

[57] ETSI. *Electromagnetic Compatibility and Radio Spectrum Matters (ERM); Short Range Devices (SRD); Radio Equipment to be Used in the 25 MHz to 1000 MHz Frequency Range with Power Levels Ranging up to 500 mW; Part 1: Technical Characteristics and Test Methods, ETSI Std. ETSI EN 300 220-1 V2.4.1*. European Telecommunications Standards Institute. Jan. 2012.

[58] J. C. Rautio. “Deembedding the effect of a local ground plane in electromagnetic analysis”. In: *IEEE Transactions on Microwave Theory and Techniques* 53.2 (Feb. 2005), pp. 770–776. ISSN: 0018-9480. DOI: `10.1109/TMTT.2004.840576`.

[59] Rohde & Schwarz. *R&S NRP Power Meter Family - Datasheet PD 5213.5539.22*. Rohde & Schwarz. May 2014.

[60] Keysight. *Keysight N6700 Modular Power System Family - Specifications Guide N6700-90001*. Keysight. Mar. 2017.

[61] International Telecommunication Union. *Radio Regulations*. 2012.

[62] K. Chen and D. Peroulis. “Design of Broadband Highly Efficient Harmonic-Tuned Power Amplifier Using In-Band Continuous Class-F-1/F Mode Transferring”. In: *IEEE Transactions on Microwave Theory and Techniques* 60.12 (Dec. 2012), pp. 4107–4116. ISSN: 0018-9480. DOI: `10.1109/TMTT.2012.2221142`.

[63] P. Butterworth, S. Gao, S. F. Ooi, and A. Sambell. “High-efficiency class-F power amplifier with broadband performance”. In: *Microwave and Optical Technology Letters* 44.3 (2005), pp. 243–247. ISSN: 1098-2760. DOI: `10.1002/mop.20599`. URL: `http://dx.doi.org/10.1002/mop.20599`.

[64] P. Wright et al. “A Methodology for Realizing High Efficiency Class-J in a Linear and Broadband PA”. In: *IEEE Transactions on Microwave Theory and Techniques* 57.12 (Dec. 2009), pp. 3196–3204. ISSN: 0018-9480. DOI: `10.1109/TMTT.2009.2033295`.

[65] P. Saad et al. “Design of a Highly Efficient 2-4GHz Octave Bandwidth GaN-HEMT Power Amplifier”. In: *IEEE Transactions on Microwave Theory and Techniques* 58.7 (July 2010), pp. 1677–1685. ISSN: 0018-9480. DOI: `10.1109/TMTT.2010.2049770`.

[66] K. Chen and D. Peroulis. “Design of Highly Efficient Broadband Class-E Power Amplifier Using Synthesized Low-Pass Matching Networks”. In: *IEEE Transactions on Microwave Theory and Techniques* 59.12 (Dec. 2011), pp. 3162–3173. ISSN: 0018-9480. DOI: `10.1109/TMTT.2011.2169080`.

[67] Ji Lan, Jianyi Zhou, Zhiqiang Yu, and Binqi Yang. “A broadband high efficiency Class-F power amplifier design using GaAs HEMT”. In: *2015 IEEE International Wireless Symposium (IWS 2015)*. Mar. 2015, pp. 1–4. DOI: `10.1109/IEEE-IWS.2015.7164618`.

[68] H. M. Nemati, C. Fager, and H. Zirath. “High Efficiency LDMOS Current Mode Class-D Power amplifier at 1 GHz”. In: *2006 European Microwave Conference*. Sept. 2006, pp. 176–179. DOI: `10.1109/EUMC.2006.281247`.

[69] H. Nakamizo et al. “Over 65% PAE GaN voltage-mode class d power amplifier for 465 MHz operation using bootstrap drive”. In: *2015 IEEE Topical Conference on Power Amplifiers for Wireless and Radio Applications (PAWR)*. Jan. 2015, pp. 1–3. DOI: `10.1109/PAWR.2015.7139202`.

[70] S. Shukla and J. Kitchen. “GaN-on-Si switched mode RF power amplifiers for non-constant envelope signals”. In: *2017 IEEE Topical Conference on RF/Microwave Power Amplifiers for Radio and Wireless Applications (PAWR)*. Jan. 2017, pp. 88–91. DOI: `10.1109/PAWR.2017.7875581`.

[71] G. Gronau. *Höchstfrequenztechnik: Grundlagen, Schaltungstechnik, Messtechnik, Planare Antennen*. Springer Berlin Heidelberg, 2001. ISBN: 9783540417903.

[72] K. Kark. *Antennen und Strahlungsfelder: Elektromagnetische Wellen auf Leitungen, im Freiraum und ihre Abstrahlung*. Aus dem Programm Informationstechnik. Vieweg, 2006. ISBN: 9783834802163.

[73] H. Zuhrt. *Elektromagnetische Strahlungsfelder: Eine Einführung in die Theorie der Strahlungsfelder in dispersionsfreien Medien*. Springer Berlin Heidelberg, 2013. ISBN: 9783642926129.

[74] P. S. Carter. "Circuit Relations in Radiating Systems and Applications to Antenna Problems". In: *Proceedings of the Institute of Radio Engineers* 20.6 (June 1932), pp. 1004–1041. ISSN: 0731-5996. DOI: `10.1109/JRPROC.1932.227723`.

[75] V. Rumsey. "Frequency independent antennas". In: *1958 IRE International Convention Record*. Vol. 5. Mar. 1957, pp. 114–118. DOI: `10.1109/IRECON.1957.1150565`.

[76] O. Zinke, A. Vlcek, H. Brunswig, and H.L. Hartnagel. *Hochfrequenztechnik 1: Hochfrequenzfilter, Leitungen, Antennen*. Springer-Lehrbuch. Springer Berlin Heidelberg, 2013. ISBN: 9783662008126.

[77] Y. Mushiake. "Self-complementary antennas". In: *IEEE Antennas and Propagation Magazine* 34.6 (Dec. 1992), pp. 23–29. ISSN: 1045-9243. DOI: `10.1109/74.180638`.

[78] H. G. Krauthauser. "On the Measurement of Total Radiated Power in Uncalibrated Reverberation Chambers". In: *IEEE Transactions on Electromagnetic Compatibility* 49.2 (May 2007), pp. 270–279. ISSN: 0018-9375. DOI: `10.1109/TEMC.2007.897122`.

[79] Nearfield Systems, Incorporated. *NSI-RF-SG975; WR975 Standard Gain Horn; Data Sheet*. Nearfield Systems, Incorporated. Mar. 2015.

[80] F. Auer, S. Schiller, and **M. Kamper**. "Linearity and efficiency improvement using envelope tracking power amplifier". In: *2016 German Microwave Conference (GeMiC)*. Mar. 2016, pp. 88–91. DOI: `10.1109/GEMIC.2016.7461563`.

[81] Bronstein, Semendjajew, Musiol, and Mühlig. *Taschenhandbuch der Mathematik*. Verlag Harri Deutsch, 2000.

[82] **M. Kamper**. "Effiziente HF Leistungsverstärker mit geschalteten Transistoren". In: *Electrical and Electronic Engineering for Communication Workshop - Entwicklerforum - Fachmesse*. (Ulm, DE). 2012.

Publications

M. Kamper, G. Ulbricht, R. Weigel, and G. Fischer. "Comparison of class A and class D RF amplifier operation with focus on reverse intermodulation and efficiency performance". In: *Microwave Integrated Circuits Conference (EuMIC), 2011 European*. Oct. 2011, pp. 272–275.

M. Kamper. "Effiziente HF Leistungsverstärker mit geschalteten Transistoren". In: *Electrical and Electronic Engineering for Communication Workshop - Entwicklerforum - Fachmesse*. (Ulm, DE). 2012.

C. Musolff, **M. Kamper**, Z. Abou-Chahine, and G. Fischer. "A Linear and Efficient Doherty PA at 3.5 GHz". In: *Microwave Magazine, IEEE* 14.1 (Jan. 2013), pp. 95–101. ISSN: 1527-3342. DOI: `10.1109/MMM.2012.2226998`.

M. Kamper, D. Kondakov, and G. Fischer. "Optimized Output Baluns for Current Mode Class D Power Amplifiers". In: *Microwave Conference (GeMIC), 2014 German*. Mar. 2014, pp. 1–4.

C. Musolff, **M. Kamper**, Z. Abou-Chahine, and G. Fischer. "Linear and Efficient Doherty PA Revisited". In: *Microwave Magazine, IEEE* 15.1 (Jan. 2014), pp. 73–79. ISSN: 1527-3342. DOI: `10.1109/MMM.2013.2288713`.

C. Musolff, **M. Kamper**, and G. Fischer. "Linear Doherty PA at 5 GHz". In: *Microwave Magazine, IEEE* 16.1 (Feb. 2015), pp. 89–93. ISSN: 1527-3342. DOI: `10.1109/MMM.2014.2367862`.

F. Auer, S. Schiller, and **M. Kamper**. "Linearity and efficiency improvement using envelope tracking power amplifier". In: *2016 German Microwave Conference (GeMiC)*. Mar. 2016, pp. 88–91. DOI: `10.1109/GEMIC.2016.7461563`.

M. Kamper and G. Fischer. "Optimized output baluns for wideband differential class D PAs". In: *2017 IEEE Topical Conference on RF/Microwave Power Amplifiers for Radio and Wireless Applications (PAWR)*. Jan. 2017, pp. 84–87. DOI: `10.1109/PAWR.2017.7875580`.

The digitization of the analog radio frequency (RF) domain, carried out to realize flexible, low-cost software-defined radio transmitters, has reached the power amplifier (PA).

Switched mode operation is used to implement a digital input interface and optimize the efficiency of RF amplifiers by minimizing the current-voltage overlap at the transistor. Differential (push-pull) operation is used to enhance the bandwidth of an amplifier by taking advantage of the symmetry to match even harmonics.

This work discusses differential switched mode operation to design simultaneously efficient and wideband PAs. Using the example of the current mode class-D (CMCD) amplifier, the required harmonic output impedance space is derived and optimized implementations of wideband output filters and planar baluns are shown.

The book concludes with several examples of differential switched mode PAs. Furthermore, the integration of antennas as differential loads for differential PAs is examined and an implementation of a so-called „amplitenna“ is presented.

ISBN 978-3-96147-151-5
9 783961 471515

FAU UNIVERSITY PRESS 2018